

NUREG/CR-6810
SAND2003-0840P

Overpressurization Test of a 1:4-Scale Prestressed Concrete Containment Vessel Model

Sandia National Laboratories

**U.S. Nuclear Regulatory Commission
Office of Nuclear Regulatory Research
Washington, DC 20555-0001**

**Nuclear Power Engineering Corporation
Tokyo 105, Japan**



Overpressurization Test of a 1:4-Scale Prestressed Concrete Containment Vessel Model

Manuscript Completed: March 2003
Date Published: March 2003

Prepared by
M. F. Hessheimer, E. W. Klamerus, L. D. Lambert, G. S. Rightley
Sandia National Laboratories
Albuquerque, NM 87185
Operated by
Sandia Corporation
for the U.S. Department of Energy

R. A. Dameron
ANATECH Corp.
5435 Oberlin Drive
San Diego, CA 92121

Prepared for
NRC Project Manager: J. F. Costello
U.S. Nuclear Regulatory Commission
Office of Nuclear Regulatory Research
Division of Engineering Technology
Washington, DC 20555-0001
NRC Job Code Y6131

NUPEC Project Manager: S. Shibata
Nuclear Power Engineering Corporation
System Safety Department
Tokyo 105, Japan
under FiA DE-FI04-91-AL73734



ABSTRACT

The Nuclear Power Engineering Corporation (NUPEC) of Japan and the U.S. Nuclear Regulatory Commission (NRC), Office of Nuclear Regulatory Research, cosponsored and jointly funded a Cooperative Containment Research Program at Sandia National Laboratories (SNL) from July, 1991 through December, 2002. As part of this program, a 1:4 scale model of a prestressed concrete containment vessel (PCCV) was constructed and pressure tested to failure. The prototype for the model is the containment building of Unit 3 of the Ohi Nuclear Power Station in Japan. The design accident pressure, P_d , of both the prototype and the model is 0.39 MPa (57 psi). The objectives of the PCCV model test were to simulate some aspects of the severe accident loads on containment vessels, observe the model failure mechanisms, and obtain structural response data up to failure for comparison with analytical models.

The PCCV model was designed and constructed by NUPEC and its Japanese contractors, Mitsubishi Heavy Industries, Obayashi Corp., and Taisei Corp. SNL designed and installed the instrumentation and data acquisitions systems and conducted the overpressurization tests. ANATECH Consulting Engineers conducted the pre- and posttest analyses of the model under contract to SNL.

Nearly 1500 transducers were installed on the PCCV model to monitor displacements, liner, rebar, concrete and tendon strains and tendon anchor forces. This instrumentation suite was augmented by the Soundprint[®] acoustic monitoring system, video, and still photography.

Low pressure testing, including a Structural Integrity Test to $1.125 P_d$, and an Integrated Leak Rate Test at $0.9 P_d$, was conducted in September, 2000. The Limit State Test (LST) of the model was conducted on September 27-28, 2000 by slowly pressurizing the model using nitrogen gas. A leak, presumably through a tear in the liner, was first detected at a pressure of $2.5 P_d$ and a leak rate of 1.5% mass/day was estimated. The test was terminated when the model reached a pressure of $3.3 P_d$. At this pressure, the leak rate was nearly 1000% mass/day, exceeding the capacity of the pressurization system. Posttest inspections revealed 26 tears in the 1.6mm (1/16") steel liner as the source of the leaks.

Since only limited damage and inelastic response occurred during the LST, the interior was resealed with an elastomeric membrane. The PCCV was then filled nearly full with water and repressurized on November 14, 2001. This Structural Failure Mode Test reached a maximum pressure of $3.6 P_d$ when the model ruptured violently by failure of the prestressing tendons and then the reinforcing steel.

The resulting data from all the tests are provided for comparison with pretest and posttest analyses.

CONTENTS

ABSTRACT	iii
EXECUTIVE SUMMARY	xiii
ACKNOWLEDGMENTS	xvii
ABBREVIATIONS	xix
1. INTRODUCTION	1-1
1.1 Background	1-2
1.2 Scope	1-3
1.2.1 Model Features and Scale	1-3
1.2.2 Loading	1-4
1.2.3 Response	1-5
1.3 Project Organization	1-6
1.4 Project Schedule	1-7
2. DESIGN AND CONSTRUCTION OF THE PCCV MODEL	2-1
2.1 Design	2-1
2.1.1 Liner Design Considerations	2-3
2.1.2 Concrete Design Considerations	2-4
2.1.3 Prestressing Design Considerations	2-7
2.2 Construction	2-12
2.2.1 General Construction	2-12
2.2.2 Material Properties	2-17
2.2.3 Prestressing Operations	2-31
3. INSTRUMENTATION	3-1
3.1 Background	3-1
3.1.1 Design Considerations	3-1
3.2 Types of Measurements	3-4
3.2.1 Pressure	3-4
3.2.2 Temperature	3-5
3.2.3 Displacement	3-6
3.2.4 Concrete Cracking	3-9
3.2.5 Strain Measurements	3-10
3.2.6 Tendon Measurements	3-16
3.2.7 Visual Observations	3-20
3.2.8 Acoustic Monitoring	3-20
3.3 Instrument Installation	3-22
3.3.1 Instrument Locations	3-22
3.3.2 Quality Assurance and Control	3-24
4. DATA ACQUISITION	4-1
4.1 Objectives	4-1
4.2 Hardware Description	4-1
4.2.1 Hardware Specifications	4-3
4.2.2 Gage Wiring	4-4
4.3 Software Description	4-4
4.3.1 Software Structure	4-4
4.3.2 Software Module Specifics	4-5
4.3.3 Input/Output File Structure	4-5
4.4 Miscellaneous DAS Issues	4-6
4.4.1 Loss of Power	4-6

4.4.2	Integration of DAS with Other Systems	4-6
5.	TESTING	5-1
5.1	Test Planning	5-1
5.1.1	Pressurization System Design and Operation	5-2
5.2	Test Operations	5-3
5.2.1	System Functionality Test	5-4
5.2.2	Structural Integrity Test and Integrated Leak Rate Test	5-5
5.2.3	Limit State Test	5-13
5.2.4	Structural Failure Mode Test	5-18
5.3	Test Results	5-27
5.3.1	Data Files	5-27
5.3.2	Limit State Test Results	5-32
5.3.3	Structural Failure Mode Test Results	5-73
6.	SUMMARY AND CONCLUSION	6-1
6.1	Model Design	6-1
6.1.1	Scale Artifacts	6-1
6.1.2	Material Properties	6-2
6.1.3	Prestressing System	6-2
6.2	Instrumentation and Data Acquisition	6-3
6.2.1	Displacements	6-3
6.2.2	Liner Strains	6-4
6.2.3	Rebar/Concrete Strains	6-4
6.2.4	Tendon Strains/Forces	6-5
6.2.5	Acoustic	6-5
6.2.6	Video/Still Photography	6-6
6.2.7	Data Acquisition	6-6
6.3	Testing	6-7
6.3.1	Loading	6-7
6.3.2	Failure Criteria	6-7
6.3.3	Leak Rate Measurements	6-7
7.	REFERENCES	7-1
Appendix A:	PCCV Model Design Drawings	A-1
Appendix B:	PCCV Model Material Properties	B-1
Appendix C:	As-Built Model Survey Data	C-1
Appendix D:	Final PCCV Instrumentation List	D-1
Appendix E:	PCCV Instrumentation Layout Drawings	E-1
Appendix F:	Prestressed Concrete Containment Vessel Data Acquisition System/Instrumentation Schematic ..	F-1
Appendix G:	Posttest Data Correction	G-1
Appendix H:	SFMT Instrumentation List	H-1
Appendix I:	Data File Index	I-1
Appendix J:	Data Correction for Ambient Thermal Response	J-1
Appendix K:	LST Soundprint® Acoustic System Reports	K-1
Appendix L:	Metallurgical Analysis of PCCV Liner Tears	L-1

FIGURES

Figure 1.1	Ohi Nuclear Power Station, Ohi-cho, Fukui, Japan	1-2
Figure 1.2	PCCV Model Elevation and Cross-Section	1-4
Figure 1.3	Plan of Containment Technology Test Facility-West	1-8
Figure 2.1	Elevation of PCCV Prototype and Potential Failure Locations	2-2
Figure 2.2	Liner Anchor Layout	2-4
Figure 2.3	PCCV Prototype Equipment Hatch Arrangement	2-6
Figure 2.4	PCCV Prototype Personnel Airlock Arrangement	2-6
Figure 2.5	PCCV Prototype Main Steam Penetration Arrangement	2-6
Figure 2.6	PCCV Prototype Feed Water Penetration Arrangement	2-6
Figure 2.7	PCCV Concrete Lifts and Strengths	2-8
Figure 2.8	Arrangement of Reinforcing in the PCCV Prototype and Model at the Wall-Base Junction	2-9
Figure 2.9	PCCV Prototype and Model Tendon Design Stress Profiles	2-13
Figure 2.10	PCCV Model Layout	2-15
Figure 2.11	Aerial View of CTTF-West during PCCV Construction (March, 1999)	2-16
Figure 2.12	Placement of PCCV Mudmat	2-18
Figure 2.13	Basemat Rebar Support Frame	2-18
Figure 2.14	Basemat Bottom Bars and Vertical Ties	2-18
Figure 2.15	Measuring Rebar Location	2-18
Figure 2.16	F1 Formwork	2-19
Figure 2.17	Placing F1 Concrete	2-19
Figure 2.18	Measuring Concrete Slump	2-19
Figure 2.19	Concrete Test Cylinders and Beams	2-19
Figure 2.20	F2 Rebar Erection	2-20
Figure 2.21	F3 Rebar	2-20
Figure 2.22	F3 Rebar and Formwork	2-20
Figure 2.23	Basemat Top Rebar (F3) and Wall Dowels	2-20
Figure 2.24	F3 Concrete Placement	2-21
Figure 2.25	F4 Concrete	2-21
Figure 2.26	Wall Mock-Up Rebar	2-21
Figure 2.27	Wall Mock-up Form w/ Concrete ‘Window’	2-21
Figure 2.28	Delivery of Liner Panels	2-22
Figure 2.29	Liner Panels after ‘Uncrating’	2-22
Figure 2.30	Instrumentation Frame Column ‘Trees’	2-22
Figure 2.31	Instrumentation Frame Erection	2-22
Figure 2.32	Instrument Frame Erection	2-23
Figure 2.33	Completed Instrument Frame	2-23
Figure 2.34	Liner Panel Erection	2-23
Figure 2.35	Dome Liner Erection	2-23
Figure 2.36	Liner Panels with Jigs	2-24
Figure 2.37	Liner Panel Instrumentation	2-24
Figure 2.38	Liner Strain Gages after Welding	2-24
Figure 2.39	Close-Up of Liner Strain Gages near Weld	2-24
Figure 2.40	Inner Rebar at M/S Penetrations	2-25
Figure 2.41	Installation of Inner Dome Rebar	2-25
Figure 2.42	Tendon Sheath Support Frame	2-25
Figure 2.43	Dome Tendon Sheaths and Support Frame	2-25
Figure 2.44	PCCV Model Tendon Sheaths	2-26
Figure 2.45	Outer Rebar for C1	2-27
Figure 2.46	C1 Formwork Installation	2-27
Figure 2.47	Placing C1 Concrete	2-27
Figure 2.48	Installation of Instrumented Hoop Tendon	2-27
Figure 2.49	C2 Formwork	2-28
Figure 2.50	C4 Concrete Placement	2-28
Figure 2.51	D1 Formwork Erection	2-28

Figure 2.52	D3 Concrete Placement	2-28
Figure 2.53	Final Basemat Concrete Lifts	2-29
Figure 2.54	Completed PCCV Model	2-30
Figure 2.55	Pulling Hoop Tendons	2-32
Figure 2.56	PCCV Model Tensioning Sequence	2-34
Figure 2.57	Tensioning Hoop Tendons	2-37
Figure 2.58	Tensioning Hardware Assembly and Load Cell	2-37
Figure 2.59	Tendon H11 Tensioning Force Time History	2-38
Figure 2.60	Tendon H35 Tensioning Force Time History	2-38
Figure 2.61	Tendon H53 Tensioning Force Time History	2-39
Figure 2.62	Tendon H67 Tensioning Force Time History	2-39
Figure 2.63	Tendon H68 Tensioning Force Time History	2-40
Figure 2.64	Tendon V37 Tensioning Force Time History	2-40
Figure 2.65	Tendon V46 Tensioning Force Time History	2-41
Figure 2.66	Tendon V85 Tensioning Force Time History	2-41
Figure 2.67	H11 Tendon Force Distribution, Elev. 1854	2-43
Figure 2.68	H35 Tendon Force Distribution, Elev. 4572	2-43
Figure 2.69	H53 Tendon Force Distribution, Elev. 6579	2-44
Figure 2.70	H67 Tendon Force Distribution, Elev. 8153	2-44
Figure 2.71	H68 Tendon Force Distribution, Elev. 8280	2-45
Figure 2.72	V37 Tendon Force Distribution, Azimuth 240 Degrees	2-45
Figure 2.73	V46 Tendon Force Distribution, Azimuth 135 Degrees	2-46
Figure 2.74	V85 Tendon Force Distribution, Azimuth 325 Degrees	2-46
Figure 3.1	Cardinal Instrumentation Layout Lines	3-3
Figure 3.2	CPOT Mounted on Instrumentation Frame and Attachment to PCCV Liner	3-7
Figure 3.3	LVDTs at Wall-Base Junction (Azimuth 324 degrees, Elev. 0.0 and 250.0)	3-8
Figure 3.4	TLDT Mounted on Instrumentation Frame and Attachment to PCCV Liner	3-9
Figure 3.5	External LVDT Measuring Displacement between Basemat and Mudmat	3-10
Figure 3.6	Rebar Strain Gage	3-12
Figure 3.7	Rebar Strain Gages Installed in PCCV Model	3-12
Figure 3.8	Concrete Strain Gage Bars	3-13
Figure 3.9	Sample Rebar and Gage Bar Strain Gages	3-13
Figure 3.10	SOFO Fiber Optic Strain Gage	3-15
Figure 3.11	Liner and Liner Anchor Strain Gages	3-16
Figure 3.12	Grid Layout around Inside of E/H	3-17
Figure 3.13	HBM Load Cell (a) Installation Jig, (b) In-Place	3-19
Figure 3.14	Geokon Load Cell (a) Installation Jig, (b) In-Place	3-19
Figure 3.15	Tendon Strain Instrumentation Arrangement	3-21
Figure 3.16	Video and Camera Layout	3-22
Figure 3.17	Interior and Exterior Acoustic Sensor (clamps during installation only)	3-22
Figure 3.18	Displacement Instrumentation Locations	3-25
Figure 3.19	Rebar Instrumentation Locations	3-26
Figure 3.20	Liner and Liner Anchor Instrumentation Locations	3-27
Figure 3.21	Tendon Instrumentation Locations	3-28
Figure 3.22	Concrete Instrumentation Locations	3-29
Figure 3.23	Temperature Instrumentation Locations	3-30
Figure 4.1	PCCV/DAS Hardware Configuration	4-2
Figure 4.2	DAS Software Tree	4-5
Figure 4.3	Top-Down Data File Folder Structure	4-7
Figure 4.4	Basic PCCV Data Flow Diagram	4-8
Figure 5.1	Original Pressurization and Depressurization Sequence	5-1
Figure 5.2	Final Pressurization Plan	5-2
Figure 5.3	Pressurization System Schematic	5-3
Figure 5.4	PCCV Test Organization	5-4
Figure 5.5	System Functionality Test Pressure Time History	5-5
Figure 5.6	System Functionality Test Leak Rates	5-6

Figure 5.7 Structural Integrity and ILRT Pressure and Temperature Time Histories	5-6
Figure 5.8 Concrete Crack Map Grid	5-8
Figure 5.9 Integrated Leak Rate Test Leak Rates	5-9
Figure 5.10 Pre-SIT Cracks at Azimuth. 350 degrees, Elev. 4680 to 6200 (Grid 45)	5-10
Figure 5.11 Post-SIT Cracks at Azimuth. 350 degrees, Elev. 4680 to 6200 (Grid 45)	5-11
Figure 5.12 SIT/ILRT Radial Displacement at Cylinder Midheight (Elev. 4680)	5-11
Figure 5.13 SIT/ILRT Vertical Displacement at Springline (Elev. 10750)	5-12
Figure 5.14 PCCV SIT/ILRT, LST, SFMT Exclusion Zone	5-12
Figure 5.15 Limit State Test Pressure and Average Temperature	5-13
Figure 5.16 LST Calculated Leak Rates at 1.5, 2.0 and 2.5 P _d	5-14
Figure 5.17 Internal Acoustic Sensor Signals at the E/H	5-15
Figure 5.18 LST Pressure Time History, 2.5 to 3.3 P _d	5-15
Figure 5.19 LST Pressure and Flow Rates at Maximum Pressure	5-16
Figure 5.20 LST - Estimated Leak Rates (2.5-3.1 P _d)	5-17
Figure 5.21 LST Estimated Terminal Leak Rates	5-17
Figure 5.22 Post-LST Cracks at Azimuth 350 degrees, Elev. 4680 to 6200 (grid 45)	5-18
Figure 5.23 LST Radial Displacement at Azimuth 135 degrees, Elev. 4680	5-19
Figure 5.24 PCCV Structural Failure Mode Test Concept	5-20
Figure 5.25 Test Specimen of Elastomeric Lining	5-21
Figure 5.26 SFMT Displacement Transducer Layout	5-22
Figure 5.27 Pre-SFMT Leak Test Pressure and Temperature	5-23
Figure 5.28 Pre-SFMT Leak Rate Test	5-24
Figure 5.29 Pre-SFMT Leak Test Acoustic Data	5-24
Figure 5.30 Pre-SFMT Hydrostatic Pressures	5-25
Figure 5.31 SFMT Pressure Time Histories	5-26
Figure 5.32 SFMT Wire Break Events vs. Pressure vs. Displacement	5-26
Figure 5.33 SFMT Pressurization System Data	5-27
Figure 5.34 SFMT: Rupture of the PCCV Model	5-28
Figure 5.35 PCCV Model after the SFMT	5-29
Figure 5.36 PCCV Test Data File Matrix	5-30
Figure 5.37 Radial Displacement at Azimuth 135 degrees, Elev. 6200	5-31
Figure 5.38 Radial Displacement History at Azimuth 135 degrees, Elev. 6200 (DT-R-Z6-01)	5-31
Figure 5.39 LST - Radial Displacement at Azimuth 135 degrees	5-34
Figure 5.40 LST - Radial Displacement at Azimuth 324 degrees	5-34
Figure 5.41 LST - Radial Displacement (DOR) at EL 4680	5-35
Figure 5.42 LST - Vertical Displacements (DOR) at Springline, El. 10750	5-35
Figure 5.43 LST - Deformation at Azimuth 90 degrees and 135 degrees (D and Z) × 100	5-38
Figure 5.44 LST - Deformation at Azimuth 240 degrees and 324 degrees (I and L) × 100	5-39
Figure 5.45 LST - Deformation at Elev. 4680 (5) × 100	5-40
Figure 5.46 LST - Free-Field Liner Hoop Strains	5-42
Figure 5.47 Liner Tear (#15) at E/H	5-42
Figure 5.48 Equipment Hatch Liner Strain Gage Layout (Inside View)	5-43
Figure 5.49 E/H Liner Strains at 'Left' Edge of Embossment	5-43
Figure 5.50 E/H Liner Strains at 'Right' Edge of Embossment	5-44
Figure 5.51 E/H Liner Strains at 'Left' Corners of Embossment	5-44
Figure 5.52 Liner Strains (DOR) at M/S (Ref. D-SN-P-220)	5-45
Figure 5.53 Liner Strains (DOR) at F/W (Ref. D-SN-P-220)	5-46
Figure 5.54 Liner Tear (#3) and Strain Gages at F/W Penetration	5-46
Figure 5.55 Horizontal Stiffener Detail at Vertical Seam Weld ('Rathole') near D7	5-47
Figure 5.56 Liner Strains (DOR) at D7 Anchor Detail (Ref. R-SN-P-209, a.4)	5-48
Figure 5.57 Comparison of Strain at Z6 (Azimuth 135 degrees, Elev. 6280)	5-49
Figure 5.58 Arrangement of Gage Bar Strain Gages at Azimuth 135 degrees	5-50
Figure 5.59 LST Gage Bars Strain at Azimuth 135 degrees (due to pressure only)	5-51
Figure 5.60 LST - Vertical Load Cells	5-53
Figure 5.61 LST - Hoop Load Cells at 90 degrees	5-53
Figure 5.62 LST - Hoop Load Cells at 270 degrees	5-54

Figure 5.63	LST - H68 Tendon Strains	5-54
Figure 5.64	H11 Tendon Force Distribution, El. 1854	5-55
Figure 5.65	H35 Tendon Force Distribution, Elev. 4572	5-55
Figure 5.66	H53 Tendon Force Distribution, Elev. 6579	5-56
Figure 5.67	H67 Tendon Force Distribution, Elev. 8153	5-56
Figure 5.68	H68 Tendon Force Distribution, Elev. 8280	5-57
Figure 5.69	V37 Tendon Force Distribution, Azimuth 240 degrees	5-58
Figure 5.70	V46 Tendon Force Distribution, Azimuth 135 degrees	5-59
Figure 5.71	V85 Tendon Force Distribution, Azimuth 325 degrees	5-59
Figure 5.72	LST - Tendon Ping Acoustic Events	5-60
Figure 5.73	LST - Tendon Ping Event vs. Pressure Histogram	5-60
Figure 5.74	LST - Concrete Cracking Acoustic Events	5-61
Figure 5.75	LST - Concrete Cracking Events vs. Pressure Histogram	5-61
Figure 5.76	Post-LST Concrete Crack Map	5-62
Figure 5.77	Post-LST Liner Tears	5-64
Figure 5.78	Liner Tears and Acoustic Event Locations	5-65
Figure 5.79	Post-LST Liner Tear (#2) and Liner Buckling	5-66
Figure 5.80	Tear #7 at E/H	5-66
Figure 5.81	Tear #12 at E/H	5-67
Figure 5.82	Tear #13 at E/H	5-67
Figure 5.83	Tear #15 at E/H	5-68
Figure 5.84	Tear #2, Free-Field	5-68
Figure 5.85	Tear #16 at Rathole Detail	5-69
Figure 5.86	Close-Up of Tear #13 after Removal of Paint	5-70
Figure 5.87	Liner Specimen at Tear #2	5-70
Figure 5.88	Liner Specimen at Tear #15	5-71
Figure 5.89	E/H Displacement at Grid	5-72
Figure 5.90	E/H Post-LST Displacement	5-72
Figure 5.91	SFMT - Radial Displacement at Azimuth 135 degrees (Z)	5-73
Figure 5.92	SFMT - Radial Displacement at Azimuth 325 degrees (L)	5-74
Figure 5.93	SFMT - Radial Displacement at Elev. 4680 (5)	5-74
Figure 5.94	SFMT - Radial Displacement at Azimuth 135 degrees, Elev. 6200	5-75
Figure 5.95	SFMT - Vertical Displacement at Apex	5-76
Figure 5.96	SFMT Vertical Displacements at Springline (El. 10750) and Apex	5-77
Figure 5.97	SFMT - Deformation at Azimuth 135 Degrees (Z) $\times 100$	5-78
Figure 5.98	SFMT - Deformation at Azimuth 324 Degrees (L) $\times 100$	5-79
Figure 5.99	SFMT - Deformation at Elev. 4680 (5) $\times 100$ - $0P_d$ to $3.63 P_d$	5-80
Figure 5.100	SFMT - Deformation at Elev. 4680 (5) $\times 100$ - $3.0P_d$ to $3.63 P_d$	5-81
Figure 5.101	SFMT Exterior Liner Strains	5-82
Figure 5.102	SFMT - Free-Field Hoop Rebar Strains	5-82
Figure 5.103	SFMT - Free-Field Meridional Rebar Strains	5-83
Figure 5.104	SFMT - Meridional Rebar Strains at Wall-Base Junction	5-83
Figure 5.105	SFMT - Concrete (SOFO) Strains	5-84
Figure 5.106	SFMT - Instrumented Hoop Tendon Anchor Forces	5-85
Figure 5.107	SFMT - Instrumented Vertical Tendon Anchor Forces	5-85
Figure 5.108	SFMT - Tendon H53 Strains	5-86
Figure 5.109	SFMT - Tendon H68 Strain	5-87
Figure 5.110	SFMT - Tendon V46 Strains	5-87
Figure 5.111	SFMT - Tendon H11 Force Distribution (Elev. 1854)	5-88
Figure 5.112	SFMT - Tendon H35 Force Distribution (Elev. 4572)	5-88
Figure 5.113	SFMT - Tendon H53 Force Distribution (Elev. 6579)	5-89
Figure 5.114	SFMT - Tendon H67 Force Distribution (Elev. 8153)	5-89
Figure 5.115	SFMT - Tendon H68 Force Distribution (Elev. 8280)	5-90
Figure 5.116	SFMT - Tendon H35 Computed and Measured Force Distribution	5-91
Figure 5.117	SFMT - Tendon V37 Force Distribution at Azimuth 240 Degrees	5-91
Figure 5.118	SFMT - Tendon V46 Force Distribution at Azimuth 135 Degrees	5-92

Figure 5.119 SFMT - Tendon V85 Force Distribution at Azimuth 325 Degrees	5-92
Figure 5.120 SFMT - Wire Break Map	5-93
Figure 5.121 SFMT - Acoustic Event and Pressure Time History	5-94
Figure 5.122 SFMT - Rupture Map	5-95
Figure 5.123 SFMT - Rebar and Tendon Strands at the Rupture Line	5-96
Figure 5.124 SFMT - Model Displacements	5-97
Figure 5.125 SFMT - Debris Map	5-98

TABLES

Table 2.1 Properties of Liner Materials	2-3
Table 2.2 JIS G 3112 Reinforcing Steel Properties	2-8
Table 2.3 JIS G 3112 Bar Properties	2-8
Table 2.4 PCCV Model Tendon Strand Properties	2-10
Table 2.5 PCCV Model Design Prestressing Anchor Forces	2-11
Table 2.6 PCCV Model Average Concrete Properties	2-31
Table 2.7 Model Prestressing Schedule	2-35
Table 2.8 Instrumented Tendon Gage Performance during Prestressing	2-42
Table 2.9 Prestressing Data Summary	2-42
Table 3.1 Instrumentation Objectives	3-2
Table 3.2 Pressure Transducer Specifications	3-4
Table 3.3 Thermocouple Specifications	3-5
Table 3.4 RTD Specifications	3-6
Table 3.5 Displacement Transducer Specifications (CPOT)	3-7
Table 3.6 LVDT Specifications	3-8
Table 3.7 Temposonics Linear Displacement Transducer Specifications (TLDT)	3-9
Table 3.8 Strain Gage Specifications (Rebar & Tendon wire)	3-11
Table 3.9 Strain Gage Specifications (Concrete Gage Bars)	3-14
Table 3.10 Strain Gage Specifications (Fiber Optic Gages)	3-14
Table 3.11 Strain Gage Specifications (Liner & Liner Anchor)	3-15
Table 3.12 Load Cell Specifications	3-18
Table 3.13 Tensmeg Gage Specifications	3-19
Table 3.14 Instrumentation List Format	3-23
Table 3.15 Gage Type Nomenclature	3-23
Table 3.16 PCCV Instrument Summary	3-24
Table 3.17 PCCV Instrumentation Procedures Summary	3-24
Table 4.1 Description of Raw and Reduced Data for the PCCV Test	4-7
Table 5.1 PCCV Test Personnel Matrix	5-4
Table 5.2 Summary of ASME B&PV Code SIT Instrumentation Requirements	5-7
Table 5.3 Date File (Excel®) Format	5-33
Table 5.4 LST Liner Strain Summary	5-41
Table 5.5 Rebar Strain Summary	5-48
Table 5.6 SFMT Video Event Times	5-95

EXECUTIVE SUMMARY

Introduction

The Nuclear Power Engineering Corporation (NUPEC) of Japan and the U.S. Nuclear Regulatory Commission (NRC), Office of Nuclear Regulatory Research co-sponsored and jointly funded a cooperative containment research program at Sandia National Laboratories¹ (SNL). Tests of two containment models were authorized under this program. The first model, a mixed-scale model of an Improved Mark-II type steel containment vessel (SCV) for a Boiling Water Reactor (BWR), was tested in December 1996. The second model tested was a 1:4-scale model of the prestressed concrete containment vessel (PCCV) of an actual nuclear power plant in Japan, Ohi-3. Ohi-3 is an 1127 MWe Pressurized Water Reactor (PWR) unit, one of four units comprising the Ohi Nuclear Power station located in Fukui Prefecture, owned and operated by Kansai Electric Power Company. The scale of the PCCV model was a uniform 1:4, with minor exceptions to accommodate fabrication and construction concerns. This was judged to be the minimum scale that would allow the steel liner to be constructed from prototypical materials and fabricated with details and procedures that were representative of the prototype.

By definition, the scope of this program was limited to addressing the capacity of containment vessels to loads beyond the design basis, the so-called severe accident loads. Design accident loads for light water reactor containment vessels are typically based on the loss-of-coolant accident (LOCA) and are defined by bounding pressure and temperature transients. The design accident pressure, P_d , of both the prototype and the model is 0.39 MPa (57 psi). The term “severe accidents” is used to describe an array of conditions that could result in loads, in excess of the design basis loads, on the containment. The definition of severe accident loads, which is not as rigorous as the design basis loads definition, results from a consideration of various postulated failure scenarios of the primary nuclear system, up to and including a complete core meltdown and breach of the reactor pressure vessel. The resulting pressure and thermal loading characteristics depend on the unique features of the nuclear steam supply (NSS) system and the containment structure in addition to the postulated accident.

For this test program, it was necessary to decide whether both thermal and pressure loads would be applied to the model, either separately or simultaneously, what the pressurization medium should be, and whether the transient characteristics of these loads should be considered. Programmatically, the decision to perform a *static pneumatic* overpressurization test at *ambient temperature* was dictated by risk and cost considerations and previous experience.

Design and Construction

Within the cooperative framework agreed on by NUPEC and the NRC, NUPEC and its Japanese contractors designed and constructed the PCCV model at SNL’s Containment Technology Test Facility-West (CTTF-W). This test facility was specially constructed by SNL on land temporarily permitted for this purpose on Kirtland Air Force Base (KAFB), Albuquerque, New Mexico, USA. The prime contractor to NUPEC for the construction of the PCCV model was Mitsubishi Heavy Industries (MHI), who also designed and constructed the prototype plant, Ohi-3. In addition to overall design and construction, MHI designed, fabricated and erected the steel liner and all primary steel pressure-retaining components. Supporting MHI for the reinforced concrete portions of the model and ancillary structures were several subcontractors. Obayashi Corp., a large Japanese Architect/Engineer (A/E) and construction company, performed the detailed design of the PCCV model and Taisei Corp, another large A/E/Contractor, was the construction manager. Taisei retained the U.S. construction firm, Hensel Phelps Construction Co., Greeley, CO for general construction work and management of day-to-day construction operations. MHI pre-fabricated portions of the steel liner and the penetrations at their Kobe Shipyard and transported these components to the CTTF-W for final erection. The balance of the model was constructed on-site.

¹ This work is jointly sponsored by the Nuclear Power Engineering Corporation and the U.S. Nuclear Regulatory Commission. The work of the Nuclear Power Engineering Corporation is performed under the auspices of the Ministry of Economy, Trade and Industry, Japan. Sandia is a multiprogram laboratory operated by Sandia Corporation, a Lockheed Martin Company, for the U.S. Department of Energy under Contract Number DE-AC04-94AL85000

Instrumentation and Data Acquisition

NUPEC funded SNL to provide programmatic and model design support, instrument the model, and design and assemble the data acquisition system. The PCCV model instrumentation suite was designed to measure the global behavior in free-field locations of the model and the local structural response of the model near discontinuities. Global response measurements included both displacements referenced to a global or fixed reference and strain measurements at a regular pattern of azimuths and elevations to characterize the overall shape of the model. Local response measurements consisted of strain measurements of individual structural elements (i.e. liner, rebar, tendons, concrete) to characterize the force distribution near structural discontinuities. In areas absent of structural discontinuities or where membrane behavior was expected to dominate the response, relatively simple arrays of transducers were specified. Where structural discontinuities were judged to be significant more complex arrays of strain gages were utilized. Both hoop and meridional strains were measured.

Pressure measurement requirements included careful measurement of the PCCV interior pressure for purposes of leak detection, and to a lesser extent, leak rate measurement, characterization of the mechanical response as a function of pressure and to control the pressurization rate. It should be noted, that while measurement of leak rates was not a primary objective, detection of the onset of leakage requires the calculation of very small leak rates with relatively high accuracy.

As implied by the name, the unique feature of the PCCV model is the prestressing system, comprised of the vertical and hoop tendons and associated hardware. Special efforts were made to monitor the response of the prestressing system, both prior to and during pressure testing. An extensive effort was undertaken to develop and demonstrate the reliability of the tendon instrumentation. The resulting system was comprised of two types of strain gages to monitor the strain, and by calculation, the force distribution along the length of selected tendons along with load cells to measure the forces at the tendon anchors. Since the behavior of the tendons and the overall response of the model to the pressure load would be directly affected by the initial prestressing forces, the response of the PCCV model was monitored continuously from the start of prestressing through the subsequent pressure tests.

While these force, strain and displacement measurements provide accurate information on the response of the model at discrete locations, it was desirable to have some method to monitor the overall response of the model in the (likely) event that some significant response occurs at locations remote from any transducer. The displacement transducers reflect, to a greater extent than the strain or force transducers, the overall response of the model but might still miss other local response modes. This deficiency was addressed by including an extensive array of acoustic and, to a lesser degree, video/photographic monitoring of the PCCV model. While more qualitative in nature than the discrete response measurements, some quantitative information could be obtained from these monitoring systems. The acoustic system, in particular, was designed to detect the onset of liner tearing and leakage, along with concrete cracking and rupture of tendon wires or rebar. Similarly, video and still photography was used to document the development and distribution of concrete cracking, detect liner tearing at discrete locations during pressure testing and capture any unanticipated response modes.

Analysis

NRC funded SNL to perform preliminary, pre- and posttest analyses of the model. This analytical work was subcontracted by SNL to ANATECH Consulting Engineers, San Diego, CA. The preliminary analyses supported design studies, identified critical response modes and assisted in locating instrumentation. The pretest analysis consisted of the development and analysis of detailed numerical models in an attempt to predict the response of the PCCV to the test pressures and predict the capacity and most probable failure mode. The posttest analysis compared the test results to the pretest predictions, investigated and demonstrated changes in the modeling methods to improve the comparison with the test results and provided insights into the response observed during the pressure tests. The pre- and posttest analyses have been reported separately and are not included in this report.

NUPEC and NRC also jointly provided funding to share the costs associated with organizing and conducting a pretest Round Robin analysis. The Round Robin analysis euphemistically refers to an activity where a number of nuclear safety research organizations from government, industry and academia in the United States, Japan and other countries are provided with a common set of data on the model test (design drawings, material properties, test specifications, etc.) and then complete independent predictions of the model response, failure mode and pressure capacity. SNL was the focal

point for this effort in terms of disseminating and consolidating the work of the participating organizations. Seventeen independent organizations, including NUPEC and SNL, participated in this effort, performing pretest analyses and meeting before and after the PCCV model test to discuss and compare analysis results. The efforts of these Round Robin participants are documented in separate NUREG Contractor Reports. While a formal posttest Round Robin exercise was not conducted for the PCCV, most of the participants attended a posttest workshop and have reported the results of their posttest analyses independently.

Testing

NRC funded the planning and conduct of test operations. After extensive discussions between NUPEC, the NRC and SNL, a detailed Test Plan was developed by SNL to describe the conduct of the pressurization tests of the PCCV model. A final series of three tests were agreed upon:

- A leak check and System Functionality Test (SFT) @ $0.5 P_d$ (2.0 kg_f/cm² or 28.4 psig)
- A Structural Integrity Test (SIT) @ $1.125 P_d$ followed by an Integrated Leak Rate Test (ILRT) @ $0.9 P_d$
- A Limit State Test (LST) to the static pressure capacity of the PCCV model (or the pressurization system, whichever comes first)

The *pneumatic* Limit State Test was the final test in the original program plan. This test was terminated following a functional failure, i.e. a leak, in the PCCV model, with only limited structural damage occurring. Subsequently, it was decided to re-pressurize the PCCV model, prior to demolition, in an attempt to observe larger inelastic response and, possibly, a global structural failure. This Structural Failure Mode Test (SFMT) was a combined *pneumatic-hydrostatic* test, where the PCCV model was filled nearly full with water, to reduce the volume of gas to be pressurized, and nitrogen gas was used to generate the overpressure.

The SFT was conducted beginning approximately 9:00 AM, July 18, 2000. The model was pressurized using nitrogen to $0.5 P_d$ (0.2 MPa or 28.4 psig) in three increments holding pressure for one hour or longer at each step, depending on the duration needed to perform all system functionality and leak checks. The model was then isolated and a leak rate check was performed by monitoring the model pressure and temperature for approximately 18 hours. After 18 hours, the calculated leak rate was 0.15% mass/day, which was interpreted as confirming that the model was leak-tight. After the model leak rate check, the model was allowed to depressurize through a pair of orifice plates calibrated to leak rates of 1% and 10% mass/day to perform a calibration test on the leak rate measurement instrumentation. The calculated leak rates for each test were 0.87% and 7.86%, respectively, indicating that the leak rate instrumentation was capable of accurately detecting a leak of 1% mass per day, which is the goal specified for the ILRT. The SFT was concluded on July 20 by opening the vent valve, allowing the model to depressurize.

The Structural Integrity Test and the Integrated Leak Rate Test were conducted on September 12-14, 2002 as a combined test, with the ILRT following immediately after the SIT. The SIT/ILRT reproduced the pre-operational tests conducted at the prototype plant and allows for a comparison of the model's elastic response characteristics and leak behavior with the prototype and pretest analyses. The SIT test pressure, P_{SIT} , was $1.125 P_d$. After the SIT pressure was maintained for one hour, the PCCV model was depressurized to the ILRT pressure, $0.9 P_d$. The calculated leakage rate at P_{ILRT} , L_{tm} , after 24 hours at $0.9 P_d$, was 0.06% mass/day.

The Limit State Test (LST) was designed to fulfill the primary objectives of the PCCV test program, i.e. to investigate the response of representative models of nuclear containment structures to pressure loading beyond the design basis accident and to compare analytical predictions to measured behavior. The LST was conducted after the SIT and ILRT were completed and the data from these tests evaluated. The PCCV model was depressurized between the SIT/ILRT and the LST. The LST began at 10:00 AM, Tuesday, September, 26, 2000 and continued, without depressurization, until the test was terminated just before 5:00 PM on Wednesday, September 27. The model was pressurized in increments of approximately $0.2 P_d$ to $1.5 P_d$ when a leak check was conducted yielding a leak rate of 0.48% mass/day. Pressurization of the model continued in increments of approximately $0.1 P_d$ to $2.0 P_d$ when a second leak check resulted in a calculated leak rate of 0.003%, i.e. essentially zero. Pressurization of the model resumed in increments of $0.1 P_d$ to $2.5 P_d$. At $2.4 P_d$, the acoustic system operator reported hearing a change in the acoustic output which might indicate that "something had happened". The model was isolated for a third leak check and after approximately 1-1/2 hours, a fairly stable leak rate

of 1.63% mass per day was calculated, indicating that the model was leaking, most likely from a tear in the liner in the vicinity of the E/H. The average hoop strain at $2.5P_d$, coinciding with the onset of liner tearing and leakage was 0.18%.

After concluding that the model had functionally failed between 2.4 and $2.5 P_d$, the next goal was to continue to pressurize the model as high as possible to collect data on the inelastic response of the structure and to observe, if possible, a structural failure mode. Pressurization continued in increments of $0.05 P_d$. The pressure was increased to slightly over $3.3 P_d$ before the leak rate exceeded the capacity of the pressurization system and the test was terminated. After the model had completely depressurized, it was purged with fresh air, the E/H was removed and a detailed inspection of the inside of the model revealed 26 discrete tears in the liner, all located at vertical field welds. Extensive examination and metallurgical analysis of the liner after the test revealed that fabrication defects contributed to nearly all of the liner tears.

Almost immediately after the completion of the LST, there was a recognition that while the PCCV model had demonstrated its capacity to resist pressures well above the design pressure and had exhibited liner tearing and leaking as the functional failure mode, the test objectives were not fully met with respect to observing large inelastic deformations, for comparison with analyses. NUPEC and NRC approved a concept proposed by SNL to seal the interior surface of the liner with an elastomeric membrane, fill the model with water to 1.5m (5') from the dome apex, approximately 97% of the interior, and repressurize the remaining gas pocket with nitrogen until the model failed or pressure could not be maintained.

The Structural Failure Mode Test (SFMT) began shortly after 10:00 AM on Wednesday, November 14, 2001. The model was continuously pressurized at a rate of approximately 0.035 MPa/min (5 psi/min). All active sensors were continuously scanned at intervals of approximately 30 seconds and the video cameras were continuously recording the response of the model. As the pressure was increased, evidence of leakage was visible by increasing wetting of the concrete surface. At 10:38 AM, the effective pressure in the model equaled the peak pressure achieved during the LST, $3.3 P_d$. At approximately 10:39 AM, the acoustic system recorded a very high noise level event which was interpreted as the breaking of a tendon wire. At this point in the test, events occurred very quickly. Shortly after detecting the wire break, a small spray of water was observed at approximately 0° azimuth and additional tendon wire breaks were detected by the acoustic system with increasing frequency. The rate of pressurization was decreasing and the nitrogen flow rate was increased to maintain the pressurization rate. Pressurization of the model continued until a second spray of water was observed and then, suddenly, at 10:46:12.3, at an effective pressure of $3.63 P_d$ (1.42 MPa or 206.4 psig) the PCCV model ruptured violently at $\sim 6^\circ$ azimuth near the mid-height of the cylinder. The maximum average hoop strain at the peak pressure of $3.63 P_d$ was 1.02%. The model continued to expand after reaching the peak pressure and the maximum hoop strain recorded just prior to rupture was 1.65%.

Conclusions

The over-pressurization tests of the 1:4-scale PCCV model represent a significant advance in understanding the capacity of nuclear power plant containments to loads associated with severe accidents. The data collected during the tests, as well as the response and failure modes exhibited, will be used for many years to come to benchmark numerical simulation methods used to predict the response of concrete containment structures. While lessons for actual plants can and should be drawn from this and previous large scale containment model tests, these insights are beyond the scope of this report and will be addressed in a future effort. The reader is cautioned *not* to draw direct conclusions regarding the pressure capacity of actual plants from these tests or interpret these results as a demonstration of the prototype capacity. The PCCV model tests have demonstrated the importance of the unique details and as-built characteristics of the model on the ultimate capacity. Any efforts to estimate the capacity of an actual containment must address the unique features of the plant under consideration.

With the completion of the PCCV tests, restoration of the test site and submittal of the test reports, the NUPEC/NRC Cooperative Containment Research Program was formally concluded on December 31, 2002.

ACKNOWLEDGMENTS

No one person was responsible for the success of the PCCV Test Project. Without the dedicated efforts of a team including the project sponsors, partners and contractors and supporting organizations, the outcome of this project would have been far less successful than it has proven to be. It is, however, difficult to acknowledge everyone who contributed to this project without unconsciously omitting some individuals. I would like to begin therefore by apologizing to those anonymous, but no less important contributors I may have overlooked.

But the contributions of some individuals are too significant to overlook. I would like to begin, therefore, by acknowledging the program managers of the sponsoring organizations, NUPEC and the U.S. NRC. Dr. James F. Costello, U.S. NRC, has been the guiding force behind the containment integrity research conducted at SNL for over 25 years, including this project. His perseverance, support, and guidance has been invaluable and it is no overstatement to say that this project may never have happened without his involvement. Similarly, the NUPEC project directors: Dr. Kenji Takumi, Dr. Hideo Ogasawara and Dr. Takshi Kiguchi; and the project managers: Mr. Akira Nonaka, Mr. Tomoyuki Matsumoto, Mr. Masaki Iriyama and Mr. Satoru Shibata ensured that this program had the financial and technical resources to meet the program objectives in order to make a significant contribution to the international nuclear power industry.

There were many Japanese colleagues who, as primary contractors or subcontractors to NUPEC, contributed to the planning, design, and construction of the PCCV model. These included, from Mitsubishi Heavy Industries: Toshisada Kato, Kaoru Nagata, Kazutoshi Hayashi, Nozumo Watanabe, Tomoyuki Kitani, Hiroshi Urakawa, Ryuichi Oshima, and Hiroshi Matsuoka; from Obayashi Corporation: Katsuhiko Umeki, Katsuyoshi Imoto, and Takako Kashiwase; and from Taisei Corporation: Yasuyuki Murazumi, Yutaka Kobayashi, and Shiro Mitsugi. General Construction of the model was managed by Hensel Phelps Construction Company whose on-site staff included: Guy Mills, Tina Connelly, Subba Padmendra and Norman 'Butch' Brackett.

SNL management support was provided by Walter von Riesenmann and Dennis Berry. I am especially indebted to Brad Parks who was the initial program manager responsible for the planning and organization of an excellent project team. The dedication and professionalism exhibited by the SNL project team was unsurpassed in my experience and I am fortunate and proud to have had the opportunity to work with such an outstanding group of individuals. The primary project team included Dave Pace (PCCV Lead Engineer), L. Dwight Lambert (Site Manager and Instrumentation Leader), Eric Klamerus (Instrumentation and Pressurization System Engineer), Gina Rightley (DAS Lead Engineer), Mike Rightley (DAS and Instrumentation Design), Mike Luker (DAS and Instrumentation Engineer), Vincent Luk (Analysis and Round Robin Coordinator), Ken Eckelmeyer (Liner Inspection and Metallurgical Analysis) and a team of outstanding technicians consisting of Mike Ramirez, Bob Smyth, Ed Baynes, Bob Eyers, Raymond Davis, Roy Morgan, John Mulder, Richard Padilla, Jack Pantuso, Ed Vieth, Richard Klingler, and Larry Yellowhorse. Kimberly Brower assisted in the posttest data processing and analysis. Management and Administrative support was provided by Berlinda Gonzalez, Yolanda Aragon, Viola Madrid, Mary Campos, Rebecca Campbell, Linda Flores, Barbara Meloche and Barbara Hawkins. Site support was provided by SNL's Facilities Department members Walter Heimer, Paul Schlavin, George Greer, Ed Sanchez and Dave Hendrix. Nadine Williams was responsible for all permits and land-use issues. Dave Sparks and Russ Adams from SNL's Video Services Department taped the construction and testing of the model. Environmental, Safety and Health support was provided by Daniel 'Mac' MacLaughlin.

In addition to SNL's in-house staff, vital support was provided by several key sub-contractors, especially from ANATECH Consulting Engineers: Bob Dameron (Lead Analyst), Yusef Rashid, Jason Maxwell and Brian Hanson; from Pure Technologies, Ltd. Peter Paulson and Monroe Thomas; and from the University of New Mexico's ATR Institute, Lary Lenke. Faith Puffer (Tech Reps) was the technical editor responsible for producing this report.

The direction and planning of the project was greatly assisted by special advisors to the project. In Japan, NUPEC's Structural Advisory Committee included Prof. Hiroshi Akiyama, Prof. Katsuki Takiguchi and Prof. Noriyuki Miyazaki. The NRC's Peer Review Panel consisted of Tom Ahl, Bryan Erler, Ted Johnson, Richard Orr, Mete Sozen, John Stevenson, H.T. Tang, Walt von Riesenmann, Richard White, Lyle Gerdes, Harold Townsend and Joseph Ucifferro.

It is very difficult to adequately describe the contribution of all these individuals in this short space, but to each of them, I would like to express my heartfelt thanks.

Thank you.

Michael F. Hessheimer, P.E.

Project Manager
NUPEC/NRC Cooperative Containment Program
Sandia National Laboratories

December 2002

ABBREVIATIONS

A/L	air lock
A/E	Architect/Engineer
AO	Acoustic System Operator
ASME	American Society of Mechanical Engineers
BWR	Boiling Water Reactor
CE	fiber optic gages
CONV	converted data
COR	corrected data
CPOT	Cable Potentiometer
CTTF	Containment Technology Test Facility
CVDT	converted
DA	data analyst
DAS	Data Acquisition System
DET	Division of Engineering Technology
DISP	displacement
DO	Data Acquisition System Operator
DOE	Department of Energy
DOR	data of record
DT	displacement
DYN	dynamic
E/H	equipment hatch
EPRI	Electric Power Research Institute
ES&H	Environmental Safety and Health
F/W	feedwater
GBST	gage bar strains
GFAC	gage-specific factors
ILRT	Integrated Leak Rate Test
KAFB	Kirtland Air Force Base
LI	liner strain gage
LINST	liner strains
LOCA	loss-of-coolant accident
LST	Limit State Test
LVDT	Linear Variable Differential Transformer
M/S	main steam
METI	Ministry of Economy, Trade and Industry
MHI	Mitsubishi Heavy Industries
NO	Nitrogen Supply Operator
NRC	U.S. Nuclear Regulatory Commission
NSS	nuclear steam supply
NUPEC	Nuclear Power Engineering Corporation
PCCV	prestressed concrete containment vessel
PLC	Programmable logic controller
PRES	pressure
PWR	Pressurized Water Reactor
REBST	rebar strain
RES	Office of Nuclear Regulatory Research
RS	rebar strain gages
RTD	Resistance Temperature Detectors
SCV	steel containment vessel
SFMT	Structural Failure Mode Test
SFT	System Functionality Test
SIT	Structural Integrity Test
SNL	Sandia National Laboratories
SOL	Standard Output Location

T/C	thermocouple
TC	test conductor
TEMP	temperature
UTS	ultimate strength
YS	yield strength

1. INTRODUCTION

The Nuclear Power Engineering Corporation (NUPEC) of Japan and the U.S. Nuclear Regulatory Commission (NRC), Office of Nuclear Regulatory Research have cosponsored and jointly funded a cooperative containment research program at Sandia National Laboratories (SNL). NUPEC was founded in 1976 as the Nuclear Power Engineering Center under the initiative of academia and private corporations. Supported by the Agency for Natural Resources and Environment of the Ministry of Economy, Trade and Industry (METI), NUPEC is mandated to advance the performance and public acceptance of commercial nuclear power plants through engineering tests, safety analyses, information acquisition and analyses, and public relations activities. Within NUPEC, the Systems Safety Department is conducting research on the integrity of reactor containment vessels during severe accidents. Containment integrity tests include experiments and analyses of debris cooling phenomena, hydrogen combustion behavior, fission products transport behavior, and containment structural behavior. In addition, the department coordinates the cooperative containment program with the NRC and manages program activities with SNL and other subcontractors.

The Office of Nuclear Regulatory Research (RES) at U.S. NRC plans, recommends, and implements programs of nuclear regulatory research, standards development, and resolution of safety issues for nuclear power plants and other facilities regulated by the NRC. Within RES, the Division of Engineering Technology (DET) plans, develops, and directs comprehensive research programs and standards development for nuclear and materials safety. In the nuclear safety area, there are programs for the design, qualification, construction, maintenance, inspection, and testing of current and advanced nuclear power plants. For materials safety, program activities include material characteristics, aging, and seismic and engineering aspects of these facilities and materials. Within DET, the Engineering Research Applications Branch has the lead for determining adequacy of structures and systems and for the coordinating and interfacing activities associated with the American Society of Mechanical Engineers (ASME) Code Section III. This branch coordinates the cooperative containment program with NUPEC and manages SNL activities.

SNL is a multi-program national security laboratory, operated by Sandia Corporation, a subsidiary of Lockheed Martin Company, for the National Nuclear Security Administration, U.S. Department of Energy (DOE). SNL's Nuclear Energy Technology Center has provided engineering and scientific support in the areas of reactor safety and safeguards to the NRC and the DOE for more than 20 years. A significant area of support has included analytical and experimental efforts to address issues related to severe accidents and containment integrity.

This cooperative containment program builds on the combined expertise of these organizations and continues to advance the understanding of nuclear containment structure's response to pressure loading beyond the design basis accident and the ability to predict, analytically, the structural behavior. This is accomplished by conducting static, pneumatic overpressurization tests at ambient temperature of scale models of actual containment vessels for nuclear power plants in Japan. NUPEC and the NRC formulated the overall scope of the program, and NUPEC, under contract with METI, is responsible for designing and constructing the models. SNL is funded by NUPEC to develop and operate a facility for conducting these tests, review the model designs and provide design support, instrument the models and collect data during the pressure tests, and report the results of the test. The NRC is funding SNL to perform pre- and posttest analyses of the models and to conduct the pressure tests. All funding is directed to SNL through agreements with the DOE's Work-for-Others Office in the Science and Technology Transfer Division.

Tests of two containment models were authorized under this program. The first model, a mixed-scale model of an Improved Mark-II type steel containment vessel (SCV) for a Boiling Water Reactor (BWR), was tested in December 1996. The results of the SCV tests and analyses have been published [1-5]. The second model tested was a 1:4-scale model of the prestressed concrete containment vessel (PCCV) of an actual nuclear power plant in Japan, Ohi-3 (Figure 1.1). Ohi-3 is an 1127 MWe Pressurized Water Reactor (PWR) unit, one of four units comprising the Ohi Nuclear Power station located in Fukui Prefecture and owned and operated by Kansai Electric Power Company.

This report describes the design, construction, and instrumentation of the PCCV model, the conduct of the pressure tests, and the results of those tests. The pre- and posttest analyses performed by ANATECH Corp (San Diego, CA) under contract to SNL are reported separately [6, 7]. Independent pretest analyses, conducted by a number of international organizations, were also conducted and presented in a summary report [8].



Figure 1.1. Ohi Nuclear Power Station, Ohi-cho, Fukui, Japan

1.1 Background

Containment vessels in nuclear power plants comprise, with the penetrations and other pressure boundary components, the final barrier between the environment and the nuclear steam supply system. The functions of the containment are to:

- contain any radioactive material that might be released from the primary system (reactor vessel, steam generators, piping) in the event of an accident;
- act as a supporting structure for operational equipment.

Containment buildings have been an integral part of commercial nuclear power plants in Japan and the United States since the first units were constructed in the 1960s. For U.S. containments, the design loads and their combinations, as well as the response limits, are specified in the ASME Boiler and Pressure Vessel Code [9]. Initially, severe accidents were not part of the design basis due to their perceived low probability of occurrence, and pressure relief valves were not required. In Japan, METI Directives control the design of nuclear power plants, and the design standards for containments are specified in the METI Notification No. 501 and in JEAG4601.

After the accident at Three Mile Island in the United States in 1979, attention turned to the capacity of containment systems beyond their design basis. SNL conducted a preliminary study [10], commissioned by the NRC, to identify experiments conducted to investigate this issue, but concluded that the scope of the tests and the data did not provide sufficient insight into the problem. As a result, a program, including scale model tests coupled with detailed structural analysis, was formulated by the NRC to investigate the integrity of containment systems beyond their design basis. The primary objective of the NRC program was, and continues to be, the validation of analytical methods used to predict the performance of light water reactor containment systems when subjected to loads beyond those specified in the design codes. While some insights could be gained into structural response and failure mechanisms of actual containments, it was also recognized that the capacity of actual containments could not be determined solely from tests of simplified scale models. The results of this program, as summarized by Parks [11], concluded that there was significant reserve capacity in the containment vessels to resist loads above the design basis and that although the analytical efforts were encouraging, uncertainties remained about structural response and failure mechanisms.

Remaining uncertainties regarding the response of containment structures led to discussions among NUPEC, the NRC, and SNL that culminated in a 1991 agreement to start the NUPEC/NRC Cooperative Containment Program. In parallel with this cooperative program, there are independent efforts sponsored and conducted by both NRC and NUPEC. These efforts include investigating the response of penetrations [12,13], the effects of aging on containment structure capacity [14], and the seismic capacity of containment structures [15, 16].

1.2 Scope

Nuclear power plants in Japan and the U.S. generally utilize one of two types of light water reactor systems; BWR and PWR. The containment vessels for the pressurized water reactors in Japan and the U.S. are typically free-standing reinforced concrete shells with an integral steel liner. A few have only regular steel reinforcing bars (rebar); however, the majority use both regular and posttensioned reinforcing. (For this report, the terms prestressed and posttensioned are used synonymously, even though the reinforcing is, technically, posttensioned; i.e. tensioning of the reinforcing is conducted after the concrete has been placed and cured to the specified minimum strength.) A variety of prestressed reinforcing or tendon configurations are represented in the fleet of PWR containments. However, the evolution of prestressed containment designs has been toward the use of longer, continuous tendons, culminating in the two-buttress containment with meridional 'hairpin' tendons and 360-degree hoop tendons, represented by the Ohi-3 design. No two-buttress prestressed concrete containments were constructed in the U.S. (although some were planned prior to the TMI-2 accident); however, many of the features of the Ohi-3 containment are similar to features in existing U.S. plants and the design philosophy is similar. As a result, NUPEC and the NRC agreed on a scale model of the Ohi-3 containment for the second test subject in the Cooperative Containment Program.

1.2.1 Model Features and Scale

The Ohi-3 containment is a thin prestressed concrete cylindrical shell with a hemispherical dome and a continuous steel liner anchored to a reinforced concrete basemat that extends beyond the containment to support other plant structures. Consistent with the objectives of the sponsoring organizations, the features and scale of the PCCV model were chosen so that the response of the model would mimic the global behavior of the prototype, and local details, particularly those around penetrations, would be represented. One of the primary considerations in determining the scale of the model was the desire to utilize nearly identical construction materials to the material used in the construction of the prototype. Preliminary design studies, conducted to determine the appropriate scale of the model, initially focused on a mixed scale model where the scale on the overall geometry would be 1:6, while the scale on the liner thickness would be 1:3. These preliminary studies indicated, however, that use of this mixed scale might upset the relationship between failure modes that might be expected in the prototype. In particular, the use of a steel liner, which was twice as thick, relative to the prestressed concrete shell, as the prototype, might retard the onset of liner tearing (leakage) failure modes and increase the likelihood of a structural failure mode occurring. As a result, it was decided that the scale of the model would be a uniform 1:4, with minor exceptions to accommodate fabrication and construction concerns. This was judged to be the minimum scale that would allow the steel liner to be constructed from prototypical materials and fabricated with details and procedures representative of the prototype. The overall geometry and dimensions of the PCCV model are shown in Figure 1.2.

Although both NUPEC and SNL (under NRC sponsorship) had conducted component tests of both full-size and scaled penetrations [12-13, 17], the PCCV model included both a functional representation of the major penetrations, namely the equipment hatch (E/H) and the personnel air lock (A/L), and nonfunctional representation of the main steam (M/S) and feedwater (F/W) penetrations. The E/H and A/L penetrations were fully-functional, one-fourth scale models of the penetrations in the prototype, while only the penetration sleeves of the M/S and F/W penetrations, terminated with pressure seating blind flanges, were included in the model. The liner and concrete reinforcing details around these penetrations were also retained in the model.

During construction and instrumentation of the model, primary access to the interior was through the E/H, while the A/L was used to provide heating, cooling, and ventilation for personnel working inside the model. The M/S and F/W penetrations provided portals for interior instrumentation cabling, power and, during testing, the pressurization medium. Prior to testing, after the E/H cover was installed and sealed, the A/L provided the means for final egress and sealing of the model with a specially-designed pressure seating cover that could be closed from the outside.

Details of the design and fabrication of the PCCV model are described in Chapters 2 and 3.

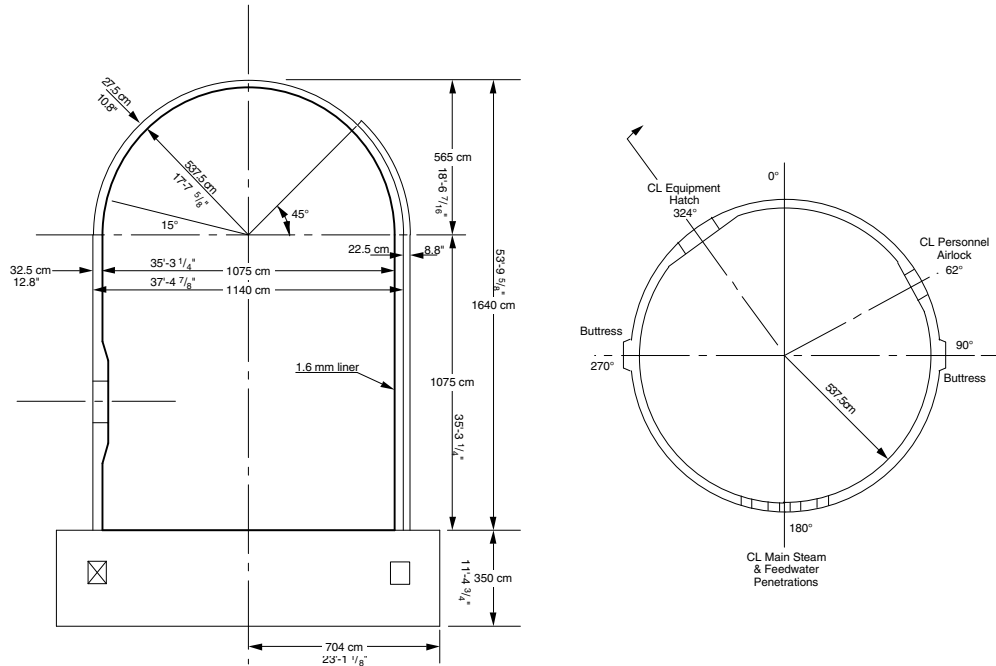


Figure 1.2 PCCV Model Elevation and Cross-Section

1.2.2 Loading

By definition, the scope of this program was limited to addressing the capacity of containment vessels to loads beyond the design basis, the so-called severe accident loads. Design accident loads for light water reactor containment vessels are typically based on the loss-of-coolant accident (LOCA) and are defined by a “bounding” pressure and temperature transients. The term “severe accidents” is used to describe an array of conditions that could result in loads exceeding the design basis on the containment. The definition of severe accident loads, which is not as rigorous as the design basis loads definition, results from considering of various postulated failure scenarios of the primary nuclear system, up to and including a complete core meltdown and breach of the reactor pressure vessel. The resulting pressure and thermal loading characteristics depend on the unique features of the nuclear steam supply (NSS) system and the containment structure, in addition to the postulated accident.

For this test program, it was necessary to decide whether both thermal and pressure loads would be applied to the model, either separately or simultaneously; what the pressurization medium should be; and whether the transient characteristics of these loads should be considered. Programmatically, the decision to perform a *static, pneumatic* overpressurization test at *ambient temperature* was dictated by risk and cost considerations and previous experience.

The effects of severe accident *temperature* loads on the structural response of the containment building are primarily limited to (1) the effects of elevated temperatures on the mechanical properties of the materials and (2) the mechanical loads resulting from differential or constrained thermal expansion. The effects of temperature on the material properties can be determined from standard material tests methods. These test results could be incorporated into the evaluation of the prototypical containment vessels without adding this complexity and cost (in terms of generating the thermal environment and protecting the instrumentation) to the PCCV model test. Regarding the stresses imposed by differential thermal expansion, there are only a few locations in a steel and/or concrete containment building where these effects are significant, notably at the junction of the containment wall and the basemat or, in the case of the PCCV model, the differential thermal expansion between the steel liner and the concrete shell under non-steady-state thermal conditions. Again, the added complexity and cost of simulating the thermal environments to reproduce these local effects was judged not justified for the PCCV model. It was further concluded that the effects of temperature could be addressed using

analytical methods that had been benchmarked against the pressure tests. Therefore, the decision was made to conduct the PCCV model test at *ambient temperature*.

The containment atmosphere during a severe accident consists of air, steam, and other by-products of the accident, including hydrogen and particulates (aerosols). The program's primary interest is in observing and measuring the structural response of the containment to pressure loads, and identifying failure modes. Containment failure (see Section 1.2.3) includes both functional failure, i.e. leakage, and structural failure, i.e., rupture of the pressure-resisting elements. There is not a rigorous distinction between functional and structural failure, and it is conceivable that they might occur simultaneously. Conventional wisdom holds, however, that local, limited structural failure (i.e. liner tearing) and leakage will occur prior to, and at pressures well below those required to cause extensive structural failure. As a result, *detection* of leakage, which indicates a tear in the steel liner or failure of a penetration seal, not *measurement* of actual leak rates for real containment atmospheres (see Section 1.2.3), is the objective of the test. Hence, there is no need to reproduce the containment atmosphere resulting from a severe accident. The choice of a pressurization medium, then, becomes somewhat arbitrary and is dictated by safety and operational considerations. Hydrostatic testing is preferable from a safety viewpoint; however, it raises operational problems and requires protection of sensitive electronics and wiring from the water under high pressure. *Pneumatic* testing, while more dangerous, does not present any risks that cannot be managed cost-effectively and does not require any unusual measures to protect the instrumentation. Nitrogen gas was chosen as the pressurization medium for the PCCV model tests primarily for operational considerations. Fairly large quantities could be delivered at the test site in liquid form with a limited amount of fixed equipment. Nitrogen gas also has the advantage of being dry for instrumentation considerations, and it allows simpler and more accurate calculations to detect a small leak.

The test plan and conduct of the pressure tests, along with the design and operation of the pressurization system, are described in Chapter 5.

It should be noted that the *pneumatic* Limit State Test (LST) was the final test in the original program plan. This test was terminated following a functional failure, i.e. a leak, in the PCCV model, with only limited structural damage occurring. Subsequently, it was decided to repressurize the PCCV model, prior to demolition, in an attempt to observe larger inelastic response and, possibly, a global structural failure. This test was a combined *pneumatic-hydrostatic* test, where the PCCV model was sealed inside with an elastomeric membrane and filled nearly full with water to reduce the volume of gas to be pressurized, and nitrogen gas was used to generate the overpressure. The rationale and design of this Structural Failure Mode Test (SFMT) are also described in Chapter 5.

1.2.3 Response

One important aspect of the PCCV model response in the high pressure tests is the concept of *failure*. In the U.S., the functional failure for the prototypical containment is defined in the regulations as containment leak rates exceeding 0.1 to 0.5% of the containment mass per day [18], considering maximum offsite dose rates due to fission product released to the environment. In Japan, the functional failure is defined in design specifications made by the utility company, not the regulations. (The specified leak rate for the PCCV prototype is 0.1% mass/day.) The functional failure criteria are not particularly useful to test the structural capacity of a containment vessel model, especially when one of the objectives is to generate large inelastic response modes for comparison with analytical predictions, which may be well beyond the levels required to cause functional failure; and secondly to gain some insight into design margins, i.e. the functional and structural capacity beyond the specified design load conditions. In the case of the PCCV model test, the pressurization system allows the model to be pressurized to levels significantly above those expected to cause local strains in the model to exceed the ultimate strain limits of the materials. The test(s) were terminated when the model and the pressurization system were incapable of maintaining or increasing the model pressure due to excessive leakage or gross rupture. In this report, the maximum pressure achieved prior to the termination of the tests will *not* be identified as the *failure pressure*, since failure is defined in terms of some acceptance criteria, not the operational inability to maintain pressure in the model.

The PCCV model instrumentation suite was designed to measure the global behavior in free-field locations of the model and the local structural response of the model near discontinuities. Global response measurements included both displacements referenced to a global or fixed reference, and strain measurements at a regular pattern of azimuths and elevations to characterize the overall shape of the model. Local response measurements consisted of individual structural element (i.e. liner, rebar, tendons, concrete) strain measurements to characterize the force distribution in the free field and near structural discontinuities. In areas without structural discontinuities or where membrane behavior was expected to dominate the response, relatively simple arrays of transducers were specified. Where structural discontinuities were

judged to be significant, more complex arrays of strain gages were utilized. Both hoop and meridional strains were measured.

Pressure measurement requirements included careful measurement of the PCCV interior pressure for leak detection (to a lesser extent); leak rate measurement; characterization of the mechanical response as a function of pressure; and controlling the pressurization rate. Note that while measurement of leak rates was not a primary objective, detecting the onset of leakage requires calculating very small leak rates with relatively high accuracy.

While there was no attempt to simulate severe accident temperature conditions, a fairly extensive set of thermal measurements were taken to measure both the interior and exterior atmospheric temperature for accurate leak rate calculation. Given the large volume of the PCCV model, gas temperatures inside the model could vary significantly and multiple measurements were required to limit errors resulting from nonuniform gas temperatures. During pressurization steps, large thermal gradients could occur as the gas inside the model was compressed. Furthermore, since the model was exposed to the environment, ambient thermal variations, both spatial and temporal, affected the interior gas temperature and could affect the accuracy of the leak rate calculations if not considered. Similarly, ambient thermal effects could affect the model response measurements. Multiple measurements of the model temperature using both embedded and surface mounted temperature transducers were employed to account for this effect.

As implied by the name, the unique feature of the PCCV model is the prestressing system, comprised of the vertical and hoop tendons and associated hardware. Special efforts were made to monitor the response of the prestressing system, both prior to and during pressure testing. An extensive effort was undertaken to develop and demonstrate the reliability of the tendon instrumentation. The resulting system was comprised of two types of gages to monitor the strain, and, by calculation, the force distribution along the length of selected tendons along with load cells to measure the forces at the tendon anchors. Since the behavior of the tendons and the overall response of the model to the pressure load would be directly affected by the initial prestressing forces, the response of the PCCV model was monitored continuously from the start of prestressing through the subsequent pressure tests.

While these force, strain, and displacement measurements provide accurate information on the response of the model at discrete locations, it is desirable to monitor the overall response of the model in the (likely) event that some significant response occurs at locations remote from any transducer. The displacement transducers reflect, to a greater extent than the strain or force transducers, the overall response of the model, but might still miss other local response modes. This deficiency was addressed by including an extensive array of acoustic and, to a lesser degree, video/photographic monitoring of the PCCV model. While more qualitative in nature than the discrete response measurements, some quantitative information could be obtained from these monitoring systems. The acoustic system, in particular, was designed to detect the onset of liner tearing and leakage, along with concrete cracking and rupture of tendon wires or rebar. Similarly, video and still photography were used to document the development and distribution of concrete cracking, detect liner tearing at discrete locations during pressure testing, and capture any unanticipated response modes.

The design and implementation of the model instrumentation suite are described in Chapter 3. Performance requirements and features of the data acquisition system and data management are summarized in Chapter 4. A summary and discussion of the high pressure tests and posttest inspections are provided in Chapter 5. The test results are also summarized in Chapter 5 and the corrected test data, including a description of the corrections applied to the raw data, are included in the appendices.

1.3 Project Organization

As noted above, NUPEC and the NRC are the sponsoring organizations for this cooperative containment research program. Programmatic authorization to pursue this area of research is provided to these organizations by the ministerial or executive offices of their respective national governments, as dictated by statute. Technical guidance was provided by panels of expert advisers from academia and industry in each country. In Japan, the Structural Advisory Committee met regularly with NUPEC personnel to review the program plans and status, while in the U.S., a special Peer Review Panel provided the same support to NRC and SNL personnel.

Within the cooperative framework agreed to by NUPEC and the NRC, NUPEC and its Japanese contractors designed and constructed the PCCV model at SNL's Containment Technology Test Facility-West (CTTF-W). This test facility was specially constructed by SNL on land temporarily permitted for this purpose by Kirtland Air Force Base (KAFB), Albuquerque, New Mexico, USA. This 'West' facility is distinct from the CTTF used for the previous large-scale model tests conducted for the U.S. NRC in the 1980s. The 'East' facility was not considered suitable for continued large-scale

model testing due to the identification of previous environmental contamination (not associated with the containment test operations) and subsequent clean-up operations that might interfere with the Cooperative program operations. The CTTF-West Land-Use Permit required NUPEC and the NRC, through their contracts with SNL, to remove all improvements within the permit boundaries and return the site to near its original condition at the conclusion of all test operations.

NUPEC and its Japanese contractors were authorized to construct the model at the CTTF-W under a specially negotiated Premise Access Agreement with SNL and the DOE. This agreement required NUPEC and its contractors to abide by all environmental health and safety regulations typically required for all capital construction activities managed by SNL, and authorized SNL to perform construction safety inspection to ensure that all requirements were being satisfied. The prime contractor to NUPEC for the construction of the PCCV model was Mitsubishi Heavy Industries (MHI), who also designed and constructed the prototype plant, Ohi-3. In addition to overall design and construction, MHI designed, fabricated, and erected the steel liner and all primary steel pressure-retaining components. Supporting MHI for the reinforced concrete portions of the model and ancillary structures were several subcontractors. Obayashi Corp., a large Japanese Architect/Engineer (A/E) and construction company, performed the detailed design of the PCCV model, and Taisei Corp, another large A/E/Contractor, was the construction manager. Taisei retained the U.S. construction firm, Hensel Phelps Construction Co., Greeley, CO for general construction work and management of day-to-day construction operations. MHI prefabricated portions of the steel liner and the penetrations at their Kobe Shipyard and transported these components to the CTTF-W for final erection. The balance of the model was constructed on-site.

NUPEC also funded SNL to provide programmatic and model design support, instrument the model, and design and assemble the data acquisition system.

NRC funded SNL to perform preliminary, pre- and posttest analyses of the model. This analytical work was subcontracted by SNL to ANATECH Consulting Engineers, San Diego, CA. The decision to subcontract this work to ANATECH was based, in part, on a successful history of collaboration on previous containment model tests [19, 20] and ANATECH's experience in developing sophisticated concrete models and related efforts for the Electric Power Research Institute (EPRI), Palo Alto, CA [21]. The preliminary analyses supported design studies, identified critical response modes, and assisted in the locating instrumentation. The pretest analysis consisted of developing and analyzing detailed numerical models in an attempt to predict the response of the PCCV to the test pressures and predict the capacity and most probable failure mode. The posttest analysis compared the test results to the pretest predictions, investigated and demonstrated changes in the modeling methods to improve comparison with the test results, and provided insights into the response observed during the pressure tests. The pre- and posttest analyses are reported separately [6,7] and are not included in this report.

NRC also funded the planning and conduct of test operations.

NUPEC and NRC also jointly provided funding to share the costs associated with organizing and conducting a pretest Round Robin analysis. The Round Robin analysis euphemistically refers to an activity where a number of nuclear safety research organizations from government, industry, and academia in the U.S., Japan, and other countries, are provided with a common set of data on the model test (design drawings, material properties, test specifications, etc.) and complete independent predictions of the model response, failure mode, and pressure capacity. SNL was the focal point for this effort in terms of disseminating and consolidating the work of the participating organizations. Seventeen independent organizations, including NUPEC and SNL, participated in this effort, performing pretest analyses and meeting before and after the PCCV model test to discuss and compare analysis results. The efforts of these Round Robin participants are documented in separate NUREG Contractor Reports [8]. While a formal posttest Round Robin exercise was not conducted for the PCCV, most of the participants attended a posttest workshop and have reported the results of their posttest analyses independently.

Regular Technical Working Group meetings were held in both Japan and the U.S., involving program personnel from NUPEC, (including its contractors), the NRC, and SNL. These meetings planned and coordinated program activities and resolve technical issues. Separate meetings were held to discuss administrative issues related to cost and schedule.

1.4 Project Schedule

The NUPEC/NRC Cooperative Containment Research Program commenced in June 1991. The tests were conducted at the CTTF-W at SNL. Figure 1.3 illustrates the layout of the test site. A safety zone consisting of a circular area with

2. DESIGN AND CONSTRUCTION OF THE PCCV MODEL

2.1 Design

The PCCV model design was directed by NUPEC with overall responsibility for the design and construction contracted to MHI, Tokyo. Responsibility for the design of the liner and penetrations was assigned to MHI's Kobe Shipyard and Machinery Works while the concrete portions of the model were subcontracted to Obayashi Corp., Tokyo.

The basic philosophy guiding the design of the PCCV model was agreed upon very early in the program [22]. Key elements of this design philosophy included:

1. The PCCV model would be a uniform 1:4-scale model of the prototype or actual prestressed concrete containment vessel of Ohi Unit 3.
2. Elements of the model that would affect the ultimate strength would be equivalent to the prototype. The model liner would be one-fourth the thickness of the prototype liner. Reinforcing ratios would be maintained and the number and arrangement of the prestressing tendons would, to the extent possible, be identical to the prototype.
3. The model would be capable of reproducing the failure modes postulated for the prototype, including
 - a. Hoop tensile failure of the cylinder wall
 - b. Bending-shear failure at the junction of the cylinder wall with the basemat
 - c. Shear failure in the basemat above the tendon gallery
 - d. Bearing failure at the tendon anchors
 - e. Bending-shear failure at the large penetrations
 - f. Bending-shear at the small penetrations
 - g. Liner tearing due to strain concentrations at local discontinuities (stiffeners/anchors, thickened reinforcing plates at penetrations and embedments)
 - h. Leakage at penetration seals due to ovalization or distortion of the sealing surfaces.

Furthermore, to the extent possible, introduction of non-representative failure modes as a result of scaling or other modeling artifacts was to be avoided.

The general arrangement and representative failure mode locations are shown in Figure 2.1.

While the PCCV model was not 'designed' in the conventional sense, its features were scaled directly from the Ohi-3 design with some simplifications to facilitate construction without compromising the objectives of the test. The prototype, Ohi-3, was designed in accordance with the "Draft Technical Code for Concrete Containment Vessels in Nuclear Power Plants" issued by Ministry of International Trade and Industry/Agency for Natural Resources and Energy (MITI/ANRE) in November, 1981 [23]. This draft code was formally adopted in 1993 as MITI Notification No. 452. The code is not identical to the American Society of Mechanical Engineers/American Concrete Institute (ASME/ACI) code [9], which governs the design of concrete containments in the U.S.; however, the basic design philosophies are similar, i.e., to ensure that all elements of the containment structure respond elastically (with some minor exceptions for secondary stresses) to the specified design loading conditions.

Construction of the prototype was also governed by Japanese Architectural Standard Specifications No. 5 and 5N for Reinforced Concrete Work at Nuclear Power Plants [24, 25]. Construction specifications for the PCCV model also followed these standards to the extent possible; however, modifications were made to adapt the specifications to U.S. construction practices.

The final design drawings for the PCCV model are provided in Appendix A. While it is beyond the scope of this report to include all the details of the design and construction specifications, a discussion of those features relevant to the model's response is appropriate and is included below.

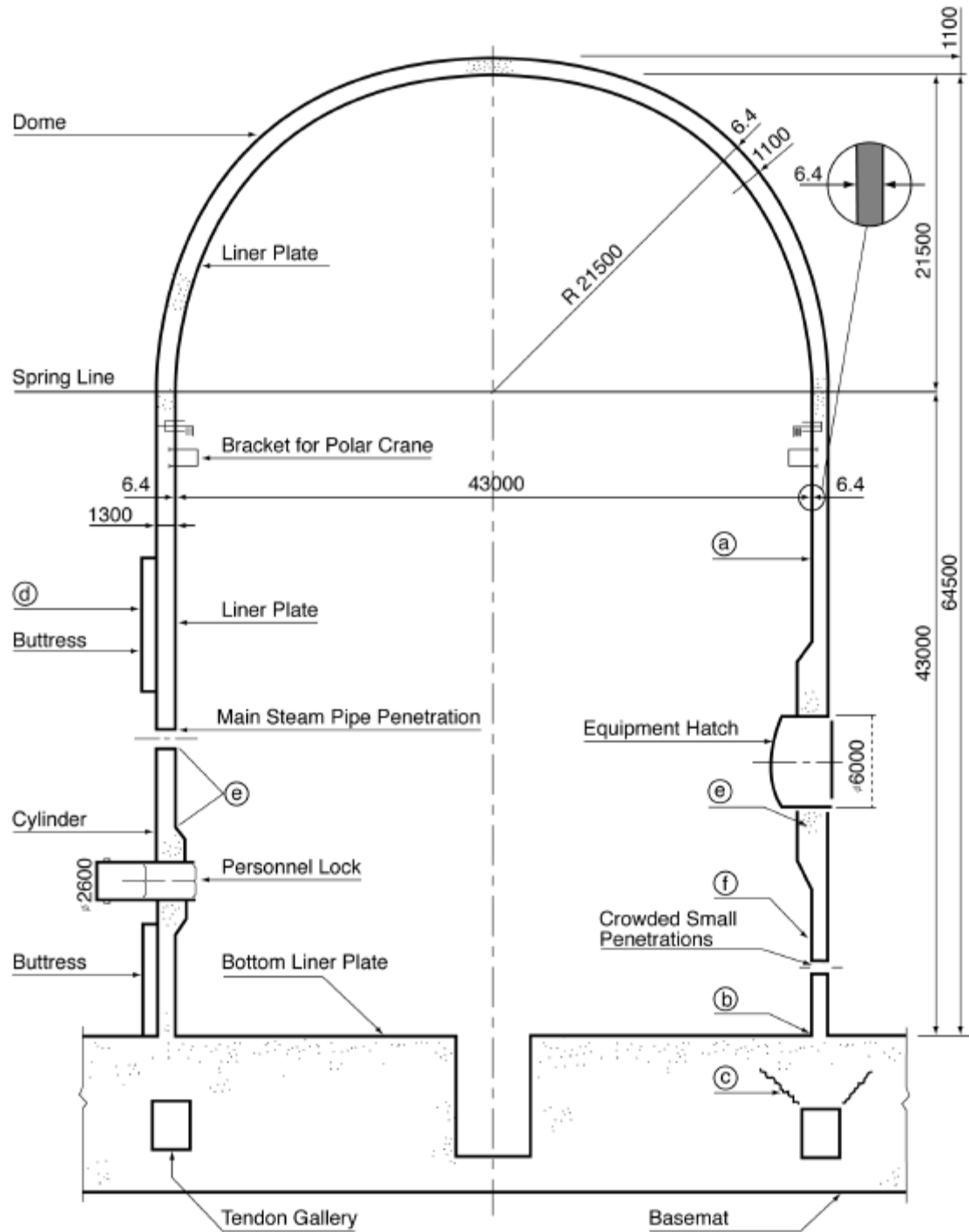


Figure 2.1. Elevation of PCCV Prototype and Potential Failure Locations

2.1.1 Liner Design Considerations

Design and fabrication/erection of the liner and penetrations was performed by MHI. The detailed specifications and practices are included in the project files. Essentially, the 1.6 mm (1/16") model liner was scaled from the 6.4 mm (~1/4") prototype liner. The as-built model liner thickness was 1.8 mm (0.070"), the extra 0.2 mm (0.008") providing a fabrication allowance. The model and prototype liner were both fabricated from SGV 410¹ carbon steel. JIS G3118 does not specify plate material under 6mm in thickness. The PCCV liner plate was fabricated to the same specifications as SGV410. Liner anchors and stiffeners were fabricated from SS 400². Penetration assemblies were fabricated from SGV 410. The nominal properties of SGV 410 and SS 400 are given in Table 2.1. Miscellaneous non-structural components, e.g. back-up bars, were fabricated from U.S. common bar stock, typically ASTM A36 carbon steel.

Table 2.1 Properties of Liner Materials

Nominal Properties	Liner Plate	Liner Anchors
	SGV 410	SS 400
Yield Strength	225 Mpa (33 ksi)	235 Mpa (34 ksi)
Tensile Strength	410 MPa (59 ksi)	392 Mpa (57 ksi)

The liner material was procured in Japan, and liner panels were prefabricated and welded at MHI's Kobe Shipyard. Jigs, to support the liner panels and facilitate field erection and assembly, were attached to the liner panels prior to shipping them to the test site in Albuquerque, NM. Note that these jigs are unique to the construction of the model. The prototype liner is thick enough to be self-supporting without the use of any jigs. All vertical and horizontal liner weld seams in the prototype were reproduced in the model. Typically, the panel assemblies for the cylinder wall fabricated in Kobe encompassed three vertical rings of individual plate segments, resulting in assemblies approximately 3 m². Dome segments and penetration assemblies were typically smaller, individual plate segments. All welding of the assemblies in Kobe, including attachment of the anchors and stiffeners, was done by computer-controlled automatic welders. All shop welding was done without the use of back-up bars.

Standard coupons were made from the liner and liner anchor materials, and these specimens were tested for quality control purposes and to determine the actual material properties. The results of these tests are summarized in Appendix B.

The general arrangement of the liner anchors on the PCCV model is shown in the design drawings and is illustrated in Figure 2.2. The vertical liner anchors in the prototype consisted of 'T-anchors' spaced 600 mm (24") on-center throughout the cylinder wall and dome. These anchors are built-up sections, continuously welded to the liner plate with double-sided fillet welds. Horizontal bar stiffeners are provided above and below each horizontal weld seam to stiffen the liner during construction. The model liner anchors and stiffeners are 1:4-scale of the prototype. At 1:4-scale, the vertical anchor spacing would be 150 mm (6"); however, because the liner anchors are, in general, ineffective at resisting pressure and facilitating fabrication, the vertical anchor spacing was increased to 450 mm (18") except near discontinuities in the liner, such as the wall-base junction, around the E/H, A/L, M/S, and F/W penetrations and around the crane rail bracket embedments, as shown in Figure 2.2. Furthermore, the vertical liner anchors were not extended into the dome. T-stiffeners were used at the perimeter of the dome liner segments, but interior T-anchors were replaced with small stud-type anchors, as shown on the drawings. Again, since the strains in the dome were expected to be well below those experienced by the cylinder wall, this modification was not judged to affect the pressure capacity of the model.

As noted previously, the majority of the liner anchors were shop-welded to the liner using welding machines. One additional deviation from the prototype was the use of intermittent, staggered fillet welds to attach the anchors and stiffeners to the liner plate. There was a concern that these 'stitch' welds might generate additional local strain concentrations from the weld geometry itself. Therefore, anchors and stiffeners adjacent to other local liner discontinuities were continuously welded to reduce the possibility of premature liner tearing.

¹ Japanese Industrial Standard (JIS) G 3118, "Carbon Steel Plates for Pressure Vessels for Intermediate and Moderate Temperature Service," Japanese Standards Association.

² JIS G 3101, "Rolled Steel for General Structure," Japanese Standards Association.

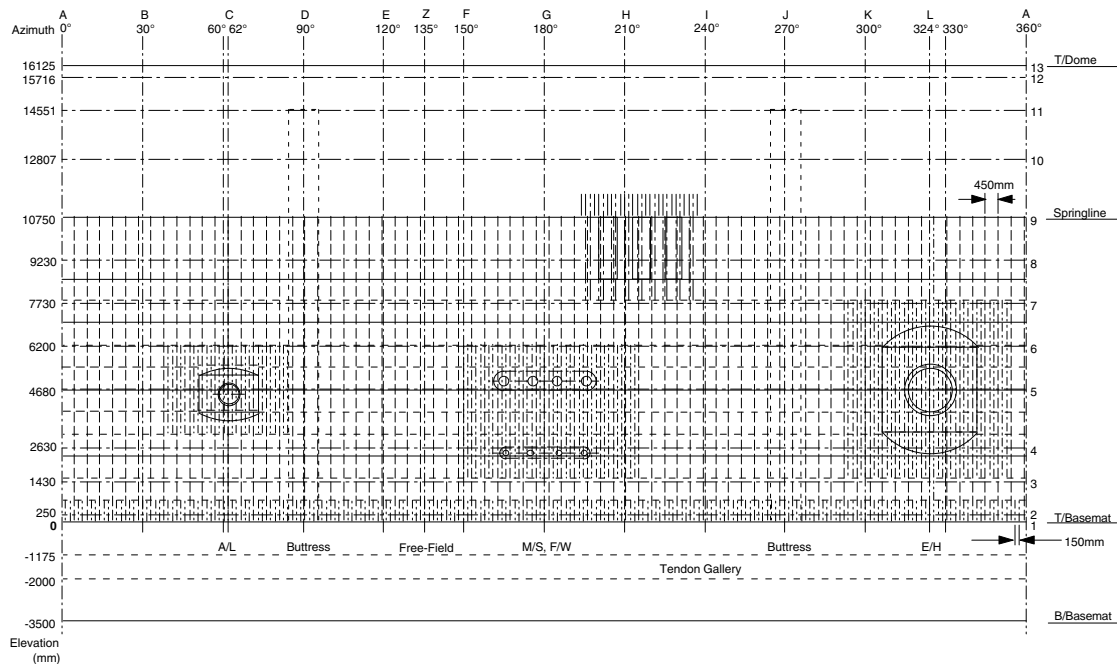


Figure 2.2 Liner Anchor Layout

While all the penetrations in the prototype were not included in the model, the major penetrations, consisting of the E/H, A/L, M/S, and F/W penetrations, were included in the model. These penetrations were representative of all the penetrations in the prototype and would be capable of reproducing the local strain concentrations in the structure and the liner. The E/H and A/L penetration assemblies in the model are 1:4-scale functional representations of the prototype assemblies, except that the A/L assembly includes only a single pressure seating cover and the interior doors are not reproduced. The model M/S and F/W penetration assemblies only included the penetration sleeve and reinforcing plates and were equipped with an interior flange and sealed with bolted pressure seating blind cover. No attempt was made to simulate the constraint conditions that might be imposed by the M/S or F/W piping. All the penetration sealing surfaces were milled and machined with grooves for double O-ring gaskets. The prototype penetration assemblies are shown in Figures 2.3 to 2.6 for comparison to the model penetration assemblies shown in the design drawings. The model did not include the polar crane rail or brackets; however, a set of three adjacent bracket embedments were included to reproduce the local discontinuities in the liner.

The erection, field welding, and quality control of the liner are described in Section 2.2.

2.1.2 Concrete Design Considerations

2.1.2.1 Geometry

While the basic geometric scale of 1:4 was maintained throughout the PCCV model, some exceptions and modifications were required. Most significantly, the configuration of the model basemat had to be determined. The thickness of the model basemat at 1:4 scale is 3.5 m (11' 5-3/4"). The primary design consideration of the model basemat is that the rotational stiffness at the wall-base junction is equivalent to the prototype, since this affects the bending-shear failure mode at this location. The prototype containment basemat is continuous with the mat for the surrounding structures and includes a large reactor cavity at the center of the containment. Simplified three-dimensional finite element analyses of both the prototype and model subjected to pressure loading were performed to select the dimensions and reinforcement for the model basemat that would yield the desired response characteristics. The scaled basemat thickness of 3.5 m was maintained and, with the reactor cavity eliminated from the model, the radius of 7.2 m (23' 7 1/2") and reinforcing were selected to match rotational stiffness of the prototype.

The location and size of the tendon gallery were scaled from the prototype. However, some modification of the construction sequence was required to accommodate this decision. Since the vertical prestressing tendons could not be inserted and tensioned inside a roughly 1-m² (2'-1" × 2'-8") tunnel, the portion of the basemat outside and below the tendon gallery was not constructed until after the tendons had been tensioned. This resulted in a somewhat different state of stress in the model basemat after prestressing; however, this difference was not significant and was unavoidable. Four access 'tunnels' to the tendon gallery were also included at 0 degrees, 90 degrees, 180 degrees, and 270 degrees to allow for visual inspection of the vertical tendon anchors and to ventilate the tendon gallery to minimize moisture that might affect the tendon anchors and the instrumentation.

Finally, some minor modifications in the geometry of the hoop tendon buttresses were required to accommodate the prestressing hardware. These were again judged to be insignificant with respect to the model's response to pressure.

2.1.2.2 Concrete Mix

The fundamental requirement of the PCCV model concrete was that it exhibit the same properties as the concrete used in the prototype. Based on prior experience with the construction and testing of a 1:6-scale reinforced concrete containment model at SNL, the approach to achieving this requirement was to specify a mix, using local (New Mexico) materials that would have the same 91-day³ compressive strength (f_c') as the prototype concrete and then test the trial mix(es) to ensure they exhibited the same mechanical and chemical properties.

Two different concrete strengths were used in the prototype: 300 kg/cm² (4300 psi) for the majority of the basemat and 450 kg/cm² (6400 psi) for the cylinder wall, dome, and the portion of the basemat above the tendon gallery. The location of each mix, along with the lifts used in the construction of the model, are shown in Figure 2.7. Note that concrete lifts were not scaled from the prototype and are unique to the model.

The mix designs for the PCCV model consisted of Type I-II cement, air-entrained with 20% Class 2 Flyash and superplasticizer. Cement, aggregate, flyash, and water were all obtained locally and were batched by a supplier and mixed in transit. Maximum aggregate size was 10 mm (3/8"). Water/cement ratio for the 300 and 450 kgf/cm² mixes were 0.43% and 0.34%, respectively.

Corrosion due to the presence of chlorides and alkalis in the mix was a concern for the prototype due to the close proximity of the plant to the ocean; however, this was not judged to be a major concern for the model, although the chemical composition of the mix would be tested. Flyash was specified for the trial mix, since the use of flyash is standard practice in the construction of Japanese nuclear power plants and minimizes possible reaction and expansion of the aggregate. (Use of flyash is not permitted in construction of U.S. nuclear power plants). Superplasticizers were specified to facilitate placement of the concrete by pumping in congested areas. A maximum slump of 10 cm (4") before and 20 cm (8") after adding superplasticizers at the site was specified.

The trial mixes were batched and tested by Construction Technologies Laboratories, Skokie, IL to determine if they met the project specifications. The properties determined from trial mix specimens are summarized in Appendix B. In lieu of actual material property data, the trial mix properties were used for the pretest analysis of the PCCV model.

Quality control and material property test results for the concrete used to construct the model are described in Section 2.2 and summarized in Appendix B.

2.1.2.3 Reinforcing Steel (Rebar)

Normal, i.e. non-tensioned reinforcing steel for the prototype included grade SD490, SD390, and SD345 deformed bars⁴. The same grade steels were used to manufacture the rebar for the model in the U.S. (Cascade Steel, McMinnville, OR) in accordance with JIS Standards. The nominal properties for the rebar used in the model are summarized in Tables 2.2 and 2.3.

³ JIS A 1108, "Method of Test for Compressive Strength of Concrete," allows specification of design strength at four weeks (28 days) or 13 weeks (91 days). Project specifications for the PCCV prototype and model specified the design strength f_c' at 91 days.

⁴ JIS G 3112, "Steel Bars for Concrete Reinforcement."

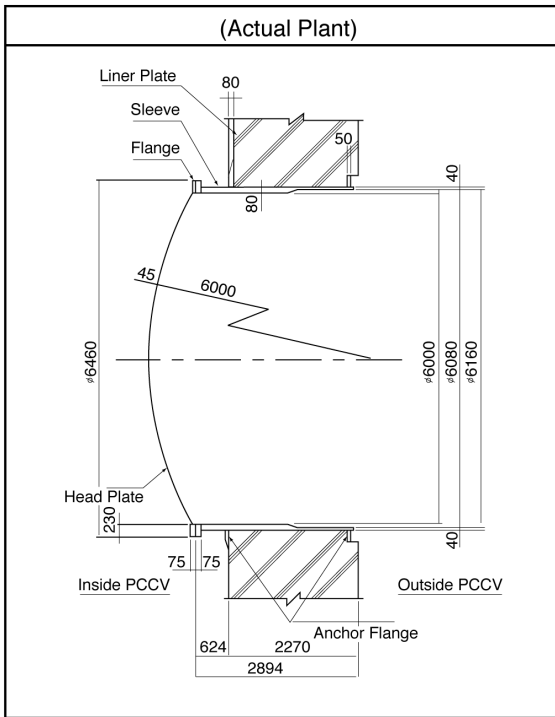


Figure 2.3 PCCV Prototype Equipment Hatch Arrangement

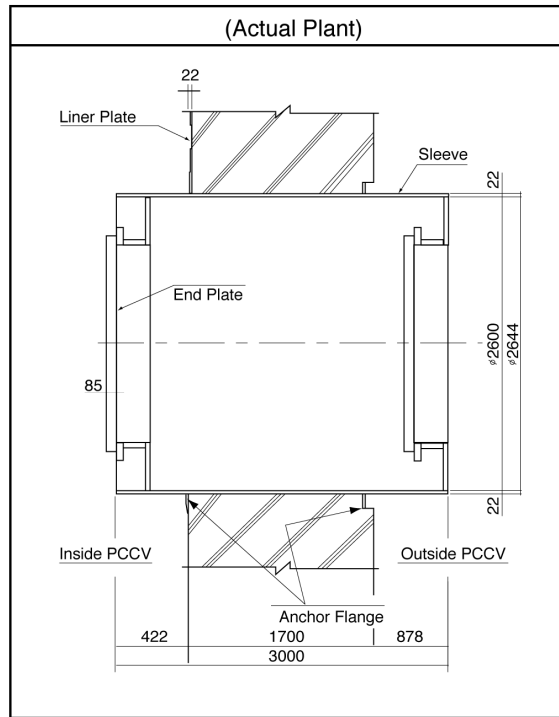


Figure 2.4 PCCV Prototype Personnel Airlock Arrangement

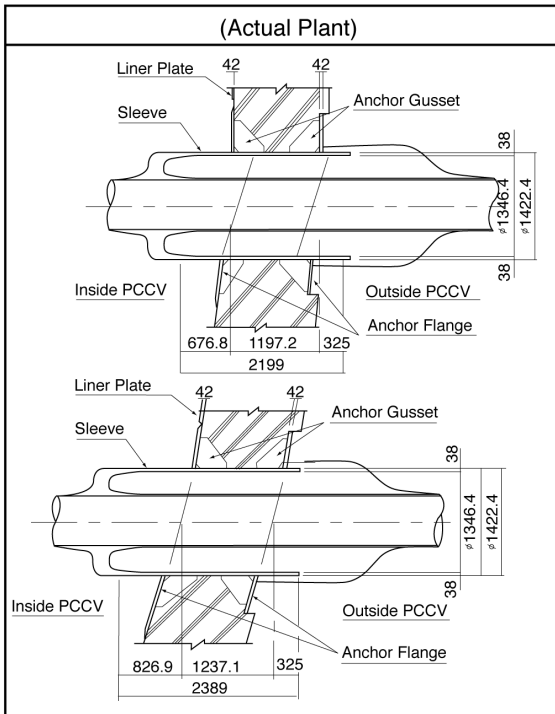


Figure 2.5 PCCV Prototype Main Steam Penetration Arrangement

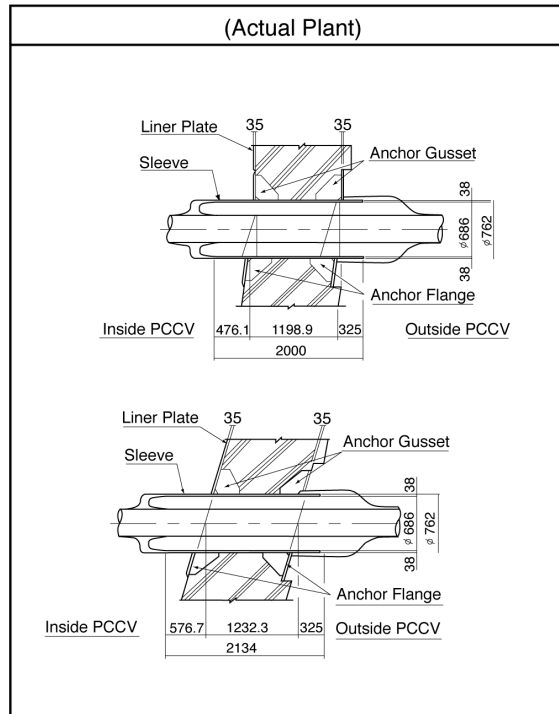


Figure 2.6 PCCV Prototype Feed Water Penetration Arrangement

In order to minimize rebar congestion in the model, all splices were originally intended to be made using swaged threaded couplers or position threaded couplers⁵. Swaged in-place couplers were not considered practical for the model due to limited clearance for the hand press. However, field considerations required some limited use of this type of coupler⁶.

Samples of all the rebar used in the model were tested for quality control and to determine mechanical properties for analysis according to JIS and ASTM methods. Tests were also conducted of both the threaded and position-threaded couplers used in the model construction. (No tests were conducted of the swaged in-place couplers.) ‘Dumbbell’ specimens were machined from SD390 D16, and D22 bars to measure the basic material properties. Finally, a series of bars were tested with strain gages installed in the same manner as the instrumented bars in the model to calibrate the strains with a standard extensometer. The results of all these tests are summarized in Appendix B.

While the basic reinforcing ratios in the model were nearly the same as the prototype, the reinforcing in the model differed from the prototype. Individual bars in the model were not scaled directly from the prototype. Generally, in the containment shell (i.e. the cylinder wall and dome), the rebar was placed in one layer in each direction on each face. Figure 2.8 compares the arrangement of the reinforcing at the base of the cylinder wall in the prototype with the model. In-plane spacing of the rebar in the model is based on the arrangement of the prestressing tendons (2 degrees on center circumferentially and 112.5 mm (4.4") on center vertically). Bar sizes were then selected to reproduce as closely as possible, within the limits of the standard bar sizes available, the reinforcing ratio of the prototype.

Tolerances on formed surfaces and placement of rebar were developed by considering the 1:4-scaled tolerances for the prototype and then adjusting these to accommodate practical construction limitations, such as congestion and clearance for concrete placement. These tolerances are specified in the model construction specifications along with the as-built records. The deviations from the nominal design dimensions were not judged significant enough to affect the response of the model and, accordingly, are not included in this report.

Additional reinforcing was also provided around the penetrations in the model. However, where prototype penetrations were eliminated, no additional reinforcing was included in the model.

2.1.3 Prestressing Design Considerations

Since the unique feature of the PCCV model, compared to previous large-scale containment model tests, was the prestressing system, particular attention was paid to the design, construction, and instrumentation of this component. An unbonded, seven-wire strand prestressing system⁷ was used in both the PCCV prototype and model. The tendons in the prototype consisted of 55, 12.7mm (½ in) diameter seven-wire strands⁸. The number and arrangement of the tendons in the model were kept the same as the prototype. The arrangement of the tendons is shown in Appendix A.

Both the prototype and model tendons were inserted in galvanized metal sheath or ducts after the concrete had been placed and allowed to cure, then tensioned. The model ducts were, generally, 35 mm (1-3/8") in diameter and were not ‘greased’ after tensioning. (The prototype tendon ducts were, as typical of most unbonded tendons, injected with a heavy grease after tensioning to protect the tendons from corrosion. Since the model tendons would only be in use for a relatively short time (< 2 years), they were not greased, although an anti-corrosion ‘shop-coat’ was brushed on prior to insertion in the ducts. Not greasing the tendons also facilitated the placement of instrumentation on selected tendons.)

In order to maintain the correct scaled cross-sectional area, the model tendons consisted of three, 13.7-mm (0.54") seven-wire strands. These model strands were custom-manufactured by the vendor for the model and nominal properties are not defined in the Japanese standard specifications, although the basic wire material was the same used for the prototype tendons⁹. The minimum properties of the model strands per the project specifications are given in Table 2.4. Extensive testing of individual strands as well as the tendon system were conducted for quality control and to determine the mechanical properties of the tendons. The results of these tests are summarized in Appendix B.

⁵ Grip-Twist® System, manufactured by BarSplice Products Co., Dayton OH.

⁶ Bar-Grip® System, *ibid*

⁷ VSL Multistrand Posttensioning System[®], VSL Corporation, Japan

⁸ JIS G 3536, “Uncoated Stress-Relieved Steel Wires and Strands for Prestressed Concrete.”

⁹ JIS G 3502, “Piano Wire Rod.”

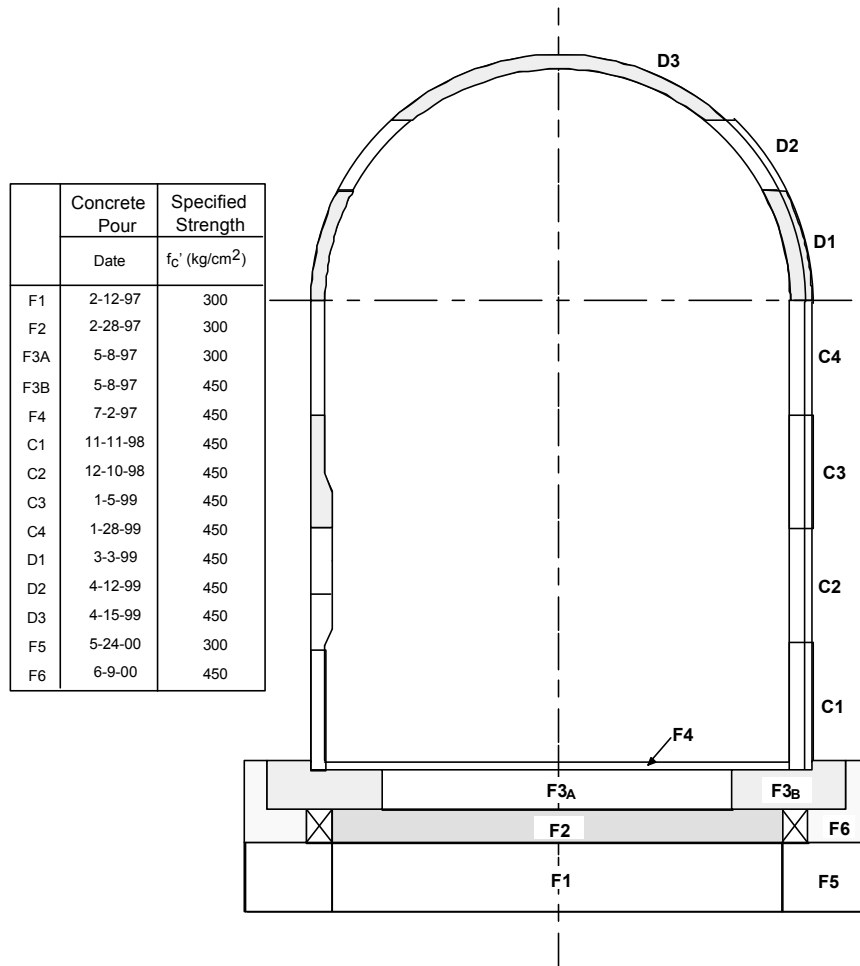


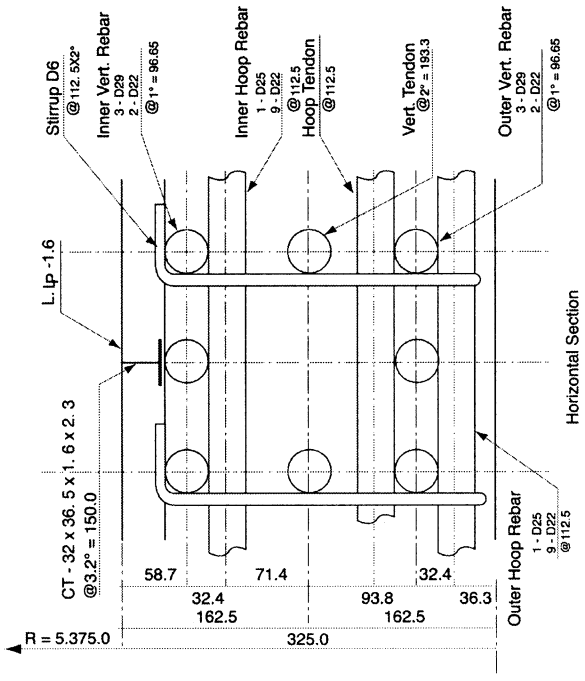
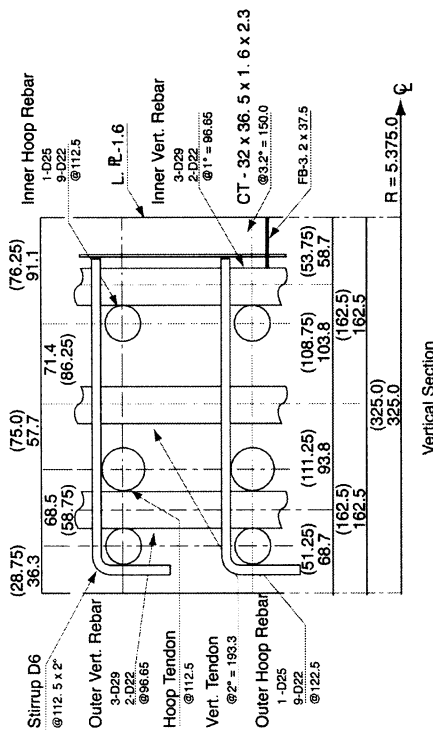
Figure 2.7 PCCV Concrete Lifts and Strengths

Table 2.2 JIS G 3112 Reinforcing Steel Properties

Grade	SD345	SD390	SD490
Model Location	Shell shear ties	Shell main bars, basemat shear bars	Basemat main bars
F_y min	343MPa ~50 ksi	392MPa ~57 ksi	490MPa ~71 ksi
F_t min	490MPa ~71 ksi	559MPa ~81 ksi	618MPa ~90 ksi
Elong.	18-20%	16-18%	12-14%

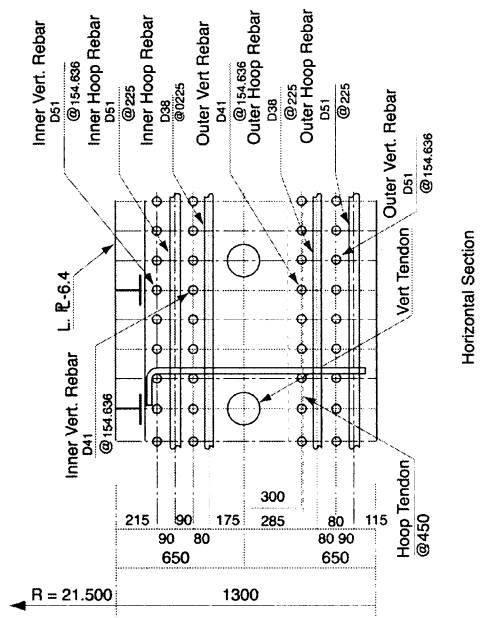
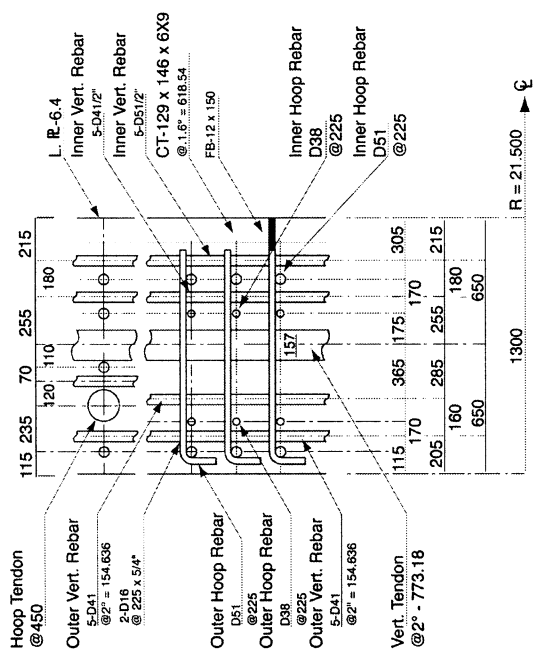
Table 2.3 JIS G 3112 Bar Properties
(Comparison with ASTM Standard Rebar)

	Nom. Diameter (d)		Nom. Area		Nom. Weight	
	millimeters	in	cm ²	in ²	kg/m	lb/ft
D6 (#2)	6.35	0.25	0.317	0.05	0.25	0.17
D10 (#3)	9.53	0.375	0.713	0.11	0.56	0.38
D13 (#4)	12.7	0.5	1.267	0.2	1	0.67
D16 (#5)	15.9	0.626	1.986	0.31	1.56	1.05
D19 (#6)	19.1	0.752	2.865	0.44	2.25	1.51
D22 (#7)	22.2	0.874	3.871	0.6	3.04	2.04



Note: The values in parentheses show those of 1/4 of the actual PCCV

Detail Drawing of the Test Model (Bottom of Cylinder)



Detail drawing of the Actual PCCV (Bottom of Cylinder)

Figure 2.8 Arrangement of Reinforcing in the PCCV Prototype and Model at the Wall-Base Junction

Table 2.4 PCCV Model Tendon Strand Properties

Diameter:min	13.5 millimeters	0.531 in
nom	13.7 millimeters	0.539 in
max	14.1 millimeters	0.555 in
Area	1.131 cm ²	0.175 in ²
Yield Strength*	190 kN	42.7 kips
Tensile Strength	210 kN	47.2 kips
Min. Elongation	4.5%	4.5%

*Load at 0.2% elongation

Given the properties and arrangement of the tendons, the tensioning forces were specified to achieve the same effect in the model as the prototype, considering the unique features of the model prestressing system that do not scale. Three basic criteria were used to establish equivalence between the prototype and model prestressing.

1. First, the state of prestressing in the model should reflect the predicted state of stress in the prototype after reaching its 40-year design life. Since the model was tested approximately six months after tensioning the tendons, it was necessary to adjust the initial tensioning forces to account for the expected creep and relaxation losses in the prototype.
2. Second, the effective hoop compressive stress due to prestressing should be the same in the model as the prototype. This relates directly to the requirement that the hoop tensile response and failure mode in the cylinder wall be accurately modeled.
3. Third, the vertical compressive stress in the concrete at the base of the cylinder wall should be the same in the model and the prototype. This relates directly to the requirement that the bending/shear response and failure mode at the base of the cylinder wall be accurately modeled.

Given these criteria, the following factors were considered:

1. Tendon friction: Tendon stresses decrease from the point where the tension load is applied, i.e., the anchor, due to friction between the tendon and the sheath and between the strands themselves. Two components of friction are considered in the design; ‘wobble’ friction, λ , which results from the internal friction between the tendon strands and ducts, and angular friction, μ , which occurs as a result of sweeping the tendons around a curve. The tendon stress at any point, σ_x , along the length of the tendon is given by:

$$\sigma_x = \sigma_0 e^{-(\mu\alpha + \lambda l)}$$

where σ_0 is the applied tension, α is the arc length, and l is the distance from the anchor along the tendon.

The values of μ and λ used in the design of the prototype were 0.14 and 0.001, respectively. Since the model strands were actually larger in diameter than those used in the prototype (and therefore stiffer) and bent to a ‘4x’ tighter radius, tests of the model tendons resulted in values for angular and wobble friction coefficients of

$$\mu = 0.21, \lambda = 0.001$$

2. Setting Losses: After the tendons are tensioned, the tensioning forces are locked in by seating the strands in the anchor blocks using tapered wedges. During this process, there is some loss of anchor force due to slipping and settling of the anchor components. The tensioning hardware (anchors, wedges, jacks, etc.) cannot be scaled and as a result, the maximum setting loss specified for the model, 5 mm (0.2"), is larger than the scaled setting loss and nearly equal to the actual setting loss specified for the prototype. (The setting loss, specified in terms of length, is the measured change in length of the projecting tails of the tendons strands before and after anchoring.)

The larger setting loss, coupled with the higher friction coefficients for the model, result in stress profiles in the model tendons that are much less uniform than those in the prototype.

- Gravity: For geometric scaling, mass densities are not scaled correctly if the same materials are used to construct the model and the prototype. For static tests, this only affects the dead load stresses, which, typically, are only a small percentage of the total stress. For the static overpressurization tests of the PCCV, this scaling artifact would not significantly affect on the model response, except, possibly, at the wall-base junction. Compressive stresses due to dead load are larger at the base of the cylinder wall than anywhere else in the model, and this stress may be an important response component for a bending/shear failure mode. Consequently, vertical tendon design loads were increased in the PCCV model to compensate for the reduced stress due to dead load at the wall-base junction.

The final tendon design stress profiles are shown in Figure 2.9. The profiles are given for a typical hoop tendon in the cylinder wall and for the longest and shortest vertical hairpin tendons. The stress distribution for the shorter hoop tendons in the dome and for both hoop and vertical tendons deflected around penetrations are not shown but can be calculated in a similar manner. (Note that the design tensioning and anchor forces for ‘deflected’ tendons are not adjusted in either the prototype or the model, to account for additional friction losses due to ‘in-plane’ curvature.) The corresponding design anchor forces are given in Table 2.5. These values were included in the model prestressing specifications. The as-built prestressing results are summarized in Section 2.2.3.

Table 2.5 PCCV Model Design Prestressing Anchor Forces

Tendons	Tensioning Force	Lift-Off Force	Losses (Creep and Relaxation)*	At Test
Vertical Tendons	49.6 tonnes (109.3 kips)	46.3 (102.1)	3.1 (6.8)	43.2 (95.3)
Hoop Tendons	44.4 tonnes (97.9 kips)	34.1 (75.2)	3.1 (6.8)	31 -68.4

*Losses evaluated at six months.

Considering the design tendon stress profiles, the prestressing design criteria can be satisfied. For the prototype, the average hoop tendon stress after 40 years is 85.3 kg_f/mm² (121.3 ksi). Calculating the equivalent pressure, p_{eqv}:

$$p_{eqv} = \frac{\sigma a}{R s} = \frac{(85.3 \text{ kg}_f/\text{mm}^2)(5429 \text{ mm}^2)}{(2150 \text{ cm})(45 \text{ cm})} = 4.8 \text{ kg}_f/\text{cm}^2 \text{ (68 psi)}$$

where

- a = the area of the tendon,
- R = the inside radius of the containment, and
- s = the hoop tendon spacing.

For the model, the average hoop stress after six months is 85.7 kg_f/mm² (121.8 ksi) and the equivalent pressure is:

$$p_{eqv} = \frac{\sigma a}{R s} = \frac{(85.7 \text{ kg}_f/\text{mm}^2)(339.3 \text{ mm}^2)}{(537.5 \text{ cm})(11.25 \text{ cm})} = 4.8 \text{ kg}_f/\text{cm}^2 \text{ (68 psi)}$$

which is essentially identical to the prototype. Comparing the design pressure, P_d, the hoop prestressing is equivalent to applying a counterbalancing pressure of 120% of the design pressure.

$$\frac{P_{eqv}}{P_d} = \frac{4.8 \text{ kg}_f/\text{cm}^2}{4.0 \text{ kg}_f/\text{cm}^2} = 1.20$$

Comparing the concrete compressive stress at the base of the wall:

For the prototype after 40 years:

$$\sigma_c = \frac{\sigma_a}{t s} = \frac{(106.3 \text{ kg/mm}^2)(5429 \text{ mm}^2)}{(130 \text{ cm})(77.32 \text{ cm})} = 57.4 \text{ kg/cm}^2 (817 \text{ psi})$$

Concrete compressive stress due to Dead Load 15.2 kg/cm² (216 psi)

Total compressive stress in Concrete 72.6 kg/cm² (1,033 psi)

where t is the thickness of the containment wall and s is the vertical tendon spacing.

For the model after 6 months:

$$\sigma_c = \frac{\sigma_a}{t s} = \frac{(127.5 \text{ kg/mm}^2)(339.3 \text{ mm}^2)}{(32.5 \text{ cm})(19.33 \text{ cm})} = 68.9 \text{ kg/cm}^2 (980 \text{ psi})$$

Concrete compressive stress due to dead load 3.2 kg/cm² (46 psi)

Total compressive stress in concrete 72.1 kg/cm² (1025 psi)

Therefore, the higher vertical tendon stress in the model, when combined with the dead load stress, yields nearly the same compressive stress in the concrete as the prototype.

2.2 Construction

2.2.1 General Construction

Prior to construction of the PCCV model, during the initial development of the containment test site in 1993, the location of the PCCV model was selected, the surface soil was removed, and the existing subgrade was excavated to a depth of over 8 m (25') and replaced with a compacted engineered backfill. The allowable bearing capacity, based on limiting soil settlement to 25 mm (1") or less, is 3.11 kN/m² (6.5 ksf) [26].

The overall site plan was shown in Figure 1.3. A detail of the areas surrounding the PCCV model is shown in Figure 2.10. The model was oriented so the E/H opening was facing due south. (This was primarily for operational considerations rather than any test requirement.) An aerial view of the test site during construction is shown in Figure 2.11.

On-site construction of the model by Hensel Phelps Construction Co. commenced on January 3, 1997 with construction of a 19.8 m × 19.8 m × 30 centimeters thick (65' × 65' × 1') mudmat placed on the engineered back-fill (Figure 2.12). This mudmat was constructed of 'lean' concrete and reinforced with welded wire fabric to provide a level working surface on which to construct the model. Benchmark monuments were constructed of small concrete pads at each of the four cardinal azimuths (0 degrees, 90 degrees, 180 degrees, and 270 degrees) outside the perimeter of the construction zone. These control points were subsequently used for the model's layout.

After the mudmat concrete had cured, a steel frame to support the basemat rebar was erected (Figure 2.13) and the rebar for the first basemat lift (F1) was erected (Figure 2.14). After verifying the position of the rebar (Figure 2.15), the formwork was set (Figure 2.16) and the F1 concrete placed (Figure 2.17). While F1 concrete was placed directly on the mudmat, there was no positive connection between the two.

Most of the model reinforcing was prefabricated by Border Steel Co., El Paso, TX, although some field fabrication was required as the construction progressed. All concrete was batched by Lafarge Construction Materials (formerly doing business as Western Mobile NM), Albuquerque, NM, mixed in transit and placed by pumping. All sampling and quality control tests were conducted by AGRA Earth and Environmental, Inc., Albuquerque, NM. Slump (Figure 2.18) and air entrainment tests were conducted on each batch/truck of concrete delivered to the site and standard cylinders and beams

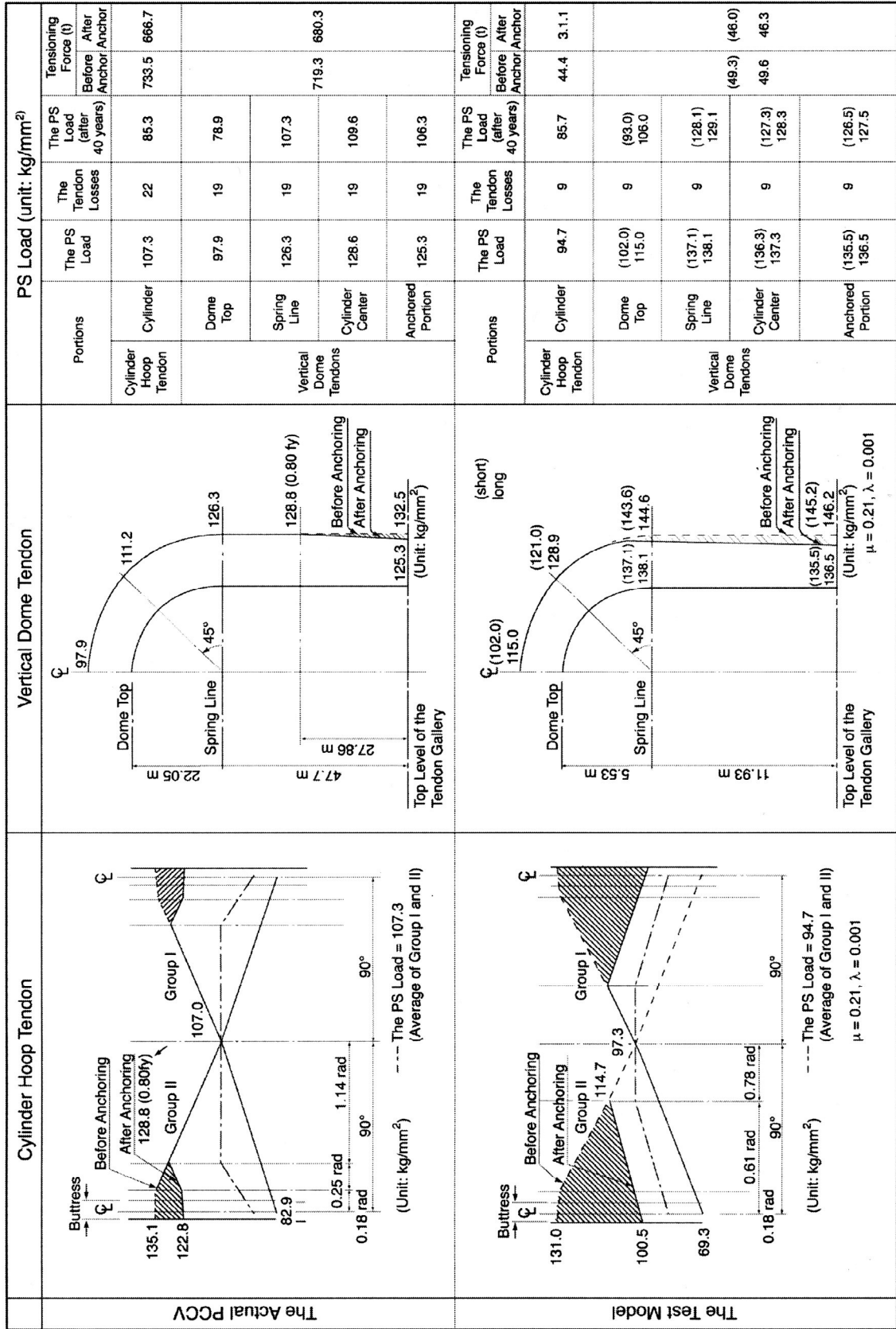


Figure 2.9 PCCV Prototype and Model Tendon Design Stress Profiles

were cast (Figure 2.19) for testing at seven, 28, and 91 days and at the time of tensioning and pressure testing. Both standard-cure, SC, (two to four days in a water bath, then stored in a humidity controlled chamber until testing), and field-cured (FC) specimens (two to seven days in a water bath, then stored on-site until testing) were produced and tested.

Installation of rebar and concrete placement for F2, F3, and F4 followed a similar sequence (Figures 2.20-2.25). Strain gages and thermocouples (T/Cs) were mounted on some of the rebar prior to installation and the lead wires were routed through the forms prior to concrete placement. As noted previously, the concrete outside the tendon gallery was not placed, thus allowing access for insertion and tensioning of the vertical tendons. The bottom basemat rebar that extended beyond the initial basemat lifts was covered with a temporary plywood deck to protect it from damage during construction until the final basemat pours (F5 and F6) were made. Other rebar that extended beyond lifts F1 to F4 were terminated and equipped with mechanical splices.

Prior to construction of the cylinder wall, a mock-up of the wall, incorporating the E/H embossment, vertical buttress, tendon sheaths, and the liner, was constructed to develop and demonstrate the erection sequence and method for placing the cylinder wall concrete (Figure 2.26). Since the wall lifts were approximately 3 m (10') in height, form 'windows' were located at mid-height (Figure 2.27) to limit the drop height of the wet concrete. Due to the dense rebar pattern, the trunk of the concrete pump could not be inserted into the forms. After placing the concrete through the form window and using spud-type vibrators to consolidate the concrete and prevent voids, the windows were blocked and placement of concrete continued at the top of the mock-up. After the concrete had cured and the exterior form was removed, the mock-up was cored to inspect for voids in the concrete. None were discovered. While this sequence of construction was not completely identical to the sequence for the model wall (e.g. continuing vertical wall reinforcing would limit placement at the top of each lift), the mock-up demonstrated that the planned construction sequence would be successful.

Since New Mexico is subject to severe summer lightning storms and the PCCV model is in an exposed desert terrain, a lightning protection system, consisting of four 30 m (100') poles connected to a buried copper cable counterpoise, was installed around the model. The lightning protection system provides an alternate path to ground around the model, thereby preventing direct lightning strikes that might damage the instruments, wires, and data acquisition components. Until the dome was completed, only two of the poles at 0 degrees and 180 degrees could be installed to accommodate crane operations, thereby providing only partial protection. Nevertheless, the protection system appears to have functioned successfully, since no direct lightning strikes were ever recorded on the model, even though there was a strike on the chain-link fence surrounding the site that damaged unprotected telephone lines strung along the fence.

While the basemat and wall mock-up construction was being completed, the liner panels, which had been fabricated by MHI in Kobe, Japan, were shipped to the test site. The liner panels arrived at the site in June, 1997 (Figure 2.28). Prior to shipping the panels to the U.S., all the cylinder wall panels were temporarily erected in Kobe to ensure that they would fit. Typical liner panels with support jigs are shown in Figure 2.29.

At the same time the liner panels were being shipped, an internal structural steel frame was fabricated (in the U.S.) and also delivered to the test site. This structure, known as the instrumentation frame, provided the support structure from which to hang the liner panels, with jigs, prior to welding; provided internal support during concrete placement; and provided a work platform during liner welding and installation of the internal instrumentation. During testing, this internal frame also acted as the reference structure for measuring model displacements. Components and erection of the instrumentation frame are shown in Figures 2.30-2.33.

Beginning in September, 1997, the liner panels were erected and bolted to the frame (Figures 2.34-2.36). After all the panels were assembled, a crew of welders from MHI began welding the liner seams. First, the basemat liner plates were welded to the embedded anchors. The liner erection plan then called for the seam between the first liner ring and the basemat to be welded, followed by the horizontal seam between the first and second liner rings. After this, the vertical seams for the first ring were completed. The liner erection and welding specifications defined overall and local dimensional tolerances and nondestructive inspection criteria. All liner welds were radiographed and inspected for flaws (undercutting, inclusions, and porosity). Initial difficulties welding the 1.6 mm liner in the field resulted in most of first ring's liner welds is being rejected. These welds were then ground out and repair welds were made. While there was some improvement, some of the repair welds contained flaws that exceeded the welding specifications. After additional repairs, inspection, and laboratory tests of welded liner specimens, it was decided that the original welding specifications were overly conservative and the criteria on flaws were relaxed. (The original weld flaw acceptance criteria had been scaled from the prototype welding specifications.)

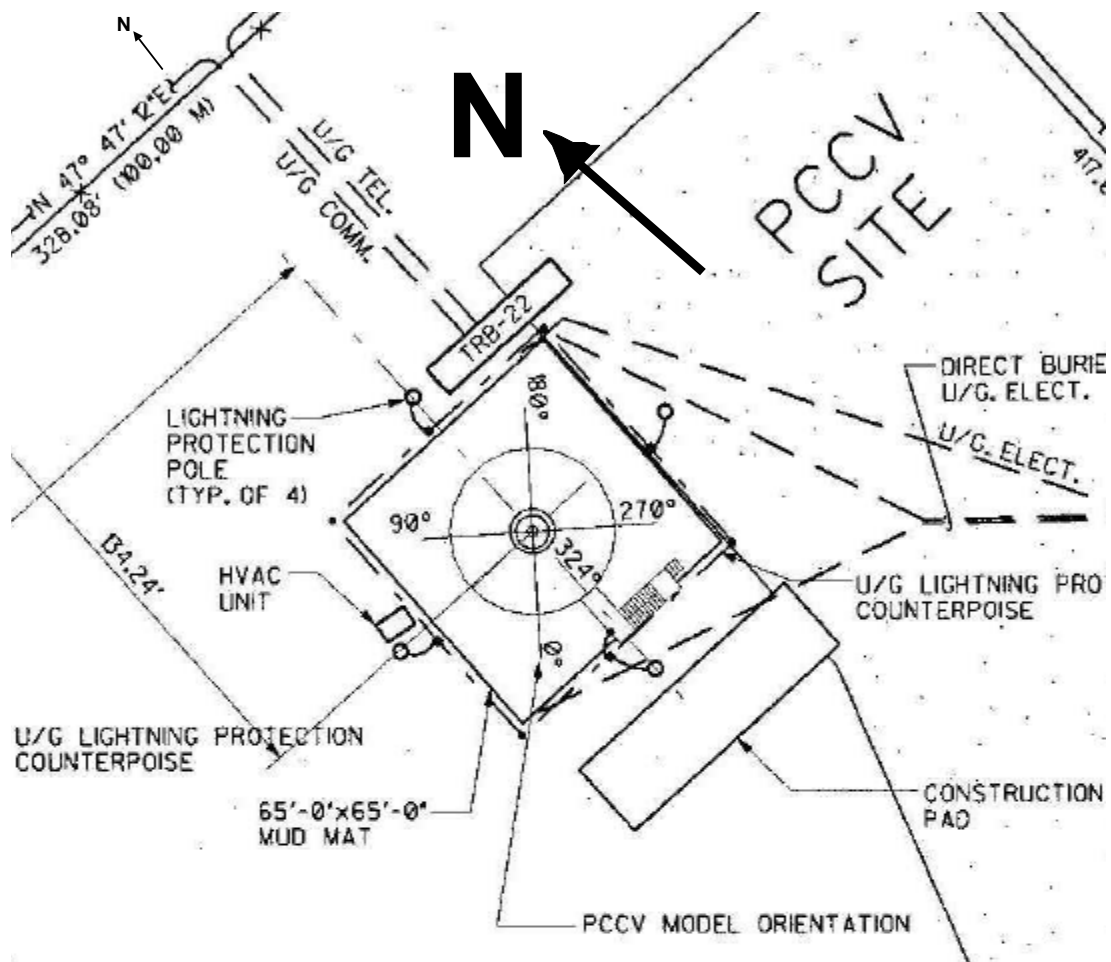


Figure 2.10 PCCV Model Layout

For the 6.4 mm (1/4") thick liner in the prototype, the liner seam welds could be made using double-sided full penetration welds. However, this method of welding could not be used for the 1.6 mm (1/16") thick model liner welds. The field welds in the model liner required back-up bars or, in some locations, back-up tape, and the full penetration welds were made from one side. Where welds were ground out and repaired, it was sometimes necessary to remove a section of the back-up bar and replace it with another segment. (Note that this created some local discontinuities in the model liner that became important during the pressure tests, but which were not representative of details in the prototype.) In areas where liner strains were expected to be high due to geometric discontinuities, the back-up bars were removed after the liner welds were completed to maintain the similarity with the prototype. In some locations, the weld bead was ground to reduce its profile, as well.

Both of these cosmetic post-weld treatments may have caused local thinning of the liner. Unfortunately, no measurements of the post-weld liner thickness were made. After the liner seam welds were completed, the penetration insert assemblies were welded to the liner and the stiffener, and liner anchor welds were completed.

To expedite the liner strain gage installation and the model's erection, a number of strain gages on the exterior surface of the liner, i.e. the concrete side of the liner, were installed prior to erection and welding of the liner panels. Since heat input from the welding operations could damage strain gages near the weld seams, only those gages over 10 cm (4") from the weld seams were installed prior to erection. This included gages on the liner anchors and stiffeners. Figure 2.36 shows two liner panels during installation of the strain gages. After the liner panels were erected and welded, the exterior



Figure 2.11 Aerial View of CTTF-West during PCCV Construction (March, 1999)

strain gages near the liner weld seams were installed. Figures 2.38 and 2.39 show typical strain gage installations near weld seams.

After all weld inspection criteria had been satisfied, construction of the model proceeded with the installation of inner horizontal and vertical rebar layers in the cylinder and dome (Figures 2.40-2.41). All instrumented rebar for these two layers was installed concurrently with the remainder of the reinforcing steel.

Next, the tendon sheath support frame, consisting of steel angles with support pins to correctly position the tendon sheaths, was installed (Figure 2.42). Except for the instrumented hoop tendons, which were preassembled with the sheath, all the tendon sheaths were all installed prior to outer reinforcing and shear reinforcing (Figures 2.43 and 2.44). The model construction then proceeded by lifts; C1 through C4 in the cylinder, and D1 to D3 in the dome. For each lift, the outer and radial rebar, including instrumented rebar and any instrumented hoop tendons, were installed first. Lead wires for the liner, rebar and tendon strain gages, embedded T/Cs, and fiber optic strain gages, were then routed through PVC ducts that had been placed in the previous lift. After checking that the gages and lead wires had not been damaged and were still functioning, the outer concrete forms were installed and concrete for each lift was placed. After the concrete had cured sufficiently, the outer forms were stripped and the cycle was repeated until the final dome pour was completed. The final dome pour, D3, was completed without the use of external forms. The plasticizer was not added for this lift, so a low slump was maintained and the final surface was hand finished, aided by a wooden template that defined the outer surface. This sequence of construction is illustrated in Figures 2.45 through 2.52.

After the D3 concrete achieved its specified strength, the liner jigs were cut loose from the liner, detached from the interior frame, and removed. This freed the containment wall from the interior frame, making both structures independent of each other. The instrumentation frame then functioned as a work platform and as the reference frame for measuring shell displacements.

After the liner jigs were removed, model construction was temporarily suspended while SNL assumed control of the model for installing of the interior instrumentation. Details of the instrumentation installation are provided in Chapter 3. Prior to installing the interior instrumentation, the interior of the liner surface was cleaned and painted white. Cardinal lines were surveyed and marked on the liner as reference for the installation of the interior instrumentation. The as-built radii at the intersections of the cardinal lines were also determined, and the results are tabulated in Appendix C.

Prior to beginning the interior instrumentation, interior lighting, power, and ventilation were installed. Structural steel stairs to the top of the basemat and E/H were erected, and a vestibule with locking doors for access control was installed over the E/H opening. Machined flange covers were installed over the M/S and F/W penetration sleeves. Six of these covers were drilled for the sealed instrumentation feedthroughs and the remaining two were equipped for the power feedthrough and the pressurization line.

While the interior instrumentation was completed, construction activities resumed after an approximately six-month hiatus with the insertion of prestressing tendons into the sheaths. After the interior instrumentation was completed and verified ready for operation, the DAS was started prior to tensioning the tendons. Details of the prestressing operations and results are described in Section 2.2.3. After prestressing was completed, model construction concluded with the placement of the final basemat concrete lifts, F5 and F6 (Figure 2.53). After the forms were stripped, Mitsubishi and Hensel Phelps demobilized and turned the model over to SNL on July 28, 2000. The completed PCCV model is shown in Figure 2.54.

2.2.2 Material Properties

Properties of all the PCCV model construction materials, except for the model concrete, were determined from tests prior to construction and summarized in Section 2.1. Model concrete properties were determined by testing standard specimens (cylinders and beams) cast during placement of each concrete lift.

All concrete testing was conducted according to ASTM standards¹⁰ and the results are summarized in Appendix B. Quality control tests, consisting of standard 6-inch cylinder, unconfined compressive strength tests, were performed by AGRA Earth and Environmental, Inc. Specimens were cast from nearly every truck of concrete placed in the model. (Each truck contained approximately 7.6 m³ (10 cubic yards.)) Standard Cured (SC) specimens were cured in a water bath for two to four days (depending on weekends) and stored in a humidity-controlled chamber until tested. FC specimens were also cured in a water bath for two to four days, then stored at the site, under blankets, until tested. Compression tests¹¹ of both SC and FC cylinders were conducted at seven, 28, and 91 days. 91-day strengths were compared to the specified design strengths.

The average 91-day FC strength results for the first two cylinder wall lifts, C1 = 389kg_f/cm² (5527 psi) and C2 = 436kg_f/cm² (6200 psi), failed to meet the minimum specified design strength of 450 kg_f/cm² (6400 psi). This may have resulted from cold weather conditions, which might have retarded the curing rate. Analysis of the test data suggested that the concrete would reach the specified minimum design strength by the time prestressing was scheduled to occur, so no action was deemed necessary. Nevertheless, the curing method of FC specimens for lifts C4 through D3 and F5 and F6 was modified to keep the cylinders in the water bath for seven days. This modified field curing method is designated FC' in the material data summary.

While the strength of the concrete in C1 and C2 was deemed adequate, there was a concern that the low strength might cause higher creep losses than anticipated in the prestressing design calculations. Creep tests¹² of two specimens each from C1 and C2 were conducted at the University of New Mexico and compared to the results of the trial mix creep tests

¹⁰ *Annual Book of ASTM Standards*, American Society for Testing and Materials (ASTM), Philadelphia, PA.

¹¹ ASTM C39-94, "Standard Test Method for Compressive Strength of Cylindrical Concrete Specimens."

¹² ASTM C512-87, "Standard Test Method for Creep of Concrete in Compression" (modified).



Figure 2.12 Placement of PCCV Mudmat



Figure 2.13 Basemat Rebar Support Frame



Figure 2.14 Basemat Bottom Bars and Vertical Ties

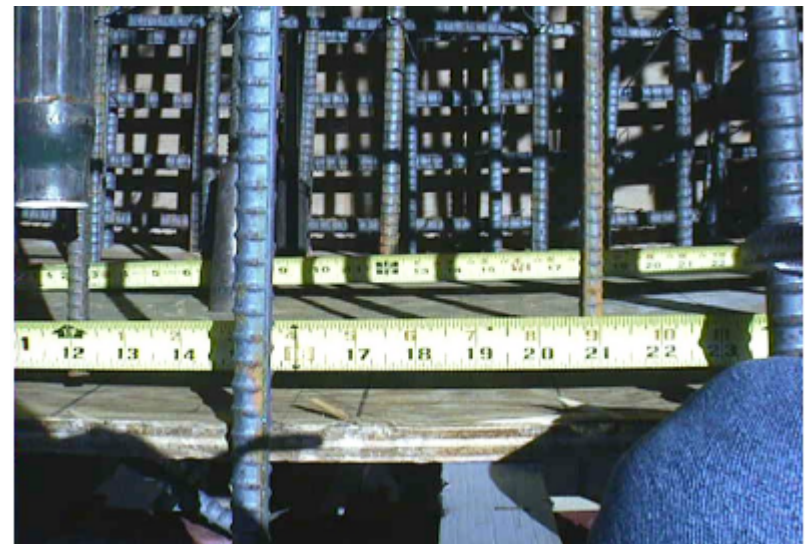


Figure 2.15 Measuring Rebar Location



Figure 2.16 F1 Formwork



Figure 2.17 Placing F1 Concrete

2-19



Figure 2.18 Measuring Concrete Slump



Figure 2.19 Concrete Test Cylinders and Beams



Figure 2.20 F2 Rebar Erection

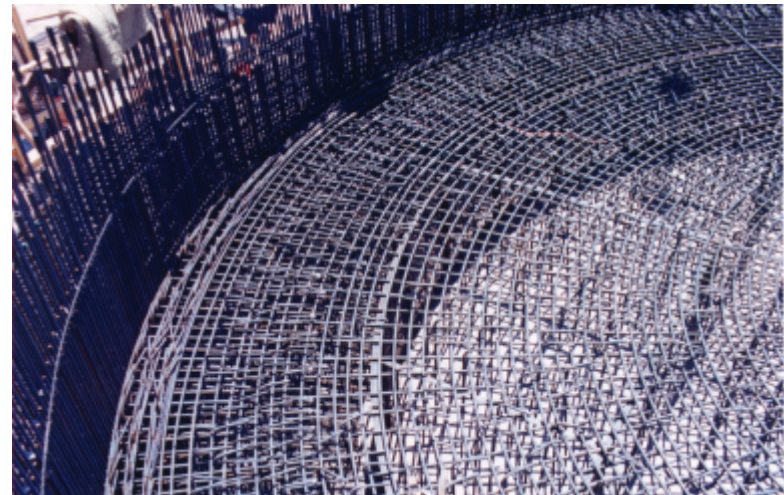


Figure 2.21 F3 Rebar

2-20



Figure 2.22 F3 Rebar and Formwork



Figure 2.23 Basemat Top Rebar (F3) and Wall Dowels



Figure 2.24 F3 Concrete Placement



Figure 2.25 F4 Concrete



Figure 2.26 Wall Mock-Up Rebar



Figure 2.27 Wall Mock-up Form w/ Concrete 'Window'



Figure 2.28 Delivery of Liner Panels



Figure 2.29 Liner Panels after 'Uncrating'



Figure 2.30 Instrumentation Frame Column 'Trees'



Figure 2.31 Instrumentation Frame Erection



Figure 2.32 Instrument Frame Erection



Figure 2.33 Completed Instrument Frame



Figure 2.34 Liner Panel Erection



Figure 2.35 Dome Liner Erection



Figure 2.36 Liner Panels with Jigs



Figure 2.37 Liner Panel Instrumentation



Figure 2.38 Liner Strain Gages after Welding



Figure 2.39 Close-Up of Liner Strain Gages near Weld



Figure 2.40 Inner Rebar at M/S Penetrations



Figure 2.41 Installation of Inner Dome Rebar

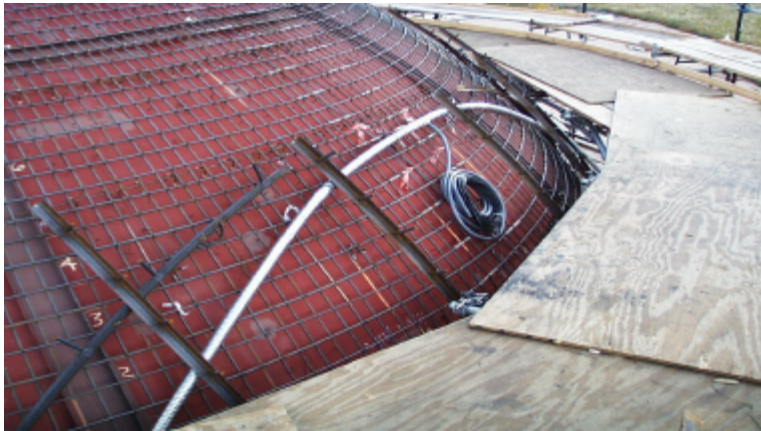


Figure 2.42 Tendon Sheath Support Frame



Figure 2.43 Dome Tendon Sheaths and Support Frame



Figure 2.44 PCCV Model Tendon Sheaths



Figure 2.45 **Outer Rebar for C1**



Figure 2.46 **C1 Formwork Installation**



Figure 2.47 **Placing C1 Concrete**



Figure 2.48 **Installation of Instrumented Hoop Tendon.**



Figure 2.49 C2 Formwork



Figure 2.50 C4 Concrete Placement



Figure 2.51 D1 Formwork Erection



Figure 2.52 D3 Concrete Placement



Figure 2.53 Final Basemat Concrete Lifts

[27]. These results, presented in Appendix B, showed higher amounts of creep and shrinkage than the trial mix data and indicated that creep losses in the prestressing might be higher than expected. This data was considered in specifying the tensioning forces for the tendons in Table 2.5.

More extensive material property tests for FC specimens were conducted around the time the model was being tensioned and just prior to the Limit State Test (LST). These tests provided more accurate material property data for concrete constitutive models used in the pre- and posttest analyses to predict and simulate the model response to pressure. These tests were also conducted at the University of New Mexico and included unconfined compression tests, compression tests to determine modulus of elasticity and Poisson's ratio¹³, split cylinder tensile strength¹⁴, and modulus of rupture¹⁵. The unit weight of the specimens was also determined and, since prediction of concrete cracking was one of the pretest analysis milestone objectives, a limited number of direct tension tests were conducted on specimens from the cylinder wall. The results of these tests and the direct tension test procedure are detailed in Reference [28] and summarized in Appendix B. A summary is also provided in Table 2.6.

A few other observations on the model concrete are worth noting:

1. The Coefficient of Variation (COV) in the compressive strength of the FC model concrete was 15.9% at 91-days and 13% at the time of prestressing. This COV is larger than typically observed for concrete from a central batch plant and indicates a significant degree of variation in the model concrete properties.
2. Compressive failure strains in the concrete specimens were typically in the range of 0.25 to 0.30%. While the tensile failure strain was not determined, the direct tension tests performed by the University yielded critical crack opening displacement data, which could be utilized in a fracture mechanics approach.
3. The modulus of elasticity in compression, determined from test data, is significantly lower than values usually computed from 'rules-of-thumb.' For example, ACI 318¹⁶ recommends that $E_c = 57,000 \sqrt{f'_c}$ in psi. Using 9300 psi as the average strength of the field cured cylinder/dome specimens yields an elastic modulus of 5.51×10^6 psi, compared to the measured value of 3.90×10^6 psi, a reduction of nearly 30%. If the modulus were based on the specified minimum strength of 6400 psi, the resulting value would be 4.56×10^6 psi, still higher than the measured value by 15%.

¹³ ASTM C469-94, "Standard Test Method for Static Modulus of Elasticity and Poisson's Ratio of Concrete in Compression."

¹⁴ ASTM 496-96, "Standard Test Method for Splitting Tensile Strength of Cylindrical Concrete Specimens."

¹⁵ ASTM C78-94, "Standard Test Method for Flexural Strength of Concrete (Using Simple Beam with Third-Point Loading)."

¹⁶ *Building Code Requirements for Structural Concrete*, ACI 318-02, American Concrete Institute, Farmington Hills, MI.



Figure 2.54 Completed PCCV Model

2.2.3 Prestressing Operations

With the majority of the model instrumentation suite installed, model construction resumed in February, 2000 with the insertion of noninstrumented tendon strands into the sheaths embedded in the model. Prior to insertion, the strands were coated with an anti-corrosive agent, but there was no other treatment. Insertion was achieved by feeding a ‘puller cable’ through the sheath equipped with a wire gripping sleeve that tightened on the strands as it was tensioned to pull them through the sheath (Figure 2.55). Except for a few minor obstacles, e.g. grout which had penetrated the sheath splices and had to be cleared, the sheaths were clear and insertion was accomplished without any difficulty.

Table 2.6 PCCV Model Average Concrete Properties

Design Compressive Strength		300kg _f /cm ²	(4300 psi)	450kg _f /cm ²	(6400 psi)
@ Prestressing					
Compressive Strength,	FC	570	(8102)	559	(7956)
	FC'	NA	NA	680	(9665)
Young's Modulus		25.7 GPa	(3.7 × 10 ⁶ psi)	27.2 GPa	(4.0 × 10 ⁶ psi)
@ Limit State Test					
Compressive Strength,	FC	562	(7998)	615	(8750)
	FC'	NA	NA	700	(9953)
Young's Modulus		27.2 GPa	(3.9 × 10 ⁶ psi)	26.9 GPa	(3.9 × 10 ⁶ psi)
Poisson's Ratio		0.21		0.22	
Split Tensile Strength		35	(497)	36	(519)
Direct Tensile Strength		NA	NA	23	(320)
Modulus of Rupture		NA	NA	42	(594)
Density		2186kg _f /m ³	(136.4 pcf)	2176kg _f /m ³	(135.8 pcf)

The suite of gages installed on the model prior to prestressing and installing the DAS cleared the final system checks, and the DAS was put into operation at 11:48 AM, March, 3, 2000. The initial data scan represented the initial or ‘zero’ reading for all the model transducers. All subsequent readings, through the LST until the DAS was shut down in October, are referenced to this initial scan. The model was scanned hourly for seven days to provide baseline information on the response to ambient temperature variations prior to tensioning the model and to verify the operational readiness of the DAS in attended and unattended modes.

Model prestressing began on March 10, 2000. The arrangement of the model tendons is shown in Appendix A. The nomenclature for identifying individual tendons consisted of an alpha designator ‘H’ for hoop tendons and ‘V’ for vertical tendons, followed by a numerical designator (1 through 98 for the hoop tendons and 1 through 90 for the vertical tendons). The hoop tendons were numbered consecutively from 1, the lowest tendon in the cylinder wall, to 98, at the midpoint of the dome. Even-numbered hoop tendons (H2, H4, H6, ..., H98) were anchored at the 90 degree buttress and odd-numbered hoop tendons (H1, H3, ..., H97) were anchored at the 270 degree buttress. Vertical tendons were numbered consecutively from V1 at 45 degrees, clockwise to V90 at 223 degrees. The vertical tendons were arranged in two orthogonal groups, with V1 through V45 spanning the dome in a plane (nearly) parallel to the 90 to 270 degree axis and V46 through V90 in an orthogonal plane approximately 0 to 180 degrees. This arrangement is illustrated more clearly in the design drawings and shown in Figure 2.44.



Figure 2.55 Pulling Hoop Tendons

Prestressing operations were defined by MHI in the project construction specifications¹⁷. The overall sequence of tensioning is illustrated in Figure 2.56. This sequence is identical to that used for the prototype and is intended to apply balanced prestressing forces to the model to prevent excessive local deformation or damage. The actual tensioning schedule is shown in Table 2.7. Prestressing operations were completed on May 3, 2000.

Thirty-four of the 188 tendons were instrumented with load cells at the anchors, and eight of these tendons, five hoop and three vertical, were also instrumented with strain gages at discrete locations along their length in an attempt to monitor and record the force distribution for comparison with the design calculations. The instrumented tendons are identified in Table 2.7 and their locations are illustrated in Figure 3.21. Details of the tendon instrumentation are given in Chapter 3.

Only one tendon was tensioned at a time (Figure 2.56). The procedure was to assemble the tensioning hardware at each end of the tendon. The tensioning hardware consisted of the tendon anchor and wedges, tensioning chair, hydraulic jack, and tensioning anchor. For the instrumented tendons, a pair of bearing plates, spherical washers, and the load cell was inserted between the tendon anchor and the bearing plate embedded in the model. This arrangement is shown in Figure 2.58. After the tensioning hardware was assembled, one end of the tendon, designated the 'B' end, was tensioned to 10% of the design load while the jack on the 'A' end was locked off. Then the B-end jack was locked off and the tensioning force was applied continuously by the jack at the A end until the jack pressure gage indicated that the force specified in Table 2.5 had been reached. (The jacks were calibrated prior to the start of prestressing and the conversion between hydraulic pressure and force was established for each jack.) In most cases, the tendon 'stretch' exceeded the maximum stroke of the jack and the strands had to be regripped to complete tensioning. When the A end was at the maximum load, the force at the B end was recorded and the friction coefficients for the tendon were computed and compared to the design values. (If the friction deviated from the design values by more than a specified range, the tendon was retensioned or, in some instances, the tendon was removed and new strands were inserted.) The B end was then tensioned to the specified force. When both ends were at the specified force, the anchors were seated.

¹⁷ MH-K10-29, "Prestressing Work Procedure," Rev. 1, Mitsubishi Heavy Industries, May, 1999.

The seating loss, defined in terms of length, was measured as the difference between the length of the tendon extending beyond the anchor, before and after seating. This indicates the loss of elongation (and hence tension) in the tendon as the load is transferred from the jack grips to the tendon anchors. The measured seating loss was compared to the maximum design seating loss of 5 mm (0.2"), and, if it was excessive, the tendon was retensioned. After seating the tendon, each end was subjected to a 'lift-off' test in which the tendons were regripped and pulled until the tendon anchor lifted off the bearing plate enough to insert a feeler gage between them. The measured lift-off force was also compared to the value specified in Table 2.5.

The instrumented tendons, those with load cells only and those with strain gages, were closely monitored during tensioning but the load cell data was not reported to the tensioning contractor, VStructural, LLC., during prestressing. The tensioning procedure was modified for the eight instrumented tendons with strain gages. Since the lead wires for these gages would be damaged if the tendon was pulled in one direction first and then the other, causing the gages and the lead wires to travel back and forth in the sheath, these tendon were tensioned simultaneously at both the A and B ends. The tensioning forces were applied in small load increments and the tendon gages were monitored continuously during tensioning. The responses of the instrumented tendons are shown as force time histories in Figures 2.59 through 2.66.

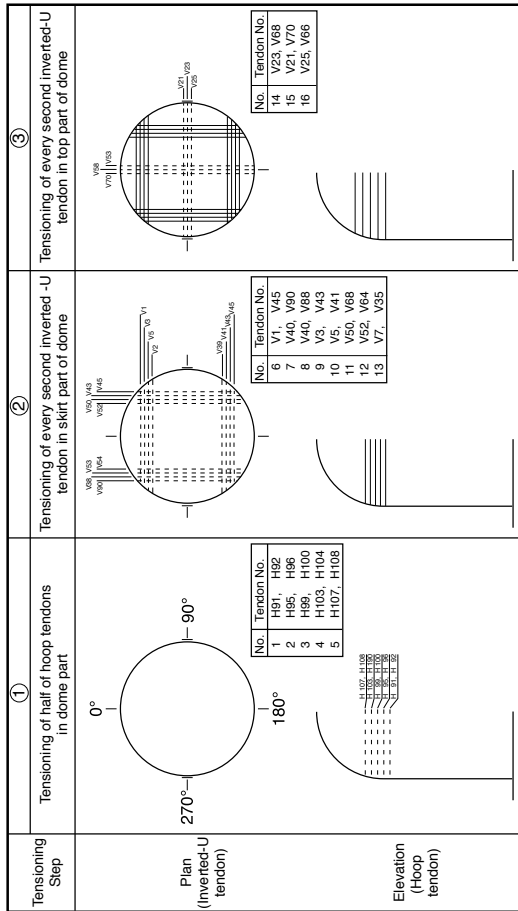
These figures show the response of the load cells at each end of the tendons and the response of the surviving strain gages (converted to force by multiplying the strain by the nominal tendon area and elastic modulus of the strand). The strain gages on these tendons suffered a high mortality rate during prestressing, as shown in Table 2.8. Nevertheless, a high mortality rate was expected, and in most cases the surviving strain gages provided insight into the behavior of the tendons during prestressing and subsequent pressure testing.

The figures illustrate the range of strain in individual strand wires at a given measurement position, and also show when some of the strain gages failed. The data was not plotted after a gage had failed. It is interesting to note that the Tensmeg gages (TT) typically gave lower strain readings than the bonded foil gages (TF) mounted on individual wire strands. This is likely due to the Tensmeg end blocks slipping relative to the strand, resulting in an inaccurate measure of the strand strain. For most future discussions of the tendon response, only the data from the TF gages is considered as a reliable measure of the tendon strain and the TT data is ignored.

Figure 2.62 illustrates how the stages of the prestressing procedure are reflected in the test data. In the figure for H67, the surviving strain gages at each measurement position along the length of the tendon were averaged before converting them to a tendon force. This was done to simplify the plot, but this also recognizes that the force in individual wires in the tendon strands vary and the load cells (TL) forces and average forces from the strain gages (TF or TT) are plotted as a function of time. The force time history shows the load being applied incrementally at both ends of the tendon until the specified tensioning force was achieved and load was stable. Note that at a force of approximately 30T, the tendon was anchored and regripped when the stroke of the jacks was exceeded. After stabilizing at the maximum force, the tendons were seated, with the corresponding drop in load at and near the anchors. The slight increase in force at the anchors after seating reflects the lift-off test. (This shows that the force required to lift-off the anchor is slightly higher than the seated anchor force.)

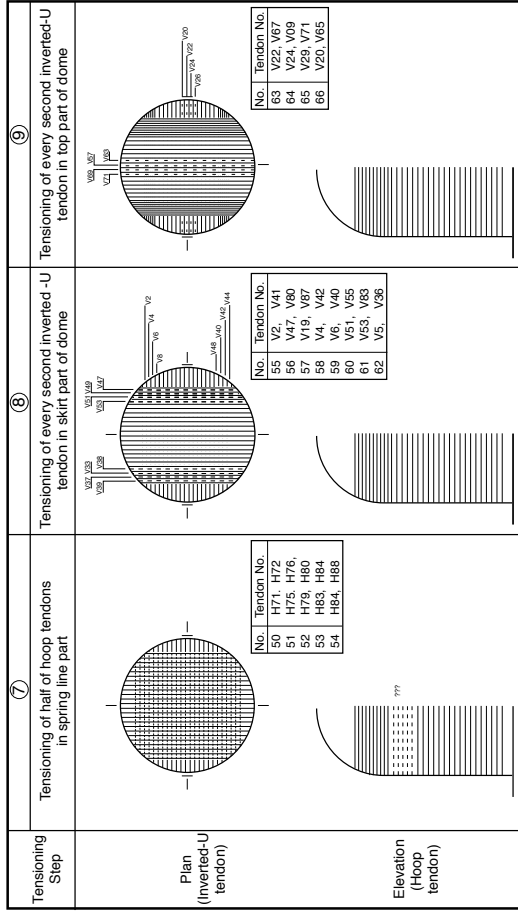
Note also that the strain gages were most likely to fail near the tendon anchors and less likely to fail at the tendon mid-point. This occurs because the strands near the anchors travel the furthest during tensioning, increasing the likelihood that the gages or their lead wires were crushed against the sheath wall or another strand.

Considering Figure 2.62, it can be seen that the general force distribution along the length of the tendons is consistent with the design assumption, i.e., the highest tendon force is near the anchor and the lowest force is at the mid-point of the tendon. Figures 2.67 through 2.74 compare the measured force distribution in the tendons during and after tensioning with the design assumptions shown in Figure 2.9. The data for the horizontal tendons generally confirms the assumed design force distribution. The surviving gages do not provide enough data points to fully define the shape of the force distribution curve, notably where the effect of the anchor set loss disappears. Due to the discontinuities in the hoop tendon force distribution, only the data points are shown and no attempt was made to interpolate the hoop tendon force between measurement locations. In general, the data is consistent with the design assumptions and does not appear to contradict the predicted response.



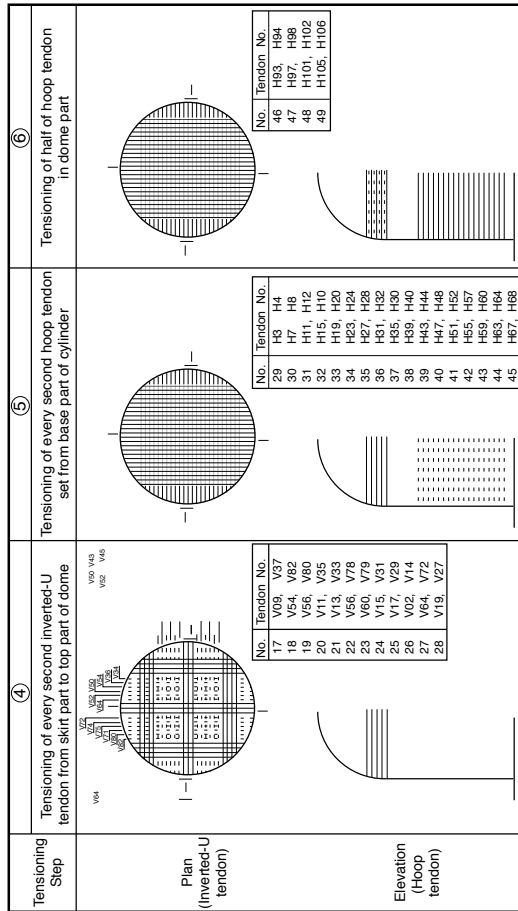
Tensioning Sequence (1/4)

Note: 1. Solid line shows tendon tensioned fully in the previous step.
2. Broken line shows tendon to be tensioned in this step.



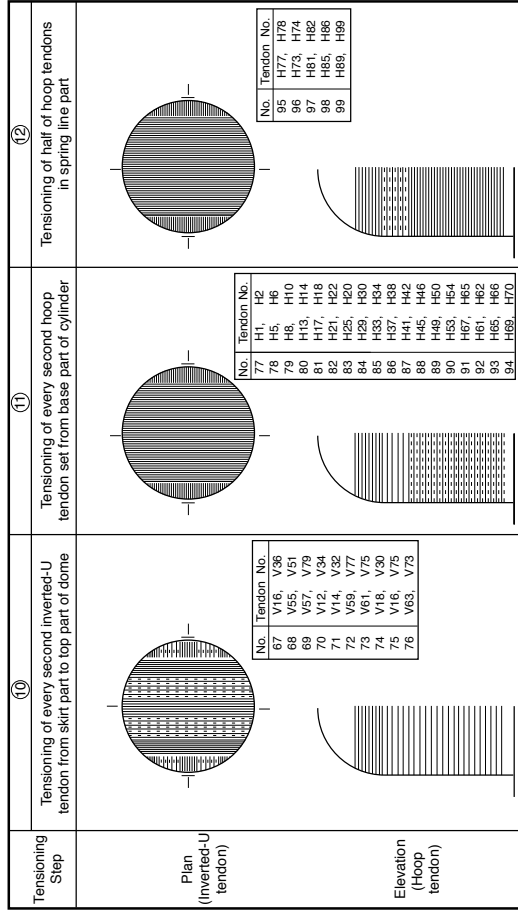
Tensioning Sequence (3/4)

Note: 1. Solid line shows tendon tensioned fully in the previous step.
2. Broken lines show tendon to be tensioned in this step.



Tensioning Sequence (2/4)

Note: 1. Solid line shows tendon tensioned fully in the previous step.
2. Broken lines show tendon to be tensioned in this step.



Tensioning Sequence (4/4)

Note: 1. Solid line shows tendon tensioned fully in the previous step.
2. Broken lines show tendon to be tensioned in this step.

Figure 2.56 PCCV Model Tensioning Sequence

Table 2.7 Model Prestressing Schedule

Sun	Mon	Tue	Wed	Thr	Fri	Sat
5-Mar	6-Mar	7-Mar	8-Mar	9-Mar	10-Mar	11-Mar
					H91 H92	
						V45
Sun	Mon	Tue	Wed	Thr	Fri	Sat
12-Mar	13-Mar	14-Mar	15-Mar	16-Mar	17-Mar	18-Mar
	H95 H96 H99 H100 H103	H103* H104 H107* H108* V1	V1* V45* V90	V46 V48 V88 V3 V43	V5 V41(1) V50	V86(2) V52 V84 V7
		*retensioning required				V54
Sun	Mon	Tue	Wed	Thr	Fri	Sat
19-Mar	20-Mar	21-Mar	22-Mar	23-Mar	24-Mar	25-Mar
	V39 V23 V68 V21 V70 V25(3) V66	V66* V25 (3) V9	V37 NUPEC AUDIT INSP. V54 V82 V56* V80	V11 PRP SITE VISIT V35* V13 V33 V58 V78 V60	V76* V15 V31 V17 V29	V62 V74 V64 V72 V19 V27
						H11
Sun	Mon	Tue	Wed	Thr	Fri	Sat
26-Mar	27-Mar	28-Mar	29-Mar	30-Mar	31-Mar	1-Apr
	H3 H4 H7* H8 H12	H11 H16 (4) H15	H16 H19 H20 H23 H24 H27 H28 H31	H32 H36 H35(5) H40	PS Op's suspended due to high winds.	H63
Sun	Mon	Tue	Wed	Thr	Fri	Sat
2-Apr	3-Apr	4-Apr	5-Apr	6-Apr	7-Apr	8-Apr
	H39* H44 H43 H48 H47 H52 H51	H56 H55 H60 H59 H64 H63*	H63 H67 H68	H93 H94 H97 H98 H102 H101	H105 H106	V49

Sequence

1	H91	58	H4
2	H92	59	H7**
3	H95	60	H8**
4	H96	61	H11
5	H99	62	H12
6	H100	63	H15
7	H103	64	H16
8	H104	65	H19
9	H107	66	H20
10	H108	67	H23
11	V1	68	H24
12	V45	69	H27
13	V46	70	H28
14	V90	71	H31
15	V48	72	H32
16	V88	73	H35
17	V3	74	H36
18	V43	75	H39
19	V5	76	H40
20	V41	77	H43
21	V50	78	H44
22	V86**	79	H47
23	V52	80	H48
24	V84	81	H51
25	V7	82	H52
26	V39	83	H55
27	V23	84	H56
28	V68	85	H59
29	V21	86	H60
30	V70	87	H63
31	V25	88	H64
32	V66	89	H67
33	V9	90	H68
34	V37	91	H93
35	V54	92	H94
36	V82	93	H97
37	V56	94	H98
38	V80	95	H101
39	V11	96	H102
40	V35	97	H105
41	V13	98	H106
42	V33	99	H71
43	V58	100	H72
44	V78	101	H75
45	V60	102	H76
46	V76	103	H79
47	V15	104	H80
48	V31	105	H83
49	V17	106	H84
50	V29	107	H87
51	V62	108	H88
52	V74	109	V2
53	V64	110	V44
54	V72	111	V47
55	V19	112	V89
56	V27	113	V49
57	H3		

Load Cell

Schedule Impact

Instrumented

**Tendon to be replaced

Completed

Weekend Milestone

Table 2.7 Model Prestressing Schedule (continued)

							<u>Sequence</u>				
Sun	Mon	Tue	Wed	Thr	Fri	Sat					
9-Apr	10-Apr	11-Apr	12-Apr	13-Apr	14-Apr	15-Apr	114	V87	157	H9**	
	Jack Re-calibration	PS Op's suspended due to high winds.	H71	H87	V87		115	V4	158	H10	
			H72	H88	V4		116	V42	159	H13	
			H75	V2	V42		117	V6(1)	160	H14	
			H76	V44	V6(1)		118	V40(2)	161	H17	
			H79	V47*	V40(2)		119	V51	162	H18	
			H80	V89	V51		120	V85	163	H21	
			H83	V49			121	V53	164	H22	
			H84				122	V83	165	H25	
						V12	123	V8	166	H26	
Sun	Mon	Tue	Wed	Thr	Fri	Sat	124	V38	167	H29	
16-Apr	17-Apr	18-Apr	19-Apr	20-Apr	21-Apr	22-Apr	125	V22	168	H30	
	V85 Op Error damaged 19/31 gages. Op's suspended	Op's suspended	V85	V8*	V26*	V36(6)	126	V67	169	H33	
			V53	V38	V71	V55	127	V24	170	H34	
			V83	V22	V20	V81	128	V69	171	H37	
				V67*	V65	V57	129	V26	172	H38	
					V24	V10		130	V71	173	H41
					V69	V36		131	V20	174	H42
								132	V65	175	H45
								H22	133	V10	176
Sun	Mon	Tue	Wed	Thr	Fri	Sat	134	V36	177	H49	
23-Apr	24-Apr	25-Apr	26-Apr	27-Apr	28-Apr	29-Apr	135	V55	178	H50	
	V79* V12 V34 V14 V32(6) V59	V77	H1	H17	H41		136	V81	179	H53	
		V61*	H2	H18	H42		137	V57	180	H54	
		V75	H5	H21	H45		138	V79	181	H57	
		V16	H6	H22	H46		139	V12	182	H58	
		V30	H9	H25	H49		140	V34	183	H61	
		V18	H10	H26	H50		141	V14	184	H62	
		V28	H13	H29			142	V32	185	H65	
		V63	H14	H30			143	V59	186	H66	
		V73		H33			144	V77	187	H69	
				H34			145	V61	188	H70	
				H37			146	V75	189	H73	
				H38			147	V16	190	H74	
							H73	148	V30	191	H77
Sun	Mon	Tue	Wed	Thr	Fri	Sat	149	V18	192	H78	
30-Apr	1-May	2-May	3-May	4-May	5-May	6-May	150	V28	193	H81	
	H54	H58	H85				151	V63	194	H82	
	H53	H61	H86				152	V73	195	H85	
	H57	H62	H89				153	H1	196	H86	
		H65	H90				154	H2	197	H89	
		H66					155	H5	198	H90	
		H69					156	H6			
		H70									
		H73									
		H74									
		H77									
		H78									
		H81									
		H82									
			H90								

Notes:

- (1) V41 removed and replaced with V6. V41 set-loss, friction and loft-off were high.
- (2) V86 (mock-up tendon) removed and replaced with V40 tendon.
- (3) Remove V25, fricton loss too high (>0.25), detension, remove LC's, remove and replace strand, reinstall LC's tomorrow (3/21) AM.
- (4) Remove and replace tendon due to lift-off force too high.
- (5) Tensioning of H35 delayed due to water in LC connectors, connectors removed and hardwired
- (6) V36 removed and replaced, friction not within specifications.



Figure 2.57 Tensioning Hoop Tendons



Figure 2.58 Tensioning Hardware Assembly and Load Cell

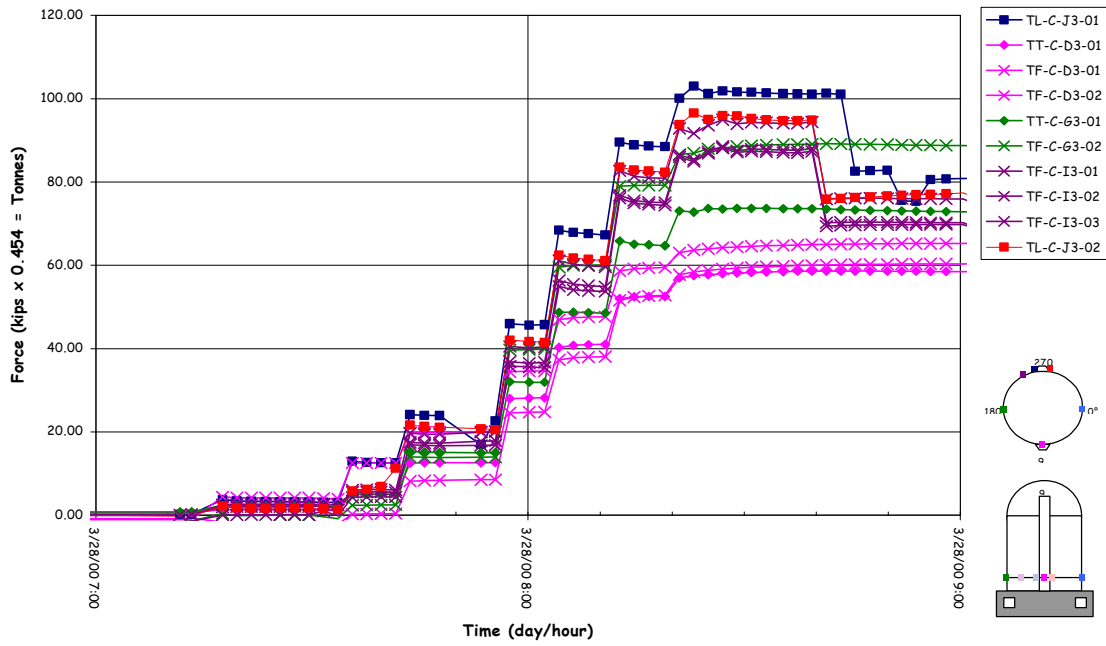


Figure 2.59 Tendon H11 Tensioning Force Time History

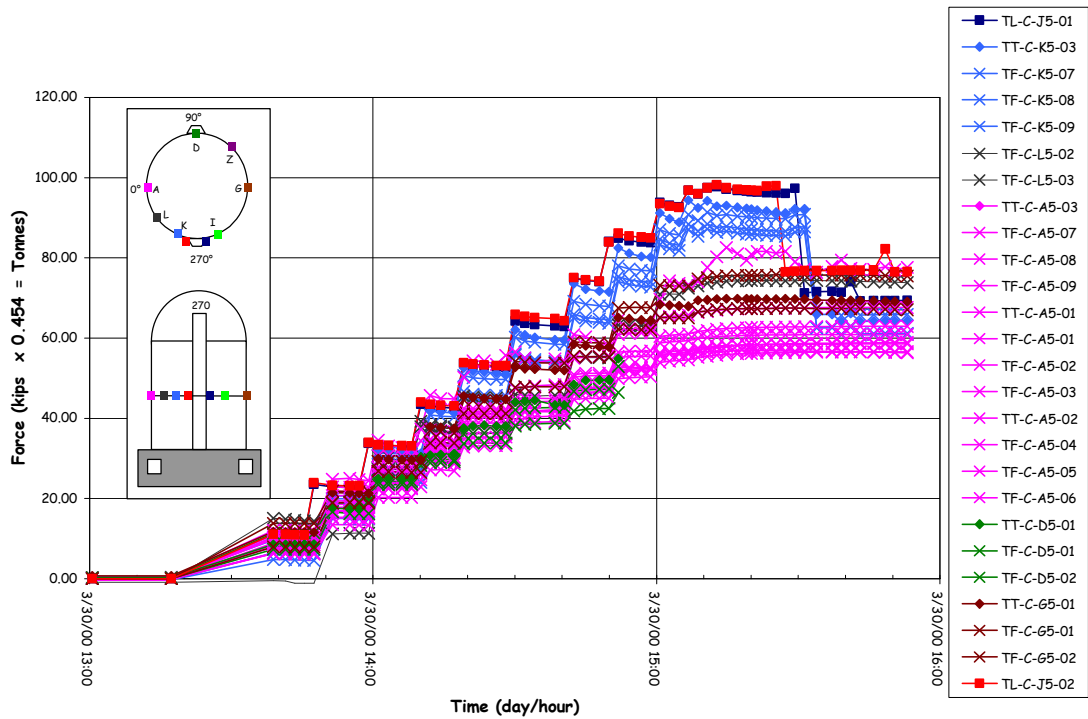


Figure 2.60 Tendon H35 Tensioning Force Time History

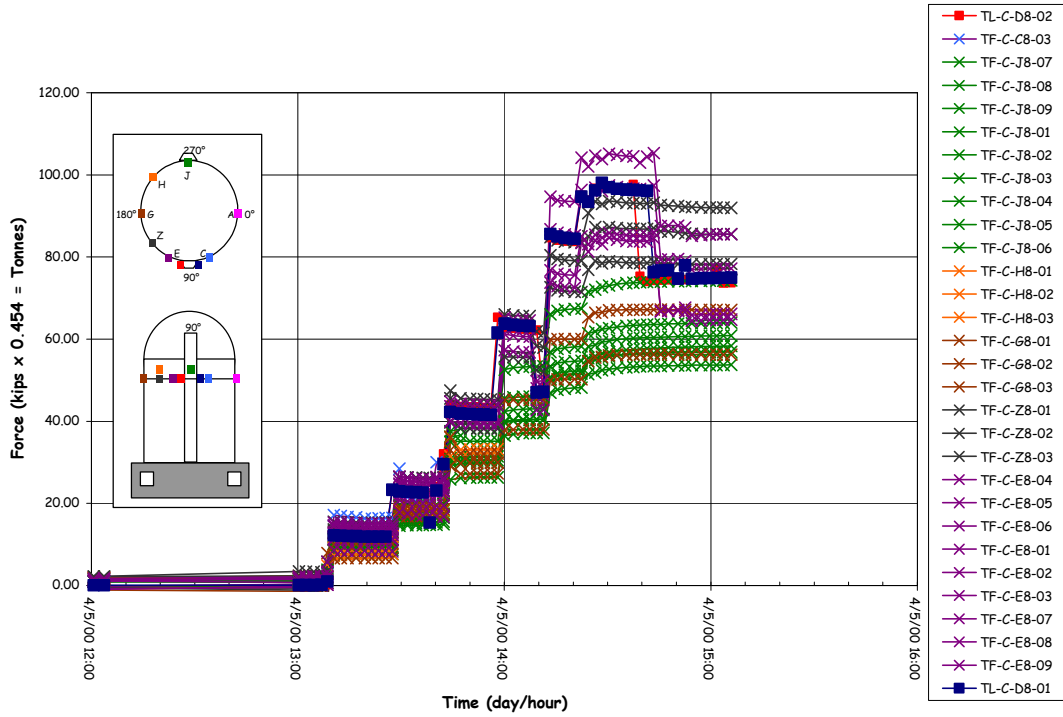


Figure 2.61 Tendon H53 Tensioning Force Time History

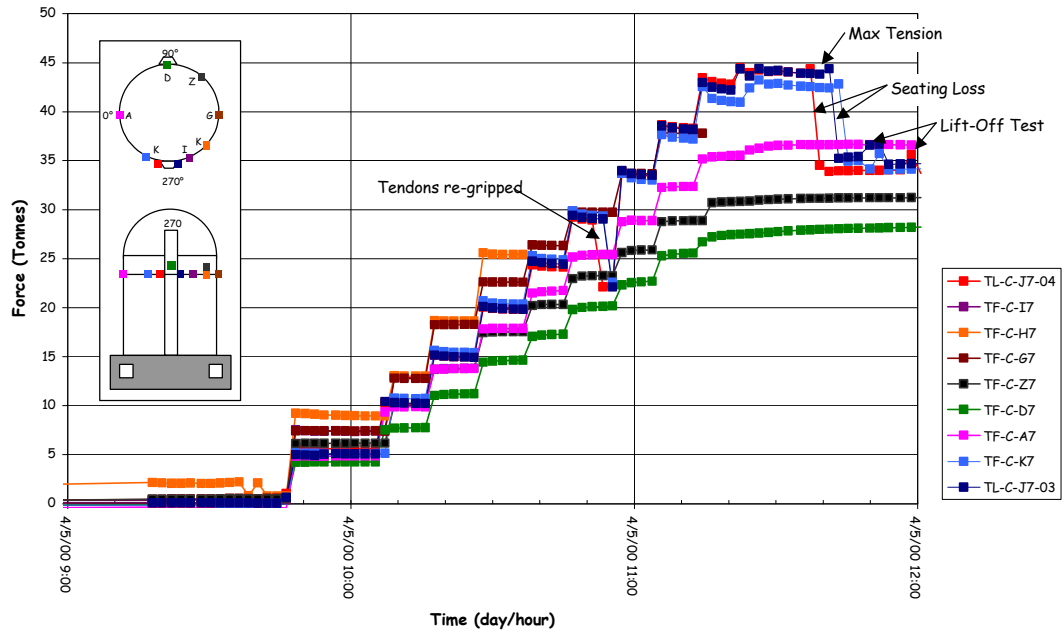


Figure 2.62 Tendon H67 Tensioning Force Time History

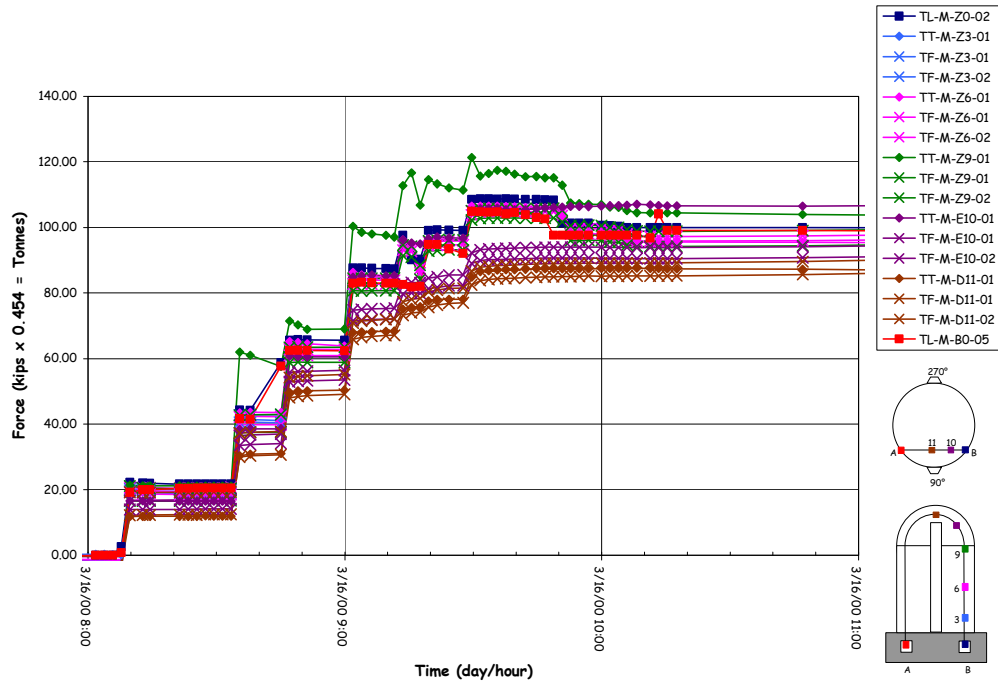


Figure 2.63 Tendon H68 Tensioning Force Time History

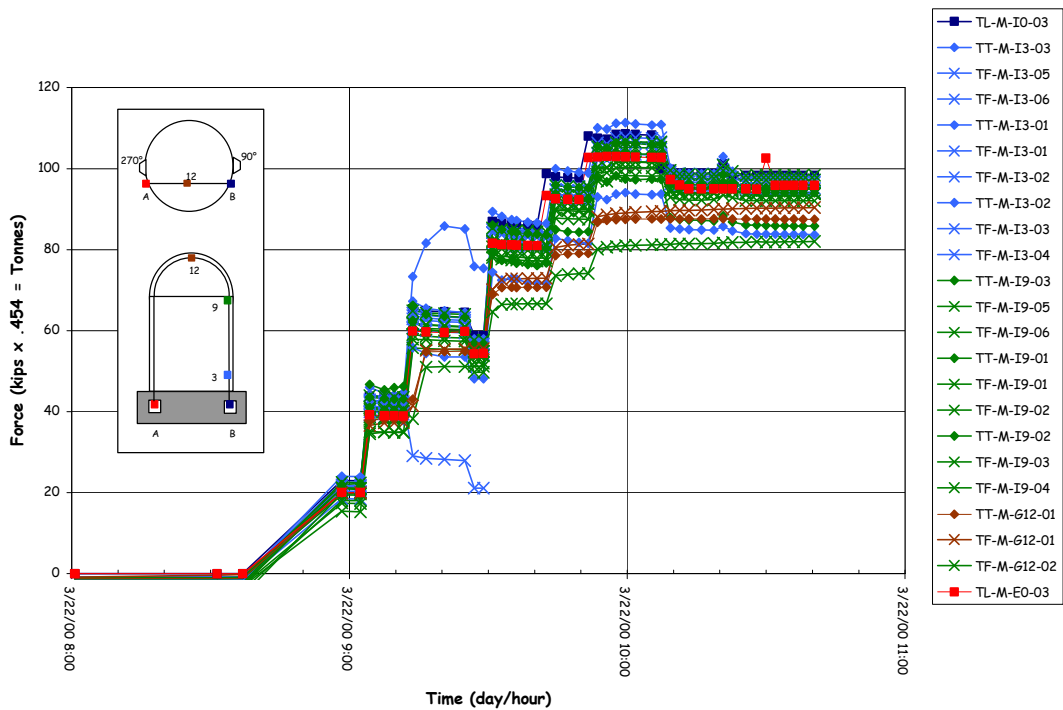


Figure 2.64 Tendon V37 Tensioning Force Time History

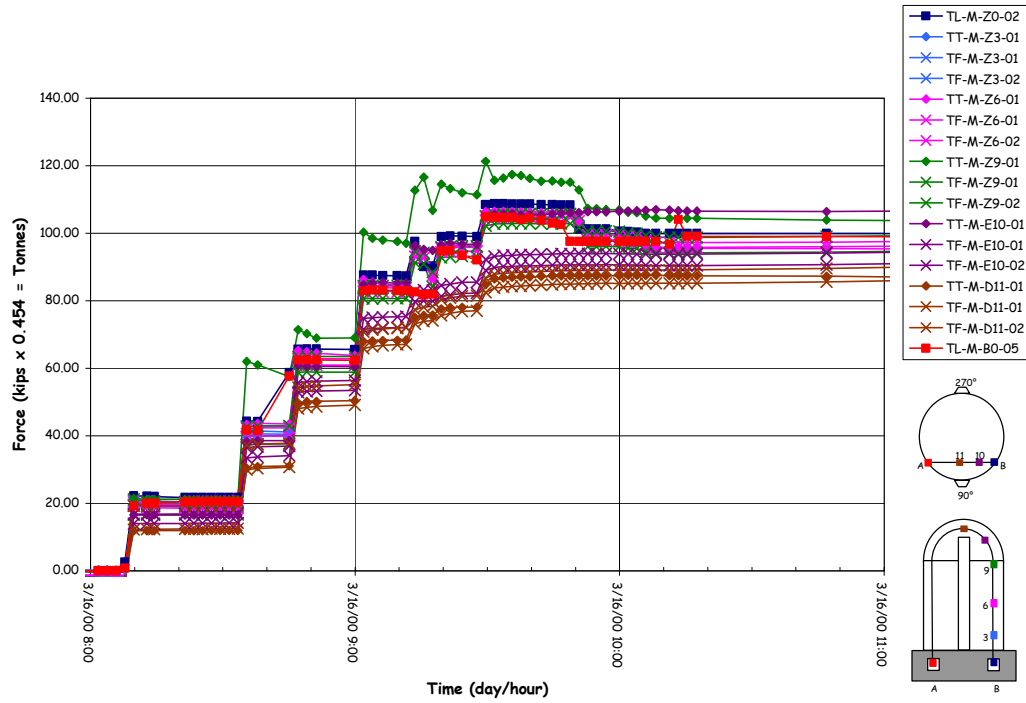


Figure 2.65 Tendon V46 Tensioning Force Time History

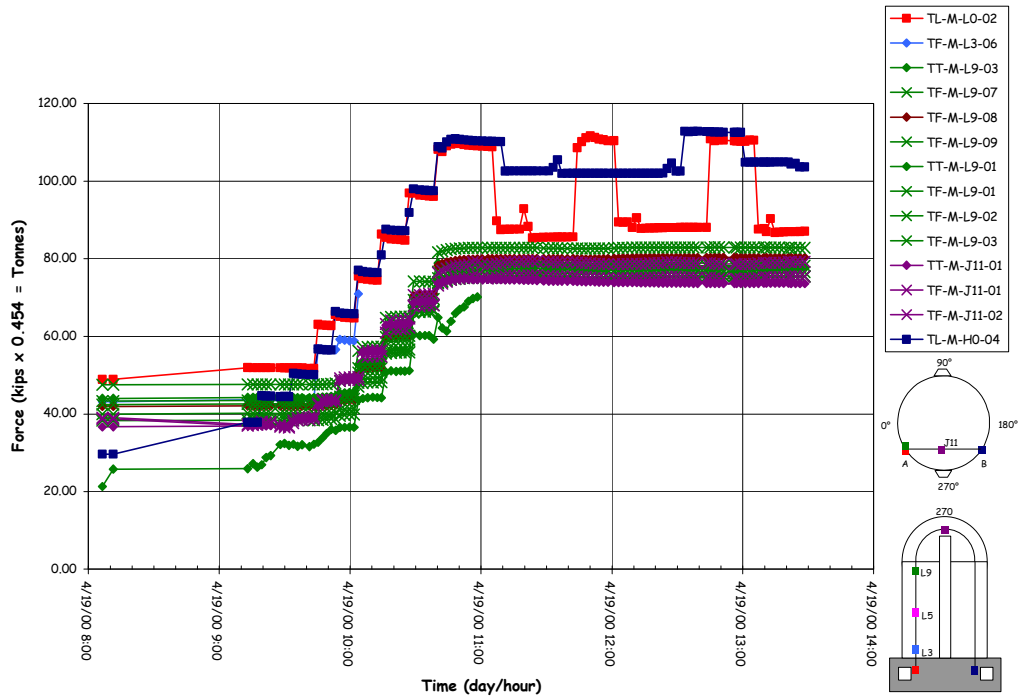


Figure 2.66 Tendon V85 Tensioning Force Time History

Table 2.8 Instrumented Tendon Gage Performance during Prestressing

H11:	4/12 strain gages failed	33% mortality
H35:	23/39 strain gages failed	59% mortality
H53:	14/22 strain gages failed	59% mortality
H67:	11/21 strain gages failed	52% mortality
H68:	18/33 strain gages failed	54% mortality
V46:	3/15 strain gages failed	20 % mortality
V85:	20/30 strain gages failed	67% mortality (operator error)
Overall*:	96/193 strain gages failed	50% mortality
*Six additional gages failed prior to pressure testing: (102/193, 53%)		

The vertical tendon data, however, appears to suggest that the wobble friction in the straight portion of the cylinder wall may be underestimated, while the angular friction in the dome may be overestimated. Since the majority of the strain gages on V37 and V46 survived and the force distribution is more nearly a continuous function, a curve was fitted through the test data to facilitate interpreting and comparing the design assumptions. Unfortunately, due to operator error prior to the start of prestressing operations, most of the gages on V85 (which is deflected around the E/H), were damaged. While the force distribution around the penetration was not obtained, it is apparent that deflecting the tendon around the penetration results in additional losses, as expected.

Finally, the prestressing contractor’s data and the load cell data was summarized for comparison with the design specification in Table 2.9.

Table 2.9 Prestressing Data Summary

	<u>Hoop Tendons</u>		<u>Vertical Tendons</u>	
Average Tension Force:				
Design:	44.41 T	97.9 kips	49.57 T	109.3 kips
Jack:	43.53 T	95.97 kips	49.02 T	108.07 kips
Jack (w/ Load Cells only):	43.61 T	96.14 kips	49.09 T	108.23 kips
Load Cells:	43.21 T	95.27 kips	48.20 T	106.27 kips
Average Lift-off Force:				
Design:	34.11 T	75.2 kips	46.31 T	102.1 kips
Jacks:	34.02 T	75.01 kips	44.22 T	97.49 kips
Average Friction Coefficient:	0.18		0.22	
Average Seating Loss:	3.95 mm	0.16”	4.9 mm	0.19”
Jack:	9.51 T	20.96 kips	4.80 T	10.58 kips
Load Cell:	9.86 T	21.75 kips	4.64 T	10.23 kips
Average Final Load Cell Force:	33.34 T	73.52 kips	43.56 T	96.04 kips
Average Elastic Loss:	0.27 T	0.59 kips	0.58 T	1.29 kips

One Tonne = 1000 kg_r = 9.807 kN = 2.205 kips

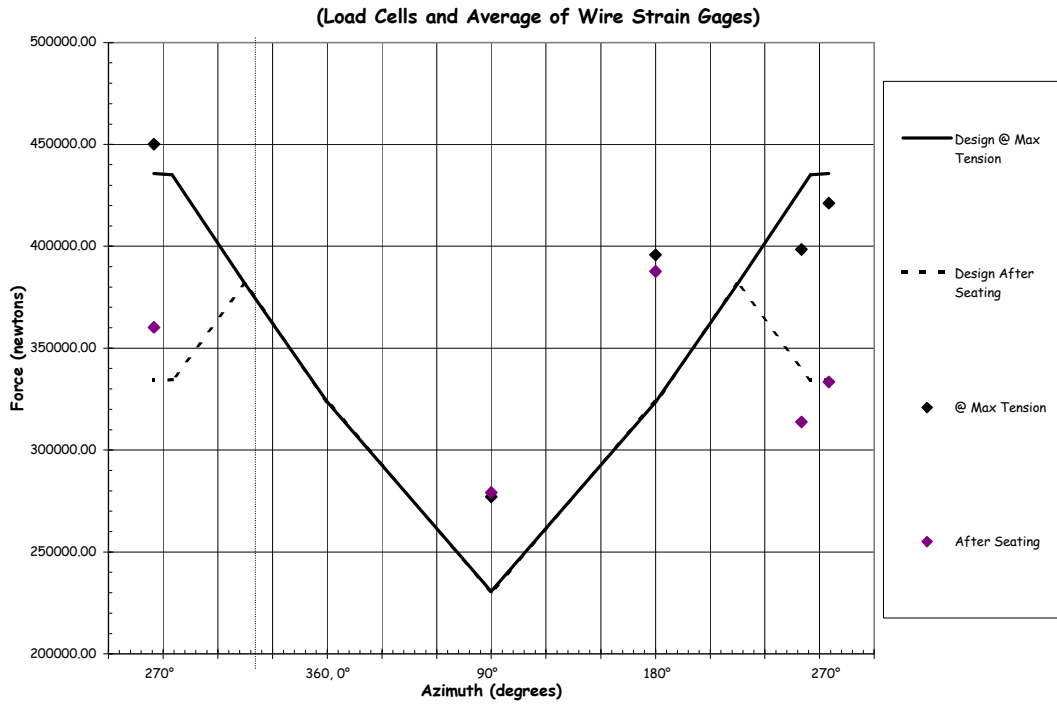


Figure 2.67 H11 Tendon Force Distribution, Elev. 1854

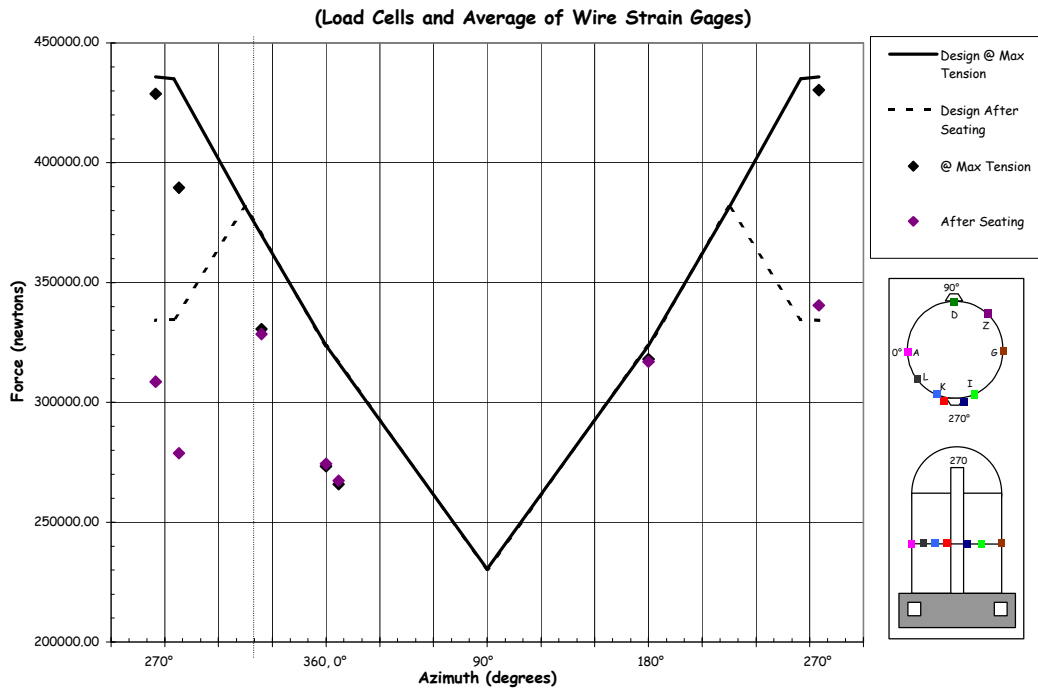


Figure 2.68 H35 Tendon Force Distribution, Elev. 4572

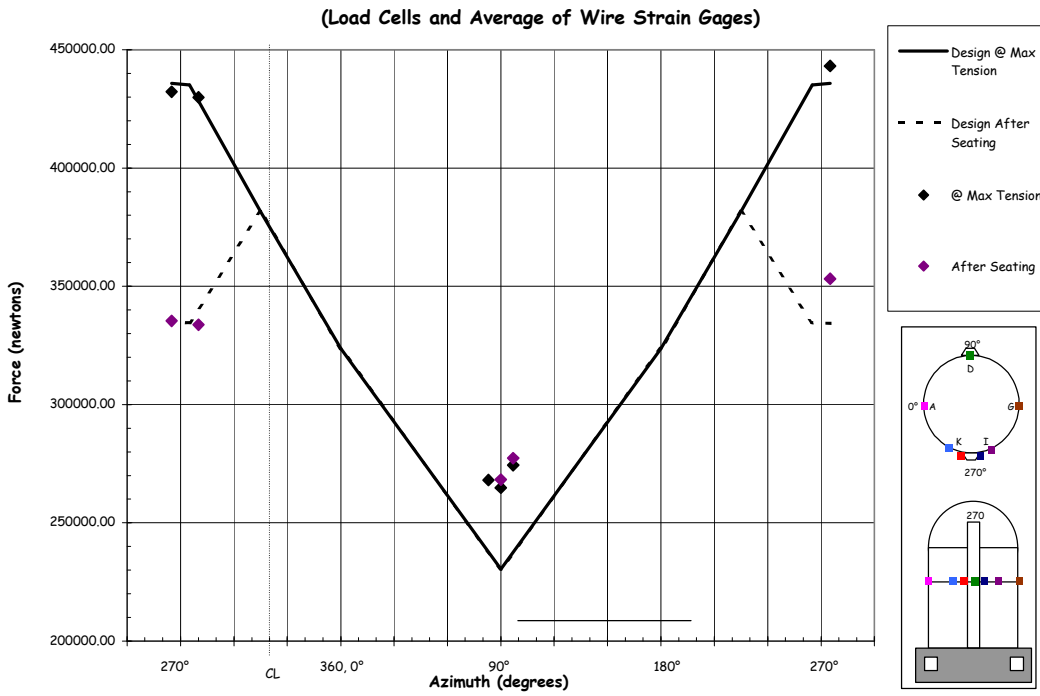


Figure 2.69 H53 Tendon Force Distribution, Elev. 6579

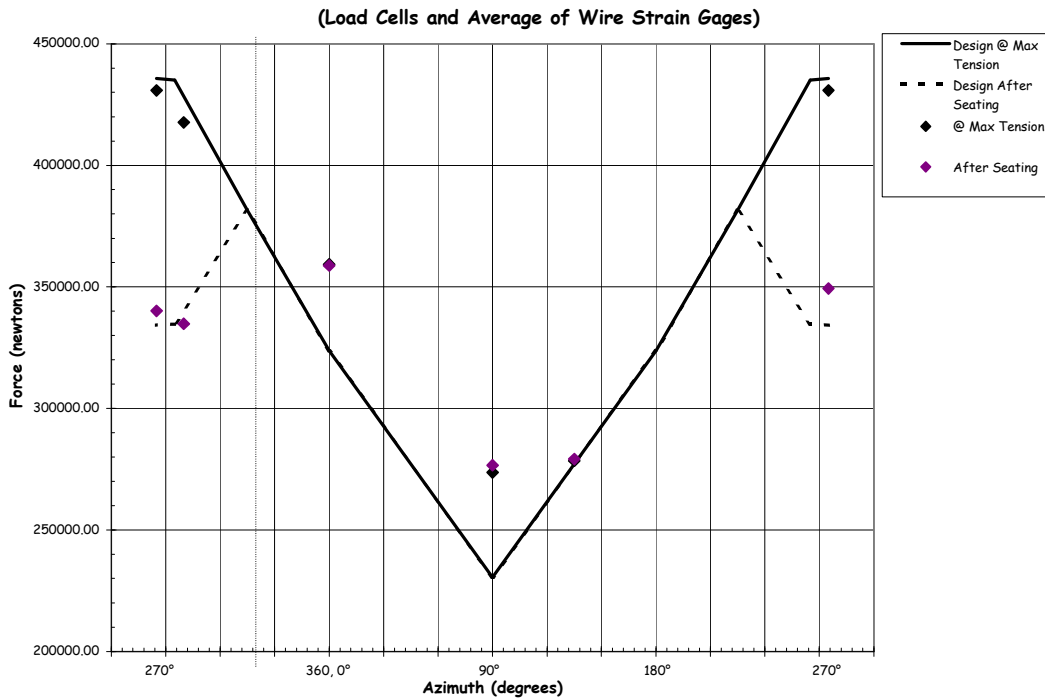


Figure 2.70 H67 Tendon Force Distribution, Elev. 8153

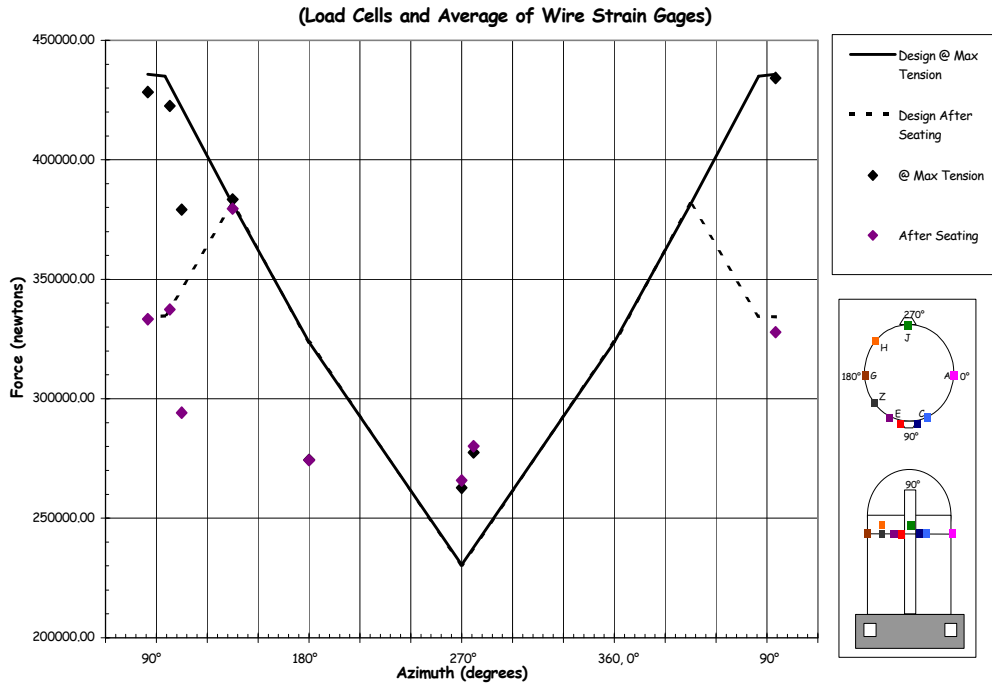


Figure 2.71 H68 Tendon Force Distribution, Elev. 8280

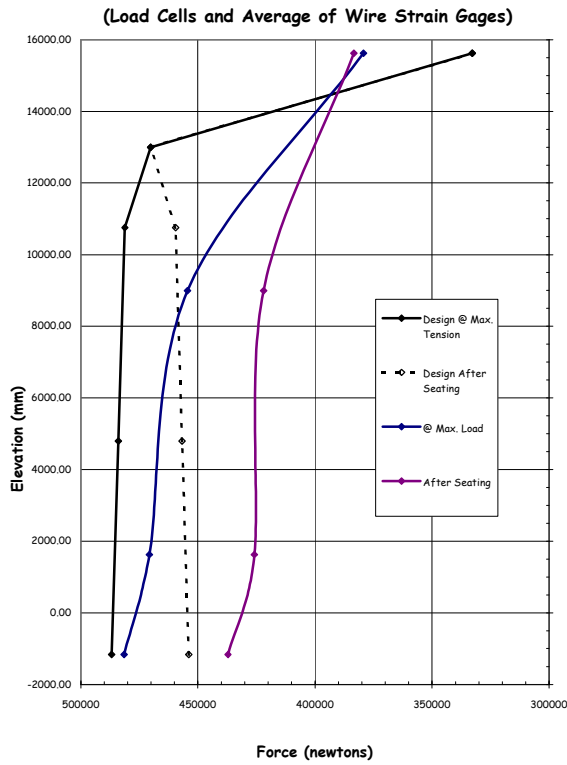


Figure 2.72 V37 Tendon Force Distribution, Azimuth 240 Degrees

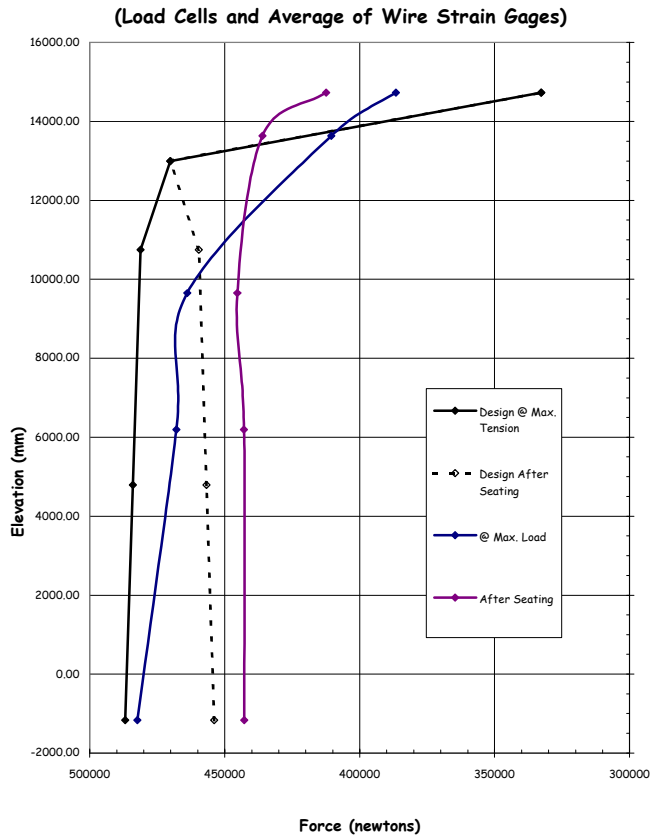


Figure 2.73 V46 Tendon Force Distribution, Azimuth 135 Degrees

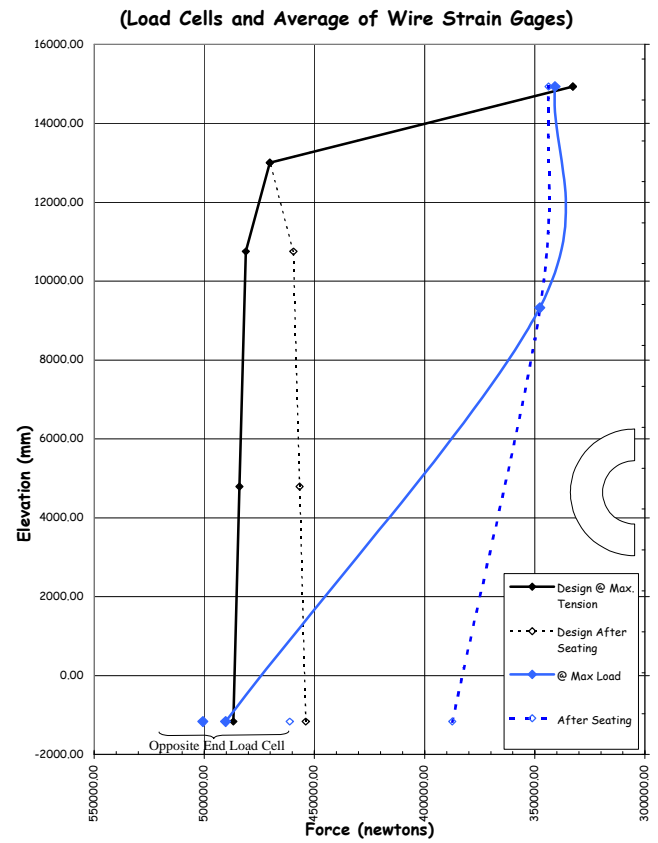


Figure 2.74 V85 Tendon Force Distribution, Azimuth 325 Degrees

3. INSTRUMENTATION

3.1 Background

The instrumentation suite installed on the PCCV model was designed to support the test program objectives, i.e., to provide data on the response of model to internal pressure loading well into the inelastic regime, for comparison with analytical models; and to provide insight and information into response and failure mechanisms that may be representative of actual nuclear power plant containment structures.

Since most types of instrumentation are only capable of measuring a single response parameter at a discrete location, the task of designing the instrumentation suite consisted of identifying critical response parameters and locations from which the overall and local response of the model could be inferred, selecting transducers with the requisite accuracy and range, meeting other operating constraints (pressure, temperature, size, etc.) and integrating them with the other transducers and the data acquisition system. The design of the instrumentation suite also required the specification of quality control procedures to ensure the transducers would perform as designed and that the output could be reliably interpreted in terms of the response parameters of interest.

This chapter describes the considerations given in the design of the instrumentation, gives specifications for the transducers selected, and provides a list of all the transducers installed on the model, along with details of the location, installation, and quality control procedures.

3.1.1 Design Considerations

The basic instrumentation plan was outlined by NUPEC in early 1992 during the initial planning for the PCCV model test [29]. After extensive discussions between NUPEC, its subcontractors, the NRC, and SNL, the details of the instrumentation were agreed upon and documented [30, 31]. Preliminary analyses of the PCCV model guided the selection and location of the final suite of measurements [32]. The detailed PCCV Instrumentation Plan provides a complete description of the instrumentation system and was updated throughout the model design and construction, finally reflecting the 'as-built' configuration employed during the pressure tests.

Considering the basic design philosophy, described in Section 2.1, the basic instrumentation plan identified the following measurements to be taken during the PCCV pressure tests:

1. load (internal pressure),
2. displacement,
3. rebar strain,
4. concrete strain,
5. concrete crack width,
6. liner and liner anchor strain,
7. tendon force, and
8. temperature.

These parameters would be measured at a number of locations to characterize both the global and local response of the model. The basic plan also called for the instrumentation to provide information regarding the potential failure modes identified in Section 2.1. Table 3.1 shows the relationship between instrument location, instrument type, measurement type, and measurement objective. The measurement objectives are either to capture global or local response at specified locations in the PCCV or to measure the behavior of potential failure modes, as shown above. The measurement types and the various instrument types to be specified are discussed in Section 3.2. Installation and locations of the instruments are discussed in Section 3.3.

The basic instrumentation plan also specified a grid of azimuths and elevations which would form the basis for the instrumentation layout and provide a scheme for incorporating the nominal gage locations in the individual gage IDs. This basic grid of cardinal lines is shown in Figure 3.1.

Thirteen cardinal elevations were established, from 1 at the top of the basemat (elev. 0.00) to 13 at the dome apex. Twelve cardinal azimuths, spaced roughly 30 degrees apart, were established with A at 0 degrees (or 360 degrees) to L at 324 degrees. A thirteenth cardinal azimuth was established at 135 degrees and designated Z. This azimuth was selected to represent the global axisymmetric response of the containment based on preliminary analysis results. While the PCCV model is not axisymmetric in terms of geometry and stiffness, Azimuth Z is reasonably distant from any major structural discontinuities and the net hoop prestressing force is close to the average.

The cardinal lines of the model were selected because they correspond to the measurement locations for the prototype Structural Integrity Test (SIT). The SITs were carried out on the containments of the Ohi Nuclear Power Station (Units 3 and 4) in 1991 and 1992. Comparison of the SIT results from the prototype with the model SIT results might be useful for investigating the similarity between the structures. The SIT for both the Ohi containment and the model were performed at 1.125 times design pressure.

Table 3.1 Instrumentation Objectives

Location	Material	Measurement Type	Instrument Type	Measurement Objective
Free-Field Cylinder and	Liner	Strain	Strain gage	Response and Liner failure
Dome	Liner anchor	Strain	Strain gage	Response
	Rebar	Strain	Strain gage	Response
	Tendon	Strain	Tensmeg & Strain gage	Response and Tendon failure
		Force	Load cells	Response
	Concrete	Strain	Strain gage	Response
		Cracking	Video	Response
	All	Displacement	CPOT and TLDT	Response
Wall-Basemat	Liner	Strain	Strain gage	Liner failure
Juncture	Liner anchor	Strain	Strain gage	Liner failure
	Rebar	Strain	Strain gage	Shear failure
	Concrete	Strain	Gage bars	Shear failure
		Cracking	Video	Shear failure
On E/H or A/L	Steel hatch	Strain	Strain Gage	E/H or A/L failure
		Displacement	LVDT	Response
Around E/H or A/L	Plate and Liner	Strain	Strain gage	Liner failure
	Liner anchor	Strain	Strain gage	Liner failure
	Concrete	Cracking	Video	Response
Other	Steel Plate	Strain	Strain gage	Penetration failure
Penetrations	Liner	Strain	Strain gage	Liner failure
	Liner anchor	Strain	Strain gage	Liner failure
Basemat/ Tendon	Tendons	Force	Load cell	Response and Tendon failure
Gallery	Rebar	Strain	Strain gage	Shear failure
	Concrete	Uplift Displacement	LVDT	Response
Buttress	Liner	Strain	Strain gage	Response and Liner failure
	Rebar	Strain	Strain gage	Response
	Tendon	Force	Load cell	Response and Tendon failure

CPOT - Cable Potentiometer

LVDT - Linear Variable Differential Transformer

TLDT - Temposonics Linear Displacement Transducer

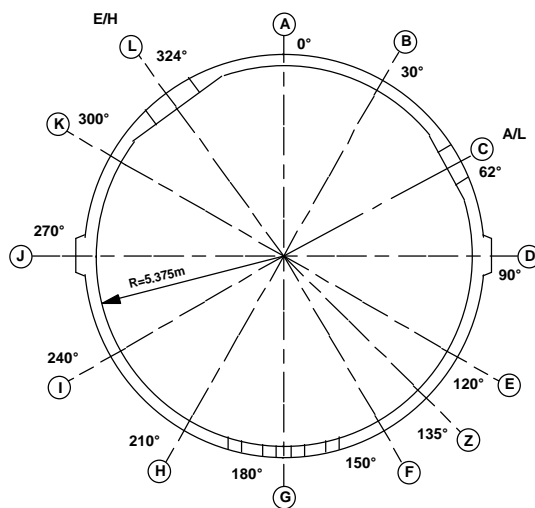
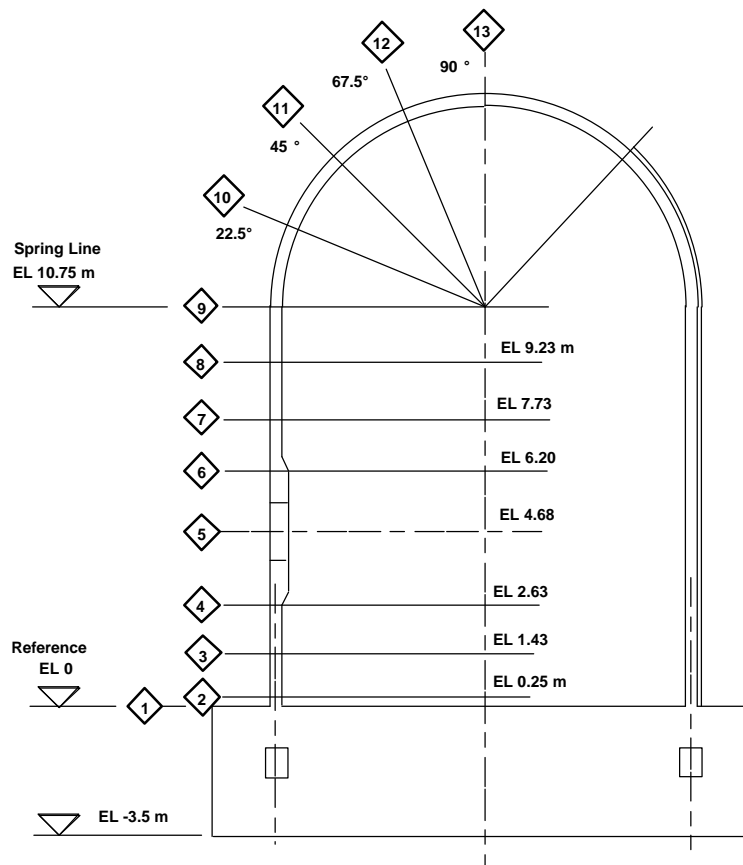


Figure 3.1 Cardinal Instrumentation Layout Lines

3.2 Types of Measurements

This section summarizes the types of measurements required to meet the PCCV test objectives. Details of what and why measurements were taken are included. These measurement types correspond to those shown previously in Table 3.1.

3.2.1 Pressure

Accurate measurement of the internal gas pressure in the PCCV during pressure tests was necessary for several reasons. First, the pressurization of the vessel for the test needed to be carefully controlled and accurately recorded to allow comparison of model response with pre- and posttest analytical results as a function of pressure. Next, accurate calculation of the integrated gross leak rate of the vessel during low pressure testing and detection of leaks and leak rate estimation during high pressure testing dictated the need for accurate pressure and temperature data. These data, along with knowledge of the gas properties in the vessel, allow calculation of leak rates during the tests.

The specifications for the pressure sensors are presented in Table 3.2. The accuracy requirements dictate voltage output devices (rather than millivolt output) with integrated signal conditioning electronics included.

Table 3.2 Pressure Transducer Specifications

Specification Item	Data
Type of measurement required	Gage pressure inside PCCV model
Anticipated exposure conditions	Non-purified nitrogen gas at pressures from ambient to approx. 2.1 Mpa-g (300 psig) for durations no more than 20 days (500 hours)
Operational range	1% of full scale < P _{op} < 2.4 Mpa-g (350 psig) (125% of anticipated rupture pressure)
Desired output	Amplified voltage
Total desired accuracy (i.e., linearity, repeatability, hysteresis, sensitivity)	Less than or equal to 0.1% of span
Temperature effect	< 0.05% full scale per /F over temperature compensated range
Logistics (electrical connection, cabling requirements, etc.)	Pressure taps from vessel will be installed so the transducer housing will represent part of the pressure boundary, typical four wire connection with independent power supply required (i.e., not provided by VXI mainframes), specifications for power supply dependent on type of pressure transducer (i.e., input voltage needs)

Two high-accuracy pressure transducers, Mensor Model 4040 high-accuracy digital units¹⁸, were installed in the vessel to provide redundancy in the measurements. Although the predicted failure pressure of the model was not known with certainty, preliminary calculations indicated it would be in the range of 1.6MPa-g (230 psig). The pressurization system and all equipment was designed for an upper-bound capacity estimate of 2.1Mpa-g (300 psig). Applying an overpressure margin of 15%, the specified range for the pressure transducers was 2.4 MPa-g (350 psig).

¹⁸ Mensor Corporation, 201 Barnes Drive, San Marcos, Texas, 78666.
(http://www.mensor.com/Digital_Pressure_Transducer_4000.htm)

(An independent pressure transducer was supplied with the pressurization system to control test operations. This transducer was independently calibrated; however, all test results are reported against the ‘official’ pressure transducers.)

3.2.2 Temperature

Both model material and internal gas temperatures were measured. Material temperature measurements were made to provide data for thermal compensation of all strain gages within the PCCV model and to provide data to correlate the response of the model to changes in ambient thermal conditions and the effects of direct radiant heating. Two types of T/Cs were used: Omega Model SA1-T T/Cs were placed on the inside surface of the PCCV liner, while Omega Model TQSS-116 were embedded within the concrete¹⁹. Due to the low sensitivity of the strain gages to temperatures around 23/C and the anticipated low temperature gradients along the inside surface of the model, low cost thermocouples were installed so that one T/C compensated several gages. Therefore, only a relatively small number of T/Cs were required to fulfill the temperature compensation requirements for the entire suite of strain gages. These were uniformly distributed, along with additional liner T/Cs near the E/H and A/L.

Internal gas temperature measurements were required to evaluate the integrated leak rate from the vessel prior to and during the pressure tests. High accuracy transducers were required for this purpose due to the small magnitude of the overall leak rate compared to the large volume of the vessel. Resistance temperature detectors (RTDs), Omega Model RD 805 precision gas temperature monitoring units¹⁹, were used for this purpose. The RTDs were distributed fairly uniformly throughout the model so that the tributary volumes associated with each sensor were approximately equal. These temperature measurements, in conjunction with the pressure measurements, provided data to detect leaks and estimate leak rates. Fans were available to circulate the gas inside the model in order to minimize thermal stratification during testing. A single RTD was also located outside the model (on the north side, i.e., in the shade) to provide ambient air temperature data.

The requirements for each of the two temperature monitoring instruments are provided in Tables 3.3 and 3.4. For the PCCV tests, three wire, lead-resistance-compensation-type sensors with low self-heating errors were used.

Table 3.3 Thermocouple Specifications

Specification Item	Data
Type of measurement required	Temperature measurements of inside surface of PCCV model
Anticipated exposure conditions	Nitrogen, from ambient to 2.1 MPa-g (300 psig), expected maximum temp. range from -5 to 50/C
Operational range	-10 to 100 /C
Desired accuracy	< 2% of total input range
Temporal response times	Unspecified, not critical
Junction characteristics	Ungrounded, sheathed
Logistics (electrical connection, cabling requirements, etc.)	Two-wire twisted, insulated leads of same material as thermoelement junction pair, junctions at pin-type pressure feedthroughs (requires pins of same materials as conductors)

¹⁹Omega Engineering, Inc., One Omega Drive, Stamford, Conn. 06907-0047. (<http://www.omega.com/temperature/tsc.html>)

Table 3.4 RTD Specifications

Specification Item	Data
Type of measurement required	PCCV internal gas temperature measurements
Anticipated exposure conditions	Nitrogen, ambient to 2.1 MPa-g (300 psig)
Operational range	-10 to 100/C
Desired accuracy	< 2% of total input range
Desired sensitivity	N/A
Logistics (electrical connection, cabling requirements, etc.)	Four-wire twisted, insulated leads. Requires constant current source (typically 1ma).

3.2.3 Displacement

Displacements were measured at discrete locations to compare with analysis and allow construction of the global response of the model. The types of displacement measured included:

1. radial displacements of the cylinder wall at regular azimuths and elevations relative to a reference point on the instrumentation frame,
2. vertical displacements at the springline at regular azimuths relative to the top of the basemat liner,
3. horizontal and vertical displacements in the dome at regular azimuths and elevations relative to the instrumentation frame,
4. vertical displacements at the apex of the dome relative to the instrumentation frame,
5. changes in internal diameter (i.e. ovalization) of the E/H and A/L barrels,
6. vertical displacement or uplift of the basemat relative to the mudmat.

The range of displacements to be measured included small, elastic deformations during prestressing and subsequent changes due to ambient temperature variation, creep, etc., through large inelastic deformations during pressure testing.

For the PCCV model test, three types of displacement transducers allowed a wide range of expected displacement to be measured. Overall global deformations at the cardinal points were typically measured using CPOT Celesco Model PT 101²⁰ (Figure 3.2). Where deformations were expected to be small, such as at the wall-junction or where higher precision was desirable, such as measuring local deformations at penetrations, Schaevitz HCD series²¹ LVDTs with ranges on the order of 4" or less were used (Figure 3.3). In some locations where both high accuracy and long range were required, Temposonics® magnetostrictive high-accuracy TLDTs²² were used (Figure 3.4). The specifications for each of these displacement transducers are provided in Tables 3.5, 3.6, and 3.7.

Note that all displacement data represents the relative motion between the point of interest and a reference point. Ideally, the reference point is fixed and not influenced by the loads applied to the test structure; however, in most cases, this is impractical. For the case of the PCCV model, most displacements were measured internally and referenced to the instrumentation frame or the top of the basemat. Since the basemat was judged to be, essentially, a rigid mass, the only consideration required for the instrumentation frame was its response to variations in internal temperature. A set of transducers were mounted on the instrumentation frame to measure changes in height and plan dimensions and determine if there was any effect on the cylinder or dome displacements. These frame displacement transducers consisted of

²⁰ Celesco Transducer Products, Inc., 20630 Plummer St., Chatsworth, CA, 91311. (<http://www.celesco.com/cet/index.html>)

²¹ Measurement Specialties, Inc., Sensor Products Division, 950 Forge Ave. Bldg B, Norristown, PA 19403. (<http://www.msiusa.com/schaevitz/products/LVDT/index.html>)

²² MTS Systems Corp., Sensors Group, 3001 Sheldon Drive, Cary, NC 27513. (<http://www.mtssensors.com/>)

CPOTs and two Spectron Model SSY0140 dual-axis inclinometers²³ to monitor tilt of the frame due to possible basemat curvature.

In addition, the internal displacement transducers were attached to the liner surface, assuming that the liner was ‘perfectly’ bonded to the concrete. This assumption, while valid in most cases, was incorrect in a number of cases (which will be discussed in Chapter 5) and it is worth remembering that all internal displacement data represents the position or motion of the liner, not necessarily the concrete wall.

Similarly, uplift of the basemat was measured relative to the mudmat (Figure 3.5) and, as was previously identified, any motion of the mudmat would affect the uplift data.

Table 3.5 Displacement Transducer Specifications (CPOT)

Specification Item	Data
Type of measurement required	Radial or vertical displacement of internal surface of the PCCV model
Anticipated exposure conditions	Nitrogen, from ambient to 2.1 MPa-g (300 psig)
Operational range	5 cm, 12.5 cm, 25 cm, and 38 cm (2", 5", 10" and 15")
Desired accuracy (linearity and repeatability)	0.15 to 0.25% full scale
Logistics (electrical connection, cabling requirements, etc.)	Power supply required (not included on VXI card), multi-pin cable connector needed



Figure 3.2 CPOT Mounted on Instrumentation Frame and Attachment to PCCV Liner

²³ Spectron Systems Technology, Inc., 595 Old Willets Path, Hauppauge, NY 11788. (<http://www.spectronsensors.com/inclinomter.htm>)

Table 3.6 LVDT Specifications

Specification Item	Data
Type of measurement required	Radial or vertical displacement of internal surface of the PCCV model Ovalization of equipment hatch and personnel airlock, basemat uplift
Anticipated exposure conditions	Nitrogen, from ambient to approx. 2.1 MPa-g (300 psig)
Operational range	2.5 and 10 cm (1" and 4")
Desired sensitivity	< 1% total input range
Deviation from linearity	0.25% full scale
Logistics (electrical connection, cabling requirements, etc.)	Same as CPOT requirements

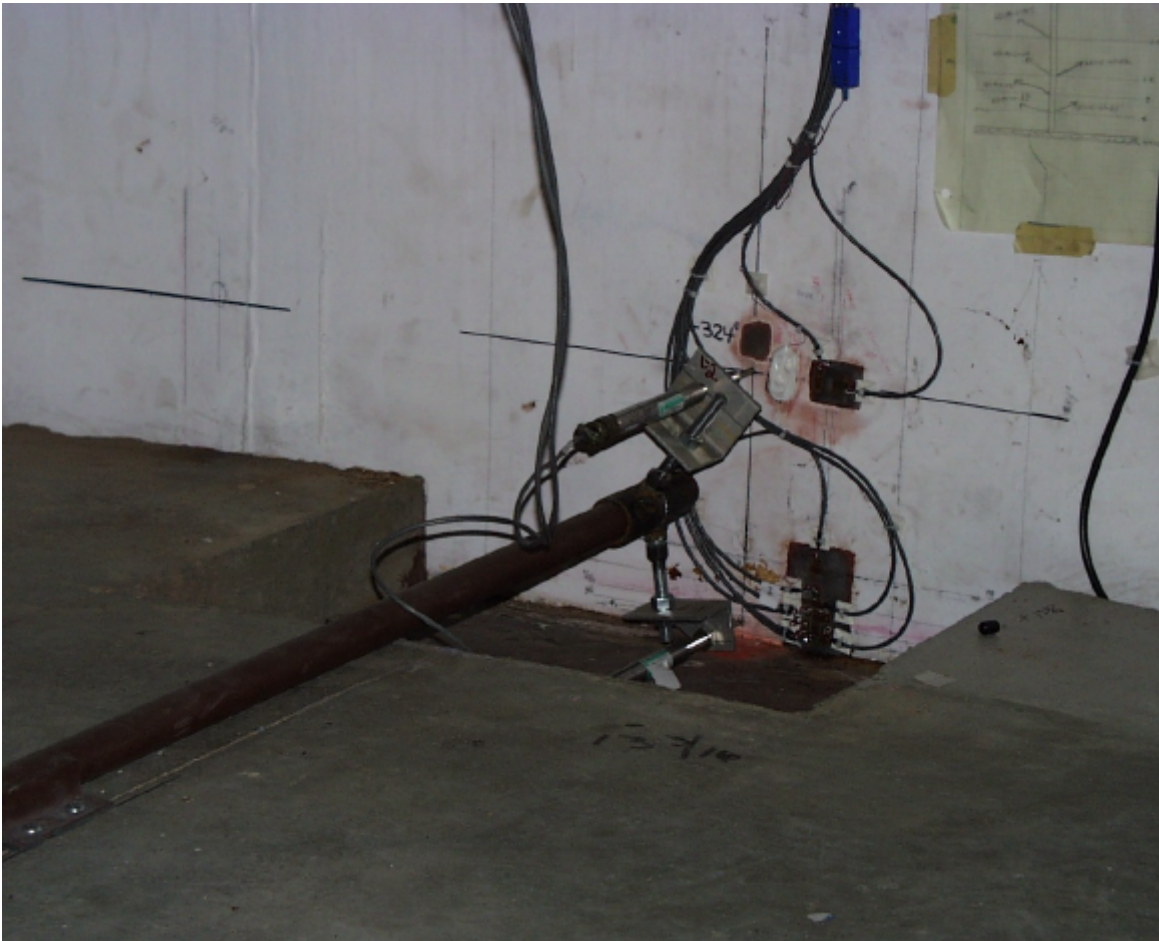


Figure 3.3 LVDTs at Wall-Base Junction (Azimuth 324 degrees, Elev. 0.0 and 250.0)

Table 3.7 Temposonics Linear Displacement Transducer Specifications (TLDT)

Specification Item	Data
Type of measurement required	Accurate and high range measurements of linear displacement of internal surface of PCCV model
Anticipated exposure conditions	Nitrogen, from ambient to approx. 2.1 MPa-g (300 psig)
Operational range	38 cm (15")
Desired sensitivity	< 1% total input range
Deviation from linearity	0.02% full scale (min 13 mm)
Logistics (electrical connection, cabling requirements, etc.)	Same as CPOT requirements



Figure 3.4 TLDT Mounted on Instrumentation Frame and Attachment to PCCV Liner

3.2.4 Concrete Cracking

The basic instrumentation plan identified the relationship between concrete cracking and load or pressure as one of the response mechanisms to observe during the PCCV test. In order to thoroughly model and understand concrete cracking mechanisms, several parameters to measure were identified:

1. the strain in the concrete,
2. when and where a crack first occurs,
3. crack propagation, and
4. crack width.

Measurement of discrete concrete crack width is, however, difficult to perform in practice. A discrete crack must be identified prior to placing a gage at the crack location. However, since most cracks of interest will not form until the test pressure exceeds the design pressure (and the prestressing load), safety constraints prohibit the installation of gages during testing. Several schemes for measuring concrete crack width were considered, including pre-cracking the model, placing crack width gages at a number of shrinkage cracks, or using high resolution video monitoring. However, none of these schemes was considered to be practical or cost-effective. The decision was made to abandon requirements to measure concrete crack width and focus on crack detection and crack propagation.



Figure 3.5 External LVDT Measuring Displacement between Basemat and Mudmat

Crack initiation and propagation were monitored by performing detailed visual inspection to construct crack maps in areas of interest following critical load steps. These crack maps are supported by photographic records of all the areas inspected. Detection of crack initiation during pressure testing was also attempted via acoustic monitoring, described in Section 3.2.8.

Concrete strain measurements are discussed in Section 3.2.5.2.

3.2.5 Strain Measurements

Strain gages applied to individual structural elements provide information on the discrete strain in the element being interrogated and are also capable, when used in groups, of providing insight into local and global strain fields in the structure. Extensive experience through the previous history of containment testing at SNL and elsewhere formed the basis for the specification of strain gage requirements for the PCCV experiment. Standard electrical-resistance type, bonded strain gages were chosen for their simplicity and accuracy, as well as low relative cost. All foil-type strain gages used on the PCCV model were high-elongation-type EP Micro-Measurements gages constructed of annealed constantan on a polyimide backing.²⁴ These gages were used to measure strains in the rebar, concrete, liner, liner anchor, hatches and penetrations, and tendons. In some cases, noted below, special types of strain gages were used in addition to the bonded foil gages to provide additional response information.

Care must be exercised, however, when interpreting strain gage output, since very small gage length strain gages are highly susceptible to the influence of local structural discontinuities or as-built conditions and positioning of the gage in areas with high strain gradients can significantly affect the results. These factors should be considered when comparing strain data with analysis results at discrete points in a structure. Furthermore, the application of the strain gage to the structural element may perturb the strain fields in the vicinity of the gage and these effects should, if present, also be considered.

²⁴ Micro-Measurements Division, Vishay Measurements Group, Inc., Raleigh, NC 27611.
(http://www.vishay.com/brands/measurements_group/strain_gages/mm.htm)

3.2.5.1 Reinforcing Bar Strain

Strain gages, mounted to meridional, hoop, and transverse reinforcing steel, were used to measure the global ‘free-field’ or local membrane, bending and shearing strains in the model as a function of pressure. Reinforcing strain measurements were generally not made in areas where the reinforcing was highly congested, such as around penetrations, or to determine local strain concentrations. Exceptions to the latter case included the wall-basemat intersection and around the tendon gallery. In areas of highly congested reinforcing, rebar strains were measured at the perimeter of the reinforcing grid to confirm boundary conditions for comparison with pretest analyses. Typical reinforcing strain measurements included:

1. Free-field strain measurements of meridional and hoop reinforcing steel at regular azimuths and elevations in the cylinder wall and dome for comparison with pretest axisymmetric and global 3D analyses and to determine the global strains at which local failures were expected to occur. Typically, both inner and outer reinforcing strains were measured to resolve membrane and bending behavior.
2. Near-field strain measurements of meridional and hoop reinforcing steel at the boundaries of local reinforcing areas, e.g. E/H, A/L, etc., were acquired for confirm boundary conditions for local submodels in pretest and posttest analyses.
3. Near-field strain measurements of radial ties in the vicinity of structural discontinuities where large shears or large bending moments were predicted to occur, and to measure triaxial state of strain (stress) for evaluating failure models. In addition, inclined gage bars were used, based on the predicted orientation of principal tensile stresses.

The specifications for the rebar (and tendon wire) strain gages are summarized in Table 3.8. Figures 3.6 and 3.7 show a typical rebar strain gage after mounting on the bar and in place in the model, with protective epoxy cover.

Understanding the method of mounting the strain gages on the rebar is important to interpreting the rebar strain data. One of the first considerations is that the surface of the rebar to which the gage is to be bonded must be ground smooth. This typically removes a portion of the bar’s cross-section, which can result in a local strain concentration in the bar. This phenomenon is described in more detail in Section 5.3.2.1.5. Second, requirements to protect the strain gages during erection and concrete placement locally debond the rebar from the concrete, so that local strains between the rebar and concrete may not be compatible. Finally, strain gages on rebar are located away from the ends of bars or mechanical splices to ensure the bars are fully developed and to avoid end effects. However, in some cases, end effects may be a factor and the location of the gage relative to the bar end should be known.

Table 3.8 Strain Gage Specifications (Rebar & Tendon wire)

Specification Item	Data
Type of measurement required	Point strain (approx.) in the “hoop,” “meridional,” and “radial” directions attached to the reinforcing steel and the prestressing tendon strand wires.
Anticipated exposure conditions	Concrete placement, curing, long term exposure, temperatures from -5 to 50/C
Operational range	Wire gages: 4 - 6% Rebar gages: 5 - 10%
Desired strain sensitivity (gage factor, k)	$1 < k < 2$ (all gages)
Transverse sensitivity, k_t	$k_t < 2\%$ (all gages)
Mounting configuration	Strain gages will be adhesively bonded to the reinforcing steel and tendon wire strands
Logistics (installation, electrical connection, cabling requirements, etc.)	Three wire twisted, insulated cables



Figure 3.6 Rebar Strain Gage



**Figure 3.7 Rebar Strain Gages Installed in PCCV Model
(Note SOFO Fiber Optic Concrete Strain Gage at right)**

3.2.5.2 Concrete Strain

As noted above, since rebar gages are susceptible to local strain concentration and may be debonded from the concrete, rebar strains may not provide an accurate indication of the concrete strain. Measurement of concrete strains, therefore, may require the use of independent gages designed specifically for this purpose. Based on experience during previous model tests, commercially-available concrete strain gages were not judged reliable or cost-effective. Measurement of global concrete strain can be most accurately and reliably be determined from displacement data using the kinematic relationship $\epsilon = \Delta r/R$. Specially fabricated bars, or gage bars, which are not part of the normal reinforcing, along with long-gage length fiber-optic gages, were installed to help measure local concrete strains, such as where significant bending occurs (e.g. at the wall base junction, adjacent to the buttresses and near penetrations) and for comparison with rebar strain measurements.

Specifications for the gage bar strain gages are summarized in Tables 3.9. The configuration of the gage bars is illustrated in Figure 3.8. Sample rebar and gage bar strain gages are compared in Figure 3.9.

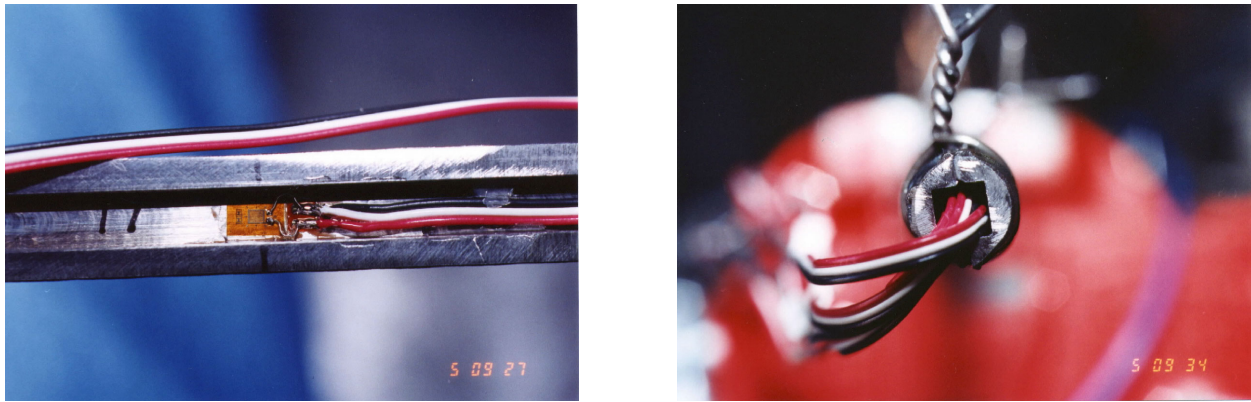


Figure 3.8 Concrete Strain Gage Bars



Figure 3.9 Sample Rebar and Gage Bar Strain Gages

Table 3.9 Strain Gage Specifications (Concrete Gage Bars)

Specification Item	Data
Type of measurement required	Point strain (approx.) in the “hoop” and “meridional” directions, embedded in the concrete.
Anticipated exposure conditions	Concrete placement, curing, long term exposure, temperatures from -5 to 50/C
Operational range	5 – 10%
Desired strain sensitivity (gage factor, k)	$1 < k < 2$ (all gages)
Transverse sensitivity, k_t	$k_t < 2\%$ (all gages)
Mounting configuration	Attached to the reinforcing steel prior to concrete placement
Logistics (installation, electrical connection, cabling requirements, etc.)	Three wire twisted, insulated cables

Specifications for the fiber optic gages SOFO Model 500²⁵ are summarized in Table 3.10. The SOFO gage, prior to installation, is shown in Figure 3.10. The active gage length is between the two ‘anchors,’ shown at the bottom, and the remainder is the fiber optic transmission cable. The installed SOFO gage was shown in Figure 3.7.

Table 3.10 Strain Gage Specifications (Fiber Optic Gages)

Specification Item	Data
Type of measurement required	Global or ‘near-field’ strain in the “hoop” and “meridional” directions in the concrete
Anticipated exposure conditions	Concrete placement, curing, long term exposure, temperatures from -5 to 50/C
Operational range	50 cm (20") gage length, 1 – 2%
Desired strain sensitivity (gage factor, k)	NA
Transverse sensitivity, k_t	NA
Mounting configuration	Place between reinforcing steel prior to concrete placement
Logistics (installation, electrical connection, cabling requirements, etc.)	Fiber optic leads running to 10 channel SOFO DAS reader

3.2.5.3 Liner and Liner Anchor Strain

Both the membrane and bending strains in the liner, as well as strains in the liner anchors, were measured. Strain gages were used to measure both free-field and local strains near liner discontinuities where strain concentrations might occur. Liner anchor strain measurements were included to investigate shear transfer across anchor, pullout force on anchor, and reinforcement contribution in the axial direction of the liner anchor. The specifications for the liner and liner anchor strain gages are summarized in Table 3.11.

At particular details and locations, arrays of gages were applied to allow characterization of the local strain fields and provide insight into the mechanism that tears the liner. Note that gages located adjacent to tears often exhibit much lower strains than expected since the tear acts as a strain relief mechanism on the surrounding structure. In areas where bending strains were likely to occur, strain gages were applied to both sides of the liner to allow them to be resolved into bending and membrane components. In areas where bending was unlikely, strain gages were only applied to the inside surface of the liner. Typical interior and exterior liner and liner anchor gages are shown in Figure 3.11.

²⁵SMARTTEC SA, Via Pobbiette 11, 6928 Manno, Switzerland. (<http://www.smartec.ch/Home.htm>)

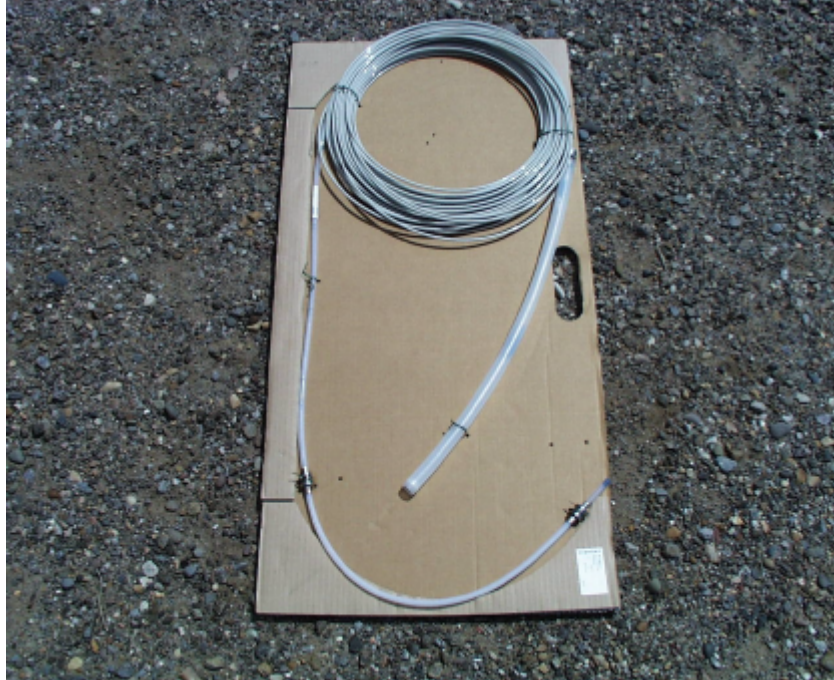


Figure 3.10 SOFO Fiber Optic Strain Gage

Table 3.11 Strain Gage Specifications (Liner & Liner Anchor)

Specification Item	Data
Type of measurement required	Point strain (approx.) in the “hoop,” “meridional,” and “radial” directions, both internal and external on the liner, liner anchors, and stiffeners embedded in the concrete.
Anticipated exposure conditions	Internal: non-purified nitrogen gas at pressures from ambient to approx. 2.1 MPa-g (300 psig), duration of elevated pressures not more than 20 days (500 hours), temperatures from -5 to 50/C. External: concrete placement, curing, and long term exposure
Operational range	Strip gages (2-10 elements): 20% 0-45-90 rosettes (3 elements): 20% single gages: 10 - 20%
Desired strain sensitivity (gage factor, k)	$1 < k < 2$ (all gages)
Transverse sensitivity, k_t	$k_t < 2\%$ (all gages)
Mounting configuration	Carrier matrix material bonded to surface of liner (both internal and external), model liner material is carbon steel, painted internally
Logistics (installation, electrical connection, cabling requirements, etc.)	Three wire twisted, insulated cable, junctions to pin-type pressure feedthroughs



Figure 3.11 Liner and Liner Anchor Strain Gages

3.2.5.4 Residual Liner Strain

Considering pretest analysis results that predicted high liner strain concentrations around the E/H insert plate and ranked them most likely to tear the liner, an attempt was made to measure the residual strain fields in the liner at this location after high pressure testing. This was performed by placing a grid on the interior liner surface and, using a digital position mapping tool, recording the position of the grid points before and after testing. Based on the change in position, coupled with strain data from liner strain gages located within the grid, it was hoped that a more accurate map of the strain field could be obtained. The grid placed around the E/H is shown in Figure 3.12

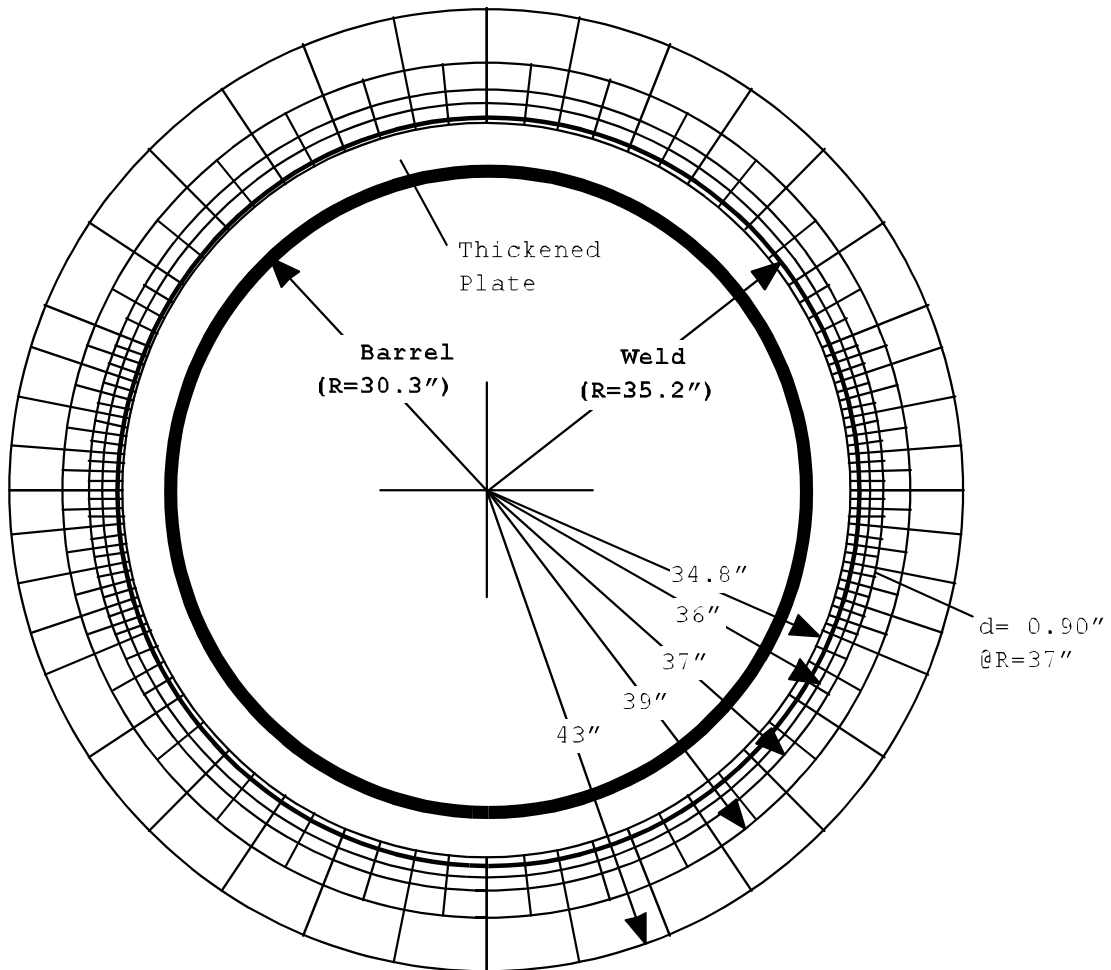
3.2.6 Tendon Measurements

Tendon strain and force measurements were discussed Section 2.2.3 in the context of prestressing operations. The basic instrumentation plan called only for tendon anchor forces to be measured during the tests. It was, however, desirable to measure the force at points along the tendon length to confirm the design force distribution described in Section 2.1.3, both initially, after prestressing, and during pressure testing as the PCCV model deformed.

3.2.6.1 Tendon Anchor Force (At Ends)

Load cells were installed at both ends of selected hoop tendons and meridional hairpin tendons to measure the anchor forces during and after prestressing and during pressure testing. Due to the relatively high cost of the load cells, only approximately one-sixth of the model tendons were monitored with load cells. The load cells were inserted between the tendon anchor and the bearing plate embedded in the concrete to measure the compressive force.

GRID LAYOUT



E/H Inside View

5 radial Circles
120 radial Lines
480 points
Smallest grid ~ 1" x 1"

Figure 3.12 Grid Layout around Inside of E/H

From this data, tensile stresses at each end of the tendons were computed. All loads cells were installed just prior to the prestressing operations and measurements were taken throughout the prestressing operations. The requirements for the load cells are provided in Table 3.12.

Table 3.12 Load Cell Specifications

Specification Item	Data
Type of measurement required	Tendon load at both ends
Anticipated exposure conditions	Ambient outdoor temperatures and humidity
Operational range	0 to 890 kN (200 kips)
Desired accuracy	1% of total input range
Temporal response times	Unspecified, not critical
Logistics (electrical connection, cabling requirements, etc.)	Six wire, twisted insulated pairs

Due to limited availability and to reduce cost, two different load cells were used in the model. Higher accuracy (and higher cost) HBM Model C6-100t load cells²⁶ were used for the instrumented tendons, while somewhat lower accuracy (and less expensive) Geokon Model GK-3000-200-2.0²⁷ load cells were used for the remaining tendons. The HBM load cell with spherical washers (provided to balance the force applied to the load cell) and bearing plates are shown in Figure 3.13. Both the installation jig used for positioning the load cells for the hoop tendons and the arrangement for the vertical tendons is shown. The Geokon load cell with the bearing plates is shown in Figure 3.14. Although the Geokon load cells came equipped with spherical washers provided by the manufacturer, laboratory calibration tests showed the output was more accurate if very thick bearing plates were used in place of the spherical washers. (Also, the spherical washers exhibited an unfortunate tendency to shatter at loads below the load cell capacity, ejecting fragments in a highly energetic manner.) Both the installation jig used for positioning the load cells for the hoop tendons and the arrangement for the vertical tendons is shown.

3.2.6.2 Tendon Force Distribution (Along Length)

The tendon force distribution was determined by measuring the strain at discrete points of individual wires and strands comprising the tendon. Extensive research was conducted to investigate the efficacy of commercially-available transducers to provide the desired data. Laboratory and mock-up testing of tendon strands were conducted to investigate the performance of the gages and led to a scheme utilizing two types of gages. These tests were also used to develop calibration relationships between wire or strand strain and tendon force, and demonstrate methods to protect the gages from damage during construction and tensioning.

In addition to standard strain gages placed directly on the wires (specified in Table 3.8), strain gages specially designed to measure the axial strain in seven-wire strands, Tensmeg^{®28} gages, were used. Tensmeg gages are a single wire gage attached with rubber end-blocks around a tendon strand to measure uniaxial strain in the tendon. The specifications for the Tensmeg gages are summarized in Table 3.13.

Based on the laboratory and mock-up tests that demonstrated the variability of strain from wire to wire within a given strand and from strand to strand, along with the likelihood of a high mortality rate for the strain gages, each measurement location used combinations of wire and strand strain gages, along with special hardware, to protect the gages and lead wires. Special handling and tensioning procedures were also employed to minimize damage to the tendon strain gages.

²⁶ HBM, Inc., 19 Bartlett Street, Marlborough, MA 01752. (<http://www.hbm.com>)

²⁷ Geokon, Inc., 48 Spencer Street, Lebanon, NH 03766. (<http://www.geokon.com/>)

²⁸ Roctest Ltd., 665 Pine Avenue, Saint-Lambert, Quebec, Canada J4P 2P4. (<http://www.roctest.com/roctelemac/product/product/tensmeg.htm>)

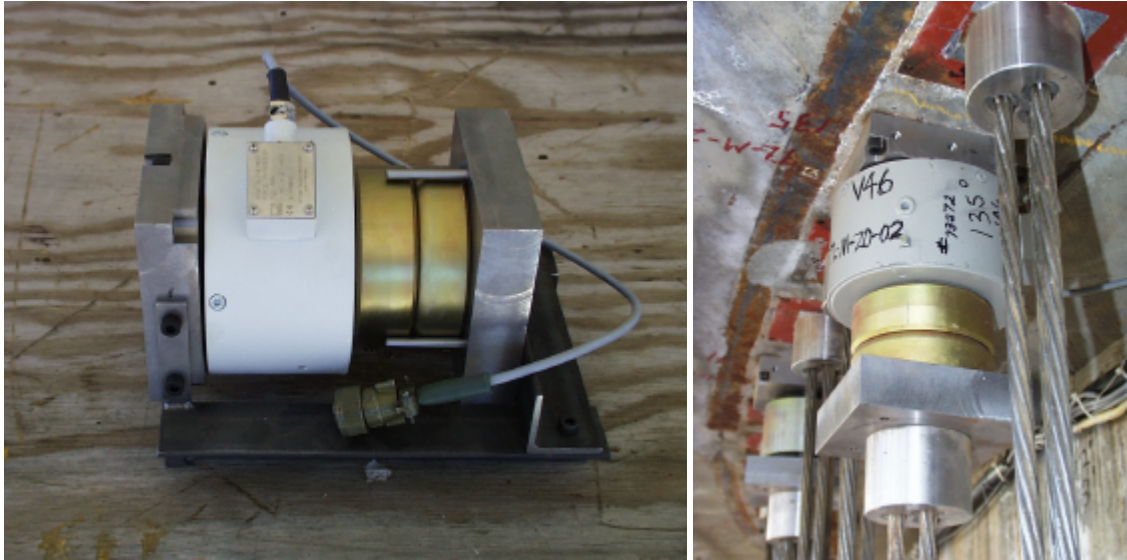


Figure 3.13 HBM Load Cell (a) Installation Jig, (b) In-Place



Figure 3.14 Geokon Load Cell (a) Installation Jig, (b) In-Place

Table 3.13 Tensmeg Gage Specifications

Specification Item	Data
Type of measurement required	Point strain (approx.) in the “hoop” and “meridional” directions, inside the tendon ducts, embedded in the concrete
Anticipated exposure conditions	Concrete placement, curing, and long term exposure
Operational range	4 – 6%
Desired strain sensitivity (gage factor, k)	$1 < k < 2$ (all gages)
Transverse sensitivity, k_t	$k_t < 2\%$ (all gages)
Mounting configuration	Gages will be adhesively bonded directly on each strand
Logistics (installation, electrical connection, cabling requirements, etc.)	Three wire twisted, insulated cable

A set of representative hoop and vertical hairpin tendons were instrumented with gages along the length of the tendon. Five hoop tendons were instrumented: H11 near the base of the cylinder wall, H53 near the mid-height, H35 (which is deflected around the E/H and A/L penetrations), and a pair of tendons H67 and H68 halfway between the cylinder mid-height and springline, which were not equipped with the protective hardware. Three vertical tendons were also instrumented: V46, which had the shortest radius in the dome, V37, which had the largest radius in the dome, and V85, which was also deflected around the E/H penetration.

The typical arrangement of the strain gages at a measurement location is shown in Figure 3.15. This figure also illustrates the positioning of the load blocks on the tendons to protect the gages from damage. The specific arrangement of gages at a given measurement location is described in Section 3.3.

3.2.7 Visual Observations

Both video and still photography was employed inside and outside of the PCCV model at locations where large deformation or other signs of damage, such as liner tearing, concrete cracking, or crushing might be expected to occur. These observations were intended to supplement the discrete measurements obtained by the other transducers. Visually monitoring the model with live video during the test was also a safety requirement. It was important to observe various sections of the model visually to properly conduct the high-pressure test.

The video cameras were placed outside the model to monitor the overall behavior, while some were placed close to the model to monitor specific areas, such as the E/H, A/L, and wall-basemat junction. Interior video cameras monitored the liner behavior. A sketch of the video and camera layout is shown in Figure 3.16. In addition, several still cameras were placed near the outside of the model to record snap-shots at each pressure step during the test. Based on the pseudostatic nature of the pressure tests and the unlikelihood of a catastrophic rupture, the video cameras were of normal speed (30 frames/sec) and there were no requirements to use high-speed video cameras during testing.

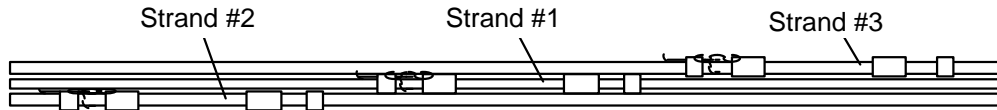
3.2.8 Acoustic Monitoring

Acoustic monitoring was not specified in the basic instrumentation plan, but incorporated into the final instrumentation plan to allow monitoring of the entire structure and identify damage that could occur at locations not monitored via other methods. The specific goals of the acoustic monitoring system were to:

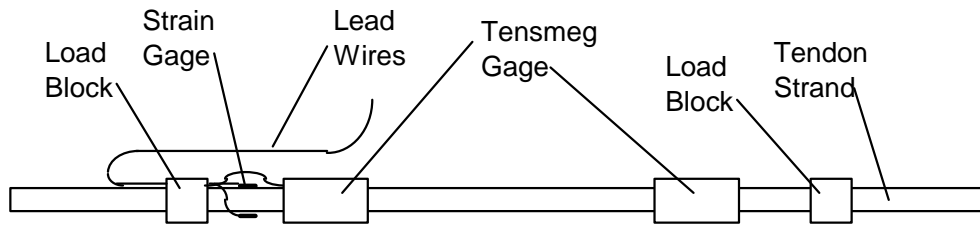
1. detect tendon wire breaks,
2. detect rebar breaks,
3. detect concrete cracking and crushing, and
4. detect liner tearing and leakage.

Acoustic monitoring of the PCCV model during both the prestressing and low and high pressure tests was performed by Pure Technologies Inc. of Calgary, Canada under a turn-key contract. Pure Technologies developed the SoundPrint® acoustic monitoring system²⁹ and has extensive experience in acoustically monitoring structures, especially prestressed concrete structures, such as parking garages and bridges. This system was run independently of the main data acquisition system (DAS). The system consisted of acoustic sensors, essentially piezo-electric accelerometers, bonded to the structure and connected to a separate DAS. One unique feature of this system is the capability to perform real-time data processing and analysis to identify event types and locations. Thirty-two sensors were glued to the external surface of the model and 16 sensors were placed inside the model. The sensors are shown in Figure 3.17.

²⁹Pure Technologies Ltd., 705 11th Avenue SW, Calgary, AB, Canada T2R 0E3 (<http://www.soundprint.com/>)



(a) Tendon Instrumentation Layout (Typical)



(b) Strand Instrumentation Layout (Typical)



(c) Tensmeg End Block and Wire Strain Gage

Figure 3.15 Tendon Strain Instrumentation Arrangement

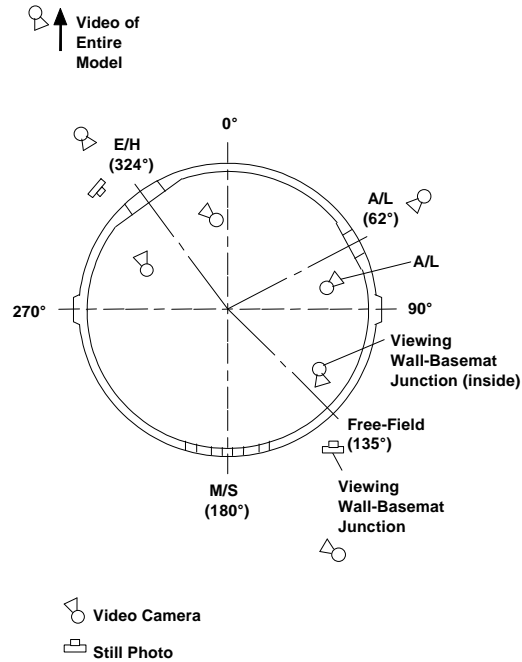


Figure 3.16 Video and Camera Layout



Figure 3.17 Interior and Exterior Acoustic Sensor (clamps during installation only)

3.3 Instrument Installation

3.3.1 Instrument Locations

The final list of gages installed on the PCCV model is provided in Appendix D. This list identifies every gage installed on the model and any gages that were damaged during construction or testing. The format of the tables in Appendix D is given in Table 3.14.

Because of the large number of transducers and the DAS requirement to have a unique address or label, a Gage ID scheme was developed to provide basic information about the type of gage and its orientation and location while providing each gage with a unique identity for subsequent reference and data management. A set of gage type abbreviations were developed to form the first part of the name. These abbreviations are listed in Table 3.15.

Table 3.14 Instrumentation List Format

Column	Description
1	Gage ID (name) AAA-B-CC-DD AAA Type abbreviation (Table 3.15) B Orientation (R-radial, M-meridional, C-circumferential) CC General location designator (azimuth <i>letter</i> / elevation <i>number</i> from Figure 3.1) DD Sequential numbering (for each similar type and location)
2	Azimuth
3	Vertical Elevation
4	Radial Distance (from centerline of containment)
5	Transducer Designation (for procurement)
6	Location Drawing No. (Appendix E)
7	Details Drawing No.
8	Basic Mark Number (construction designation)
9	Modified Mark Number (instrumented designation)
10	Comments
11	Calibration (pre- and post-calibration status)

Table 3.15 Gage Type Nomenclature

Type Abbreviation	Description
RS	rebar strain, single element gage
GB	gage bar, multiple elements
CE	concrete strain, embedded fiber optic gage
LSI	liner strain, single element gage, inside surface
LRI	liner strain, rosette gage, inside surface
LSO	liner strain, single element gage, outside surface
LRO	liner strain, rosette gage, outside surface
LSA	liner strain, single gage, on anchor
LRA	liner strain, rosette gage, on anchor
LSS	liner strain, single gage, on stiffener
LRS	liner strain, rosette gage, on stiffener
DL	linear variable differential transformer displacement transducer
DT	Temposonics linear displacement transducer
CP	cable potentiometer displacement transducer
IT	inclinometer displacement transducer
TC	thermocouple, embedded in concrete basemat, type K
TW	thermocouple, embedded in cylinder wall, type T
TI	thermocouple, inside liner surface, type T
RT	resistance temperature detector
PG	pressure gauge
TL	tendon load cells
TT	tendon strain, Tensmeg
TF	tendon strain, foil

The location designation is based on the cardinal azimuth and elevation lines shown in Figure 3.1. For example, gage DT-R-Z6-01 is easily recognized as a Temposonics displacement transducer (DT) measuring the radial displacement (R) at Azimuth 135 degrees (Z), Elevation 6200 (6). Since there is only one transducer at this location, it is by default number one (01). These gage IDs are used in reporting and discussing the test data in Chapter 5.

The nominal location of the gages are shown in Figures 3.18 to 3.23. A set of detailed instrumentation drawings is provided in Appendix E. The total number of each type of instrument installed on the PCCV Model is shown in Table 3.16.

Table 3.16 PCCV Instrument Summary

Instrument Type		Number of Gages
Strain	Liner	559
	Rebar	391
	Tendons (Tensmeg)	37
	Tendons (wire)	156
	Concrete	94
Displacements		101
Load Cells (1/3 of Tendons)		68
Temperature and Pressure		100
Acoustic		54
Total		1560

3.3.2 Quality Assurance and Control

The PCCV Instrumentation QA Task Plan [33] describes and documents the SNL process for installing instrumentation on the PCCV model. The Task Plan addresses transducer calibration, installation, and wiring to the terminal boards, instrument check-out procedures, and compliance records. In addition, personnel roles, responsibilities, and training appropriate to accomplish the PCCV instrumentation installation task are described. As-installed measurements were made and the exact location of each instrument was recorded as a permanent quality record for the experiment. The tasks, objectives, and responsible project team member described in the Task Plan are summarized in Table 3.17.

Table 3.17 PCCV Instrumentation Procedures Summary

Tasks	Objectives	Responsible Member
1. Provide Instrumentation Drawings for: Transducer Location Deliver As-Built Drawings	Assure proper sensor location to match predicted deformation analysis Assure correct channel assignment to terminal board Assure integrity of instrumentation installation	Instrumentation Engineer
2. Instrument the PCCV Model	Monitor PCCV deformation behavior	Instrumentation Leader
3. Develop/Issue Environmental Safety and Health (ES&H) Operating Procedure	Control hazardous material/processes	Test Leader
4. Install Terminal Boards/Sensor Wiring	Maintain channel assignments	Instrumentation Leader
5. Check Instrument Functionality	Assure sensor integrity	Instrumentation Leader
6. Obtain Required Transducer Calibrations	Assure data accuracy/acceptance	Instrumentation Engineer
7. Complete All Documentation	Assure integrity/traceability of acquired data	Instrumentation Engineer

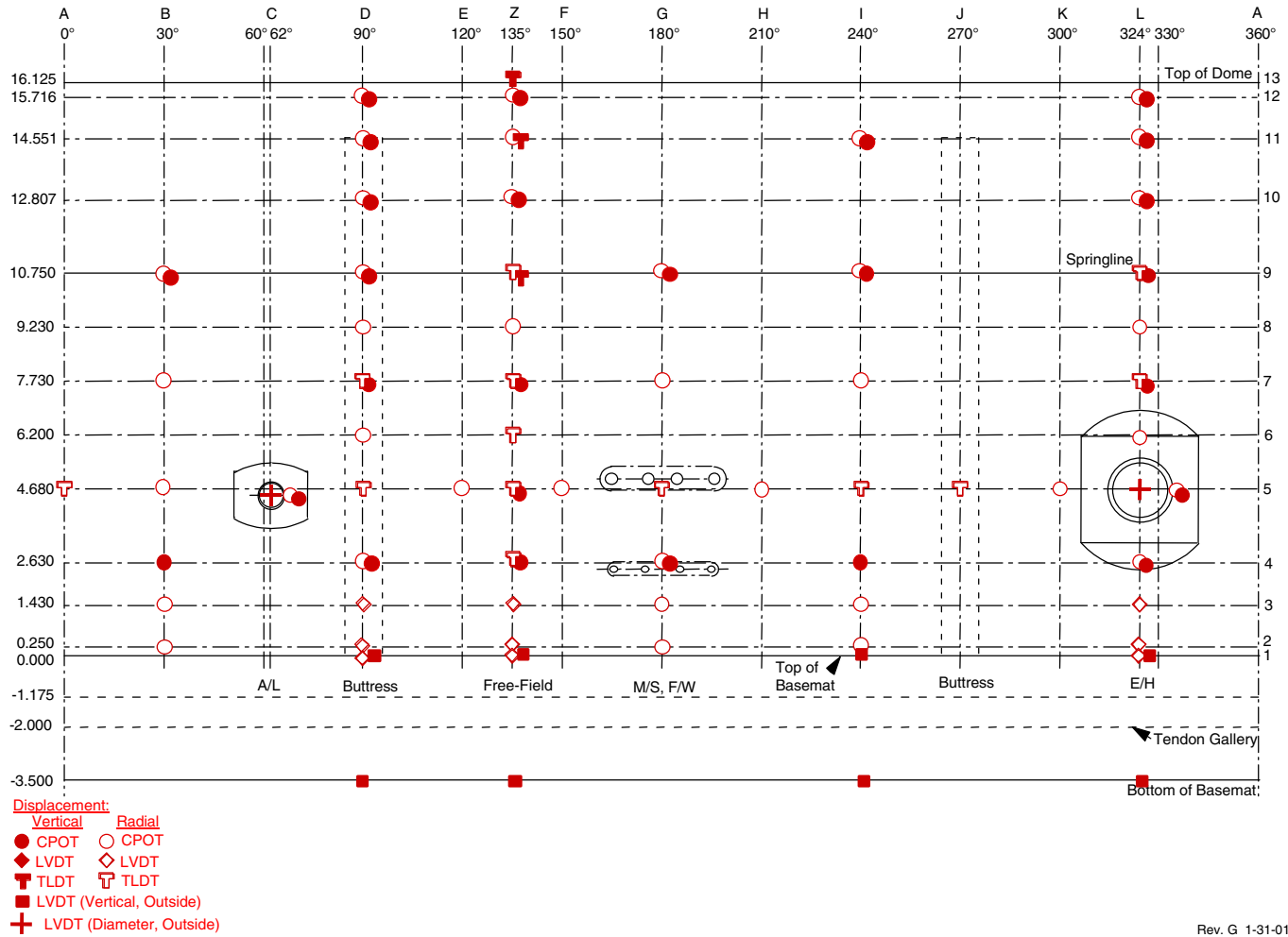
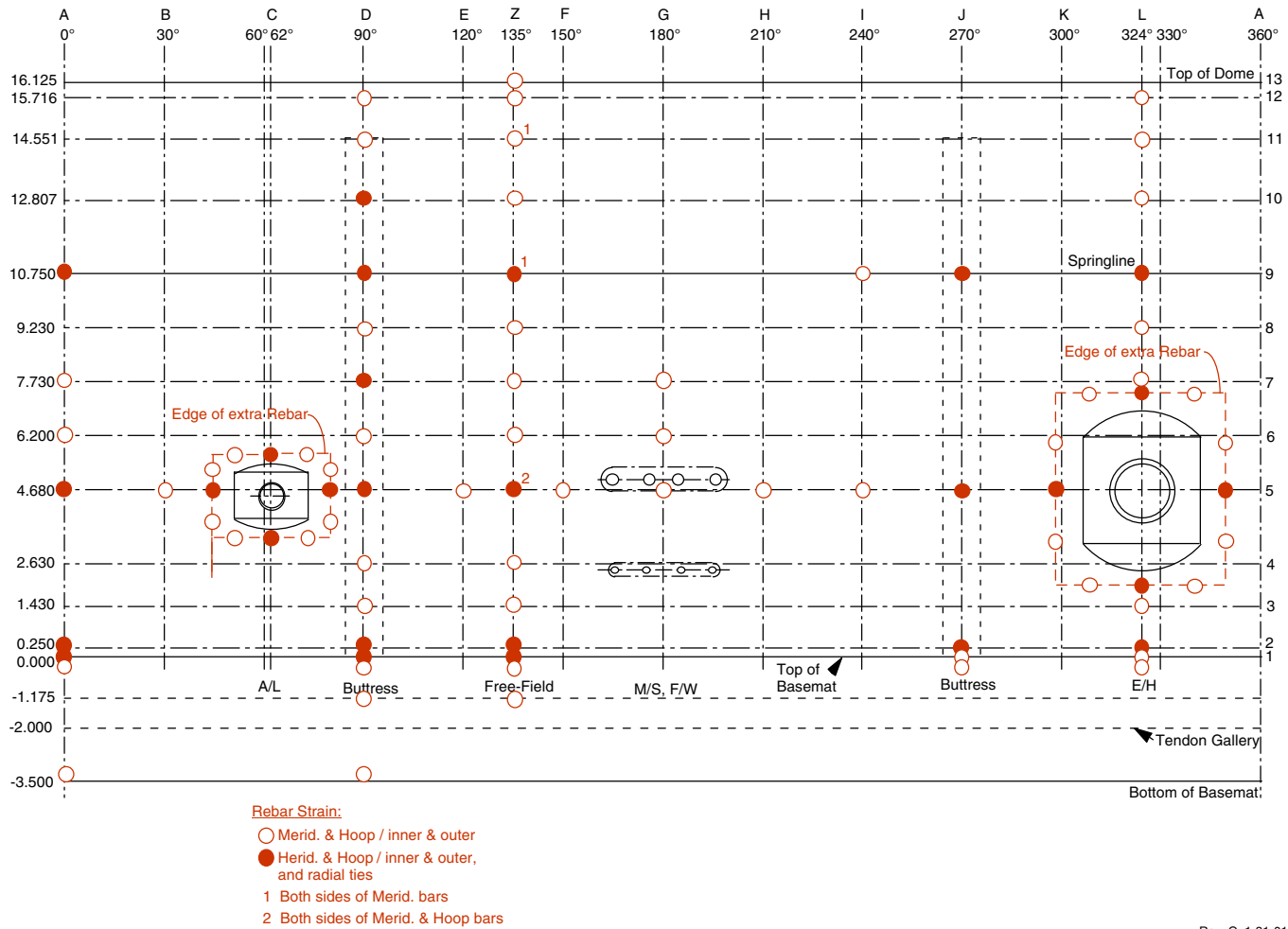


Figure 3.18. Displacement Instrumentation Locations



Rev. G 1-31-01

Figure 3.19. Rebar Instrumentation Locations

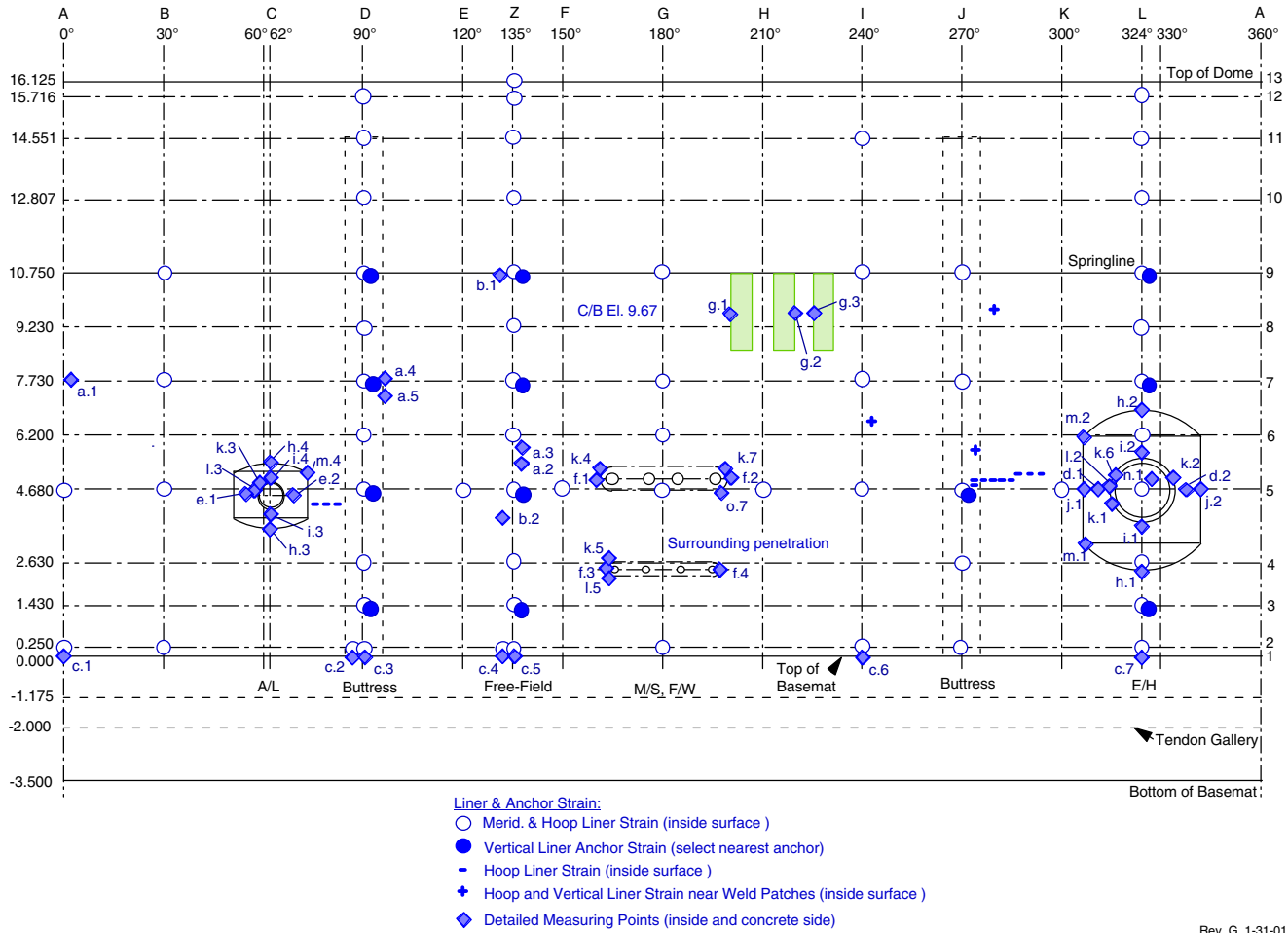


Figure 3.20. Liner and Liner Anchor Instrumentation Locations

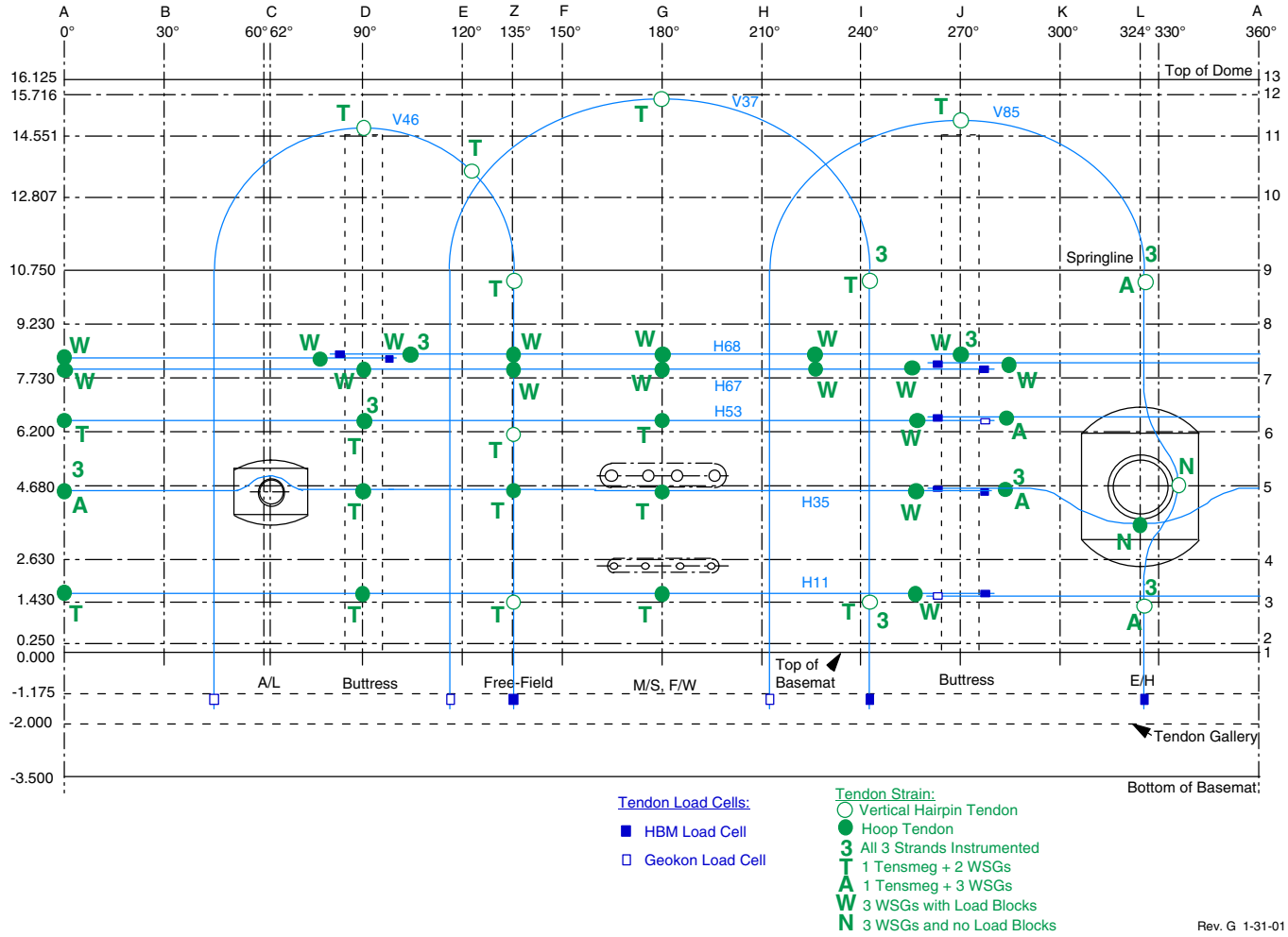


Figure 3.21. Tendon Instrumentation Locations

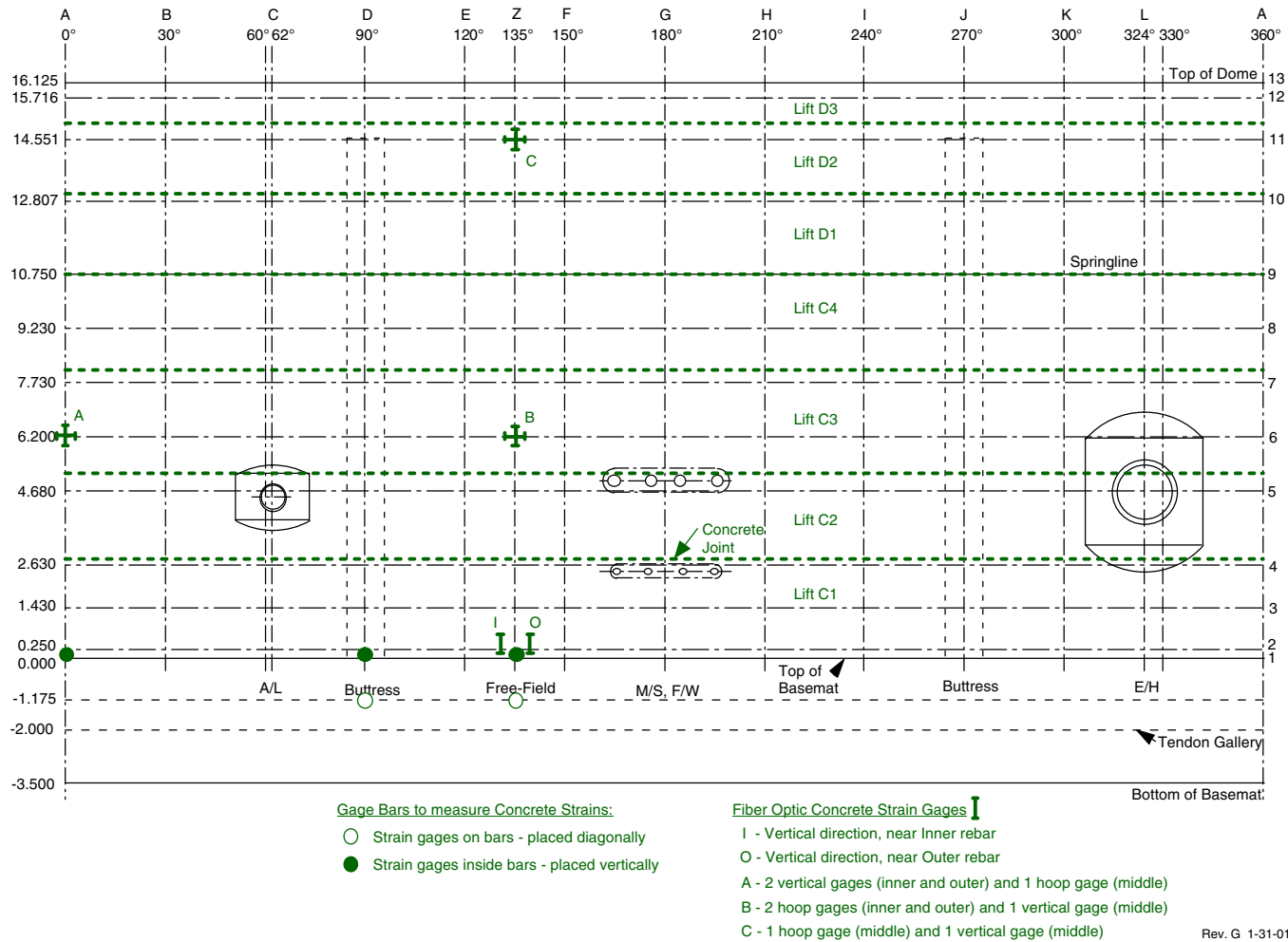


Figure 3.22. Concrete Instrumentation Locations

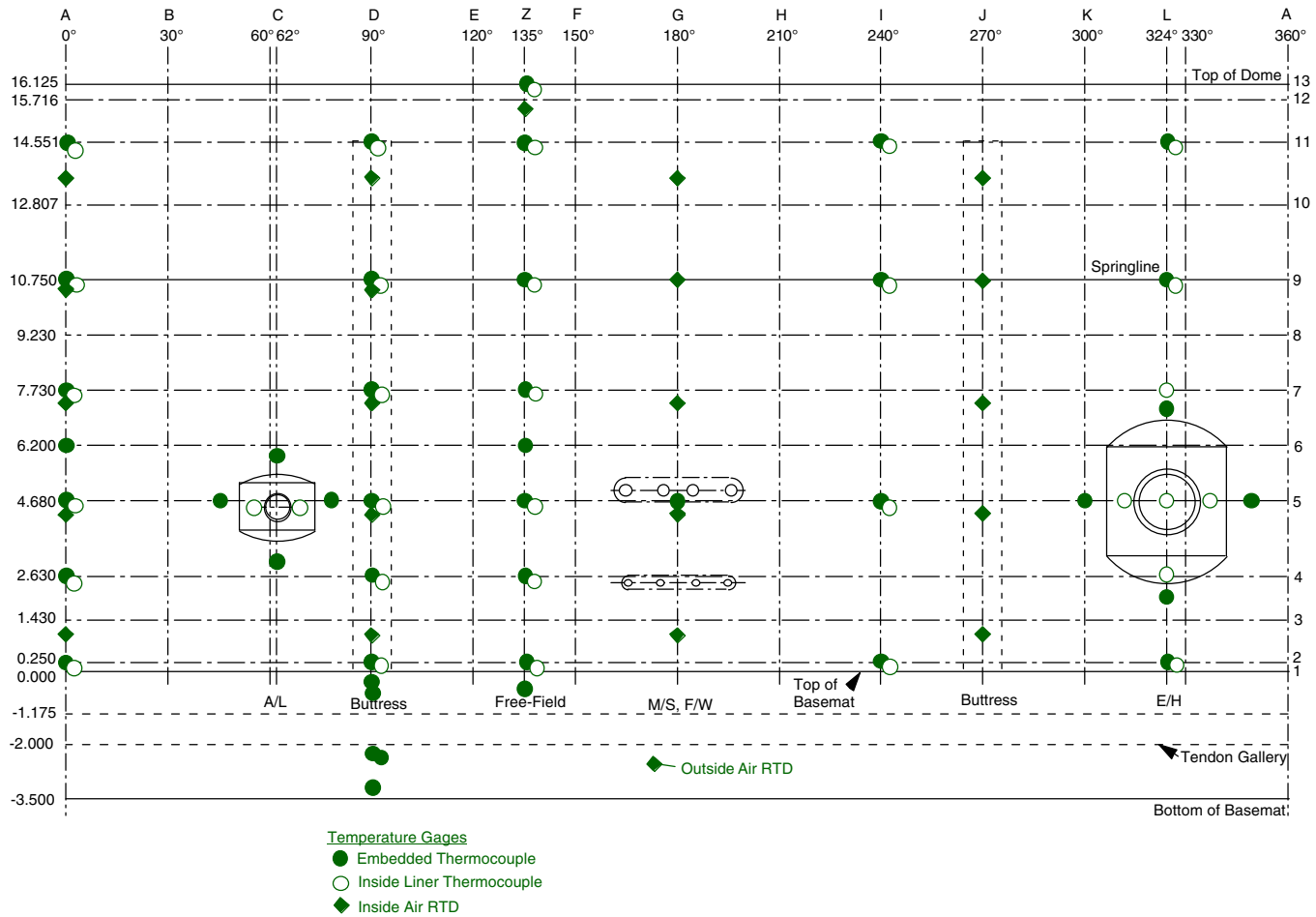


Figure 3.23. Temperature Instrumentation Locations

4. DATA ACQUISITION

The DAS comprises integrated hardware and software components to acquire, interpret, record, display, correct, and archive data from the suite of transducers installed on the PCCV model. The basic data acquisition requirements were specified by NUPEC and, after discussions with the NRC and SNL, a detailed DAS Plan [29] was developed and approved. The DAS Plan specified the objectives, performance requirements, and basic architecture of the DAS. A DAS QA Task Plan [30] specified and documented the detailed procedures that guaranteed the DAS satisfied the operational specifications. The key elements of the DAS Plan and QA Task Plan are summarized in this chapter.

4.1 Objectives

The primary program objectives the DAS must satisfy included the following.

1. The DAS must be fully functional, verified, and approved at the time of model prestressing. This means that the output signal from all operational sensors can be read, that the source and location of all output signals was known with certainty, and that the output signal can be converted to accurate engineering measurement units within the tolerances specified in the Instrumentation Plan.
2. During prestressing operation, the DAS must:
 - a. be capable of monitoring all instruments, including all strain gages, displacement transducers, and T/Cs, except those gages in the uncompleted portion of the basemat,
 - b. provide a real-time display of selected sensor output (especially load cells and tendon gages) in engineering units to monitor prestressing operations, and
 - c. retain a record of final data after prestressing as initial conditions for subsequent readings.
3. The DAS must be capable of periodic data acquisition between prestressing and testing phases.
4. During low and high pressure testing, the DAS must be capable of scanning all active sensor data and storing dynamic data and data of record (DoR) data. The DAS must be capable of providing real-time displays of any sensor output (uncorrected) in engineering units and facilitating comparison with pretest predictions to guide the conduct of the test. The DAS may also be integrated with other systems controlling and monitoring the test, such as the pressurization system, acoustic monitoring system, visual monitoring system (video and still photography), lighting systems, and audio systems.
5. The DAS must record the data in a manner that facilitates timely and accurate correction of the raw data after the test is complete.

4.2 Hardware Description

The PCCV hardware configuration for both the instrumentation system and the DAS is shown in Figure 4.1. A more detailed schematic is provided in Appendix F. This schematic not only graphically “maps” all component classifications important to the data acquisition effort, but also provides details on where documentation pertaining to each component of the system may be found. This documentation includes installation, wiring, and quality control information. For the PCCV tests, there were approximately 1500 instruments mounted on the model. Each of these gages had lead wires extending from the gage itself to a terminal board. From the terminal board, the gage’s signal was carried to a specific channel on a card located in a mainframe. The channel location defined the General Purpose Interface Bus (GPIB) address for that gage. This address was used for acquisition, tracking, and recording of the gage’s data. There were 13 mainframes located in a DAS trailer. From the mainframes, a fiber optic cable carried the signals from all of the gages to the data acquisition computer located in the control room (9950). The hardware from the gages to the front side of the terminal boards made up the instrumentation system. The remaining hardware (shown on the right of Figure 4.1) made up the DAS. The data acquisition computers stored the data on redundant media and also made the data available to the display computer. The display computer allowed test personnel to track the behavior of the gages in real time. The stored data were protected and used for posttest data analysis.

The primary hardware component involved in the data gathering was the Hewlett Packard 75000 Series B system, which included the HP1302A VXI Mainframe and its associated 5 ½ digit multimeter (HP1326B). Analog signals from the instruments were sent to plug-in cards installed into the mainframe housing. An analog bus jumper connected the signals to the digital multimeter where the analog-to-digital (A-D) conversion occurred.

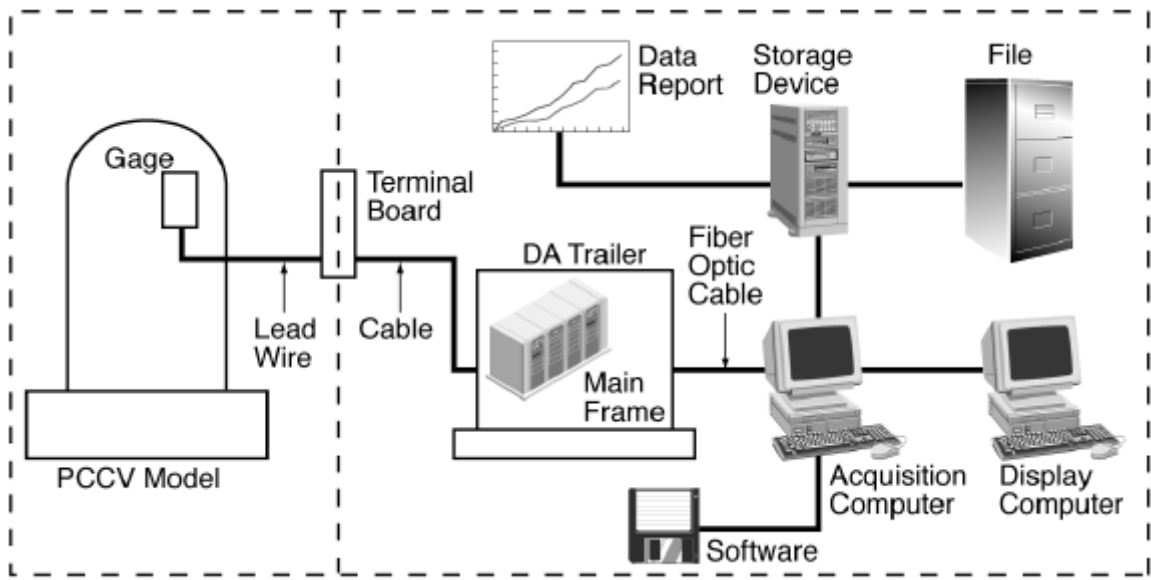


Figure 4.1 PCCV/DAS Hardware Configuration

Data were then stored in input/output (I/O) buffers dedicated to the multimeter, or in the RAM of the mainframe, for eventual transfer over a standard GPIB cable to the data acquisition computer. The mainframe was able to manage the channel switching and data transfer operations as well as respond to controller commands over the GPIB. In addition, the status of the data transfer operations was monitored.

The digital multimeter can be used as a stand-alone device through the VXI bus. However, for this test, it was connected through the analog bus jumper to a series of relay multiplexers. It measured and converted five types of input signals: DC voltage, RMS AC voltage, 2-wire resistance, 4-wire resistance, and electrically-based temperature sensing devices (T/Cs and RTDs).

The characteristics of the multiplexer cards varied based on the type of signal they carried. This experiment used three types of cards: 350 Ω and 120 Ω strain gage cards (Wheatstone quarter-bridge circuits, 8-channel capacity) and a 16-channel voltage card (i.e., non-bridged voltage producing device). To service the different types of instruments installed on the PCCV model, 137 350 Ω cards, 26 120 Ω cards, and 23 voltage cards were used. Two types of VXI mainframes were used. One accepted seven multiplexer cards, and the other type accepted 16 cards. There were no basic differences between these mainframes other than their card capacities. In order to accommodate the cards needed, 13 mainframes were utilized.

Strain gage multiplexer cards are designed to measure the voltage produced in a bridge circuit due to resistance changes in a strain gage. Consequently, these circuits require excitation voltage, which is provided by external power supplies. The strain gage multiplexer cards provide excitation and scale the output of the strain gages. The 1326B digital multimeter measures the voltage and converts the reading to strain units. Thus, the raw data received by the data acquisition computer is in strain units.

The data are held in the VXI bus buffer until the GPIB controller-in-charge (the data acquisition computers) commands a transfer. The mainframes were located in a data analysis trailer situated near the mudmat of the PCCV model and an opening to the Tendon Gallery tunnel, as well as the small penetrations that would feed all internal instrumentation cables (180 degrees). The location, near 180 degrees, was chosen as it allowed cable lengths to be as short as reasonable, thus preserving signal integrity. The data acquisition computers were located remotely at the 9950 site. Adapting the standard GPIB cable to a fiber-optic bundle minimized digital signal loss and degradation. This cable could be extended over long distances and eventually readapted to standard GPIB format for installation into GPIB cards on the DAS computer chassis.

From the perspective of the data acquisition computers, each mainframe/multimeter pair represents a single GPIB instrument. One GPIB card is capable of controlling seven GPIB instruments. For the PCCV experiment, two GPIB interface cards and two data acquisition computers were used, as more than eight GPIB instruments were needed.

The data acquisition software used for the PCCV test was designed as a general instrumentation monitoring system, with a single GPIB card and controlled by a single data acquisition computer. This implies that any computer running the acquisition software can scan any instrumentation suite with an accurate configuration file. Thus, each data acquisition computer scanned approximately half of the instruments on the model. Each data acquisition computer operated independently of the other. The display computer read data from both computers, one at a time.

The final major piece of hardware involved in the DAS was a display computer. This computer read the experimental data from the data acquisition computers upon demand and presented it in optional formats (plot form, array form, comparison form). The display computer provided the test conductor information to help make real-time decisions during the test.

The display computer had additional monitors allowing observers (located outside the test control room) to view the display.

Additionally, the DAS included two separate data storage devices (one connected to each data acquisition computer). These stored redundant copies of the data files to ensure data protection.

4.2.1 Hardware Specifications

Manuals and hardware specifications for each DAS component were included in the DAS Plan. All of the hardware chosen for the PCCV data acquisition effort was expected to meet requirements for the overall system operation.

The total time required for the actual acquisition of data from the VXI mainframes was governed by two primary factors: the switching and settling time of the on-board multiplexer and the aperture setting for each sampled channel. This statement assumes very short times for I/O from the controller to the multimeters. By far, the largest of these components is the aperture setting for a static DAS with unfiltered data signals. (The settling time for the mechanical relays in the PCCV's VXI mainframes is on the order of μ seconds.) For the PCCV tests, the aperture time was set to 16.5 ms, which ensures electrical filtering of common 60 Hz noise sources. Decreasing the aperture time allows for more rapid data acquisition, but significantly increases signal noise, particularly for unfiltered data. Signal degradation is further complicated by the moderate to long cable lengths, which are necessary in a test of this sort. Therefore, the default 16.5 ms aperture for each channel was used. This setting results in a maximum possible sampling frequency of 60 Hz. This value is decreased incrementally by the relay operation and I/O to the controller.

Scan time is defined as including: 1) the time required for the GPIB-based READ command to reach the mainframe from the control computer; 2) the time for the command module in the appropriate mainframes to receive the request for data and set the multiplexer for operation; 3) the time for multiplexer switching and the multimeter aperture delay for each configured channel; and 4) the time required to transfer all the data from the controller buffer back to the DAS computers. Thus, the scan time was larger than the product of the sampling frequency multiplied by the number of gages scanned, because of the time required to transfer the large controller buffer contents via the GPIB. Scan times were slightly different for the two DAS computers, with PCCV1 requiring approximately 50 seconds and PCCV2 requiring approximately 70 seconds.

Cycle time includes the scan time plus the time to store the data on the requested storage devices. The plan was to immediately generate two copies of the data, one on an internal hard disk and one on a removable disk. The storage required the largest amount of time by far. To shorten this as much as possible, the DAS software was written to facilitate this operation (i.e., separation of data display and data acquisition computers, up-front creation and preparation of data files, use of binary high-speed I/O data file formats rather than ASCII, termination of all unnecessary processing during data storage, etc.) and the data storage hardware was chosen to minimize disk seek time, transfer rate, and access time. Cycle time was approximately 120 seconds during system checkout, a setting that was used for the remainder of the testing.

4.2.2 Gage Wiring

The criteria to determine from which opening each gage's wires left the model was based solely on the route requiring the shortest length of wire. Thus, in the majority of cases, each gage's wires exited the model from the opening closest to the gage itself. Once the wires exited the model, they went to one of several terminal boards. The wires leaving the terminal boards entered the DAS trailer and connected to the data acquisition mainframe cards.

As stated, lead wires were as short as reasonable while still enabling the needed connections. All gage/wire combinations were reviewed, and corrections to gage factors were made posttest, as per Appendix G.

4.3 Software Description

The software used to control the DAS and display the acquired data during the experiment was developed using National Instrument's Labview™ software package.³⁰ The basic building block of Labview™ is called the virtual instrument (VI). A VI is similar to a subprogram or a module of code.

The data acquisition program is made up of VI trees, each representing a code module with a specific purpose. Graphics objects (such as knobs, dials, switches, etc.) visible on the screen during the data acquisition process can adjust instrument and data acquisition control parameters. Users may manipulate these objects with mouse commands.

The PCCV/DAS software is separated into three major groups: the primary program group used to gather and store the data during the experiment, a secondary program group to display the data during the experiment, and a utility group of programs used either before or after the test. These utility routines were designed to accomplish several tasks:

1. Form the configuration file and channel set-up,
2. Run DAS diagnostics and self-testing,
3. Perform channel and instrument integrity evaluations,
4. Evaluate noise, and
5. Present posttest data and storage to customer-defined formats.

4.3.1 Software Structure

The software was separated into two main groups of programs and a group of utility routines. (The term "group" refers to a series of linked subprograms existing as separate files.)

The data acquisition software (the primary group) was used to both gather and store the data during each of the tests (e.g., pre-stressing, SIT, final). This program group required input in the form of configuration files and was primarily responsible for data scanning, immediate redundant data storage, and fault limit detection and announcement.

The data display software (the secondary group) used the data gathered by the primary group. The display software did not access the stored data files on the acquisition computer, but rather global variables that were shared by the acquisition and display computers. In Labview™, global variables are used to easily access a set of values from any active VI. This allows values to be shared between Labview™ programs without requiring any other connections between the programs. This software group was responsible for displaying the experimental data on demand in the form requested by the user. Several different display modes were developed to meet the need of the PCCV experiments. These included a stability review, strain and displacement distributions, and a primary graphical user interface.

The utility group provided the necessary input channel configuration information to the main group software. There were many other secondary tasks the utility group performed as needs arose.

³⁰ National Instruments Corporation, Austin, TX (<http://amp.ni.com/niwc/labview/what.jsp?node=1381>)

4.3.2 Software Module Specifics

The three PCCV DAS software groups were divided into seven main modules. Modules 1, 2, and 4a composed the main acquisition group. Module 4b was the main display software group. Modules 3, 5, 6, and 7 composed the Utility Group. Figure 4.2 shows a schematic of the modules and how they were grouped.

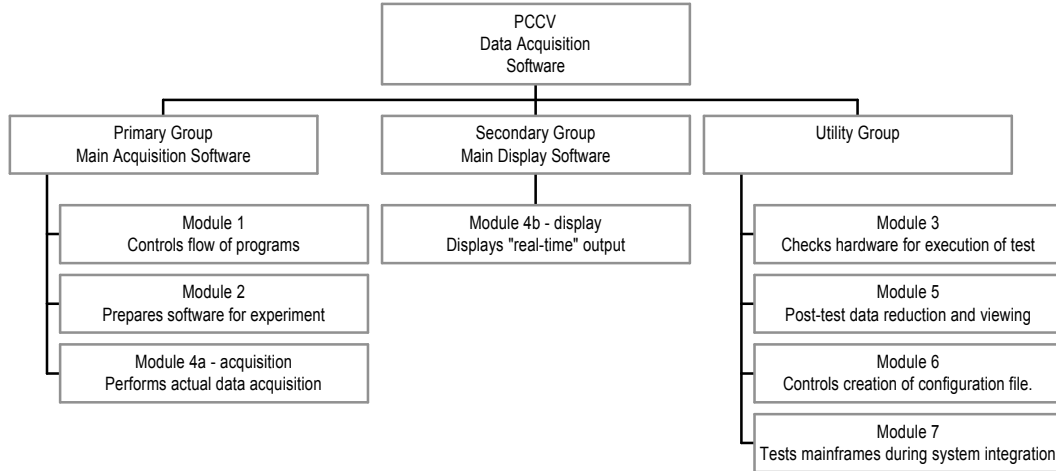


Figure 4.2. DAS Software Tree

The modules are listed below with a brief description of each.

- Module 1: Controls flow of program through Modules 2, 3, and 4a.
- Module 2: Prepares the software package to conduct a test including configuration information input to the acquisition software.
- Module 3: Prepares the hardware for executing the test. Includes checking the GPIB bus for the configured listeners and card layouts, and diagnosing the status (electronically) of the mainframes, digital multimeters (DMMs), and any other hardware.
- Module 4a: Performs the actual data acquisition, including readings during non-steady-state operation as well as the steady-state (DOR) scans. Includes writing raw data to disk as soon as possible. Provides continuous pressure information as well.
- Module 4b: Allows the user to select and display the desired real-time output.
- Module 5: Provides posttest data reduction and viewing.
- Module 6: Simplifies creating the configuration file and putting configuration information into the configuration file to minimize errors.
- Module 7: Facilitates mainframe testing during system integration. Easily configurable to rapidly indicate status of connected instruments.

4.3.3 Input/Output File Structure

4.3.3.1 File Structure Description

The two basic sets of I/O files necessary in the DAS software package were:

1. A configuration that file that provided the necessary input data to the DAS software, and
2. Data files into which the recorded data were placed.

Data File Structure

The design of the output data file structure allowed standard plotting software to select segments of data for plotting.

The output data file structure:

- Provided users with a clear map between the columns of numbers in a data file and the location and type of instrument originating the data,
- Used nomenclature for naming the files that provided the nature of the data contained and the types of instruments represented in the files,
- Generated an easily accessible set of files for archival purposes, anticipating future inquiries for analysis and presentation, and
- Facilitated rapid data correction and post-processing.

Two levels of folders below a “main” data folder were required to properly organize the data files. These levels are shown in Figure 4.3.

All data from this experiment was stored as *raw* data signals (i.e., the output of the A-D conversion step in the DAS process). Posttest data reduction converted the raw data into standard engineering units.

Table 4-1 lists the raw and reduced data units for the instruments in the PCCV experiment.

Note that the term “raw” in this table indicates the nature of the data signal after hardwired, “firmware” processing, which occurred automatically within the digital multimeter of the HP VXI Mainframe.

The data from some instruments was used to compensate or correct the raw data from other instruments. Details on this practice are found in Appendix G. Figure 4-4 illustrates the basic data flow diagram for the PCCV project.

4.4 Miscellaneous DAS Issues

4.4.1 Loss of Power

During the verification and validation testing, the results of losing electrical power to the DAS computers were determined. This determination involved actually shutting down electrical power to the computers while the DAS software was running. Several iterations of this were done, each at a different point in the acquisition process. It was necessary that data be maintained in the event of a power outage.

4.4.2 Integration of DAS with Other Systems

In general, the DAS was independent of all other systems involved in the PCCV experiments. There were two exceptions: still camera operation and the activation of redundant interior model lights. It was possible from the main data acquisition screen to operate the still cameras positioned throughout the PCCV model. Similarly, the interior model lighting was controlled from the main data acquisition screen. It was possible to turn the redundant lights on or off from the DAS computer.

The Soundprint acoustic monitoring system and the SOFO fiber-optic gages were equipped with their own independent DASs, also located in the data acquisition trailer. The only interface between these systems and the main DAS was manual synchronization of clock time. This provided the correlation between gage output and pressure subsequently used to analyze the test data.

Table 4.1. Description of Raw and Reduced Data for the PCCV Test

Instrument Type	Raw Data Units	Reduced Data Units
Strain gage (includes Tensmegs gages)	strain or microstrain (depending on gage factor format)	Strain
Cable-type displacement transducer	DC volts	Displacement (mm)
LVDT	DC volts	Displacement (mm)
Temposonic	DC volts	Displacement (mm)
Inclinometer-type displacement transducer	DC volts	Tilt angle (degrees)
Thermocouple	temperature (°C)	Same as raw
RTD	temperature (°C)	Same as raw
Pressure gage	DC volts	Pressure (MPa)
Load cells	DC volts	Load (Newtons)
Power supplies	DC volts	Same as raw (data used to reduce instrument voltages to CPOT distances)

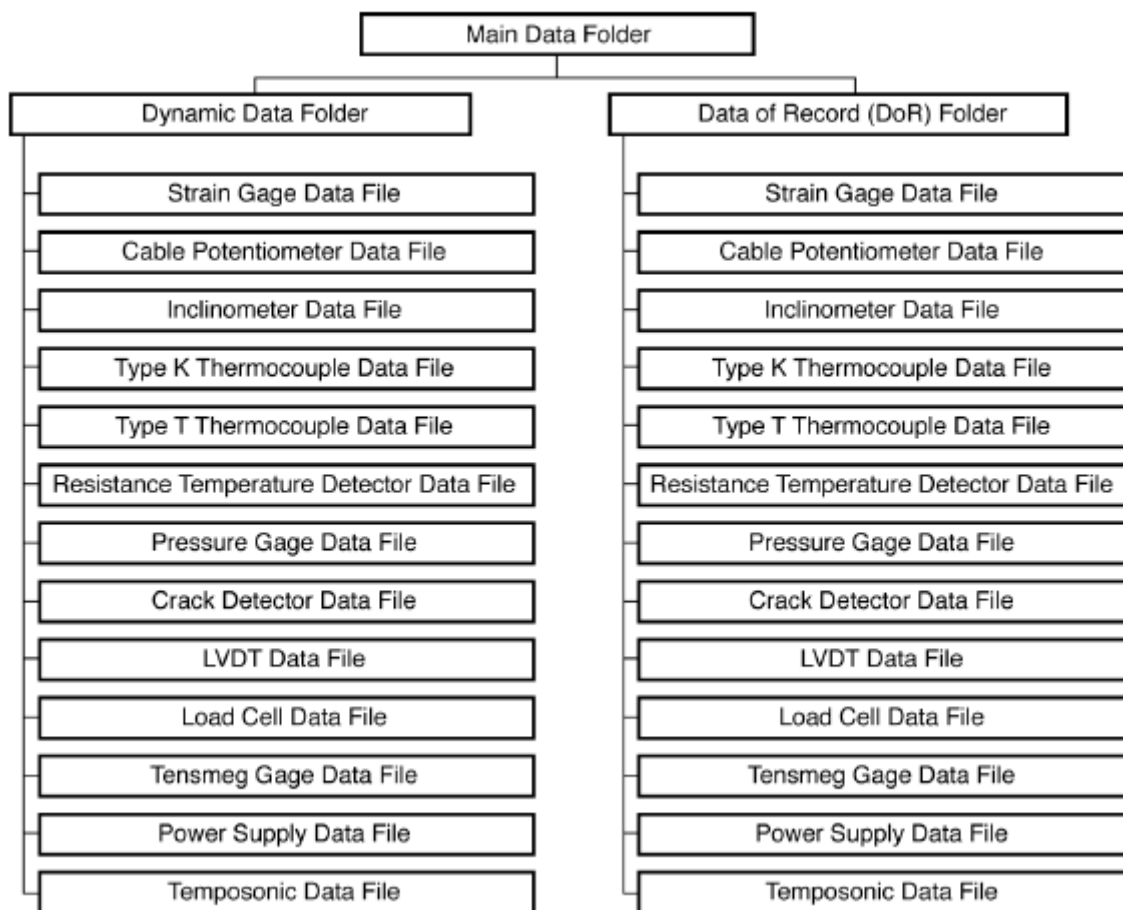


Figure 4.3 Top-Down Data File Folder Structure

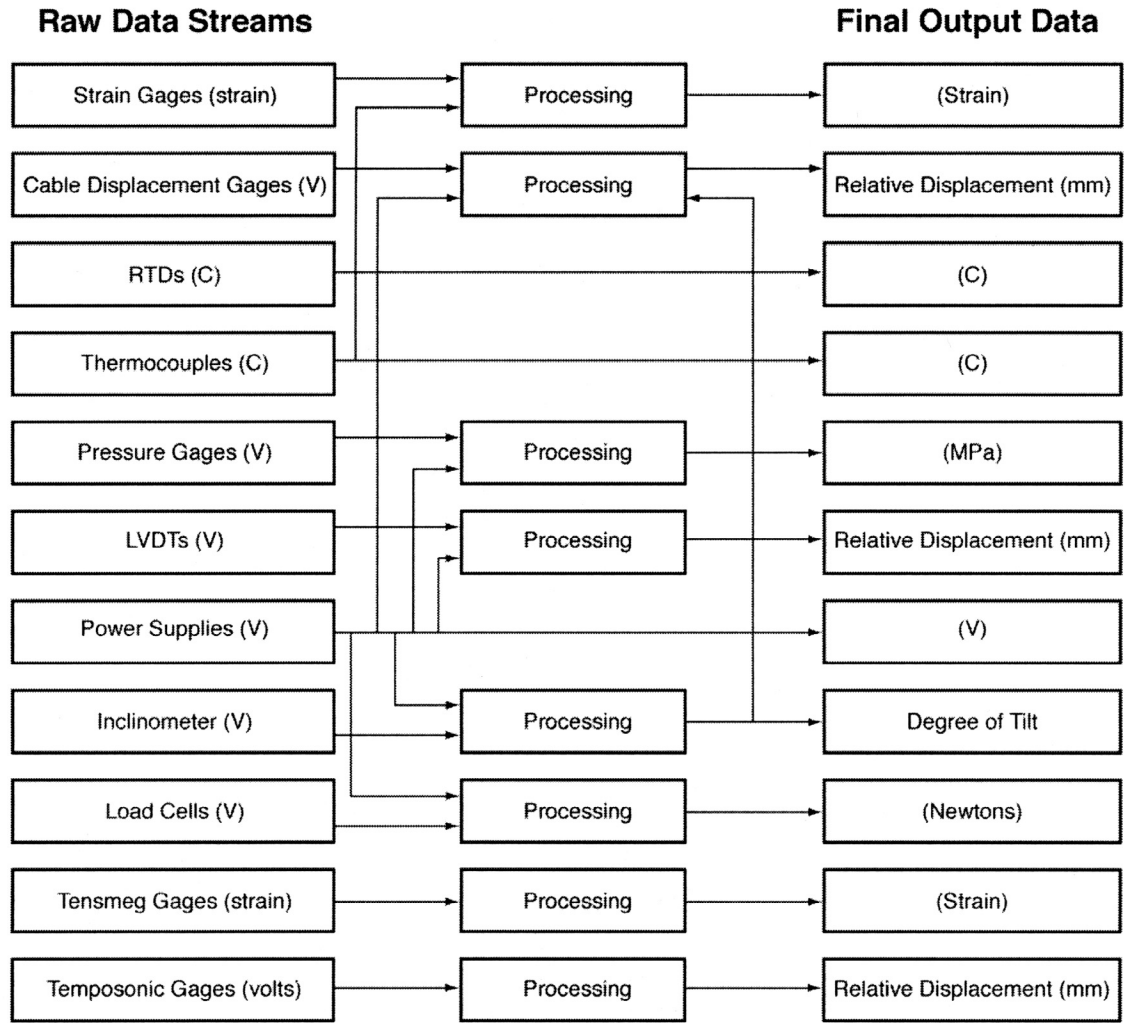


Figure 4.4 Basic PCCV Data Flow Diagram

5. TESTING

5.1 Test Planning

The basic objectives of the PCCV test were specified by NUPEC in the Master Project Plan [34]. The stated objective of this plan was to... “investigate the ultimate behavior of PCCV under pressure beyond the design basis accident and to prove the pressure retaining capacity of PCCV.” NUPEC originally specified a series of five tests, illustrated in Figure 5.1: 1) trial pressurization to 0.4 kg/cm² (5.7 psig or 0.1 P_d), 2) structural integrity and integrated leak rate tests to 4.5 and 3.6 kg/cm² (64.1 and 51.2 psig or 1.125 and 0.9 P_d), respectively, 3) two design pressure tests to 4.0 kg/cm² (57 psig or 1.0 P_d), and 4) a Limit State Test (LST) terminating with excessive leakage or structural failure.

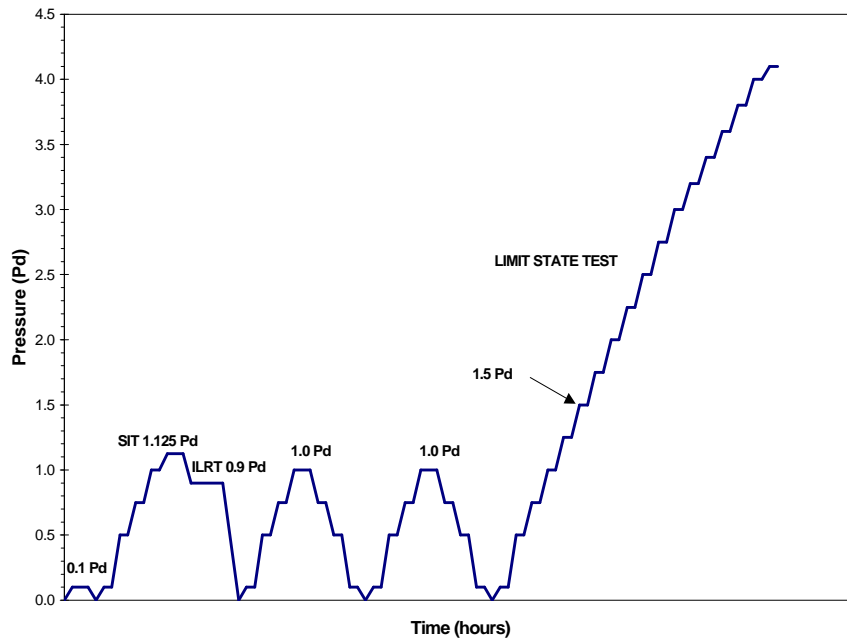


Figure 5.1 Original Pressurization and Depressurization Sequence [34]

After extensive discussions between NUPEC, the NRC and SNL, a detailed Test Plan [35] was developed by SNL to describe the conduct of the PCCV model's pressurization tests. Additional procedures that addressed the safe conduct of the tests were defined in the Operating Procedure [36]. The Test Plan includes:

- procedures to be conducted prior to tests to assure that all systems are ready;
- a list of test personnel required to conduct the tests and an outline of functions and checklists assigned to each person;
- procedures to be followed during the tests, including the general test philosophy;
- procedures to be conducted after pressure tests are completed.

Detailed checklists were prepared to ensure that all test operations were conducted as planned and completed in the appropriate sequence. Detailed procedural logs, stored in the project files, were generated to document the conduct of each test. A summary of the test plan is included in this chapter.

A final series of three tests were agreed upon. These tests are defined as follows and are illustrated in Figure 5.2.

1. A leak check and System Functionality Test (SFT) at 0.5 P_d (2.0 kg/cm² or 28.4 psig)

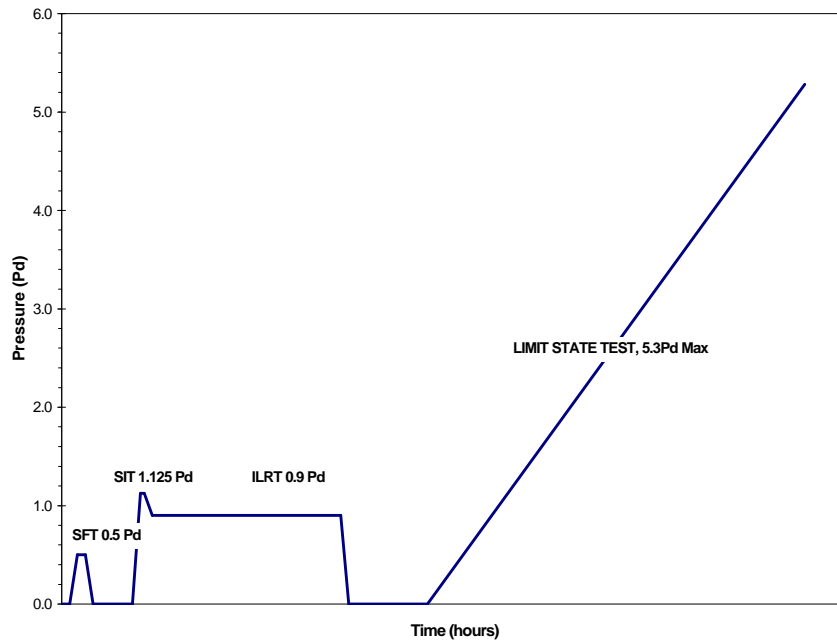


Figure 5.2 Final Pressurization Plan

2. A Structural Integrity Test (SIT) at $1.125 P_d$ followed by an Integrated Leak Rate Test (ILRT) at $0.9 P_d$
3. An Limit State Test (LST) to the static pressure capacity of the PCCV model (or the pressurization system, whichever comes first)

A fourth test was added to the test program after the conclusion of the LST. After careful evaluation of the LST results, NUPEC, the NRC, SNL, and their technical advisors concluded that not all of the program's objectives were met after the LST. SNL was tasked with designing and conducting a test that would allow the PCCV model to be pressurized beyond the level reached during the LST in an attempt to observe greater inelastic response of the model and, hopefully, generate a structural failure mode. This Structural Failure Mode Test (SFMT) is described in Section 5.2.4.

5.1.1 Pressurization System Design and Operation

The pressurization system for the PCCV model test consisted of a pressure source, a valve gallery (consisting of several valves, a flow meter, and several sensors) used to control the flow of nitrogen, a programmable logic controller (PLC), control computer, and high pressure piping which interconnects all the components. A schematic of the pressurization system is shown in Figure 5.3

For the SFT, SIT/ILRT, and SFMT, the pressure source consisted of a pressurized nitrogen tube trailer. The trailer was located adjacent to the PCCV model, next to the valve gallery with a short flexible hose connecting them. For the LST, the pressure source consisted of a truck with liquid nitrogen that was gasified and regulated to a constant pressure and temperature. This source was located more than 600 m (2000') away from the PCCV model for safety reasons, near Building 9950. The pressurized nitrogen gas was piped aboveground onto the CTF site and into the valve gallery.

In addition to the temperature being controlled at the source location during the pressure testing, the gas was heated in the piping prior to entering the PCCV model. These heaters helped increase the temperature of the gas prior to entering the PCCV model. Several additional heaters were located inside the model to help maintain temperatures to within ± 5 degree C of the average ambient temperature ($\sim 15^\circ \text{C}$) outside the PCCV model.

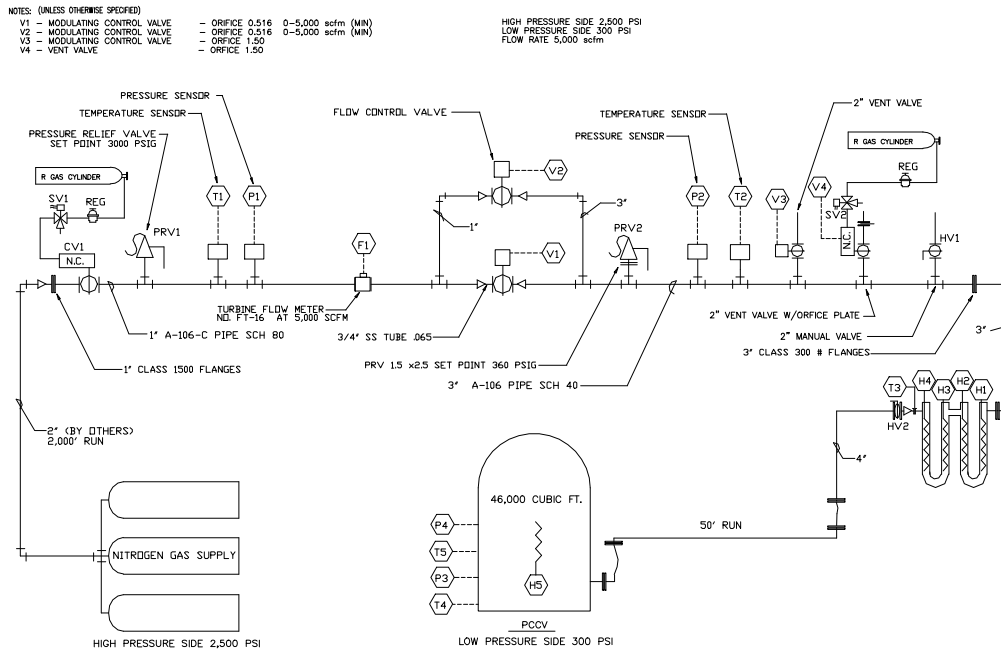


Figure 5.3 Pressurization System Schematic

The pressurization system was controlled by the PLC, which was located on the valve gallery skid next to the PCCV model. Communication with the PLC was performed by the control computer located in Building 9950. A more detailed description of the entire pressurization system is provided in the PCCV Pressurization System Data Package [37].

The entire pressurization system was designed and fabricated by an outside contractor (Rupert Plumbing and Heating Company, Inc., Albuquerque, NM). Initial testing of the system (primarily the valve gallery and heaters) was performed by the contractor prior to delivery to the CTTF site. After the system was installed at the site, the system was tested again before connecting to the PCCV model and conducting the pressure tests of the model.

The system tests performed by the contractor were approved by SNL personnel and encompassed all possible conditions the system might have to deal with during both the low- and high-pressure testing. These system tests checked all wiring, valve functionality, instrument functionality, and the control hardware and software.

After the system was installed and tested, the piping into the PCCV model was hooked up. All pressure lines connected to the valve gallery and the PCCV model were clean and dry before they were connected. Before the flex hose and flange were connected to the PCCV model, the line was “blown out” to clean it. The pressure source line up to the valve gallery was also blown out prior to the final hook-up.

5.2 Test Operations

The over-pressurization tests of the PCCV model were conducted at the CTTF-W, shown in Figure 1.3.

Building 9950, an ancillary facility for the test site (shown in the background in Figure 2.11), was the headquarters for conducting the pressure tests. It housed the control room and the observation room. During the test, key project members were inside the control room to execute the test plan and monitor the response of the model. Visitors observed the test progress and received periodic information on test status in the observation room.

The basic test team for each test is shown in Figure 5.4. The test team was only fully staffed for the LST and the SFMT. Test staffing for prestressing and the low-pressure tests is shown in Table 5.1.

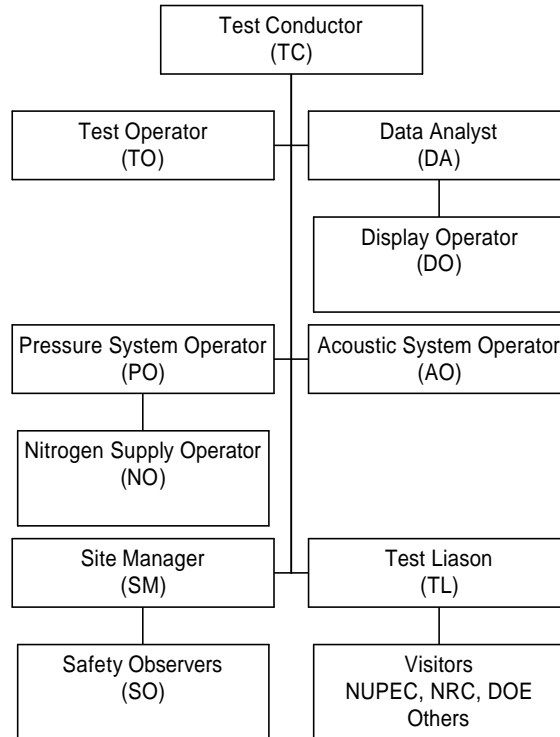


Figure 5.4 PCCV Test Organization

Table 5.1 PCCV Test Personnel Matrix

Position	Prestressing	SFT	SIT/ILRT	LST	SFMT
Test Conductor	X*	X	X	X	X
Test Operator	X	X	X	X	X
Data Analyst				X	X
Display Operator			X	X	X
Pressure System Operator		X	X	X	X
Acoustic System Operator	X	X	X	X	X
Site Manager	X	X	X	X	X
Safety Observers			X	X	X
Nitrogen Supply Operators		X	X	X	X
Test Liaison			X	X	
Visitors			X	X	X

*Part-time

5.2.1 System Functionality Test

The system functionality test and leak check was designed to verify the functionality of all the systems (instrumentation, data acquisition, pressurization, etc.) and the initial leak-tightness of the PCCV model (especially the sealing of the penetrations) prior to the performance of the pressure tests. Controlled leak tests were included to determine the accuracy of the leak detection instrumentation during the ILRT and LST.

The SFT was conducted beginning approximately 9:00 AM, July 18, 2000. The model was pressurized using nitrogen to 0.5 P_d (0.2 MPa or 28.4 psig) in three increments holding pressure for one hour or longer at each step, depending on the duration needed to perform all system functionality and leak checks. The model was then isolated and a leak rate check was performed by monitoring the model pressure and temperature for approximately 18 hours. After 18 hours, the calculated leak rate was 0.15% mass/day, which confirmed that the model was leak-tight. After the model leak rate check, the model was allowed to depressurize through a pair of orifice plates calibrated to leak rates of 1% and 10% mass/day to perform a calibration test on the leak rate measurement instrumentation. The calculated leak rates for each test were 0.87% and 7.86%, respectively, indicating that the leak rate instrumentation accurately detected a leak of 1% mass per day, which is the goal specified for the ILRT. The SFT was concluded on July 20 by opening the vent valve, allowing the model to depressurize. The SFT pressure time history and leak rates are shown in Figures 5.5 and 5.6.

5.2.2 Structural Integrity Test and Integrated Leak Rate Test

The SIT and the ILRT were conducted on September 12-14, 2000 as a combined test, with the ILRT following immediately after the SIT. The SIT/ILRT reproduced the preoperational tests conducted at the prototype plant and allows for a comparison of the model’s elastic response characteristics and leak behavior with the prototype and pretest analyses. The pressure and average temperature time histories measured during the test are shown in Figure 5.7.

5.2.2.1 Structural Integrity Test

The SIT followed the procedures specified by Japanese Standard JEAC 4203-1994 [38] and the ASME Boiler and Pressure Vessel Code, Section III, Division 2, Article CC-6000, “Structural Integrity Test of Concrete Containments.” [9]

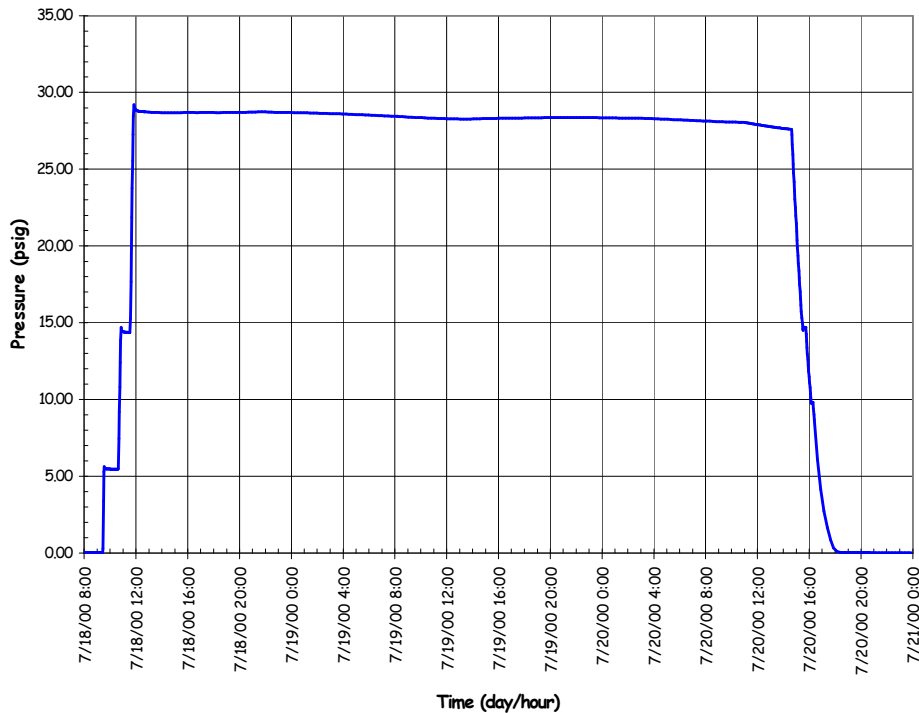


Figure 5.5 System Functionality Test Pressure Time History

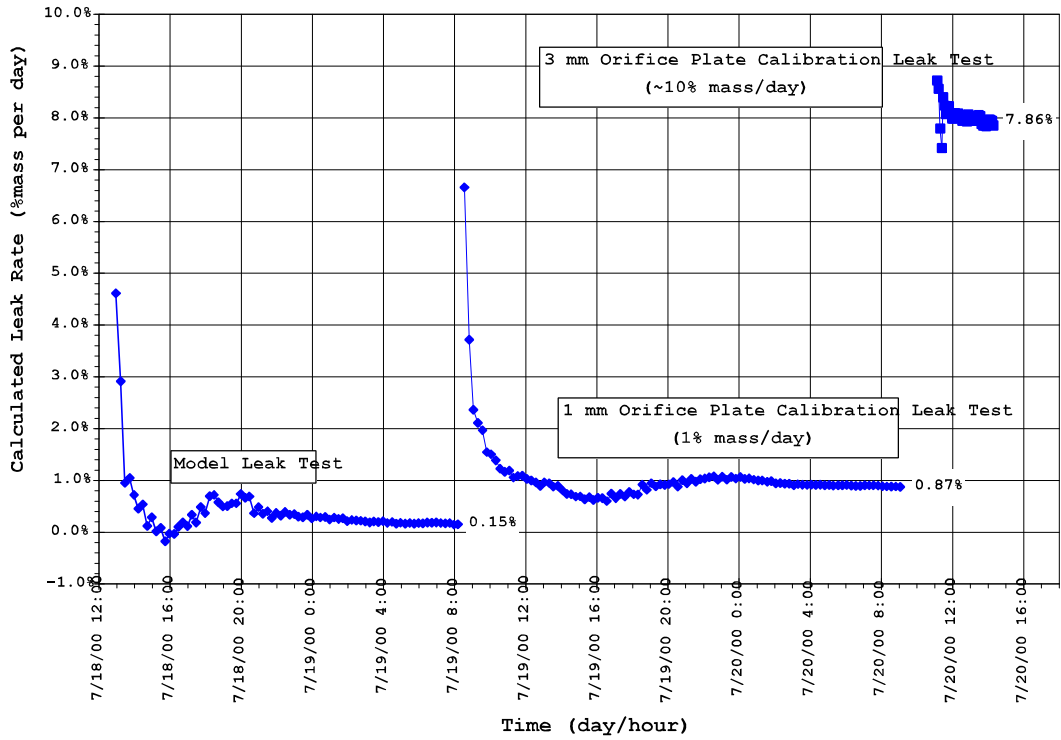


Figure 5.6 System Functionality Test Leak Rates

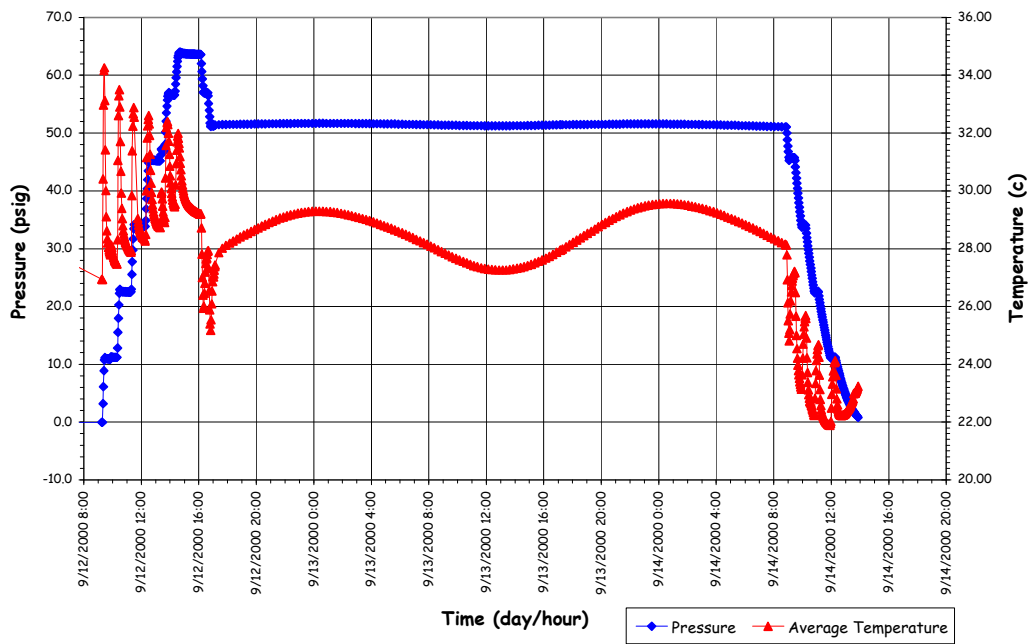


Figure 5.7 Structural Integrity and ILRT Pressure and Temperature Time Histories

Per MITI Code 501, Article 104 [39], the SIT test pressure, P_{SIT} , was $1.125 P_d$ (0.44 MPa or 64 psig). The PCCV model was pressurized in five equal increments at a rate of 20% of the test pressure per hour. (CC-6110 requires pressurization to $1.5 P_d$.) Per CC-6340, the response of the model was recorded at each pressure step (including 0 P_d). Data of Record (DOR) was recorded when the following stability criterion was achieved:

$$\frac{Q_t - Q_{t-\Delta t}}{Q_{t-\Delta t}} \leq 0.02 \quad (5.1)$$

where Q_t and $Q_{t-\Delta t}$ are the data at the current and the previous time interval, respectively. The next pressure increment followed only after this criterion was satisfied or the total step duration reached one hour.

All active gages in or on the model were recorded at each step. The locations of the gages were selected to allow for direct comparison of the PCCV model response to the prototype at the SIT pressure in addition to the primary objective of monitoring the response of the model to ultimate pressure. Table 5.2 summarizes the ASME code requirements for SIT measurements.

Table 5.2 Summary of ASME B&PV Code SIT Instrumentation Requirements

	Measurements	Accuracy/Range	Pressure	Acceptance Criteria
Cracking	CC-6350 Cracks > 0.01"x 6" @ specified locations	CC-6225 >0.005" @ 0.003"	CC-6350 Before test @ P_{SIT} After test	CC-6420 Review by Designer
Strains	CC-6370: (Concrete Strains) @ Wall/Slab @ E/H @ Shell Discontinuities @ Restraints @ Steel/Concrete Trans.	CC-6224 $\pm 5\% \epsilon_{max}$ or $10\mu\epsilon$ Gage Length > 4"	CC-6371 1. Baseline-Continuously for 24 hrs prior to test CC-6340 2. @ P_0 (Atmospheric press.) 3. During pressurization @ 20% P_{SIT} 40% P_{SIT} 60% P_{SIT} 80% P_{SIT} 100% P_{SIT} 4. @ PSIT + 1 hour 5. During depressurization @ 80% P_{SIT} 60% P_{SIT} 40% P_{SIT} 20% P_{SIT} @ P_0	CC-6410 (a) No rebar yielding (b) No visible liner or concrete damage (c-2) Residual displacements: @ Pts of Max. δ_R & δ_V : $\delta_{res} < 20\% \delta_{max}^* @ P_{SIT} + 0.01"$ (*measured or predicted) Avg. δ_R @ each elevation: $\delta_{res} < 20\% \delta_{max}^* @ P_{SIT} + 0.01"$
Displacements	CC-6361: δ_R @ 20% H & 0°, 90°, 180°, 270° δ_R @ 40% H & 0°, 90°, 180°, 270° δ_R @ 60% H & 0°, 90°, 180°, 270° δ_R @ 80% H & 0°, 90°, 180°, 270° δ_R @ 100% H & 0°, 90°, 180°, 270° δ_R @ E/H (12 points) δ_V @ Springline & 0°, 90°, 180°, 270° δ_V @ Apex δ_V @ two pts. Bet. Apex & Springline	CC-6223 $\pm 5\% \delta_{max}$ or 0.01"		
Temperature	CC-6380 Concrete @ Specified locations for Strain Correction Gas @ Interior & Exterior	CC-6226 $\pm 2^\circ F$ Range: Expected temp.		
Pressure		CC-6222: $\pm 2\% P_{SIT}$ Range < 4 P_{SIT}		

In general, the model instrumentation satisfied all of the requirements summarized in Table 5.2 with the following exceptions or modifications.

- The entire surface of the cylinder was mapped for cracks prior to the test; however, crack widths were not measured. No crack mapping was performed during the SIT. After the SIT, additional cracks within selected areas of the cylinder wall were identified but the widths were not measured. The crack map grid is shown in Figure 5.8
- Model strains were measured primarily using the gages mounted directly to the rebar and liner. Only a limited number of concrete strains were measured directly.
- Displacements were measured at all specified locations with the exception of the points around the largest penetration (i.e. the E/H)

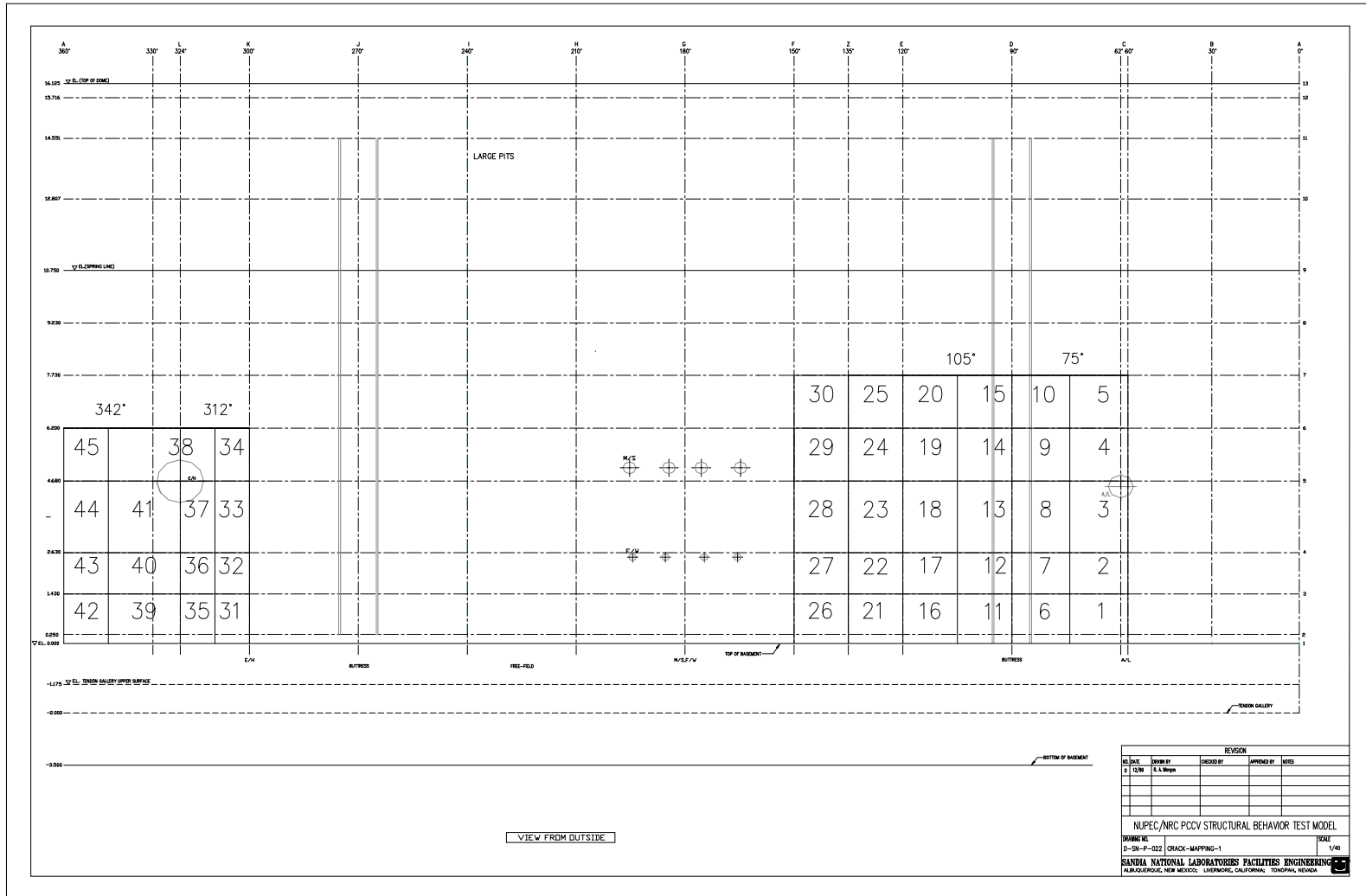


Figure 5.8 Concrete Crack Map Grid

After the SIT pressure was maintained for the required minimum of one hour per CC-6320, the PCCV model was depressurized to the ILRT pressure. First, the model was depressurized to P_d , for comparison with the pressurization phase, before depressurizing to the ILRT pressure ($0.9P_d$).

The temperature inside the model was specified to be maintained at approximately $25\text{ }^\circ\text{C}$ ($77\text{ }^\circ\text{F}$) during the test with a maximum range of $10\text{ }^\circ\text{C}$ to $38\text{ }^\circ\text{C}$ ($50\text{ }^\circ\text{F}$ to $100\text{ }^\circ\text{F}$). The average temperature during the SIT, recorded by the RTDs, was closer to $30\text{ }^\circ\text{C}$ ($86\text{ }^\circ\text{F}$). The ambient air temperature outside the model was measured near the base of the model.

5.2.2.2 Integrated Leak Rate Test

The ILRT requirements for Japanese containments are specified in JEAC 4203-1994 [38]. The ILRT requirements for U.S. containment vessels are specified in 10CFR50, Appendix J “Primary Reactor Containment Leakage Testing for Water-Cooled Power Reactors,” [40] which references the tests procedures in American National Standards ANSI/ANS N45.2-1974 “Leakage Rate Testing of Containment Structures for Nuclear Reactors [41] and ANSI/ANS N56.9-1987 “Containment System Leakage Testing Requirements.” [42]

The ILRT for the PCCV model was a hybrid of these procedures. The ILRT pressure, P_{ILRT} , was $0.9 P_d$ (0.35 MPa or 51.2 psig) based on JEAC 4203 and the Absolute Method for a Type A Test per ANSI/ANS N56.9 (Section 5.0) was followed. After depressurizing from the P_{SIT} to P_{ILRT} , the model was held at P_{ILRT} for approximately one hour to allow the model atmosphere to stabilize before the start of the leakage rate test. The ILRT commenced after all stabilization criteria were achieved and the duration of the test was “sufficient to enable adequate data to be accumulated and statistically analyzed so that a leakage rate ... can be accurately determined” but no less than 24 hours. Data was collected at least once every hour. The measured leakage rate at P_{ILRT} , L_{tm} , was determined using both the (a) total time analysis and (b) point-to-point analysis techniques. The nominal atmospheric pressure at the elevation of the test site (verified by checking the Sandia Photovoltaics Weather Station reading) was used for leak rate calculations. The calculated leak rate after 24 hours at $0.9 P_d$, was 0.059% mass/day.

After the ILRT was completed, the model was initially depressurized by venting through the 1mm orifice plate, calibrated for a leak rate of 1% mass/day. After approximately 16 hours, a stable leak rate of 0.996% mass per day was calculated, again confirming the accuracy of the leak rate instrumentation.

The calculated leak rates during and after the ILRT are shown in Figure 5.9.

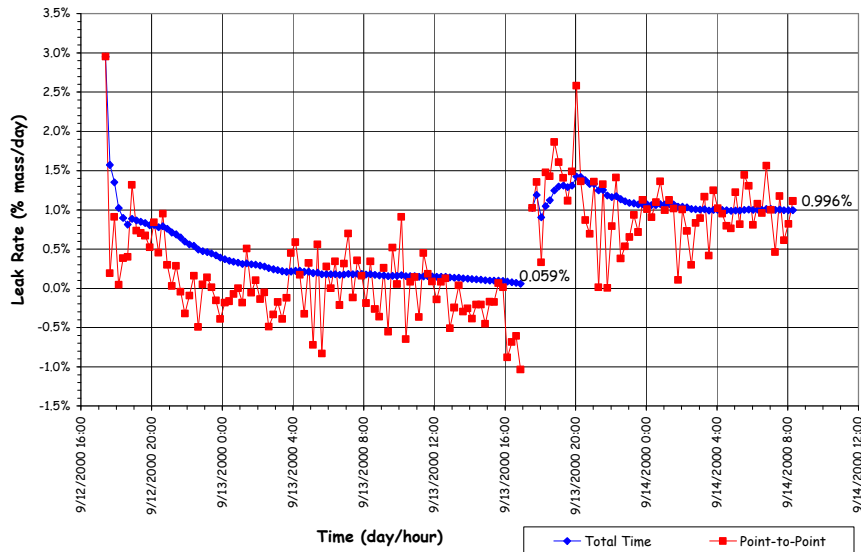


Figure 5.9 Integrated Leak Rate Test Leak Rates

Per JEAC 4203, the maximum leak rate at the ILRT pressure should be less than 0.1% mass/day. Similarly, per 10 CFR 50, the specified maximum allowable leak rate, L_a , at the design accident pressure, P_d , for the prototype containment is 0.1% mass/day. The maximum leak rate at the ILRT pressure level, L_t , is

$$L_t = L_a (P_{ILRT}/P_d) = 0.09\% \text{ mass/day}$$

Normally, the measured leak rate, L_{tm} , should be less than $0.75L_t$ (0.07% mass/day). For the PCCV model, this translates into measuring a change in pressure of approximately $0.001 \text{ kg}_f/\text{cm}^2$ (0.02 psi), which is beyond the capability of the instrumentation to resolve. While the calculated leak rates are within the limits specified in the standards, the accuracy of these leak rate estimates is questionable. Using the instruments selected for the high pressure test, however, the PCCV model exhibited a leak rate which was less than 1% mass/day, which corresponds to a pressure drop of 0.004 MPa (0.6 psi) over 24 hours.

While holding at the ILRT pressure, a limited amount of crack mapping was performed. This was accomplished by tracing all new cracks in predetermined areas and taking still photos of these areas. Cracks in the area to the left of the E/H prior to the SIT were traced in black and are shown in Figure 5.10. New cracks, traced in blue during the ILRT, are shown in Figure 5.11. Cracks widths were not measured.



Figure 5.10 Pre-SIT Cracks at Azimuth. 350 degrees, Elev. 4680 to 6200 (Grid 45)

Model response data was also recorded during and after the SIT/ILRT. Figures 5.12 and 5.13 show the radial and vertical displacement of the model as a function of time.

The initial displacements represent the net effect of prestressing, creep, shrinkage, etc. from the 'zero' reading in March to the start of the SIT in September. The cyclic response during the ILRT is an indication of the model's response to variation in ambient temperature and direct heating.

After the leak rate calibration, the PCCV model was depressurized at approximately the same rate and increments as the initial pressurization phase to compare the responses at the same pressure levels.

An exclusion zone was established for the SIT, consisting of a circular area with radius of 600 m (2,000'), centered at the PCCV model. The exclusion zone, as shown in Figure 5.14, was marked, and signs were posted to identify this area. The safety observers monitored the exclusion zone at all times during the test to make sure that no intruder entered this area. No exclusion zone was required for the ILRT because the model pressure was below the design pressure ($0.9P_d$).



Figure 5.11 Post-SIT Cracks at Azimuth. 350 degrees, Elev. 4680 to 6200 (Grid 45)

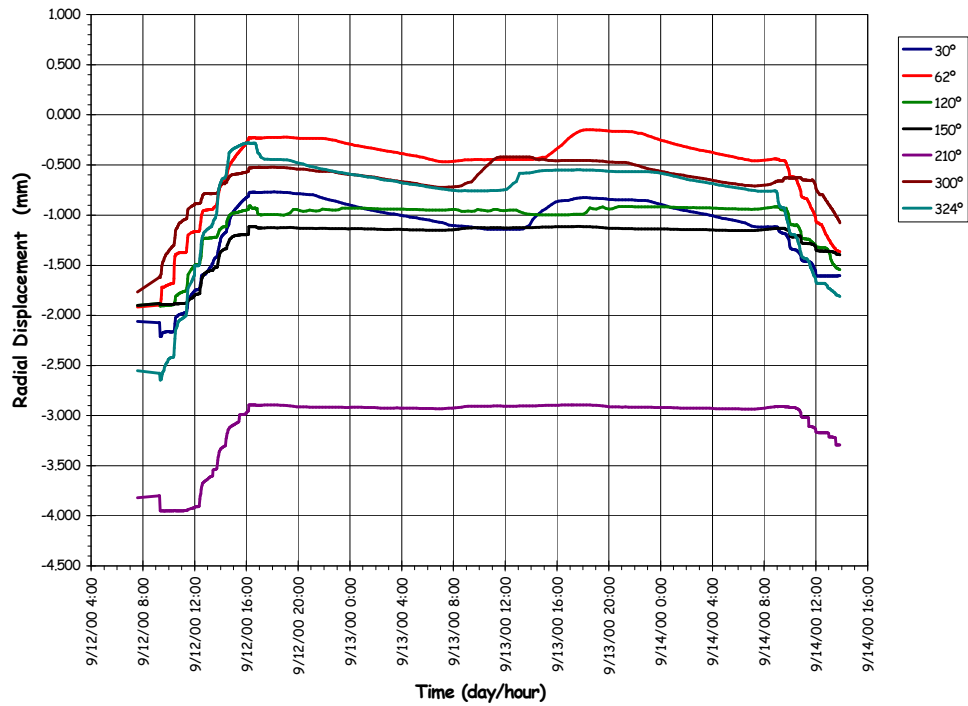


Figure 5.12 SIT/ILRT Radial Displacements at Cylinder Midheight (Elev. 4680)

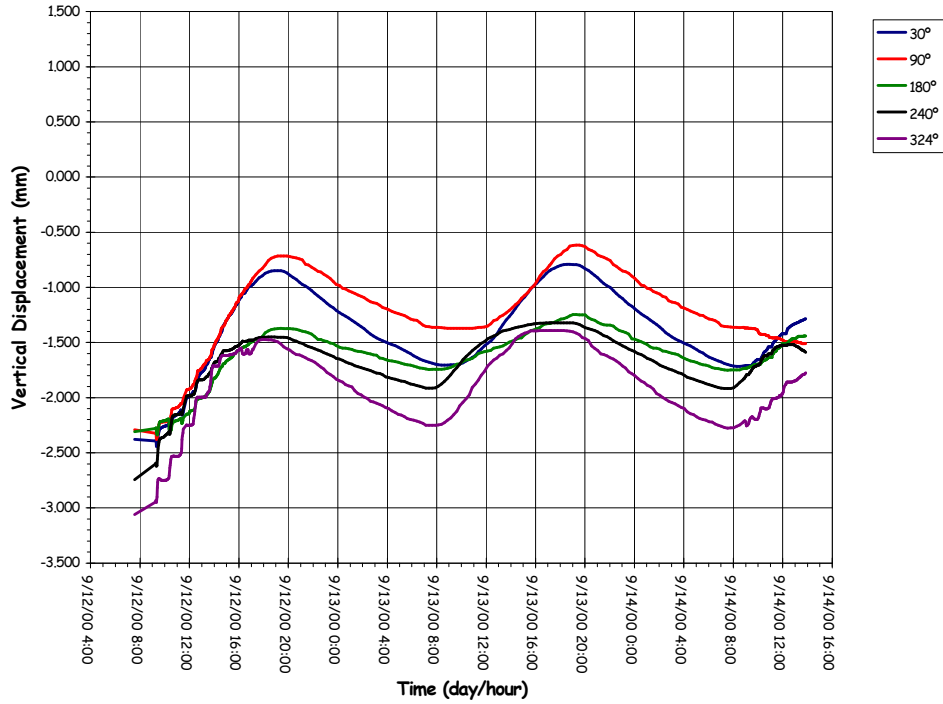


Figure 5.13 SIT/ILRT Vertical Displacements at Springline (Elev. 10750)

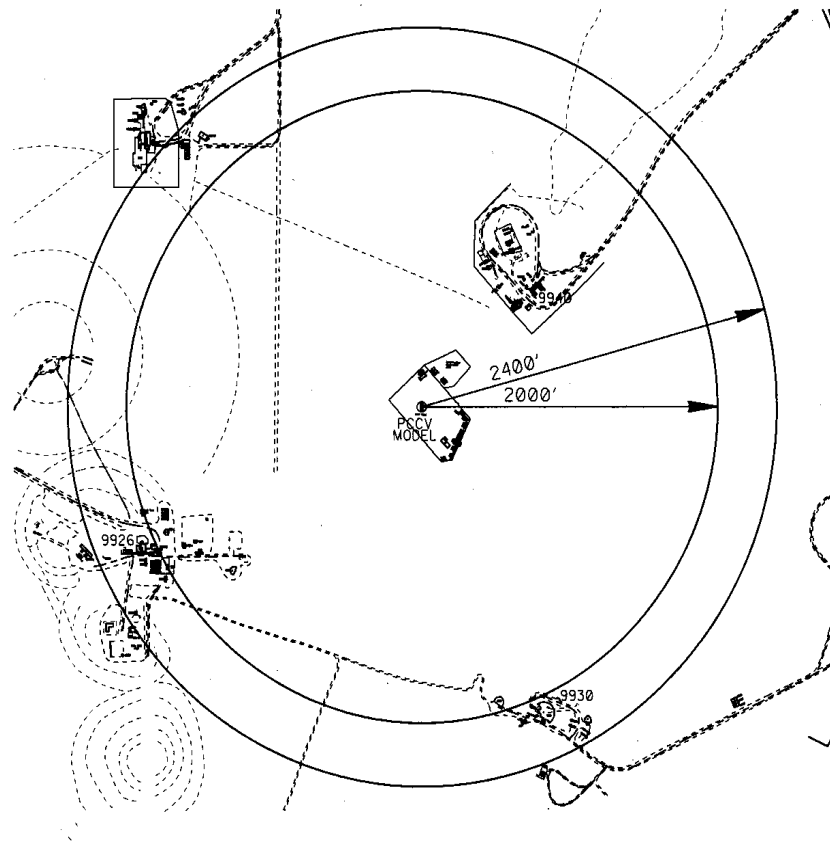


Figure 5.14 PCCV SIT/ILRT, LST, SFMT Exclusion Zone

Personnel were permitted to approach the model after the pressure has stabilized and the test conductor (TC) determined that it was safe to approach the model.

5.2.3 Limit State Test

The LST was designed to fulfill the primary objectives of the PCCV test program, i.e. to investigate the response of representative models of nuclear containment structures to pressure loading beyond the design basis accident and to compare analytical predictions to measured behavior. The LST was conducted after the SIT and ILRT were completed and the data from these tests evaluated. The PCCV model was depressurized between the SIT/ILRT and the LST. The LST began at 10:00 AM, Tuesday, September 26, 2000, and continued, without depressurization, until the test was terminated just before 5:00 PM on Wednesday, September 27.

The exclusion zone for the LST covered the same circular area of radius 600 m (2,000'), centered at the PCCV model, as shown in Figure 5.14. At this radius, the estimated peak free-field overpressure due to a sudden burst at an internal pressure 2.1 MPa or 300 psig [34] is 1.66 kPa (0.24 psi). This is below the free-field allowable whole body exposure of 3.4 kPa (0.5psi) specified by SNL Environmental Safety and Health (ES&H) regulations. The safety observers monitored the exclusion zone at all times during the LST to make sure no intruder entered this area. In addition, the safety observers monitored the area above the model for aircraft. If an aircraft had approached the exclusion zone, pressurization of the model would have been suspended or held until the aircraft cleared the exclusion zone.

The pressure and average temperature time histories during the LST, including depressurization, are plotted in Figure 5.15. The LST followed the planned pressurization sequence up to the point where the model began leaking.

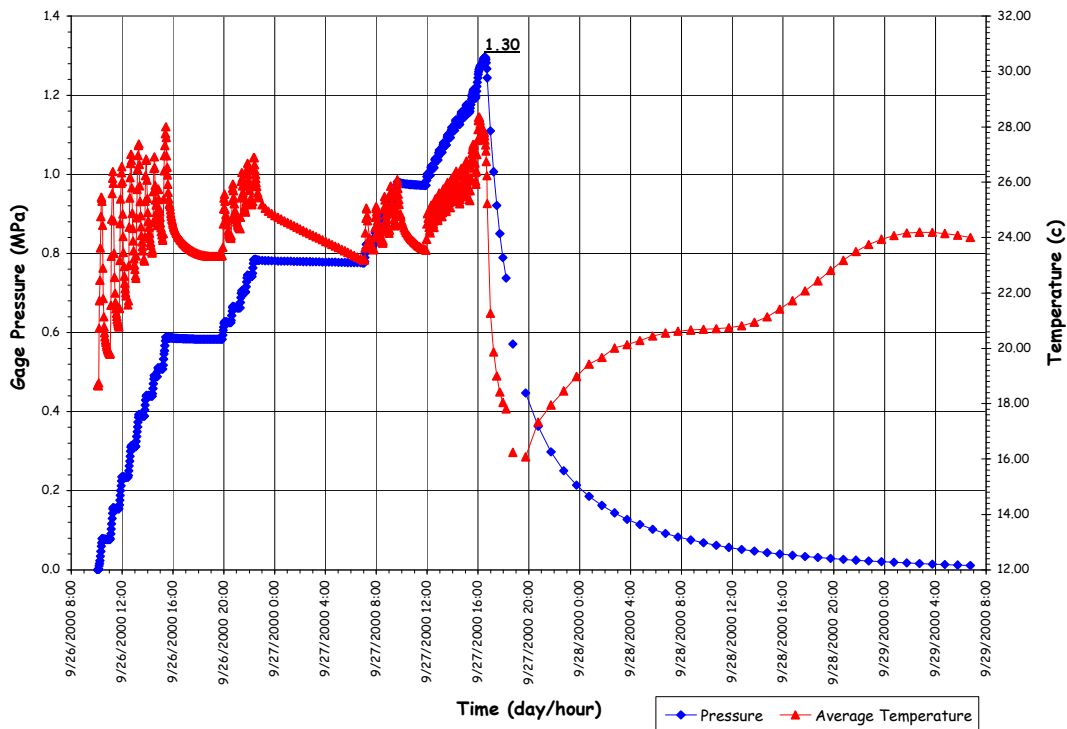


Figure 5.15 Limit State Test Pressure and Average Temperature

Initially, the model pressurization sequence matched the pressurization steps followed for the SIT to allow for comparison of the model response to two identical cycles of loading. The gage stability criteria used during the SIT (i.e. Equation 5.1) was also applied during the LST. Pressurization continued in increments of approximately $0.2P_d$ until a pressure of $1.5 P_d$ ($6.0 \text{ kg}_f/\text{cm}^2$ or 85.3 psig) was reached at approximately 4:30 PM. At this pressure, the first planned leak check was conducted by isolating the model and monitoring the temperature and pressure. After approximately three hours, a leak rate of 0.48% mass/day was calculated. Considering previous experience from the ILRT, which

demonstrated that thermal expansion of the model during the day yielded apparent leak rates in this range, the results were interpreted to indicate that the PCCV model was leak-tight.

Pressurization of the model continued in increments of approximately $0.1P_d$ until a pressure of $2.0P_d$ ($8.0 \text{ kg}_f/\text{cm}^2$ or 113.8 psig) was reached at approximately 11:00 PM. At this pressure the model was again isolated to perform a planned leak check. This leak check was also planned to be held for 8 hours to allow the test team to partially stand down for a rest period. A ‘skeleton crew’ consisting of the TC, Data Acquisition System Operator (DO), and Nitrogen Supply Operator (NO) continued to monitor the response of the model and all other systems until approximately 7:00 AM on September 27. This pressure hold and leak check was also selected below the lower bound prediction for the onset of structural yielding (i.e. yielding of the rebar or tendons) to ensure the model would remain relatively stable during this period. After approximately eight hours, the calculated leak rate was 0.003%, i.e., essentially zero. This confirmed the interpretation of the leak check results at $1.5 P_d$ and also demonstrated the greater accuracy of the leak rate results when the model is thermally stable.

Pressurization of the model resumed at 7:00 AM in increments of $0.1P_d$, with increasing dwell time between pressure steps (~30 minutes) required to meet the gage stability criteria. As the pressure was increased to the next planned leak check at $2.5P_d$, liner strain gages in the vicinity of the E/H (LSI-C-K5-12) began registering rapidly increasing strains in excess of 1%. At $2.4P_d$, the acoustic system operator (AO) reported hearing a change in the acoustic output which might indicate that “something had happened.” At approximately 10:00 AM at a pressure of $2.5P_d$ ($10.0 \text{ kg}_f/\text{cm}^2$ or 142.2 psig), the model was isolated for the third planned leak check. After approximately 1-1/2 hours, a fairly stable leak rate of 1.628% mass per day was calculated. The leak rate calculations at 1.5, 2.0, and $2.5P_d$ are plotted in Figure 5.16. Coupled with the acoustic data that continued to confirm some new event had occurred, it became clear that the model was leaking, most likely from a tear in the liner in the vicinity of the E/H. Plots of the output of the four internal acoustic sensors surrounding the E/H at 2.3, 2.4, and $2.5 P_d$ are shown in Figure 5.17.

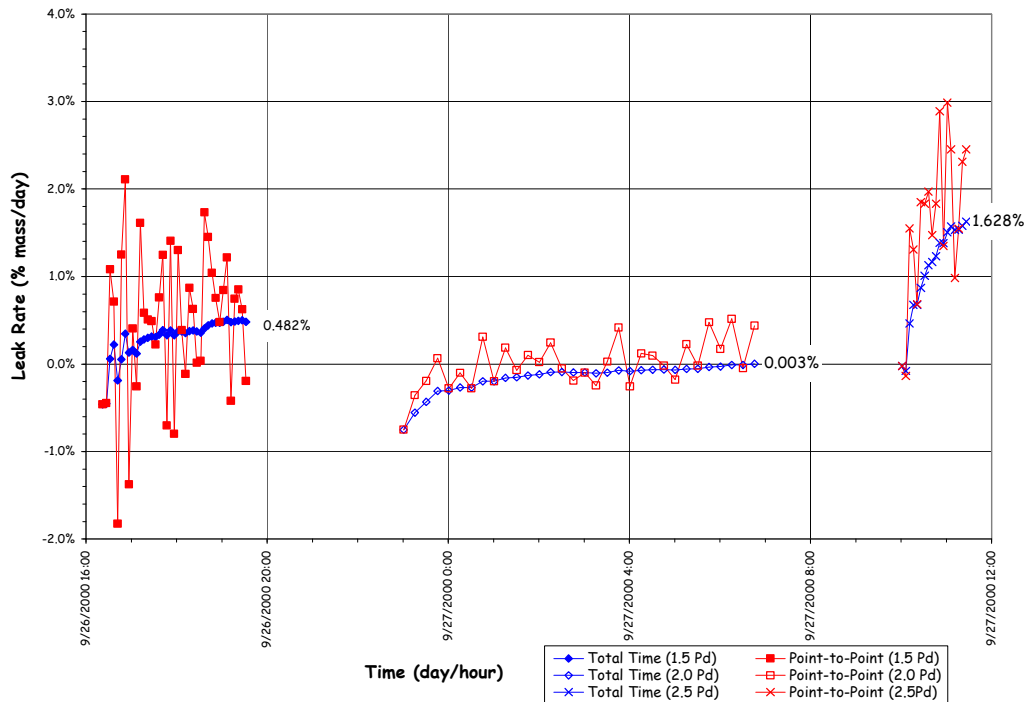


Figure 5.16 LST Calculated Leak Rates at 1.5, 2.0 and $2.5 P_d$

After consulting with NUPEC and the NRC, the TC concluded that the model had functionally failed between 2.4 and $2.5 P_d$ and directed a change in the pressurization plan. Since the model was leaking, the next goal was to pressurize the model as high as possible to collect data on the inelastic response of the structure and to observe, if possible, a structural failure mode. Pressurization continued in increments of $0.05 P_d$, as planned. However, the gage stability criteria was abandoned and the hold time at each pressure step was reduced to less than 10 minutes.

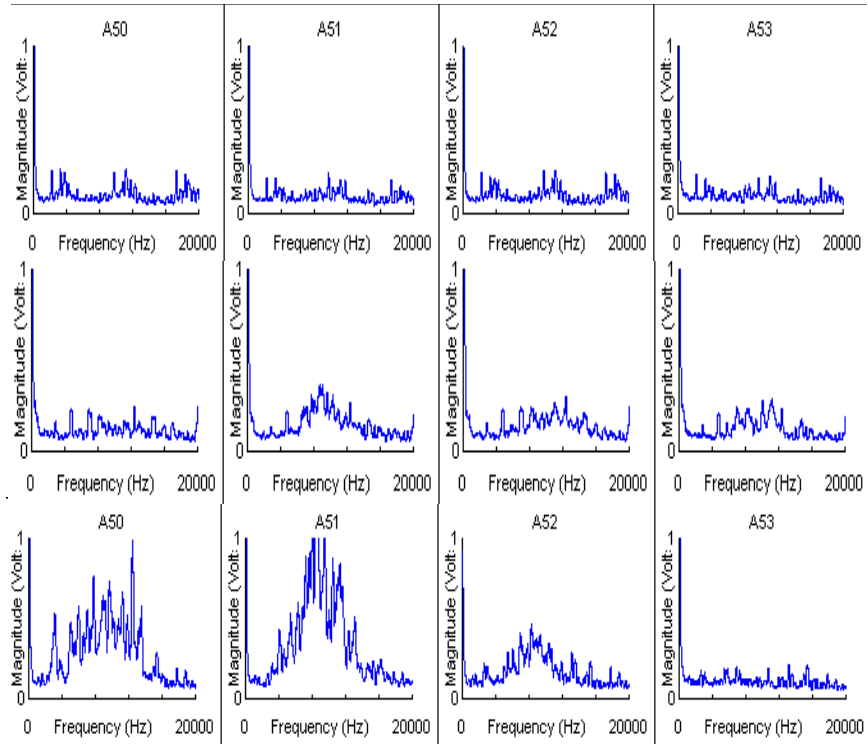


Figure 5.17 Internal Acoustic Sensor Signals at the E/H

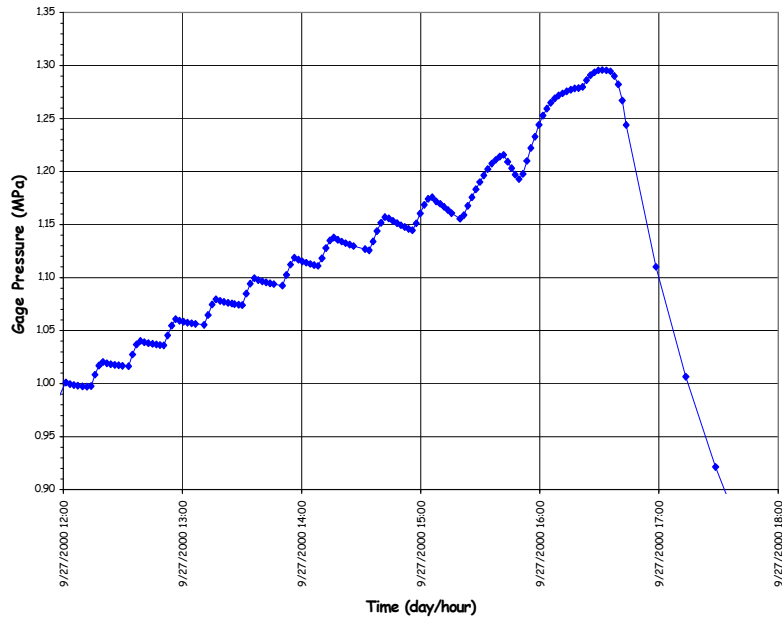


Figure 5.18 LST Pressure Time History, 2.5 to 3.3 Pa

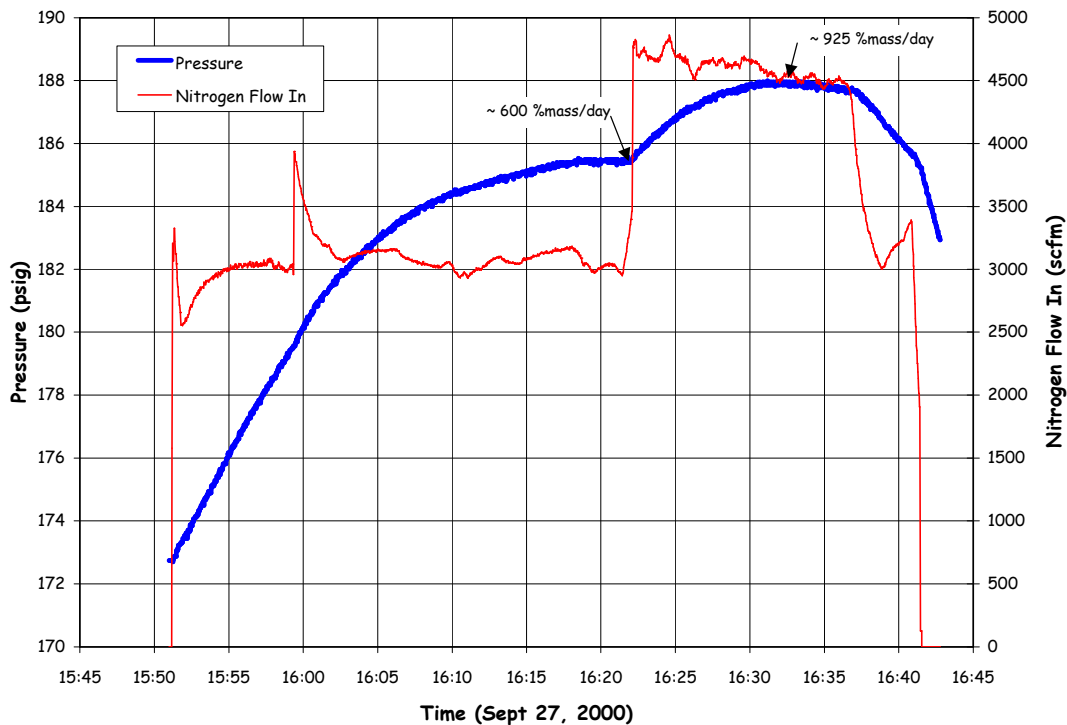


Figure 5.19 LST Pressure and Flow Rates at Maximum Pressure

The PCCV model was pressurized to approximately $3.0P_d$, with increasing evidence of leakage and increasing liner strains. At $3.0P_d$, it became increasingly difficult to pressurize the model, and the nitrogen flow rate was increased to 99 std.m³/min (3500 scfm). At this flow rate, the pressure in the model was increase to $3.1P_d$. However, the pressure dropped steadily after reaching this pressure. The leak rate at this point was estimated to be 100%.

The nitrogen flow rate was increased to the maximum capacity of the pressurization system, 142 std.m³/min (5000 scfm), and the pressure was increased to slightly over $3.3 P_d$ before the leak rate exceeded the capacity of the pressurization system. The pressure time history and flow rates during the final phase of the test are shown in Figures 5.18 and 5.19. Since it was no longer possible to increase the pressure in the model and the supply of nitrogen was nearly exhausted, the TC decided to begin terminating the test.

The isolation valve was closed and the model was allowed to depressurize on its own. The terminal leak rate was estimated to be on the order of 900% mass/day. (The maximum flow rate of nitrogen, 5000 scfm, is equivalent to a leak rate of 1000% mass/day.) Estimated leak rates during the final pressurization and depressurization phases are shown in Figures 5.20 and 5.21.

After the model pressure was reduced to $1.0 P_d$, test personnel were able to inspect the model close-up. Nitrogen gas was observed (heard and felt) escaping through many small cracks in the concrete around the penetration sleeves and at the tendon anchors. It was speculated that the liner acted as a leak chase, allowing nitrogen gas escaping through a tear or tears in the liner to travel between the liner and the concrete until it found an exit path through a crack in the concrete or a conduit in the tendon duct.

At maximum pressure, local liner strains of up to 6.5% were recorded and global hoop strains (computed from the radial displacement) at the mid-height of the cylinder averaged 0.4%. While large liner strains were observed, causing suspicion that the liner might have torn in several locations, the remainder of the structure appeared to suffer very little damage with the exception of more extensive concrete cracking at some locations. The largest crack was observed to the left of the E/H, shown in Figure 5.22. This is the same location as the crack photos shown in Figures 5.10 and 5.11. There was no indication of tendon or rebar failure. The detailed results of the LST are discussed in Section 5.3.2.1.

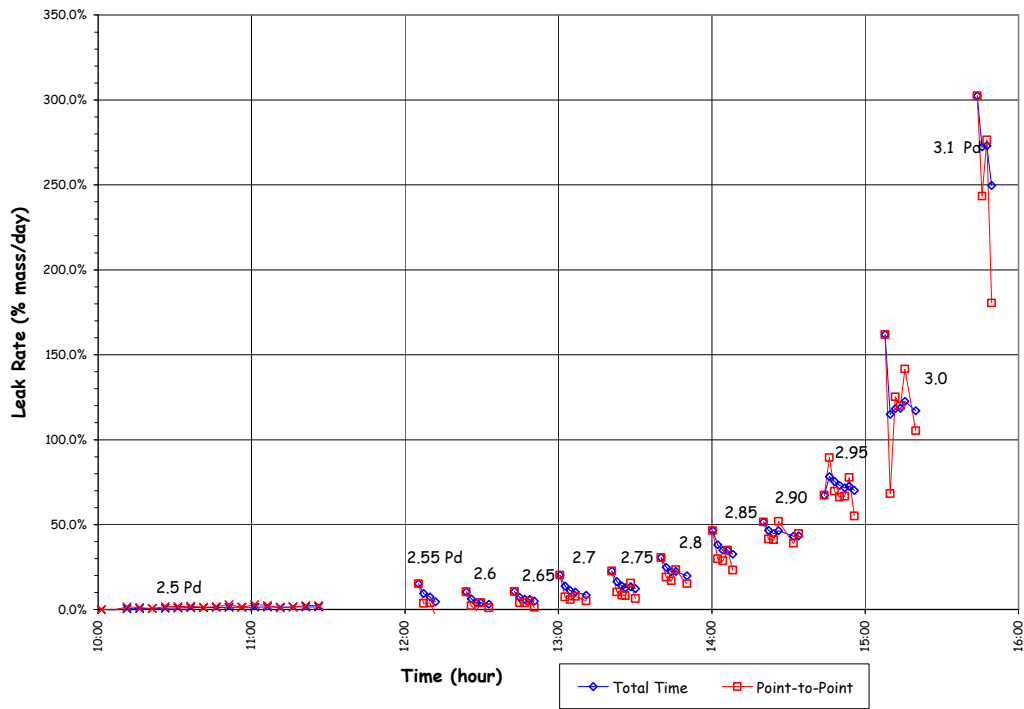


Figure 5-20. LST - Estimated Leak Rates (2.5-3.1 P_d)

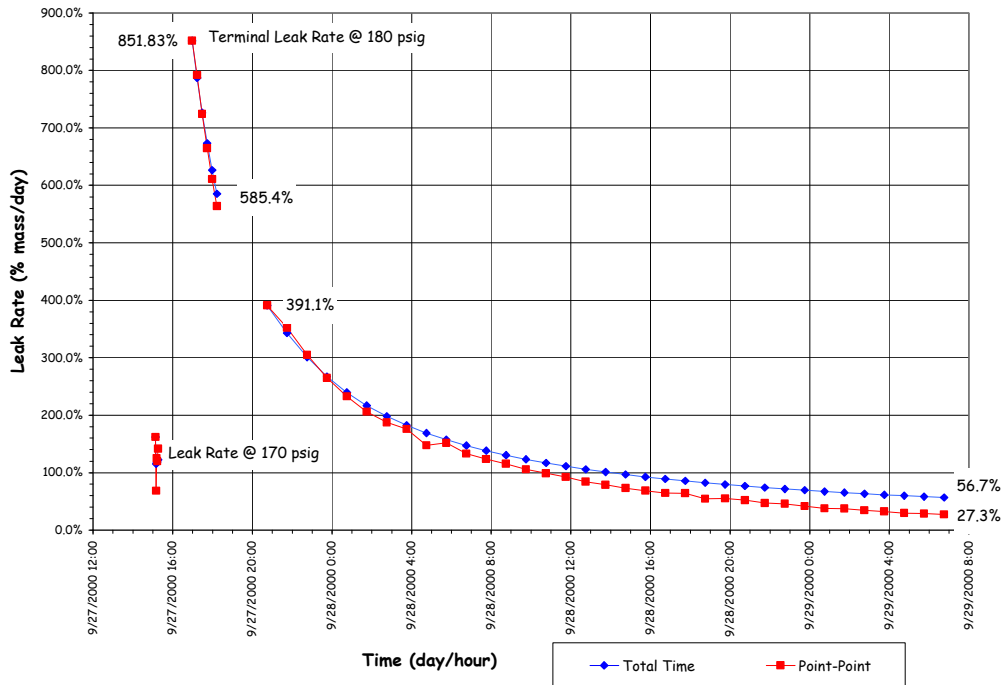


Figure 5.21 LST Estimated Terminal Leak Rates

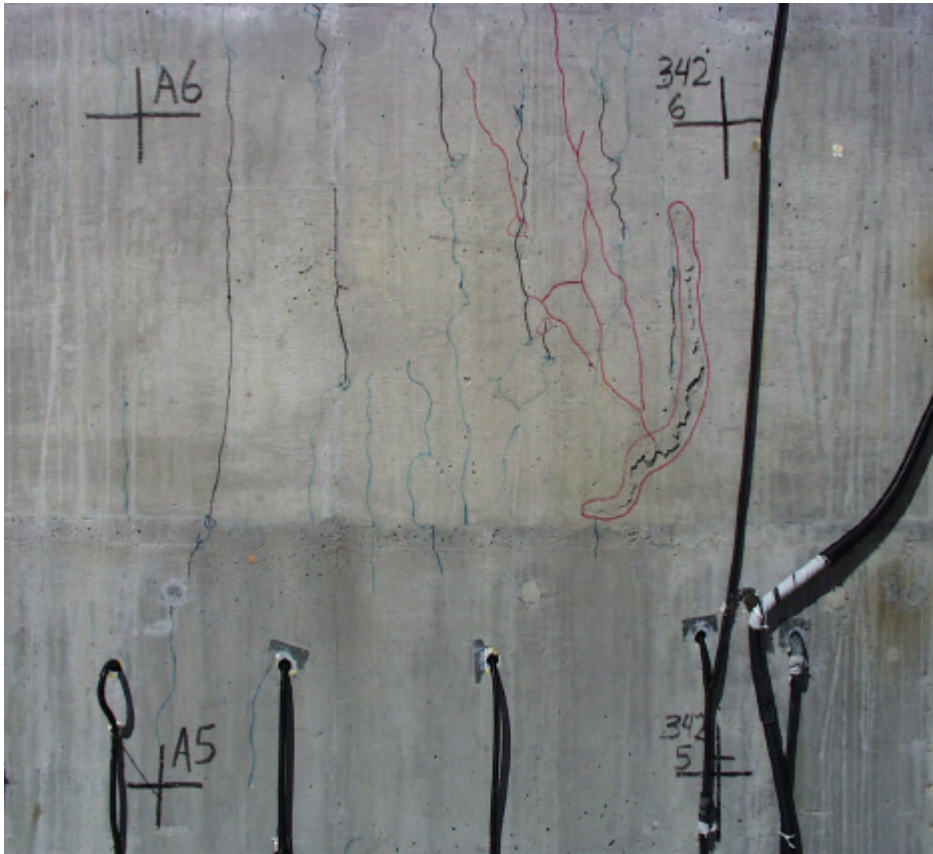


Figure 5.22 Post-LST Cracks at Azimuth 350 degrees, Elev. 4680 to 6200 (Grid 45)

After the model had completely depressurized, it was purged with fresh air, the E/H was removed, and detailed posttest inspection of the inside of the model began. A cursory inspection of the model identified 26 discrete tears at 18 separate locations. A detailed posttest inspection plan was developed, and the results of this inspection are described in Section 5.3.2.1

5.2.4 Structural Failure Mode Test

Almost immediately after the completion of the LST, it was recognized that while the PCCV model had demonstrated its capacity to resist pressures well above the design pressure and confirmed, arguably, liner tearing and leaking as the functional failure mode, the test objectives were not fully met with respect to observing large inelastic deformations for comparison with analyses, and witnessing the structural failure mode of the PCCV model. SNL was tasked by NUPEC and the NRC with investigating the possibility of conducting a second LST.

Two issues needed to be addressed to determine the technical feasibility of reloading the PCCV model. First was the question of whether the LST had caused damage to the structure such that any data obtained by reloading the structure would be compromised and of limited value for comparison with analytical results. The LST data was thoroughly reviewed and, with the exception of the liner and cracking of the concrete, there was no evidence of excessive structural damage. There was also no indication that the tendons had been strained beyond their yield limit and, except for a few isolated measurements, the same was true for the rebar. (Only 27 of the rebar gages registered strains in excess of 0.4% with a maximum of 1.7%—which likely reflects the local perturbation caused by the presence of the gage.) Comparing the radial displacement at the mid-height of the cylinder to the pretest Round Robin predictions in Figure 5.23 clearly illustrates that the structure was on the verge of global yielding but had not undergone a significant amount of inelastic

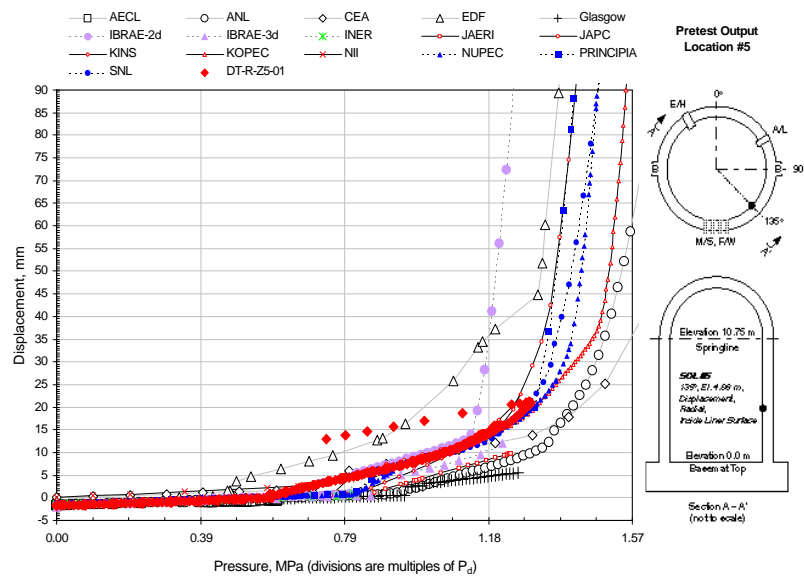


Figure 5.23 LST Radial Displacement at Azimuth 135 degrees, Elev. 4680

deformation. (In this context, only the yielding of the steel and rebar is addressed. Obviously, the loss in stiffness that occurs with global concrete cracking at approximately $1.5P_d$ cannot be recovered.) This was a positive finding for the prospect of reloading the model since most, if not all, of the capacity of the rebar and tendons was still available. Another important conclusion from the consideration of the LST data was that if, in fact, the model was on the verge of global structural yielding, the additional pressure required to cause larger, inelastic deformations was not very large; perhaps only on the order of a few tenths to half the design pressure, i.e. an additional 1.0 to $2.0 \text{ kg}_f/\text{cm}^2$ (14 to 30 psig).

The second issue was the requirement to reseal the model in order to repressurize it. Since large sections of the liner were removed as part of the post-LST inspection, the liner was no longer capable of providing an effective membrane to prevent premature leakage. Furthermore, even if the liner tears and cutouts were locally repaired or sealed, it was clear that other areas of the liner were susceptible to tearing at the same pressures (or perhaps even at lower pressures) that caused the liner to tear during the LST. It was necessary, therefore, to devise a cost-effective method of completely replacing the liner function in order to proceed with plans to repressurize the PCCV. The replacement 'liner' was also required to ensure that the model could be repressurized to a level beyond the maximum pressure achieved during the LST. (A corollary of this conclusion was that there was no further need to investigate the response of the liner, and the instrumentation applied to the liner could be abandoned.)

Furthermore, the SFMT had to be completed within the current program budget and schedule. The concept developed to repressurize the PCCV model is illustrated in Figure 5.24.

The concept consists of sealing the interior surface of the liner with an elastomeric membrane after removing all interior transducers on the liner. After closing the E/H and A/L, the model would be filled with water to 1.5 m ($5'$) from the dome apex, approximately 97% of the interior volume $1,591,000 \text{ ltr}$ ($350,000 \text{ gal}$). Filling the model with water would provide several advantages:

1. The leak rate of water through any tears in the liner is much less than the corresponding leak rate of gas. Therefore, even if a leak path developed, the flow rate capacity of the pressurization system should be adequate to compensate for the leak.
2. By maintaining a gas pocket in the model, the pressurization system used for the LST, with nitrogen gas as the pressurization medium, could be used for the SFMT without any major modifications. The only modification required would be installing additional piping inside the model to allow the gas to be introduced at the dome apex and to fill (and drain, if necessary) the model. Reducing the volume of gas to be pressurized lowered the demand on the pressurization system in the event of a leak, as well as the volume of gas required to conduct the test. In the

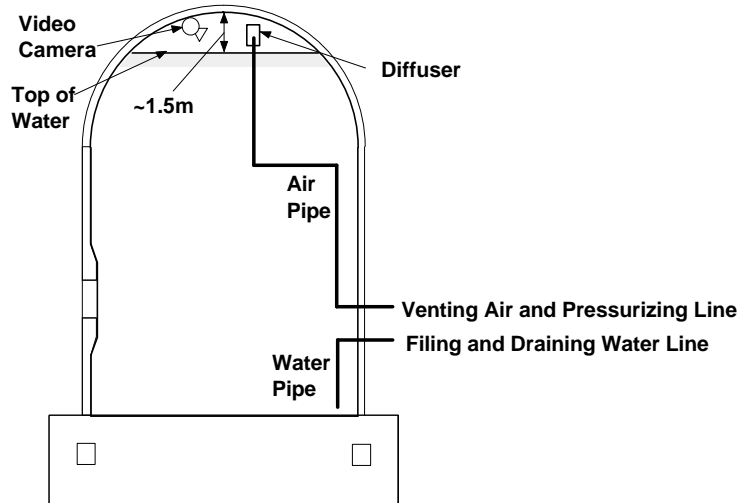


Figure 5.24 PCCV Structural Failure Mode Test Concept

case of the SFMT, a pressurized tube trailer could be used instead of the more expensive liquid nitrogen source required for the LST.

3. Since the pressurization system could compensate for small leaks, it is not essential that the elastomeric liner be completely leak-tight, only that the leaks would be small enough to allow the model to be pressurized to the desired level.
4. Water leaks would be readily visible, compared to gas leaks.
5. In the event of a catastrophic PCCV model rupture, the energy stored in the model nearly filled with water is much less than the stored energy if pressurized to the same level with gas. As a result, the safety exclusion zone around the model could be reduced, if necessary.

At the same time, filling the model with water would have some disadvantages:

1. Any instruments or other electrically-powered components (lights, cameras, etc.) inside the model would have to be removed or completely sealed.
2. The internal pressure would not be uniform due to the hydrostatic head, approximately 1.4 kg_f/cm² (20 psig).

These disadvantages, however, were not deemed significant, and efforts focused on selection of a suitable liner. A number of vendors were contacted, and two proposals for sealing the liner were considered. One proposal was to prefabricate a 5 mm (200 mil) PVC sheet liner, which would be installed inside the model by heat welding the seams and sealing around the penetrations using ring clamps. The second proposal was to spray on a two-part polyurea coating, also a minimum of 5 mm (200 mil) thick. After considering both proposals, the sprayed-on lining was selected since it could be more readily adapted to the irregular liner surface and had significant cost and schedule advantages. The elastomeric liner was installed by Ershigs Corporation³¹ in August, 2001 after the interior model inspection was completed and all the surface instrumentation was removed. The application of a test sprayed-on liner is shown in Figure 5.25.

After the elastomeric liner was installed, the interior instrumentation for the SFMT was installed. A reduced set of instruments was selected, allowing one data acquisition computer to scan all the gages in less than 60 seconds to support 'rapid' pressurization of the model. The instrumentation suite for the SFMT consisted of the following (A complete list of all the SFMT gages is provided in Appendix H):

³¹ Ershigs, 742 Marine Drive, PO Box 1707, Bellingham, WA 98277, (<http://www.ershigs.com/>)

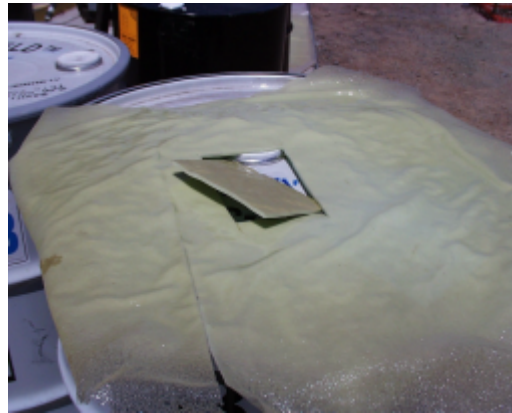


Figure 5-25. Test Specimen of Elastomeric Lining

1. All interior gages used for the LST were removed or abandoned. These were replaced by 20 waterproof LVDTs, 17 radial and three vertical, located as shown in Figure 5.26.
2. Five interior pressure transducers, three below water at the base, cylinder mid-height, and springline, and two to measure the gas pressure.
3. Two interior video cameras and lights to monitor the E/H and the water surface.
4. 18 exterior liner strain gages
 - a. 14 at meridional at wall-base junction
 - b. Four at hoop stiffener details
5. 82 rebar strain gages (Standard Output Locations (SOLs)).
 - a. 35 rebar gages (all 22 SOL plus 13 meridional at wall-base junction)
 - b. 47 gage bars (all surviving)
6. All surviving tendon strain gages and all load cells.
7. Soundprint® acoustic monitoring (external sensors only).
8. Concrete strain (six SOFO gages).
9. Four external digital video cameras at 0 degrees, 90 degrees, 270 degrees, and 360 degrees, completely covering the PCCV cylinder wall.

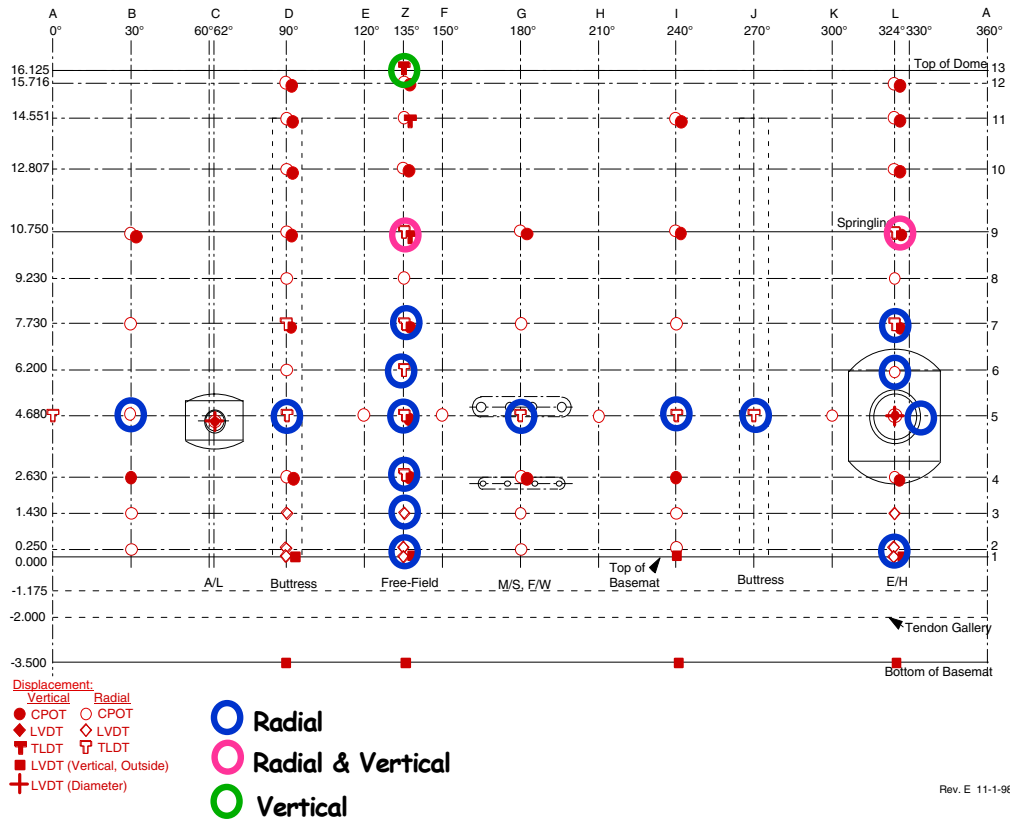


Figure 5.26 SFMT Displacement Transducer Layout

After completing the installation and all test-readiness checks, the E/H cover was installed and sealed. A low pressure pneumatic test was conducted to check for leaks on October 3, 2001. The pressure and temperature time histories for the leak test are shown in Figure 5.27. The leak test began at approximately 09:30 and a leak was detected (via the acoustic system) at approximately 0.2 Pd (~12 psig). Pressure was increased to the target pressure of 0.5Pd (30 psig), at which time the vessel was isolated and monitored for a 24-hour leak test. The acoustic system (multiple sensors) continued to output signals consistent with a leak in the model and several potential leak locations were identified.

Once the model was deemed stable, the nitrogen supply was isolated and a close inspection of the model was conducted. Through a combination of visual/auditory inspection, hand-held acoustic monitoring, and the application of soap-water solution, a number of locations were discovered where nitrogen gas was leaking from the model.

- The largest apparent leak was from a crack on the left-hand side of the 90-degree buttruss at an elevation of approximately 6 m (20') above the top of the basemat (Level 6 in the cardinal coordinate system). This leak was the first detected by the acoustic system and was immediately confirmed during the close-up inspection.
- Secondary leaks, identified by the acoustic system, were confirmed at 150 degrees/3 and 6 m (10 and 20') and 210 degrees/4.5 m (15'). These leaks appeared to be through previously existing cracks in the concrete. The leak at 150 degrees was along the horizontal construction joints between C1, C2, and C3 as well as along a vertical crack extending between C2 and C3. The leak at 210 degrees also appeared to be through a previous crack.
- The acoustic system also suggested leaks at 300 degrees/1 to 2 m (3 to 6-1/2') and 360 degrees/0 m, but close-up examination could not confirm leakage at either location.
- During the close-up inspection, a leak was also detected at 30 degrees/5 m (16') which was not initially identified by the acoustic system.
- Close-up inspection of the penetrations also revealed leakage at the F/W penetrations. There was no evidence of leakage at the E/H, A/L, or M/S penetrations.

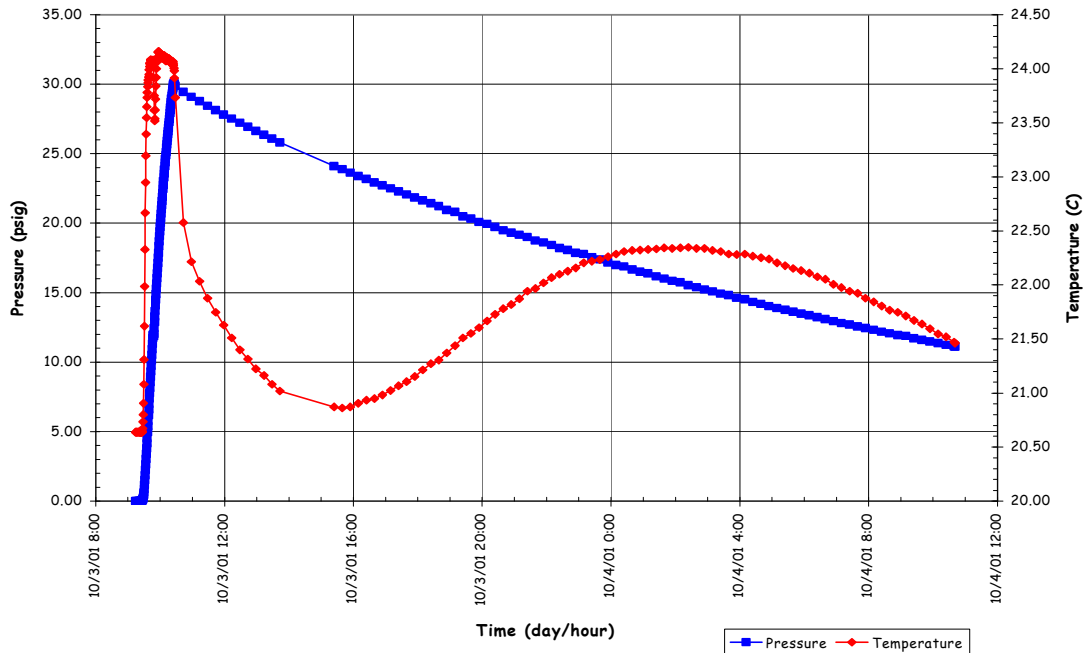


Figure 5.27 Pre-SFMT Leak Test Pressure and Temperature

These results indicated that, in spite of the manufacturer's quality control procedures coupled with detailed visual inspection (individual locations that appeared suspect were also sealed with silicone sealant prior to closing the model), the sprayed-on liner was not impermeable. Once the gas escaped through the sprayed-on and steel liners, it migrated between the steel and concrete until it found an exit path. The pressure did not appear high enough to tear the sprayed-on liner when a leak was first detected.

The calculated leak rate, shown in Figure 5.28, was initially 70% mass/day at the maximum pressure of 2.1 kg_f/cm² (psi) decaying to 45% at 0.77 kg_f/cm² (11 psi) over 24 hours. The sound levels as detected by the SoundPrint system (shown in Figure 5.29), which are roughly proportional to the rate of gas escaping, indicated a stable leak rate that was, to a large extent, independent of the pressure.

Based on these results, it was concluded that the leak was most likely due to a pre-existing hole(s) in the sprayed on liner which did not increase (or decrease) significantly during pressurization or during the leak test. (The equivalent orifice size reduced from about 6 mm (0.25") at 2.1 kg_f/cm² (30 psi) to 5 mm (0.20") at 0.8 kg_f/cm² (12 psi), based on the calculated leak rates.) As a result, the SFMT could be conducted without repairing the sprayed-on liner while maintaining a reasonable chance that the leak would not grow significantly and overwhelm the capacity of the pressurization system. (Nevertheless, during an unscheduled one-month postponement of the SFMT, the surface was retested with a 'spark-tester,' and a few small holes were discovered and sealed. The model was then resealed and readied for filling with water.)

Filling the PCCV with water and the SFMT began at approximately 09:00 November 6, after the initial data scan was taken, and continued until November 8, 2001. Slow water leaks were initially observed late November 6, after the model was about one-quarter full, however, the amount of water leaking was insignificant. The pressure time histories at various elevations in the model from the start of filling to the SFMT are shown in Figure 5.30. This figure illustrates the hydrostatic head and also reflects the slight loss of water due to leaks. The water level was 'topped off' on November 12, prior to the start of the SFMT.

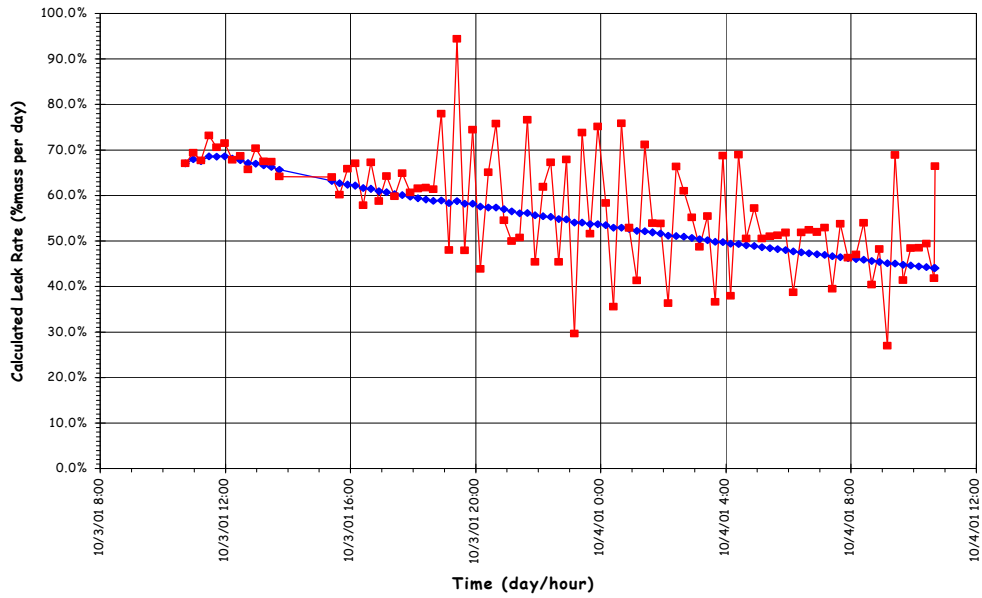


Figure 5.28 Pre-SFMT Leak Rate Test

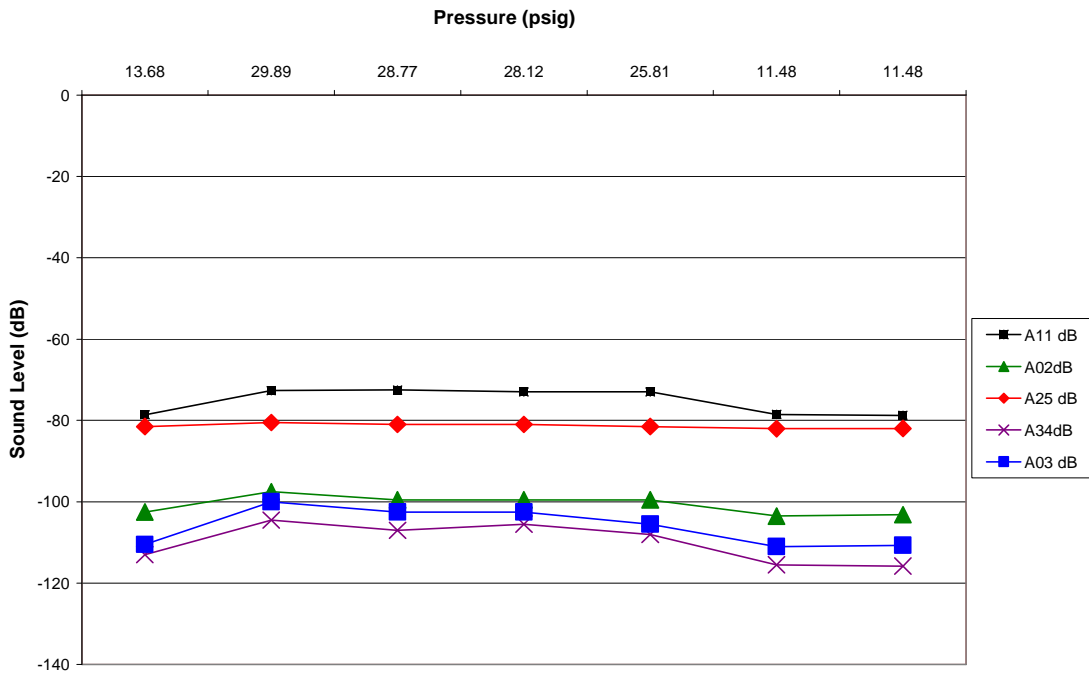


Figure 5.29 Pre-SFMT Leak Test Acoustic Data

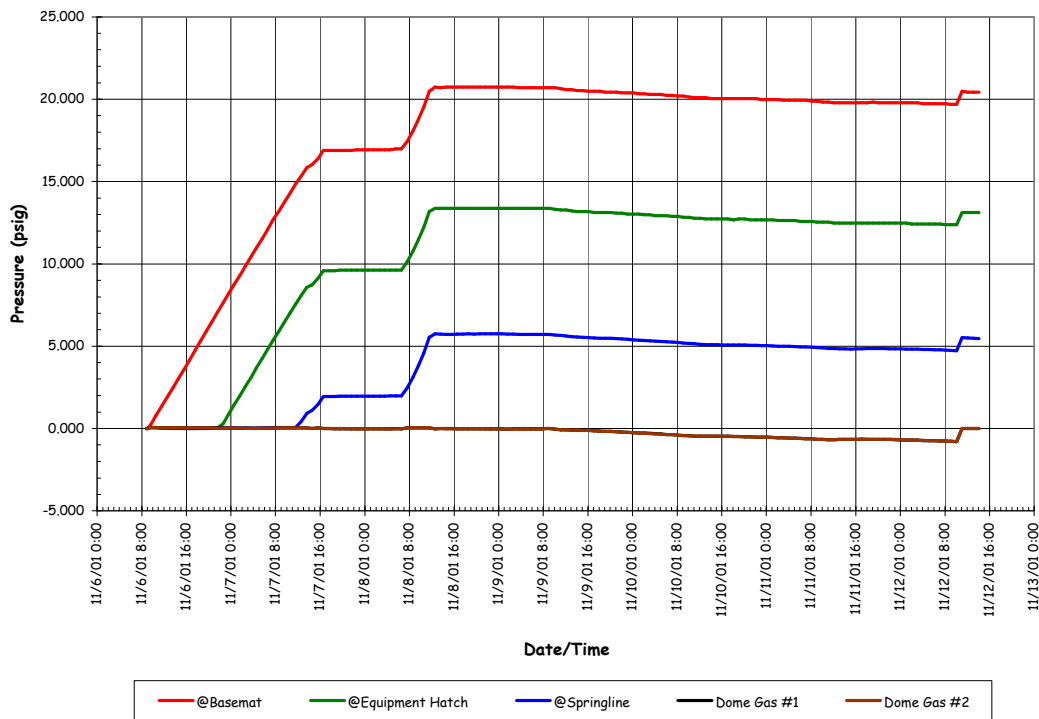


Figure 5.30 Pre-SFMT Hydrostatic Pressures

The test sequence planned for the SFMT was to rapidly pressurize the model using nitrogen gas to compensate for the known leaks in the model. The minimum flow rate capacity of pressurization system, 14 std.m³/min (500 scfm), would increase pressure in the reduced void space at a rate of about 0.35 kg_f/cm² (5 psi) every minute. At this rate, the model could be pressurized to failure in less than an hour.

The SFMT began shortly after 10:00 AM on Wednesday, November 14, 2001. The pressure time histories are shown in Figure 5.31. The pressure time history of all five gages are shown along with the effective model pressure, which is calculated as a volume-weighted average. Any references to the SFMT pressures are to the effective pressure, unless noted otherwise.

The model was continuously pressurized at a rate of approximately 0.35 kg_f/cm² (5psi)/min. All active sensors were continuously scanned at intervals of approximately 30 seconds and the video cameras continuously recorded the response of the model. As the pressure increased, evidence of leakage was visible as increasing wetting of the concrete surface. At 10:38 AM, the effective pressure in the model equaled the peak pressure achieved during the LST, 3.3 Pd (1.29 MPa or 188 psig). At approximately 10:39 AM, the acoustic system recorded a very high noise level event, which was interpreted as the breaking of a tendon wire. At this point in the test, events occurred very quickly. Shortly after detecting the wire break, a small spray of water was observed at approximately 0 degrees Azimuth and additional tendon wire breaks were detected by the acoustic system with increasing frequency. The wire break events are plotted in Figure 5.32, along with the effective pressure and the radial displacement at Azimuth L (324 degrees), elev. 6 (6280), as a function of time.

The rate of pressurization decreased and the nitrogen flow rate was increased to maintain the pressurization rate. The gas pressure and flow rates are shown in Figure 5.33. The water surface inside the model, viewed through the internal video camera, was dropping slowly, but it was unclear if this was due to leakage or radial expansion of the vessel.

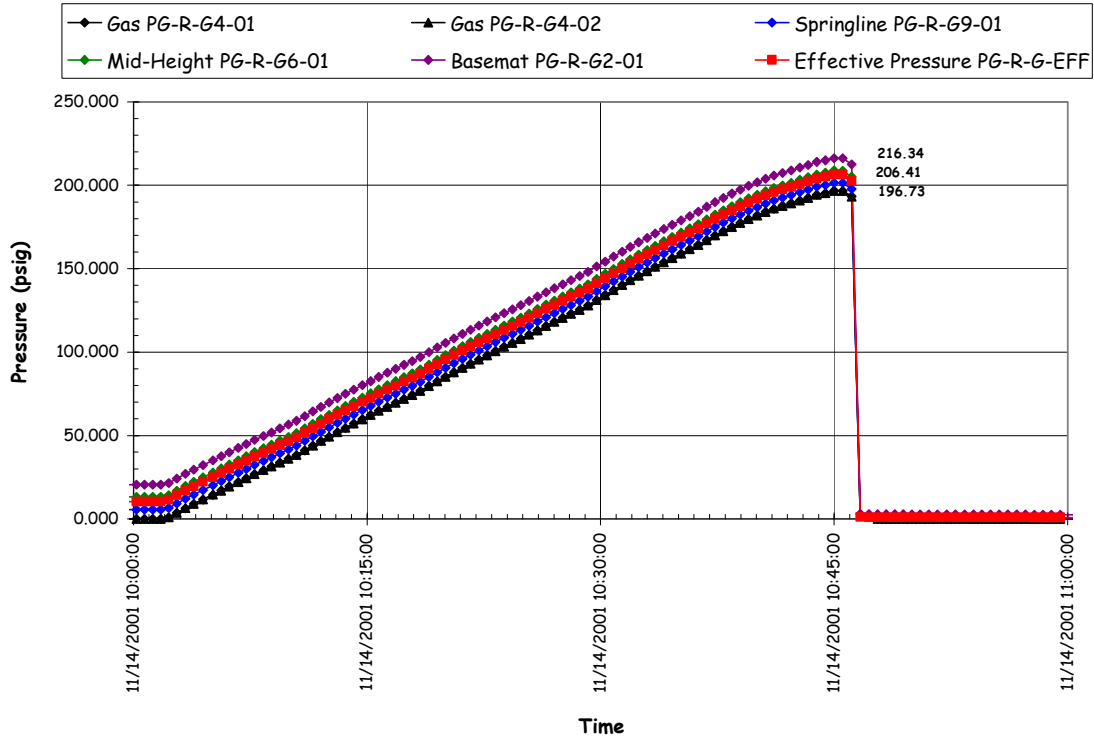


Figure 5.31 SFMT Pressure Time Histories

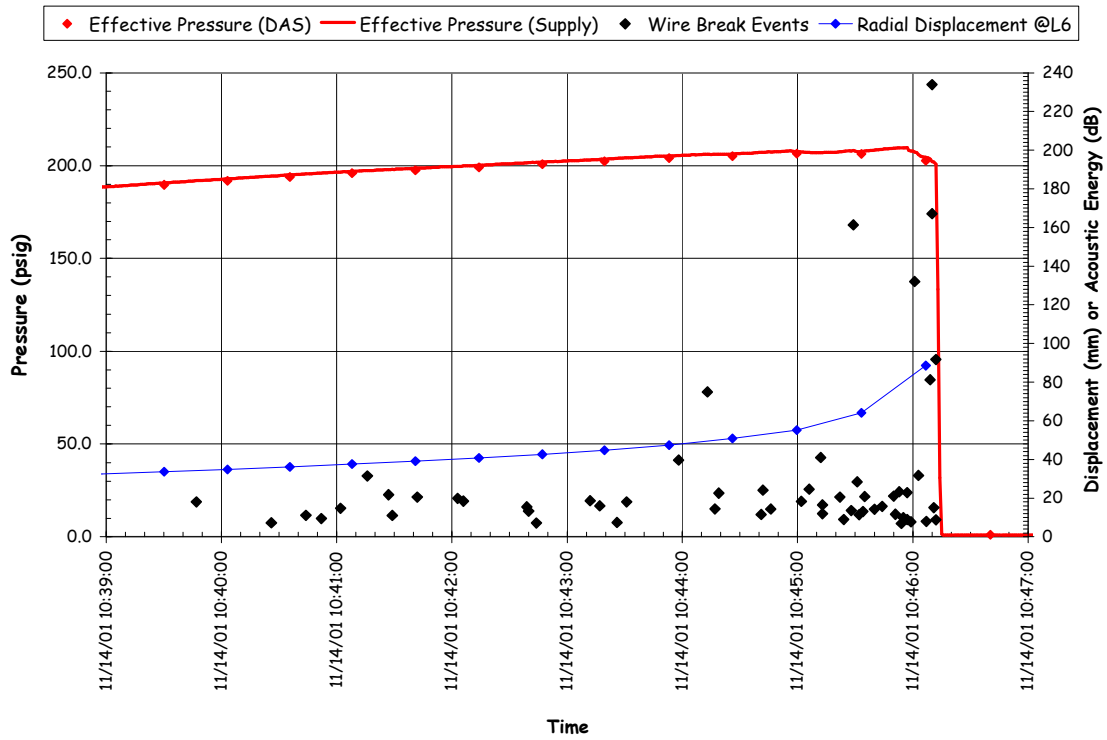


Figure 5.32 SFMT Wire Break Events vs. Pressure vs. Displacement

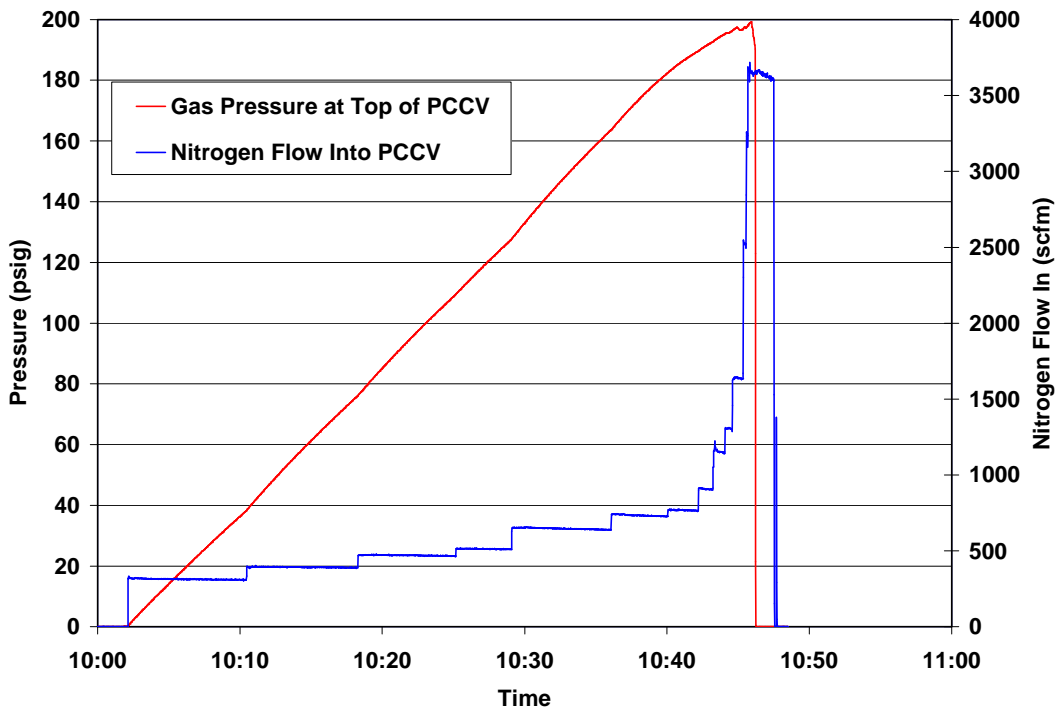


Figure 5.33 SFMT Pressurization System Data

Pressurization of the model continued until a second spray of water was observed and suddenly, at 10:46:12.3, at an effective pressure of $3.63 P_d$ (1.42 MPa or 206.4 psig), the PCCV model ruptured violently at ~ 6 degrees azimuth near the mid-height of the cylinder. The rupture propagated vertically in both directions and then radiated circumferentially about 2 m above the top of the basemat, shearing off the cylinder wall. The dome and cylinder wall then came to rest on the instrumentation frame, which apparently prevented the model from toppling over. The entire collapse was over in slightly more than one second. The entire SFMT, including the sequence of rupture and collapse, was recorded by the digital video cameras. A short movie (.mpg) file showing the rupture of the model is included on the enclosed data CD. The moment of rupture is shown from all four angles in Figure 5.34. The video recorded failure of the tendons, including ejection of tendon anchors. The condition of the model after the SFMT is shown in Figure 5.35.

The detailed results of the SFMT are discussed in Section 5.3.3, along with observations from the posttest inspection of the model. In the case of the SFMT, posttest inspection was limited to visual inspection due to the obvious damage and restricted access for safety.

Because of program schedule constraints, demolition of the PCCV model commenced in December, 2001 and was completed in April, 2002. During this period, attempts were made to further inspect the model and characterize the damage caused by the SFMT. However, these efforts were of limited value due to the difficulty of discriminating the damage caused during the SFMT from the demolition process. A few specimens from the model were retrieved, however, more for sentimental value than for providing any further technical insight into the behavior of the model.

5.3 Test Results

5.3.1 Data Files

The response of the model was continuously recorded beginning March 3, 2000, prior to prestressing, through October 11, 2000, following the LST. Additional data was recorded using a modified instrumentation suite from November 6 to 14, 2001 for the SFMT. Data for each set of transducers was saved in individual files and a data management and file



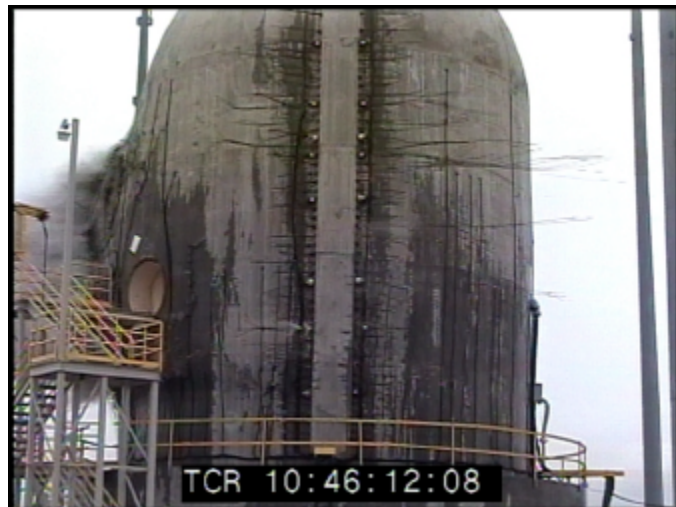
(a) 0 degrees Azimuth



(b) 90 degrees Azimuth



(a) 180 degrees Azimuth



(b) 270 degrees Azimuth

Figure 5.34 SFMT: Rupture of the PCCV Model



Figure 5.35 PCCV Model after the SFMT

naming scheme was developed to facilitate access and utilization of the data. A summary of the data file structure is shown in Figure 5.36.

The basic data was recorded as the output voltage (strain for strain gages, °C for temperature sensors) for each instrument at discrete time steps. This basic data is referred to as the raw, dynamic data. Note that the time reported in the data files is the DAS clock time at the start of a data scan. Since it took up to two minutes to complete a data scan (one minute for the SFMT), the actual time the data was recorded may be up to two minutes later than the recorded time. For pseudo-static loading, this is not a significant issue, but it may have some effect on the response recorded near the end of the LST and SFMT. The raw data is stored as ASCII, tab-delimited text files (.dat)

The raw, DOR is a subset of the raw, dynamic data. The concept of the DOR was defined to facilitate comparison of the data with analysis results. Typically, the analysis results are described as a function of pressure. The DOR is intended to provide a single, stable response value at each pressure step. The DOR were recorded separately from the dynamic data when the gage stability criteria (Eq. 5.1) was met, or at the direction of the test conductor.

The concept of dynamic and DOR data is illustrated in Figure 5.37. In this figure, the dynamic data during and after the LST is plotted along with the DOR for the radial displacement at the cylinder mid-height at 135 degrees. At lower pressures, the data are essentially identical; however, at higher pressures, the drift due to model creep and/or leakage is apparent. Furthermore, the DOR set does not capture the maximum pressure. In subsequent discussions of the DOR, the response at the maximum pressure from the dynamic data has been appended to the DOR for completeness.

Due to the extended length of time over which the data was recorded, the raw data files were separated into individual files by time periods. These periods were chosen to correspond with distinct loading periods, as shown in Figure 5.36. The acronyms for each period were used in the file naming scheme. The full response time history (from March 3 to October 11) for any transducer can be reconstructed by combining the data from the individual files, as illustrated in Figure 5.38 for the radial displacement at the cylinder mid-height at 135 degrees. Gaps in the data represent times when the DAS was shut down for maintenance or when temporary malfunctions (e.g. loss of power, etc.) corrupted the data. Times when the corrupted data was removed from the files are duly noted in the Excel® spreadsheets.

	Before Prestressing	Prestressing	Post Prestressing	System Functionality Test	DAS SHUTDOWN FOR MAINTENANCE	Post SFT	SIT/ILRT	Post SIT/ILRT	Limit State Test	Post LST	Structural Failure Mode Test
	Start	3/3/00	3/10/00	5/5/00		7/18/00	8/7/00	9/12/00	9/14/00	9/26/00	9/27/00
	End	3/9/00	5/5/00	7/18/00	7/21/00	9/11/00	9/14/00	9/26/00	9/27/00	10/11/00	11/14/01
		BPS	PS	PPS	SFT	PSFT	SITILRT	PSITILRT	LST	PLST	SFMT
RAW		DYNAMIC	DYNAMIC	DYNAMIC	DYNAMIC	DYNAMIC	DYNAMIC	DYNAMIC	DYNAMIC	DYNAMIC	DYNAMIC
		*.dat	*.dat	*.dat	*.dat	*.dat	*.dat	*.dat	*.dat	*.dat	*.dat
		DOR	DOR		DOR		DOR		DOR		
CONVERTED		*.dat	*.dat		*.dat		*.dat		*.dat		*.dat
		*.xls	*.xls		*.xls		*.xls		*.xls		*.xls
		DOR	DOR		DOR		DOR		DOR		
		*.dat	*.dat		*.dat		*.dat		*.dat		
		*.xls	*.xls		*.xls		*.xls		*.xls		
CORRECTED									DYNAMIC		
									*.xls		
									DOR		
								*.xls			

Figure 5.36 PCCV Test Data File Matrix

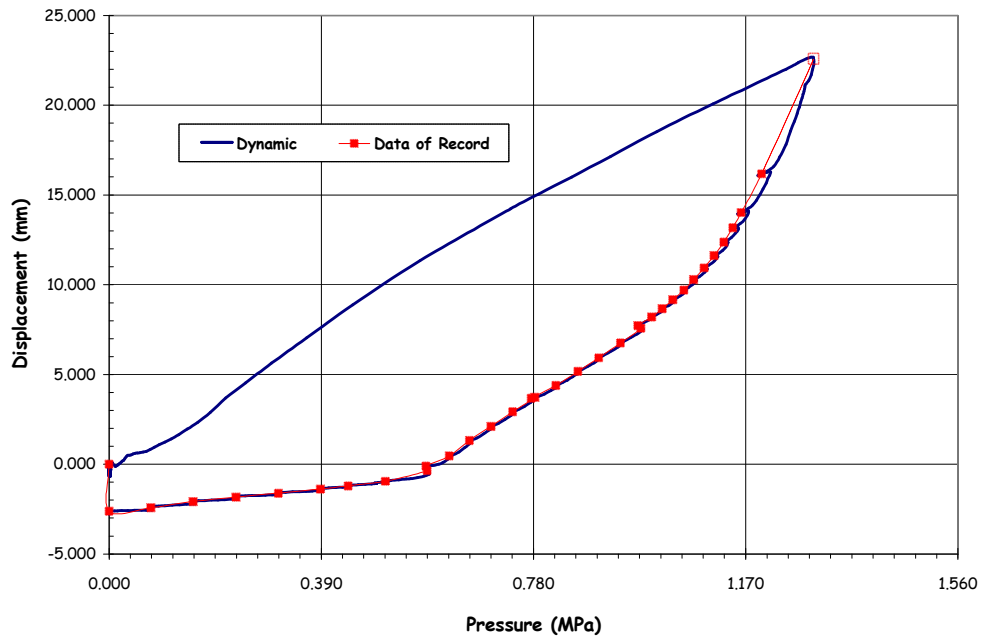


Figure 5.37 Radial Displacement at Azimuth 135 degrees, Elev. 6200

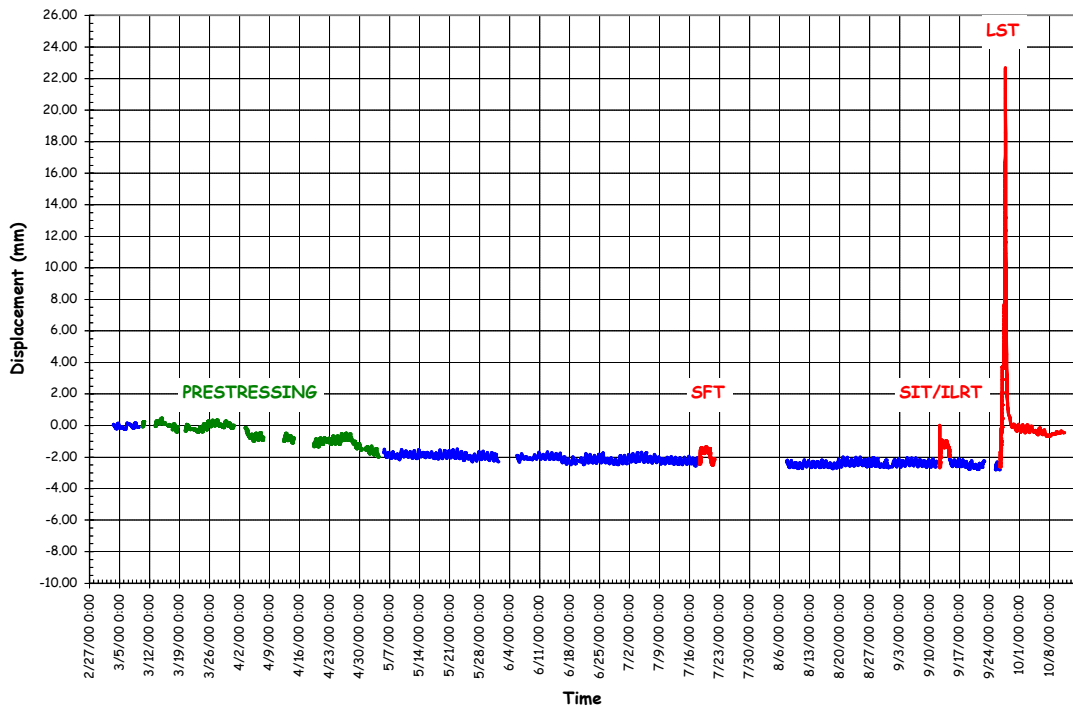


Figure 5.38 Radial Displacement History at Azimuth 135 degrees, Elev. 6200 (DT-R-Z6-01)

After the raw data was stored, it was converted using utility programs constructed as part of the DAS software. The conversion process was described in Chapter 4 and consisted of applying gage specific-gage factors (GFAC) obtained from the manufacturer or from gage calibration test data, correcting for actual gage power supply voltages. This converted data (CONV) was also stored as ASCII, tab-delimited text files (.dat) for each type of gage and loading period.

To simplify access to the data, the converted data files were further reorganized and stored in Microsoft Excel[®] spreadsheet format (.xls). The data files were grouped by response variable type according to the scheme shown in Table 5.3. Each data file was further subdivided by grouping similar gages on separate worksheets, as shown. Units for each response variable/gage are also shown. The converted data files in Excel[®] format are provided with this report on a CD. Appendix I provides a complete list of the data files on the disk. The format of each data file consists of the time (at the start of the data scan) in the first column followed by the response for each of the gages, identified by gage name in the following columns. The Excel[®] data files were also modified to add the average pressure at each time step where appropriate, (i.e., for the pressure tests), the nominal azimuth, elevation, and, in some cases, radius of the gage, and additional information (such as references to an instrumentation drawing detail or tendon number), where applicable.

The data file naming scheme consists of

- the gage type acronym,
- the data type acronym,
- a designation for dynamic (DYN) or DOR, and
- the loading period acronym.

For example, the file:

DISP_CVTD_DYN_LST.xls

contains the converted (CVTD) DYN displacement (DISP) during the LST in Excel[®] format (.xls).

One final set of data files, corrected data (COR), is also provided. The model was exposed to variations in ambient temperature, both temporal (day/night, seasonal) and spatial (due to direct solar heating), and responded accordingly. Since the converted test data includes the response to ambient thermal conditions, as well as prestressing and pressure loads, and the analyses, typically, do not, an attempt was made to correct the test data and 'remove' the effect of the temperature transient. This correction is described in Appendix J and was only applied to the LST data files.

In addition to the basic data files described above, additional data was collected by the pressurization system, acoustic system, and from visual observation and photographic (still and video records). This data is described in the following sections.

5.3.2 Limit State Test Results

5.3.2.1 Test Data

The LST data (DYN and DOR) is provided on the enclosed data CD in Excel[®] spreadsheets, as noted in Section 5.3.1. The response of every functioning transducer is provided. The following sections present a synthesis of the data focusing on the critical response measurements.

5.2.3.1.1 Displacements

The displacement data provides the most comprehensive view of the overall or global response of the model. Figures 5.39 through 5.42 show the displacement response as a function of pressure at various azimuths and elevations.

Table 5.3 Data File (Excel®) Format

Gage Type	Gage Type Acronym	Worksheet Label
Displacements	DISP	Unit: millimeters
		Radial
		Meridional
		Hatches
		Instrumentation Frame
Gage Bar Strains	GBST	Unit: strain
		Wall-Base 90 deg
		Wall-Base 135 deg
		Wall-Base 350 deg
		Above Tendon Gallery
Liner Strains	LINST	Unit: strain
		Free-Field Hoop
		Free-Field Merid
		Free-Field Merid Anchors
		E-H Details
		A-L Details
		M-S Details
		F-W Details
		Wall-Base
		Misc Details
Pressure	PRES	Unit: MegaPascal
Rebar Strain	REBST	Unit: strain
		Free-Field Hoop
		Free-Field Merid
		Free-Field Radial Bar
		Basemat
		E-H Bars
		A-L Bars
Temperature	TEMP	Unit: °Celsius
		Inside Air (includes outside air temperature)
		Inside Liner
		Embedded Concrete
Tendons	TENDON	Unit: Newtons/strain
		Load Cells (grouped by tendon)
		Tensmegs (grouped by tendon)
		Strain Gages (grouped by tendon)
Concrete Strain*	SOFO*	Unit: strain

*Concrete strains by SOFO gages were only measured during prestressing and pressure tests.

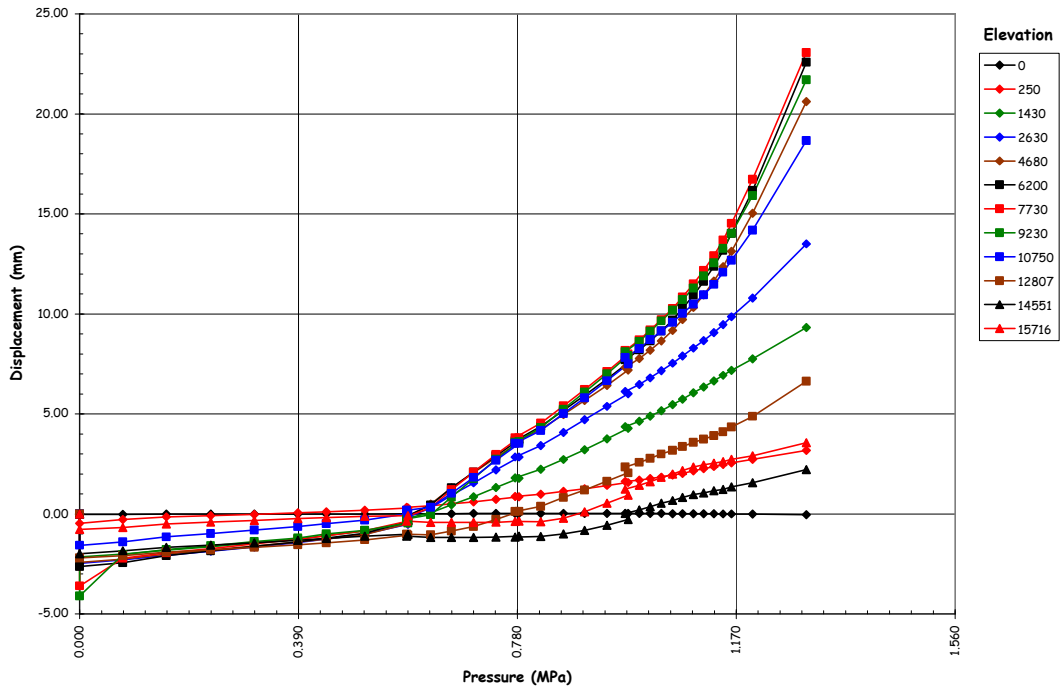


Figure 5.39 LST - Radial Displacement at Azimuth 135 degrees

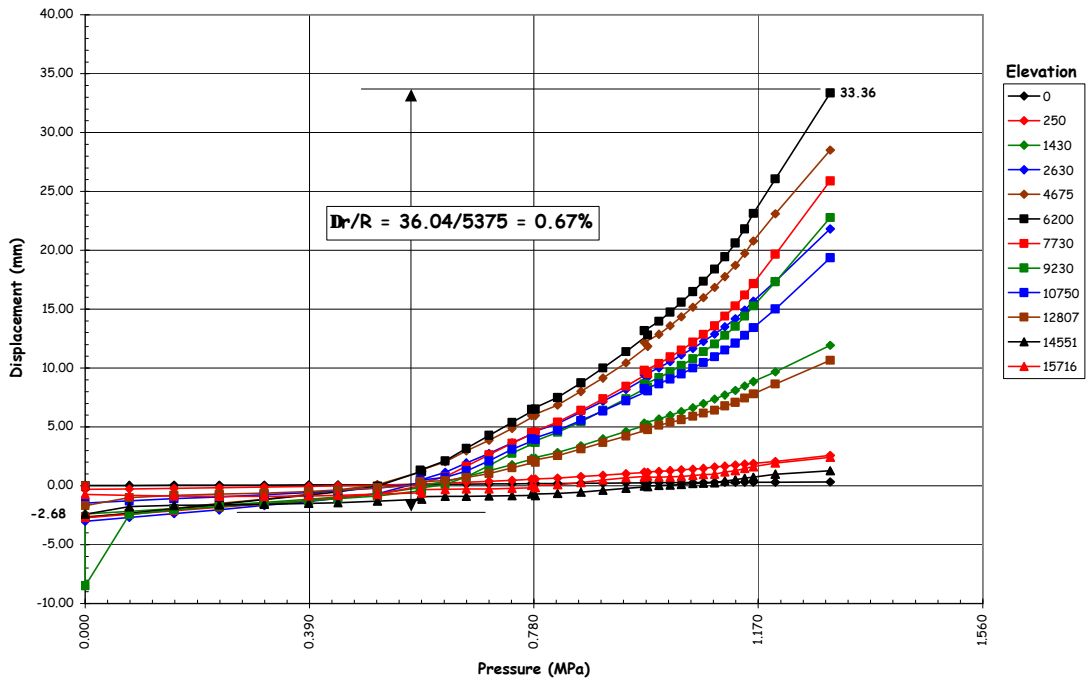


Figure 5.40 LST - Radial Displacement at Azimuth 324 degrees

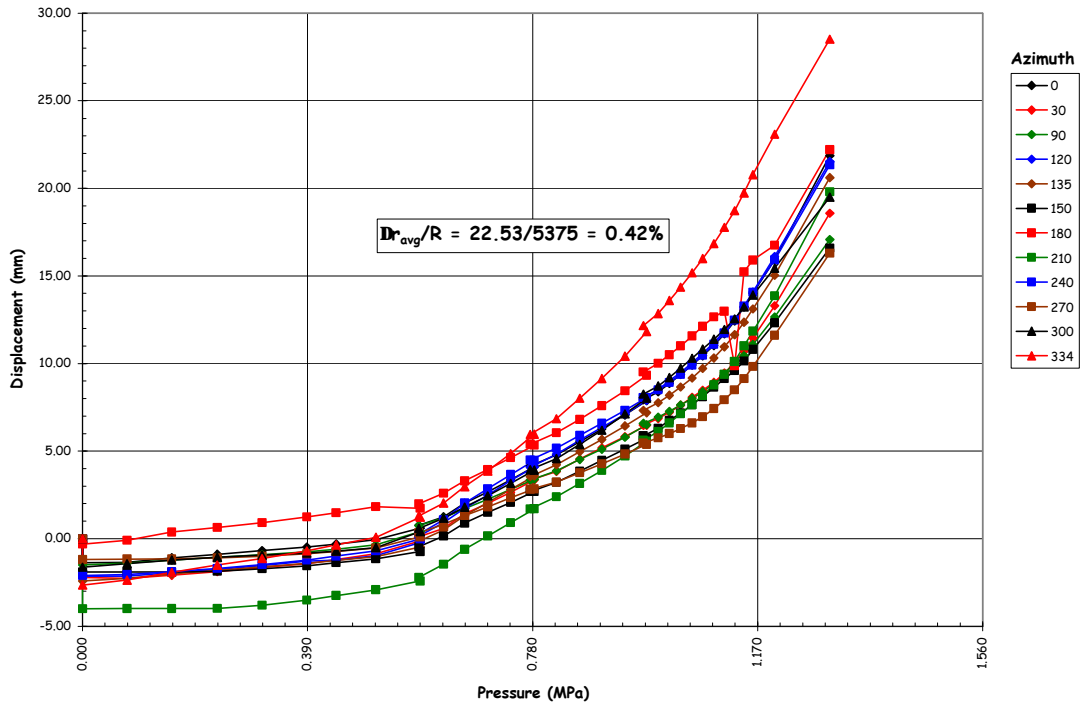


Figure 5.41 LST-Radial Displacement (DOR) at EL 4680

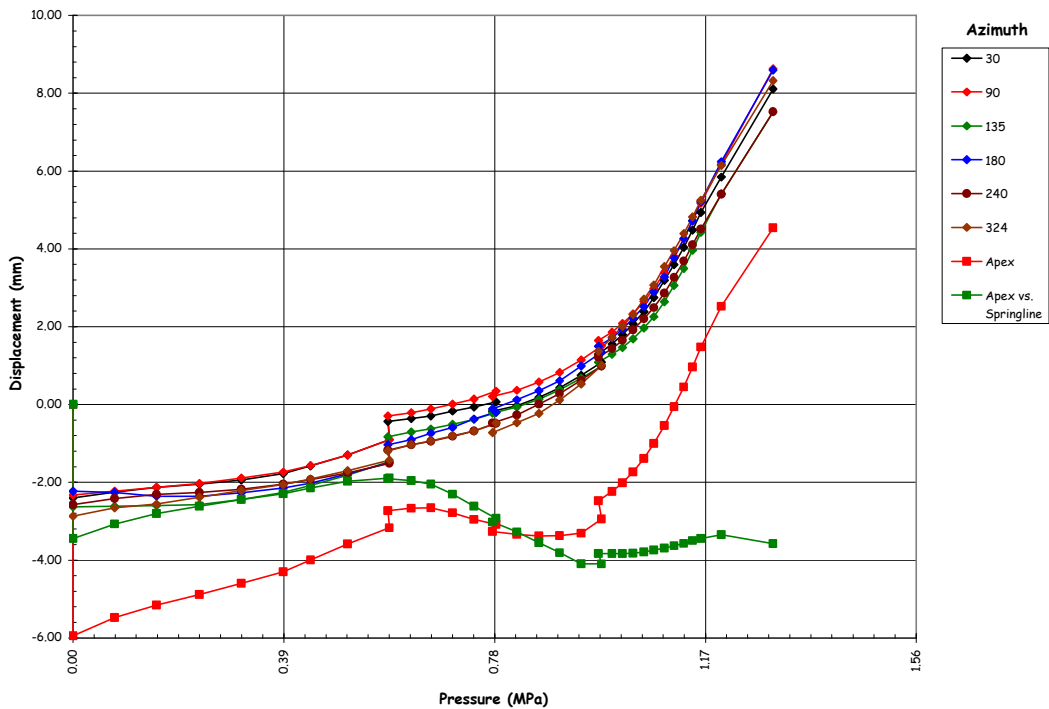


Figure 5.42 LST-Vertical Displacements (DOR) at Springline, El. 10750

The radial displacement of the model at the cardinal elevations along Azimuth 135 degrees, selected to represent the ‘free-field’ or axisymmetric response of the model, is shown in Figure 5.39. This plot illustrates several features of the response data that should be noted. The initial values (i.e. at P=0) reflect the inside surface motion of the liner between March 3rd and the start of the LST, thereby reflecting the influence of prestressing, changes in ambient temperature, creep, etc. The response due to pressure alone is the reported displacement minus the displacement at the start of the LST (i.e., at P=0 on 10:03 a.m., 26 September, 2000).

The initial data also suggests that the liner most likely separated from the concrete wall at some locations, as evidenced by the relatively large displacements that occurred during the first pressure step. At these locations, the first increment of pressure ‘pushed’ the liner back into contact with the concrete surface. This behavior can also be observed in the SFT and SIT/ILRT data, including a restoration of the gap after depressurization. The liner separation is most likely a result of differential thermal expansion and prestressing, resulting in compressive stresses that may have bowed or slightly buckled the liner.

The response remains essentially elastic up to 1.3 to 1.5 P_d, after overcoming the prestress (~1.2 P_d) and tensile cracking of the concrete. It is interesting to note that even though drying and shrinkage cracks were present prior to pressure testing, the onset of generalized concrete tensile cracking is quite distinct. Beyond 1.5 P_d to approximately 2 to 2.5 P_d, the response is still linear, although the loss of concrete tensile stiffness is quite distinct. Beyond 2.5 P_d, the response becomes increasingly nonlinear, particularly in the mid-section of the cylinder, as the model exhibits generalized yielding in the hoop direction.

The data also exhibits some apparent discontinuities at 1.5, 2.0, and 2.5 P_d. These apparent discontinuities coincide with the leak checks of the model and reflect, primarily, the response to changes in ambient thermal conditions over the time the model was isolated. The jump in displacement at 2.5P_d, however, most likely includes creep effects, since the temperature was stable over the relatively short (1-1/2 hour) hold at this pressure.

Figure 5.40 displays the displacements at Azimuth 324 degrees, which coincides with the centerline of the E/H. The largest radial displacement recorded during the LST, 33.36 mm, occurred at this Azimuth at El. 6200, above the E/H. Computing the equivalent hoop strain due to pressure at this location from kinematics,

$$\epsilon_{\text{max}} = \frac{\Delta r}{R} = \frac{(33.36 + 2.68)}{5375} = 0.67\%$$

Similarly, calculating the local hoop strain in the vicinity of the equipment hatch at 2.5P_d, corresponding with the onset of liner tearing and leakage, yields a value of approximately 0.28%.

Figure 5.40 again illustrates the liner separation phenomena, previously described, at elev. 9230. In this case the large magnitude of the displacement clearly indicates that the liner buckled. (A review of the post-prestressing data indicates that this occurred shortly after the completion of prestressing, most likely in conjunction with thermally-induced compressive strains.) This behavior did not, however, compromise the integrity of the liner and no tears were discovered at this location.

Figure 5.41 compares the displacement response as a function of Azimuth at elev. 4680, nominally the mid-height of the cylinder and the centerline of the E/H, A/L, and M/S penetrations. Ignoring some variation in initial conditions, reflecting some ‘out-of-roundness’ following prestressing, the response is fairly uniform, i.e. axisymmetric, except at 324 degrees, where largest deflections were already noted to occur. Averaging the radial deformation due to pressure yields a nominal average hoop strain of 0.42% at the peak pressure 3.3P_d. Similarly, the average hoop strain at 2.5P_d, coinciding with the onset of liner tearing and leakage, was 0.18%.

Figure 5.42 shows the vertical displacement of the springline at various azimuths. The vertical displacement at the apex and the differential displacement between the average springline displacement and the apex are also plotted. The vertical displacement exhibits similar behavior to the hoop displacements. In the vertical direction, however, the loss of stiffness due to concrete cracking occurs around 2.5 P_d. Yielding in the vertical direction does not appear to occur. This is due to the higher level of vertical prestress in the cylinder wall and the lower tensile forces induced by the pressure. The

vertical displacement is nearly uniform at the springline and the average meridional strain in the cylinder wall is less than 0.1%.

$$\text{@P}_{\max} = 3.3P_d: \quad \frac{\Delta l}{L} = \frac{(8.00+2.50)}{10750} = 0.10\%$$

The vertical displacements illustrate, much more dramatically, the effect of ambient temperature and creep during the leak checks.

Figure 5.42 also shows that beginning around $1.5P_d$, the dome apex deflects downward relative to the springline, most likely due to increasing force in the vertical tendons once the initial prestressing force is overcome by the pressure. (The vertical prestressing applies a compressive force on the cylinder wall approximately equal to the tensile force exerted by a pressure of $1.88P_d$.)

Deformed profiles of the PCCV model, constructed from the displacement data, are shown in Figures 5.43 through 5.45. These figures provide a more illuminating view of the model behavior than the pressure histories. The figures were constructed by applying the displacement data (exaggerated by a factor of 100) to the initial configuration of the model. The initial conditions were defined by the as-built model survey data (Appendix C). While these measurements were made in July, 1999, it was assumed that any changes in the position of the cardinal points by March, 2000 could be neglected without significant error. The motion of the cardinal points without displacement transducers were computed by linear interpolation. Both radial and vertical displacements were applied to the cardinal points and out-of-plane (i.e. circumferential) motion of the was not measured or considered.

The as-built position of the PCCV model is plotted along with the deformed shapes at the start of the LST ($P = 0$), at approximately $1.0P_d$ (0.398 MPa/57 psi), $2.0 P_d$ (0.776 MPa/113 psi), $2.5 P_d$ (0.978 MPa/142 psi), $3.0 P_d$ (1.162 MPa/169 psi), and $3.3 P_d$ (1.295 MPa/188 psi).

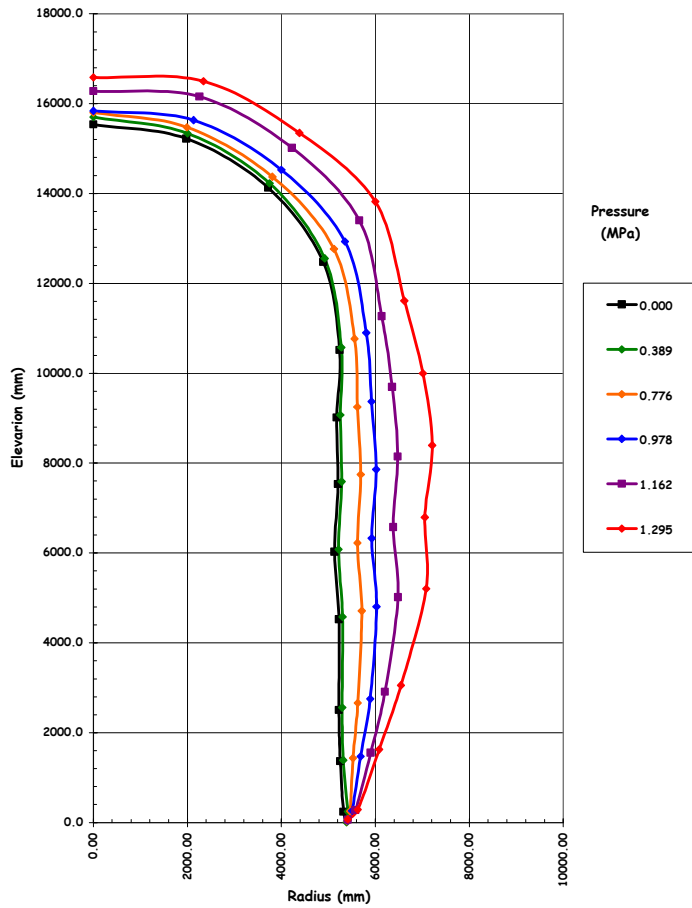
The figures illustrate a few interesting points about the behavior of the PCCV model.

First, and most importantly, the radial deformations are smallest at the buttresses (90 degrees and 270 degrees) and larger between the buttresses (0 degrees and 180 degrees), illustrating the stiffening effect of the buttresses even though the net hoop prestressing force is smallest at the buttress. The largest radial deformations are at the E/H and A/L penetrations, showing the reduced stiffness of these regions in spite of thickening and added conventional reinforcing. This reduction in stiffness is due to the lower prestressing forces as the tendons are deflected around the penetrations in addition to the opening itself.

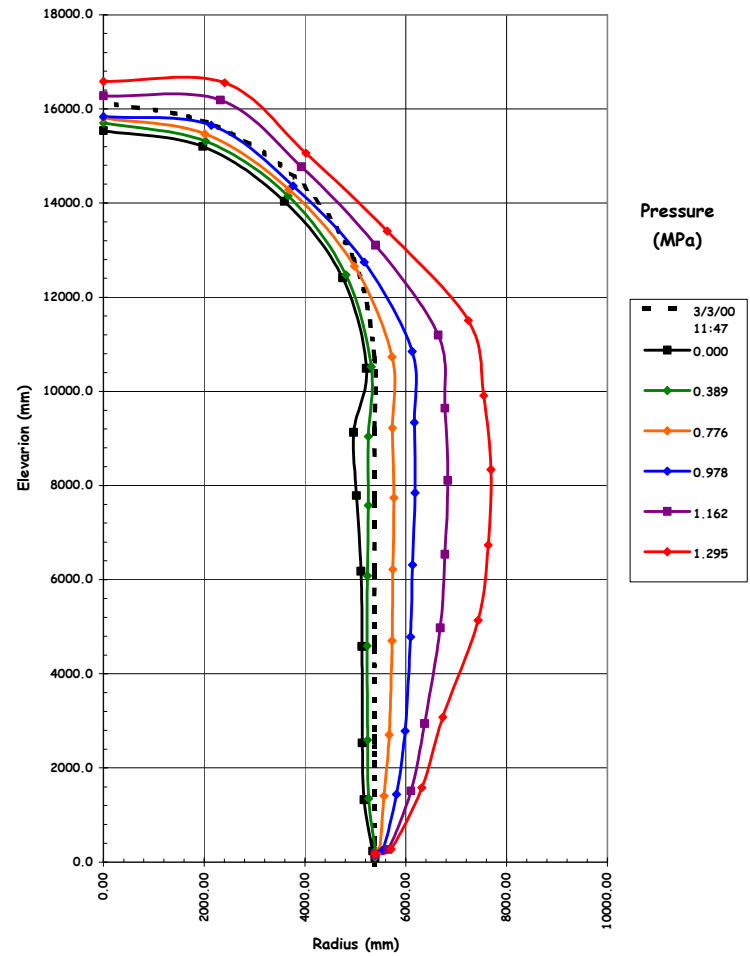
Secondly, the vertical profiles do not show any reverse curvature at the wall-base junction and seem to imply the presence of a hinge forming at this location. While a hinge may have occurred, this deformation pattern may be more reflective of an instrumentation artifact than the model's behavior in this region. The displacement transducers at the wall-base junction were anchored to the base liner immediately adjacent to the wall, while the displacements above this point were measure relative to the instrumentation frame. It is likely that the differential displacement measured at the wall-base junction does not accurately reflect the total displacement in this region, and the data should be viewed with this limitation in mind.

Finally, a few other minor observations:

- The unusual deformation patten in the dome at 135 degrees and 324 degrees coincides with the regions where the East-West and North-South sets of vertical tendons overlap with the hoop tendons in the dome, where higher prestressing forces are present than in other regions of the dome.
- The initial buckling of the liner at Azimuth 324 degrees, elev. 9230 is clearly shown in Figure 5.44.

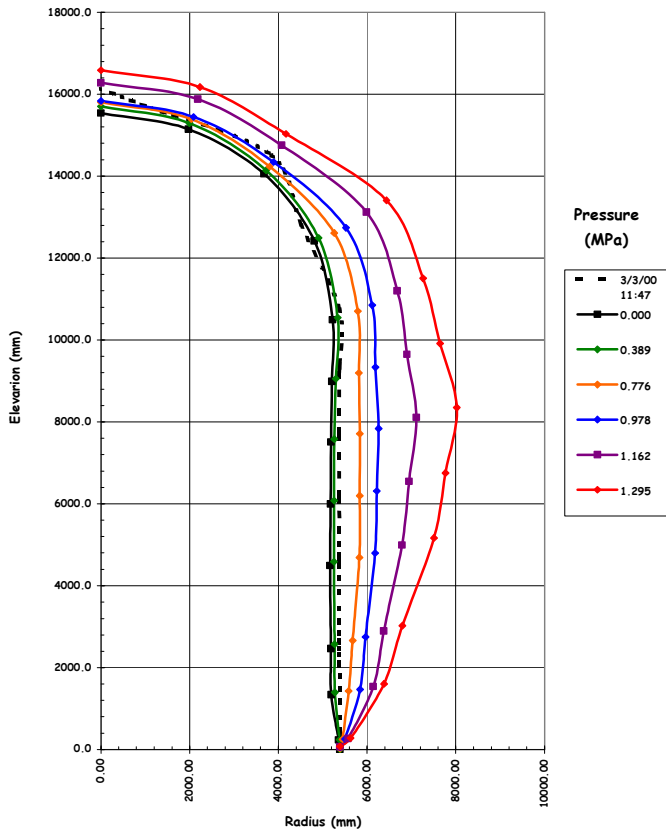


(90°)

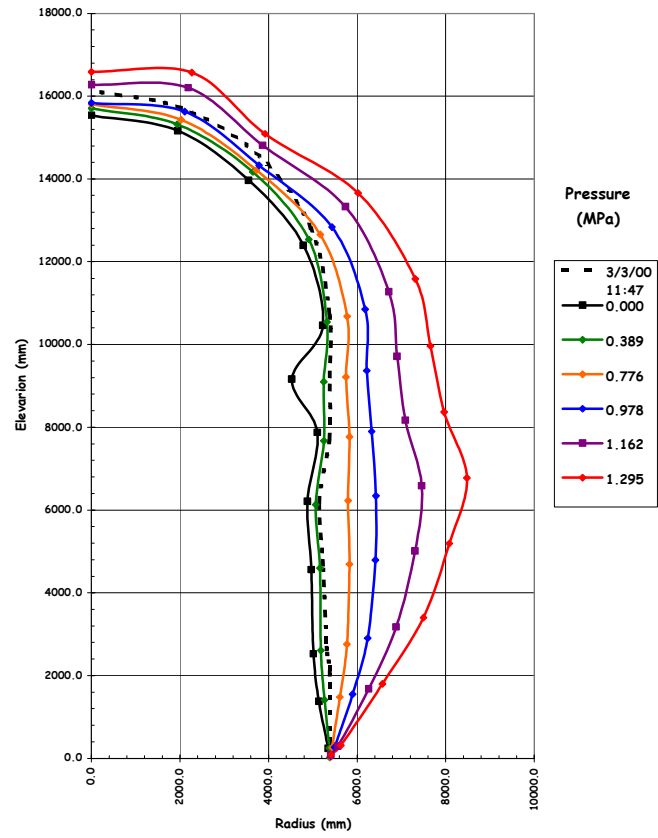


(135°)

Figure 5.43 LST - Deformation at Azimuth 90 degrees and 135 degrees (D and Z) × 100



(240°)



(324°)

Figure 5.44 LST - Deformation at Azimuth 240 degrees and 324 degrees (I and L) × 100

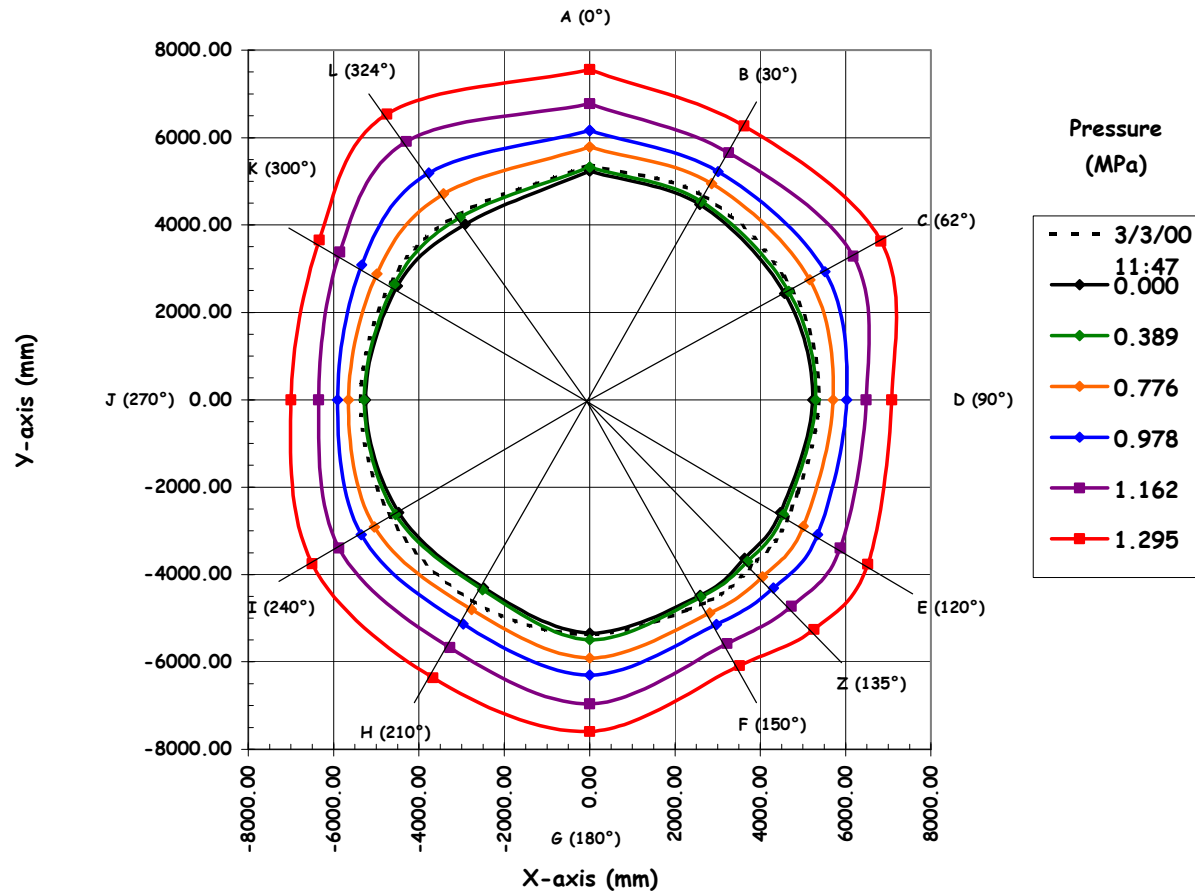


Figure 5.45 LST - Deformation at Elev. 4680 (5) x 100

5.3.2.1.2 Liner Strains

Five hundred and fifty-nine strain gages were placed on both surfaces of the liner to measure both the meridional and hoop free-field liner strains, as well as local strains at the penetrations, the wall-base junction, liner anchor, and stiffeners where discontinuities might result in high local strains prior to the liner tearing. The data for each of these gages is provided on the enclosed CD. The majority of these gages did not record significant strains, however, gages at a number of locations deserve closer inspection. Table 5.4 summarizes the maximum strains recorded during the LST at locations of interest.

Before considering several of these locations in detail, it is worth noting that individual strain gages can provide misleading information due to their sensitivity to local as-built conditions, particularly in areas of sharp discontinuities and high strain gradients. As a result, it is more meaningful to consider sets of gages in these locations, thus providing a more realistic view of the strain field in a particular area.

Figure 5.46 shows all the free-field liner hoop strain gages that exceeded 0.5% at the end of the test. It is interesting to note that up to 2.5 Pd, the free-field liner strain hoop strains were almost all below 0.2%, which compares favorably with the average hoop strain computed from the displacements, 0.18%.

Nearly all the free-field liner and liner anchor meridional strain gages were below 0.1%, which is also consistent with the displacement data.

Considering the liner strains near penetrations and other discontinuities, the strains in the vicinity of the E/H are of primary interest since there were indications during the LST that the liner initially tore in this region. Posttest inspection of the liner, described in Section 5.3.2.2, revealed several tears at the edges of the embossment (Figure 5.47), but no apparent damage near the insert plate. The layout of the liner strain gages is shown on Drawing D-SN-P-218 (Appendix E), and reproduced in Figure 5.48 for reference. The highest strains in this region were at the left and right edges of the embossment. The strains adjacent to the insert plate (#19 to #67) were small, nearly all less than 0.2% at maximum pressure, with only a few near the ends of anchors or stiffeners reaching 0.5%.

Table 5.4 LST Liner Strain Summary

Maximum Free-Field Hoop Strain	0.90%
Maximum Free-Field Meridional Strain	0.14%
Maximum Meridional Anchor Strain	0.10%
Maximum Equipment Hatch Strain	3.88%
Maximum Personnel Airlock Strain	0.75%
Maximum Main Steam Penetration Strain	4.54%
Maximum Feedwater Penetration Strain	6.39%
Maximum Wall-Base Junction Strain	1.97%
Maximum Miscellaneous Liner Details Strain	5.75%

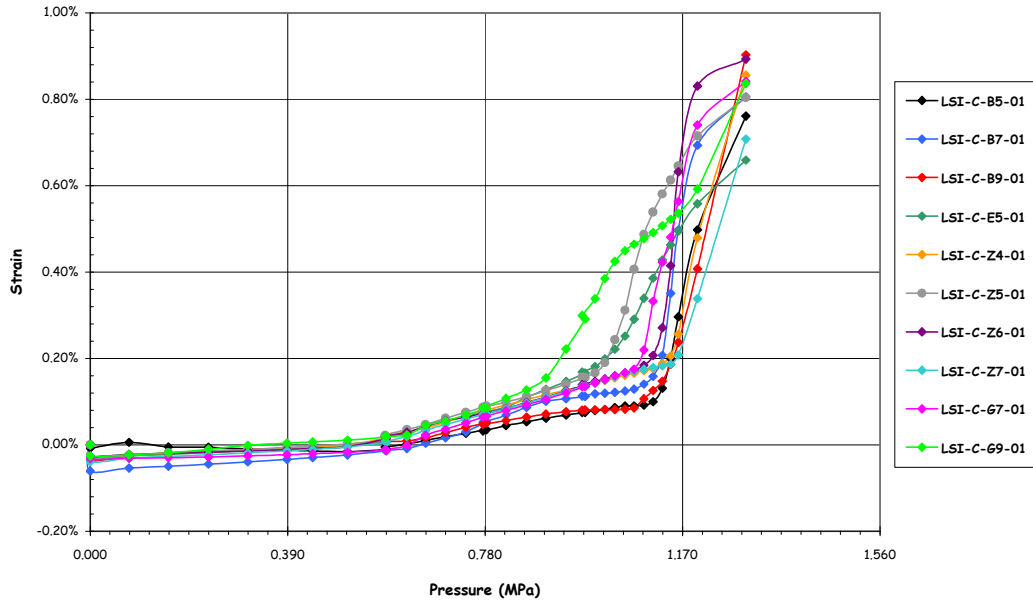


Figure 5.46 LST – Free-Field Liner Hoop Strains



Figure 5.47 Liner Tear (#15) at E/H

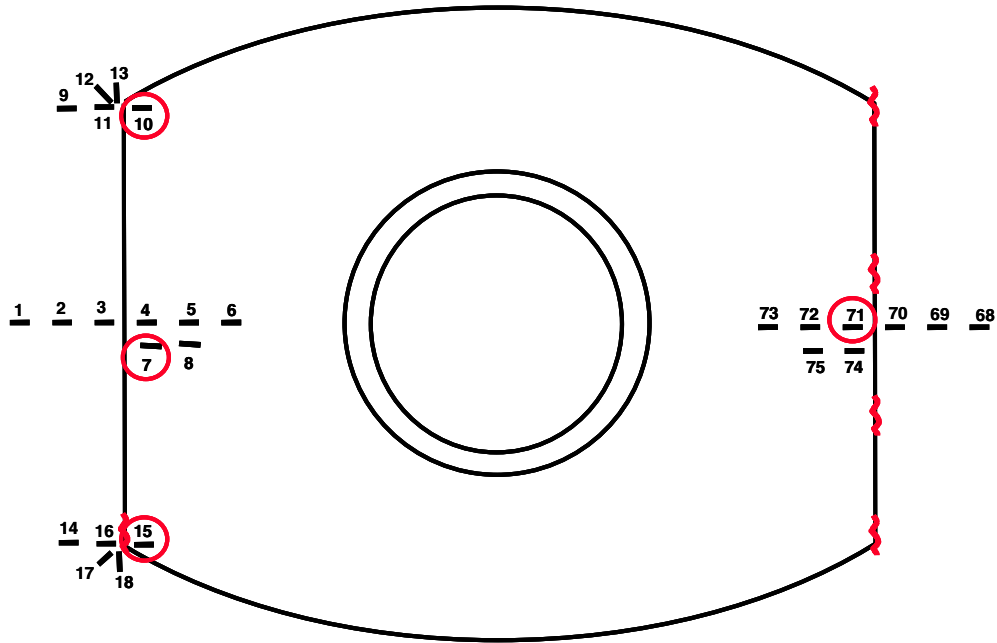


Figure 5.48 Equipment Hatch Liner Strain Gage Layout (Inside View)

The strains at the middle of the ‘left’ (#1-8) and right (#68-75) edges of the embossment are shown in Figures 5.49 and 5.50. The strains at the upper and lower ‘left’ corners are shown in Figure 5.51. With the exception of gage #7, the strains at the mid-sides of the embossment are all very small until global yielding of the model occurs just below $3P_d$. At the corners, however, liner strains begin increasing earlier, with gage #10 showing increasing strains beginning at $1.5P_d$, while most of the other gages show significant increases beginning at $2.5P_d$, when liner tearing was believed to

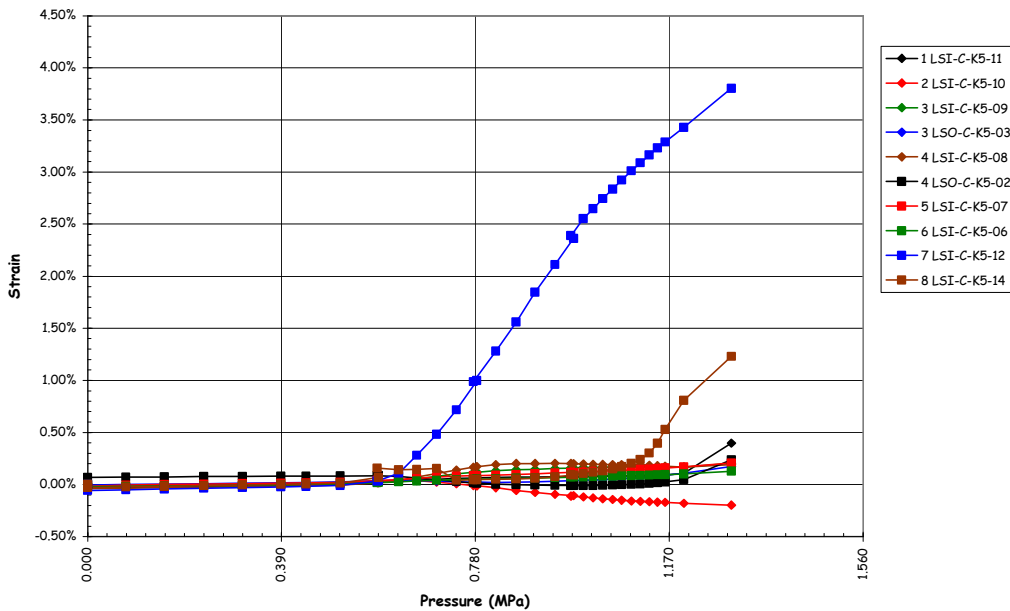


Figure 5.49 E/H Liner Strains at ‘Left’ Edge of Embossment

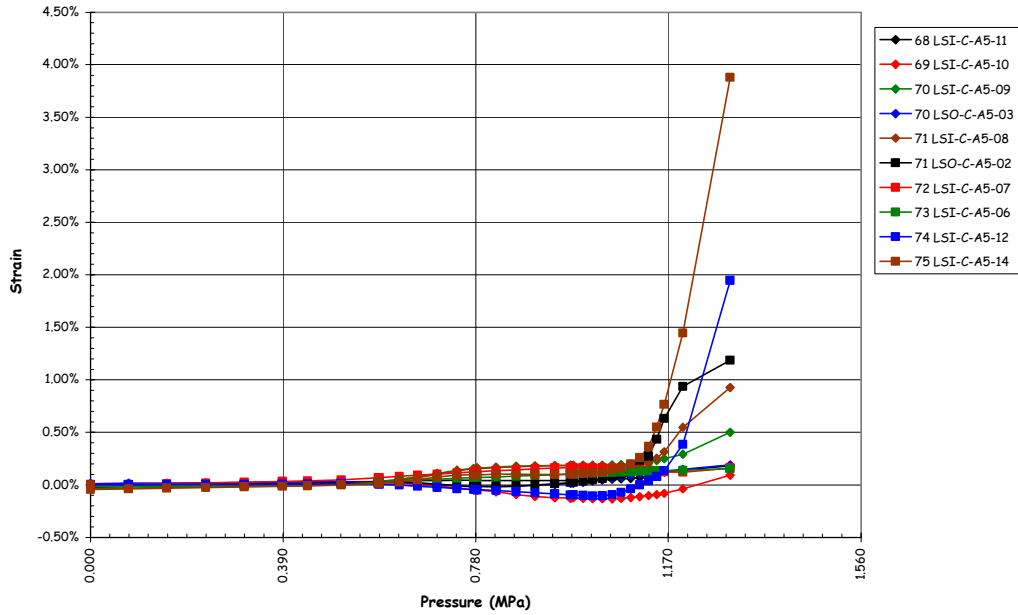


Figure 5.50 E/H Liner Strains at 'Right' Edge of Embossment

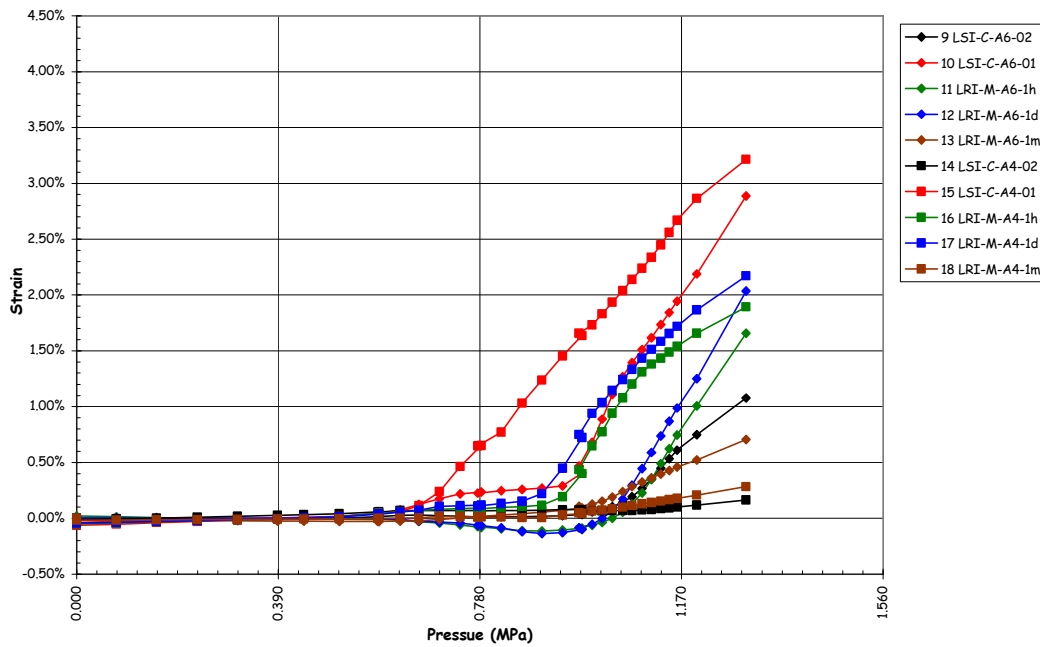


Figure 5.51 E/H Liner Strains at 'Left' Corners of Embossment

have occurred. At first glance, it appears unfortunate that the liner tore on the opposite side from the strain gages (pretest analyses suggested the highest strains would occur on the 'left' side). However, it has been found that strain gages near tears often see lower strains than would be expected, since the tear acts as a strain relief mechanism. While it is apparent that the strains on the 'right' side were higher, it is unlikely that gages at those locations would have recorded higher strains than those on the left side. This is demonstrated by comparing gages #7 on the left and its mirror image, #74, on the right.

Note that at the pressure $2.5 P_d$, when the liner tearing is believed to have begun, the measured strains were only on the order of 0.75% to 1.50%.

The liner strain at the A/L shows a similar pattern to those at the E/H, with a peak tensile strain at the corner of the embossment of 0.75%. However, no tears occurred at this penetration.

Liner strains at the M/S and F/W penetrations are shown in Figures 5.52 and 5.53. The layout of the liner strain gages is shown on Drawing D-SN-P-220 (Appendix E).

Several large tears occurred at each end of the F/W penetration, beginning at the weld between the thickened insert plate and the liner; however, no tears occurred at the M/S penetration event, though the free-field hoop strains at the M/S are higher since it is closer to the mid-height of the cylinder. There are a number of reasons why this occurred, primarily liner fabrication issues discussed in Section 5.3.2.2. It is interesting to note that even though the strain gages at the F/W penetration were located near the tear (see Figure 5.54), measured strains were relatively low until the very end of the LST, when some strains increased very rapidly. This might indicate that a tear in the vicinity of a strain gage can act as a strain relief mechanism on the surrounding material. The 'jump' in the strain near the end of the test may also be due to material distortion in the vicinity of the tear as the tear propagated. On the other hand, the strains recorded at the M/S penetration begin to climb rapidly at 2.0 to 2.5 P_d , reaching values as high as 4.5% without resulting in any liner tearing. Detailed inspections of this location did not reveal any evidence of the fabrication problems that were present at the F/W penetration.

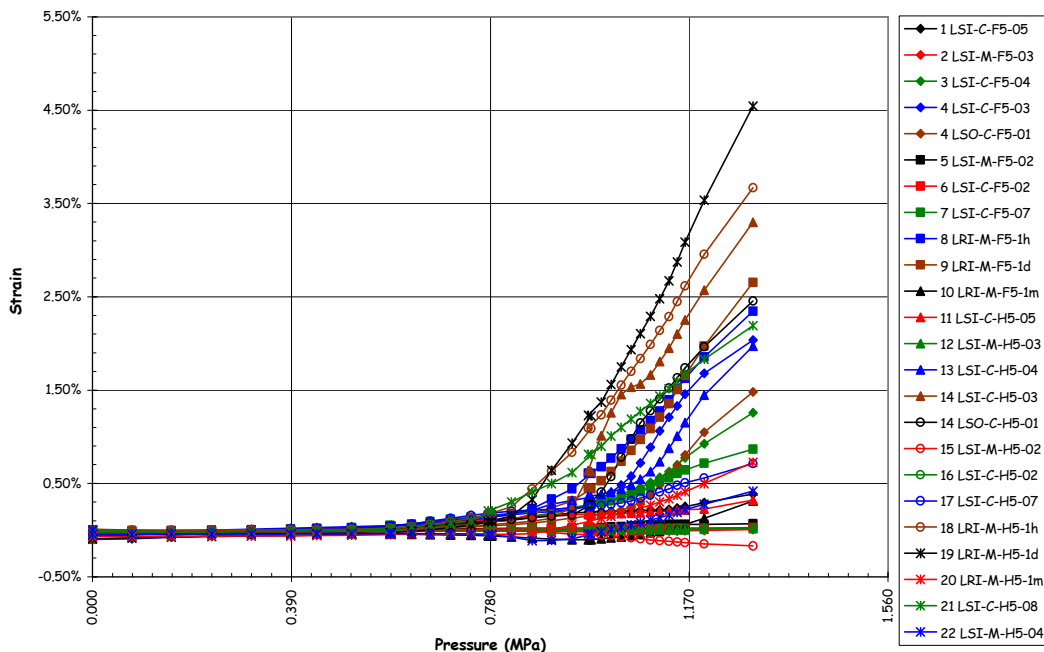


Figure 5.52 Liner Strains (DOR) at M/S (Ref. D-SN-P-220)

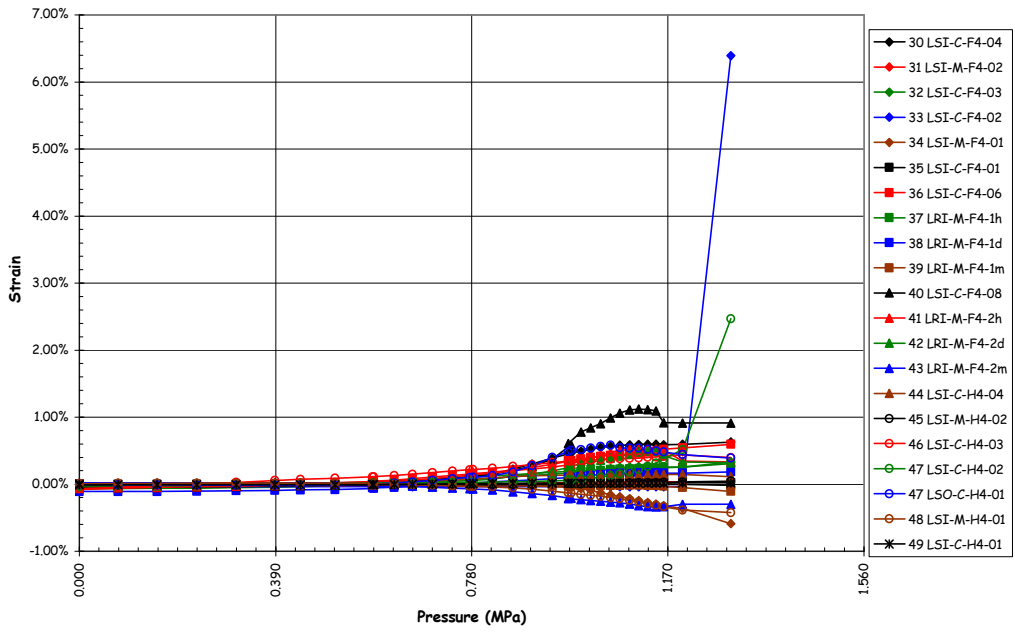


Figure 5.53 Liner Strains (DOR) at F/W (F=Ref. D-SN-P-220)

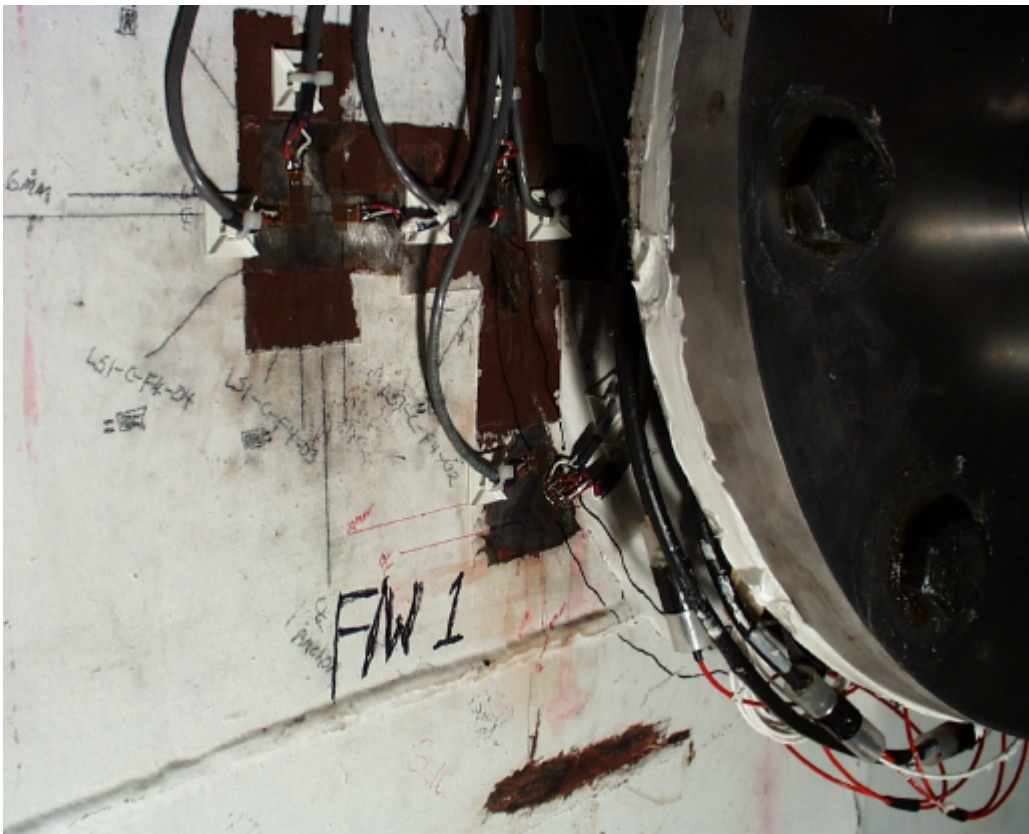


Figure 5.54 Liner Tear (#3) and Strain Gages at F/W Penetration

A number of other details believed to create potential strain concentrations in the liner were also instrumented and monitored during the test. One of these details occurs throughout the model: a gap is left in a horizontal stiffener or vertical anchor where it crosses a liner seam welds (Figure 5.55), euphemistically called a ‘rathole.’ In previous containment model tests, this detail caused significant strain concentrations when the surrounding liner began to yield. In fact, a number of the liner tears found after the test occurred at these details. One such detail that was instrumented was located near the intersection of cardinal lines D7 (Azimuth 90 degrees, elev. 7730). Although a tear occurred in a similar detail above this location, the liner did not tear at this rathole and the strains recorded at this location provided valuable information regarding the behavior of this detail for comparison with analyses.

The interior strain gages at D7 are also shown after the LST in Figure 5.56. The arrangement of these gages is shown on Drawing D-SN-P-209, Detail a.4 (Appendix E). Strains begin increasing between 2.0 and 2.5Pd, reaching a maximum of 5.7% at the maximum pressure. Nevertheless, the liner did not tear. A subsequent comparison of this detail to similar rathole details that did tear, but were not instrumented, revealed a lack of any weld repairs, which was not true of the other locations. This detail appears to demonstrate that the liner is capable of undergoing significant local strain without tearing in the absence of any other factors that might degrade the liner.

5.3.2.1.3 Rebar and Concrete Strains

The reinforcing steel strains are summarized in Table 5.5. Typically, after the onset of global yielding, the rebar strains were higher than the corresponding strains computed from displacements and the free-field liner strains. This phenomena was recognized during gage calibration and occurs due to a local reduction in cross-section from grinding away a portion of the bar to mount the strain gage. The effect of this local cross-section reduction causes the bar to yield at the gage location slightly before the rest of the bar yields. The effect on the rebar strain readings is to introduce an artificial strain increment, on the order of 0.5% strain, after the bar has yielded, compared to the strain that would occur if the gage were not present. This artifact can be illustrated by considering the hoop strain measurements at Z6 shown in Figure 5.57. Attempts were made to develop an algorithm to correct for this gage artifact; however, the results were not particularly useful. The rebar strain data included on the data CD were not corrected for this artifact, which any interpretation of this data should consider.

Figure 5.57 compares the hoop strains recorded at the mid-height of the cylinder wall (Z6: Azimuth 135 degrees, elev. 6280) by the fiber optic gages (CE), rebar strain gages (RS), liner strain gage (LI) and computed from the displacement (DT). The strains track each other very well until local yielding occurs in the liner and, shortly after, in the rebar. The fiber optic gage continues to track the displacement and provides a much more accurate measure of the hoop strain in the wall than the LI or RS gages.



Figure 5.55 Horizontal Stiffener Detail at Vertical Seam Weld (‘Rathole’) near D7

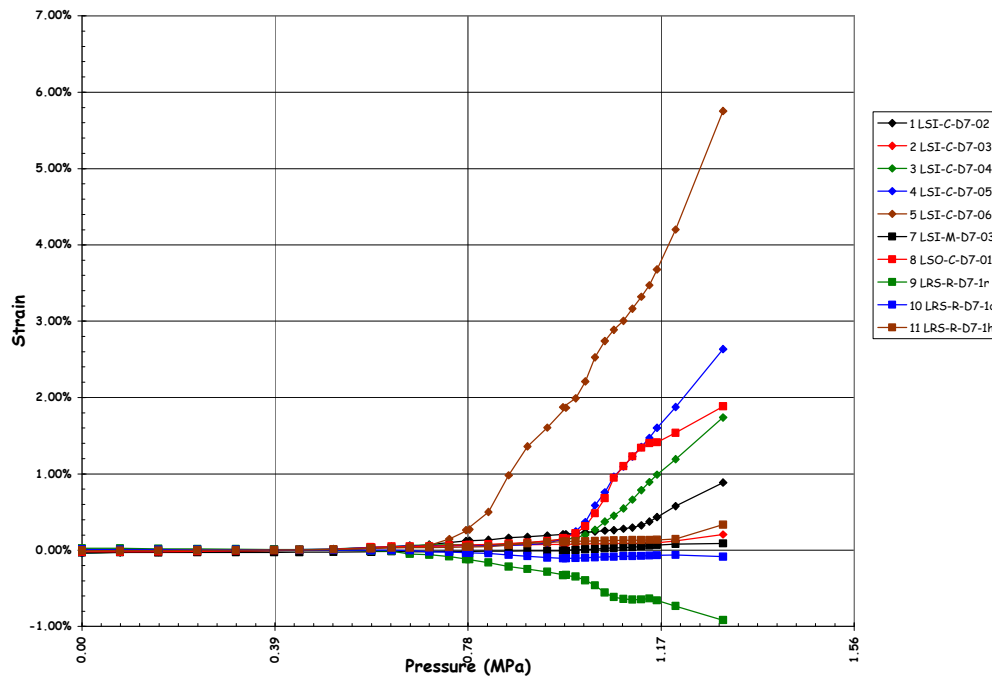


Figure 5.56 Liner Strains (DOR) at D7 Anchor Detail (Ref. R-SN-P-209, a.4)

Table 5.5 Rebar Strain Summary

Maximum Free Field Hoop Rebar Strain	1.68%
Maximum Free Field Meridional Rebar Strain*	0.47%
Maximum Free Field Radial Rebar Strain	0.88%
Maximum Basemat Rebar Strain	0.84%
Maximum Rebar Strain at E/H	1.62%
Maximum Rebar Strain at A/L	1.50%

* One gage (RS-M-A0-07) recorded a maximum strain of 6.11%. However, the initial strain of the start of the LST was 5.85%, yielding a change in strain of 0.27%. The initial high strain reading was due to an increase in resistance not associated with strain of the bar.

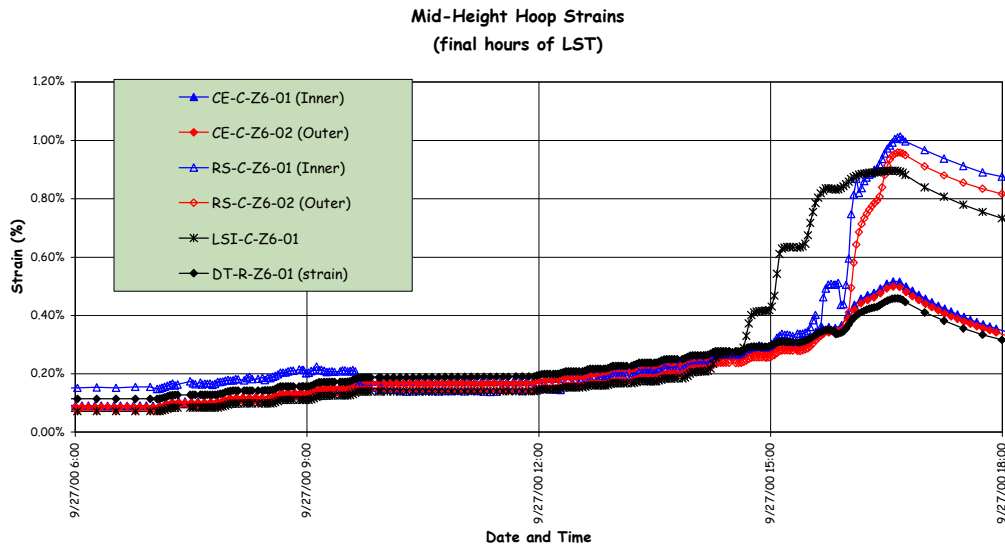


Figure 5.57 Comparison of Strain at Z6 (Azimuth 135 degrees, Elev. 6280)

Strain gages were also installed on specially fabricated ‘gage bars,’ which were located at several azimuths (90 degrees, 135 degrees and 350 degrees) at the wall-base junction in an attempt to get a more accurate picture of the strain fields at this location due to the presence of large bending forces under pressure (Figure 5.58). Unfortunately, a large number of these gages were damaged during construction and only very limited data was obtained. (Since the gage bars were embedded in the basemat, they were placed at the time of the final basemat lift and left exposed for almost two years until the first cylinder wall lift was placed. During this time, they were exposed to the weather and some rough handling by the construction workers.) However, enough gages survived at 135 degrees that it is possible to construct a picture of the strain history at this location. Figure 5.59 shows the distribution of strain *due to pressure only* at four elevations (86, 201, 312, and 427) above the top of the basemat. Only the strain due to pressure is plotted, since the initial strains due to dead load and prestressing are somewhat ambiguous and mask the pressure response. The strains recorded by the surviving gages at each elevation are plotted at pressure levels corresponding to $1P_d$, $2P_d$, $2.5P_d$, $3P_d$, and $3.3P_d$. While these results are incomplete, they do show the increasing curvature of the cross-section as a function of pressure, especially at elev. 427.

Some gage bars were also located in the basemat, above the tendon gallery, in an attempt to measure tensile strains that might develop at this location. However, there was no indication of any damage in this region and, with a few ambiguous exceptions, the gages did not record any response to the pressure loads.

Overall, in spite of the significant effort (and expense) involved in the application and installation of the rebar strain gages, the resulting data is only marginally useful and any future tests of a similar nature would be advised to consider the method of installing strain gages on rebar and to limit the number of gages to a few, critical locations.

5.3.2.1.4 Tendon Forces and Strains

Since the unique feature of this model, compared to previous large-scale containment models tested at SNL, is the prestressing system, and the behavior of this system to pressure loads beyond design levels is of particular interest, a significant effort was made to measure the response of the tendons. Both tendon anchor forces, as well as strains along the length of the tendons, were measured. Unfortunately, as noted in Chapter 2, approximately 50% of the strain gages installed on the tendons strands were damaged during construction and/or prestressing. Furthermore, data from the Tensmeg gages indicates the likelihood that these gages de-bonded or slipped relative to the tendon strands, casting some doubt on the accuracy of the data.

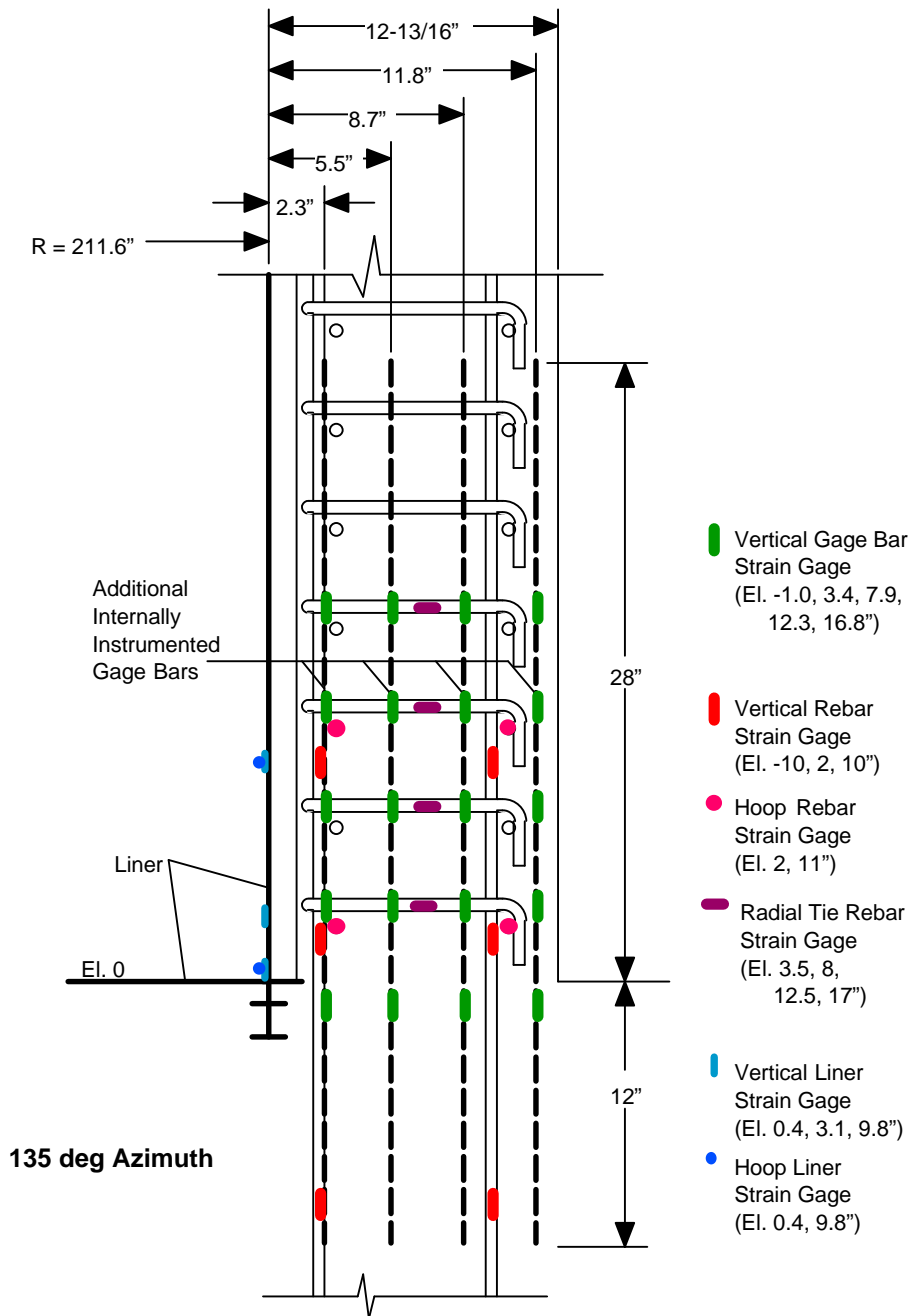


Figure 5.58 Arrangement of Gage Bar Strain Gages at Azimuth 135 degrees

Nevertheless, the surviving gages provide some significant insight into the response of the tendons to the pressure loading. All of the tendon data (load cells and strain gages) is provided on the enclosed CD, as described in Section 5.3.1. A summary of the data and a discussion of the LST results follows.

One-sixth of the tendons in the model were equipped with load cells at each anchor prior to prestressing. Figures 5.60 through 5.62 illustrate the tendon anchor forces during the LST. The anchor forces for the vertical tendons with load cells are shown in Figure 5.60. The anchor forces are shown for the maximum tensioning force during prestressing, after the completion of prestressing (on 5/4/00) and during the LST at $0.0P_d$, $1.0P_d$, $2.0P_d$, $2.5P_d$, $3.0P_d$ and at maximum pressure, $3.3P_d$. Similarly, Figures 5.61 and 5.62 show the anchor forces for the hoop tendons anchored at the 90 degree

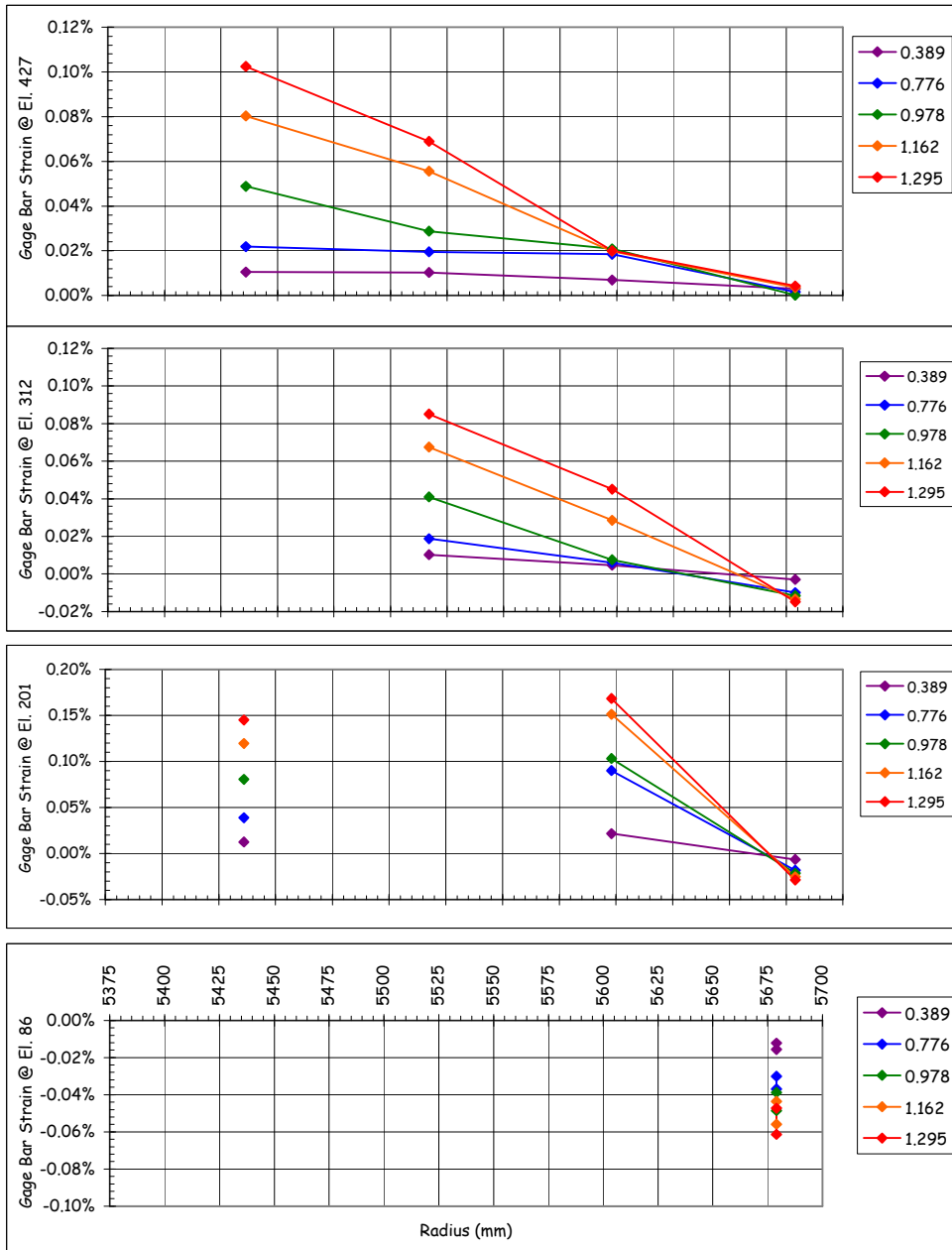


Figure 5.59 LST Gage Bars Strains at Azimuth 135 degrees (due to pressure only)

and 270 degree buttresses. In general, the vertical tendon anchor forces did not exceed the initial tensioning force. The average vertical tendon force at the peak pressure of $3.3P_d$ was 466 kN (104.7 kips) compared to the average tensioning force of 472 kN (106.3 kips). The hoop tendon anchor forces, however, did exceed the initial tensioning force of 424 kN (95.3 kips). The maximum anchor force recorded at the peak pressure of $3.3 P_d$ was 550 kN (123.64 kips) for tendon H53. The average anchor force for all the hoop tendons at the peak pressure was 496 kN (111.6 kips). The tendon yield strength (0.2% offset) is approximately 590 kN (132.6 kips), so hoop tendon forces at the anchors were approaching, but had not exceeded their yield strength.

Eight tendons, five hoop tendons (H11, H35, H53, H67, and H68) and three vertical tendons (V37, V46, and V85), were instrumented along their length by placing strain gages on individual strand wires at specified locations. The surviving bonded foil gages are believed to have provided the most reliable data on the strain in the tendons. Figure 5.63 plots the strain history during the LST of the surviving gages on tendon H68. This plot illustrates the variability between strains in different strand wires at roughly the same position along the tendon. Nevertheless, considering an average strain of approximately 0.40% at the start of the LST, the increase in the average strain to 0.80% is nearly identical to the average hoop strain computed from the displacements, at 0.42%.

A more useful way of analyzing the tendon response data is by constructing the tendon force profiles at pressures during the LST, similar to the force profiles constructed for the prestressing loads (see Figures 2.66-2.73). The tendon force profiles for the five instrumented hoop tendons are shown in Figures 5.64 to 5.68. The force profiles include the design and measured values at maximum tension and after seating, and the recorded response during the LST at $0.0 P_d$, $1.0 P_d$ (0.389 MPa/56.4 psi), $2.0 P_d$ (0.776 MPa/112.5 psi), $2.5 P_d$ (0.978 MPa/141.8 psi), $3.0P_d$ (1.162 MPa/168.5 psi), and at the maximum pressure, $3.3 P_d$ (1.295 MPa/187.8 psi). The profiles are also shown during depressurization at approximately $2.5P_d$, $2.0P_d$, $1.0P_d$, and $0.0P_d$. These force profiles were constructed by converting the average strain from all the foil strain gages at a given position to a force using the actual tendon force-strain test data and combining the computed forces with load cell data. When only a single strain gage survived at a given position, it is noted on the profile.

There is not adequate data to assume the shape of the hoop tendon force profile between the surviving measurement positions, so only the force at the measurement locations are shown. There is enough data to suggest, however, that the tendon force distribution tends to become more uniform, with the largest increase in strain occurring near the mid-point of the tendon, where the initial prestressing force was the smallest. This may be due to a combination of local yielding and/or slipping as the tendons try to maintain equilibrium and local deformation of the cylinder wall. Comparing the differential strain at the midpoint of the tendons to the hoop strain calculated from the wall displacement at that location (see Figures 5.66 and 5.67) indicates that the tendon strain is greater than what would be expected if the tendon did not slip relative to the wall. After unloading, however, the initial tendon force profile (at the start of the LST) is almost completely recovered, which implies that any redistribution occurring during the LST is entirely elastic. This is not a completely satisfying observation, since it would seem likely that any redistribution of tendon forces due to slipping would remain after depressurizing. This reinforces the observation that the change in tendon forces is also due to the local elastic deformation of the wall.

The force profiles for the vertical tendons, constructed in the same manner as the hoop tendon profiles, are shown in Figures 5.69 to 5.71. Again, since the gage mortality was lower for the vertical tendons than the hoop tendons and the force profile is more nearly a continuous function, curves were fit through the data to facilitate interpretation and comparison of the data with the design assumptions. The data again shows that the vertical tendon force distribution becomes more uniform as the pressure increases, and the largest relative increase occurs at the mid-point of the tendon, i.e. the apex, for the vertical tendons. This suggests that the tendons must slip relative to the concrete wall to allow the forces to redistribute; however, as with the hoop tendons, recovery of the initial tendon force distribution is nearly complete after depressurization. In this case, however, it is difficult to argue that the tendon force distribution is dominated by the local radial deformation of the concrete wall/dome, since those in the dome are much smaller than those in the cylinder wall, which is inconsistent with the observed change in the force distribution.

While the tendon response measurements provided new insight into the behavior of unbonded tendons under limit load conditions, some apparent paradoxes were identified that might be answered by further testing and analysis. One conclusion is apparent and undeniable, however. The change in tendon anchor forces is not a reliable indicator, by itself, of the change in force along the length of the tendons, and any attempts to preclude tendon rupture by measuring only the anchor force will not be adequate.

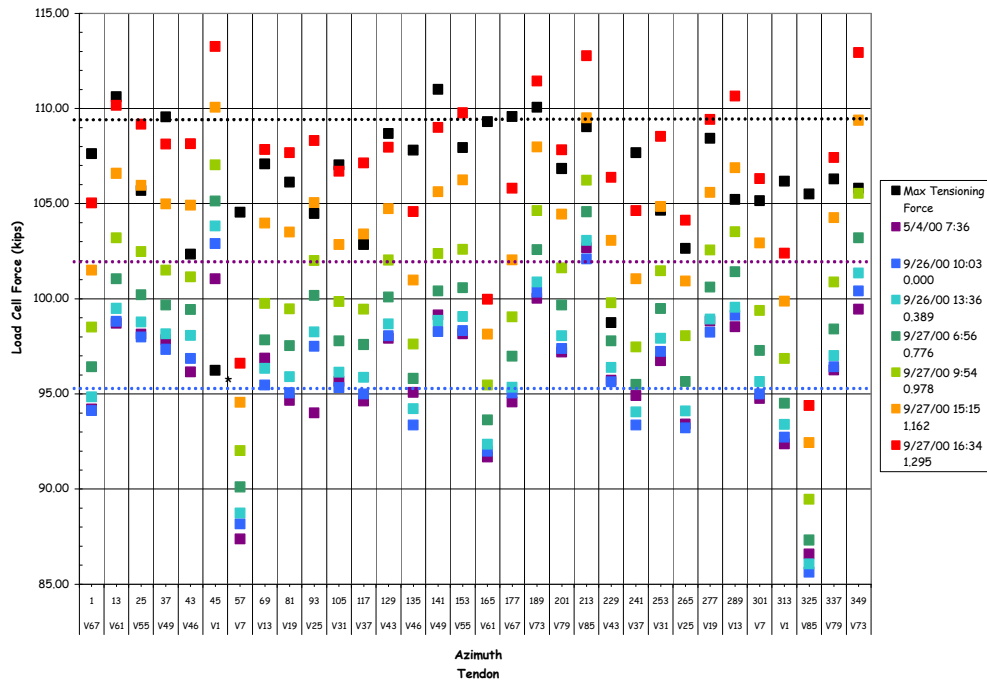


Figure 5.60 LST - Vertical Load Cells

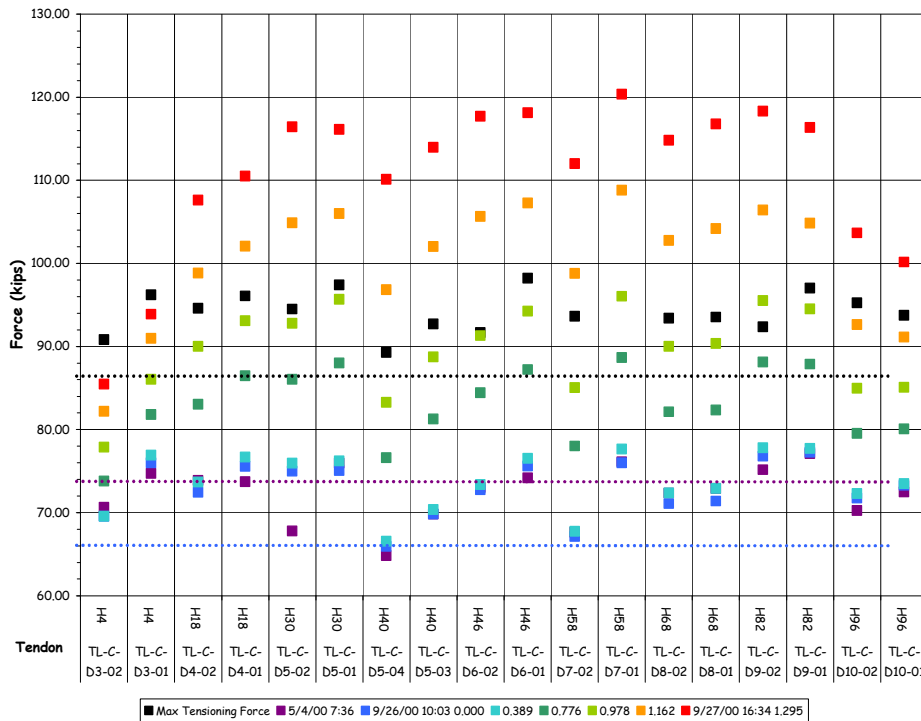


Figure 5.61 LST - Hoop Load Cells at 90 degrees

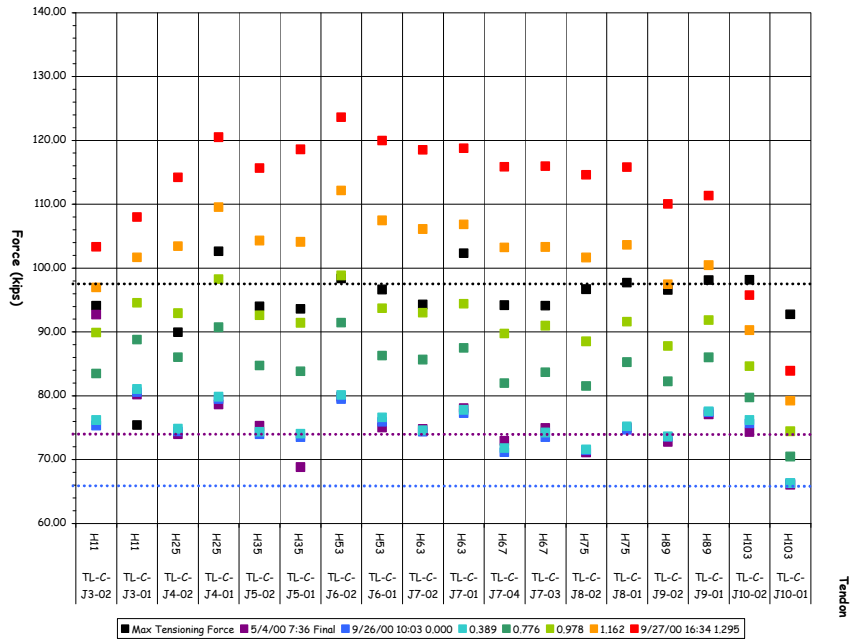


Figure 5.62 LST - Hoop Load Cells at 270 degrees

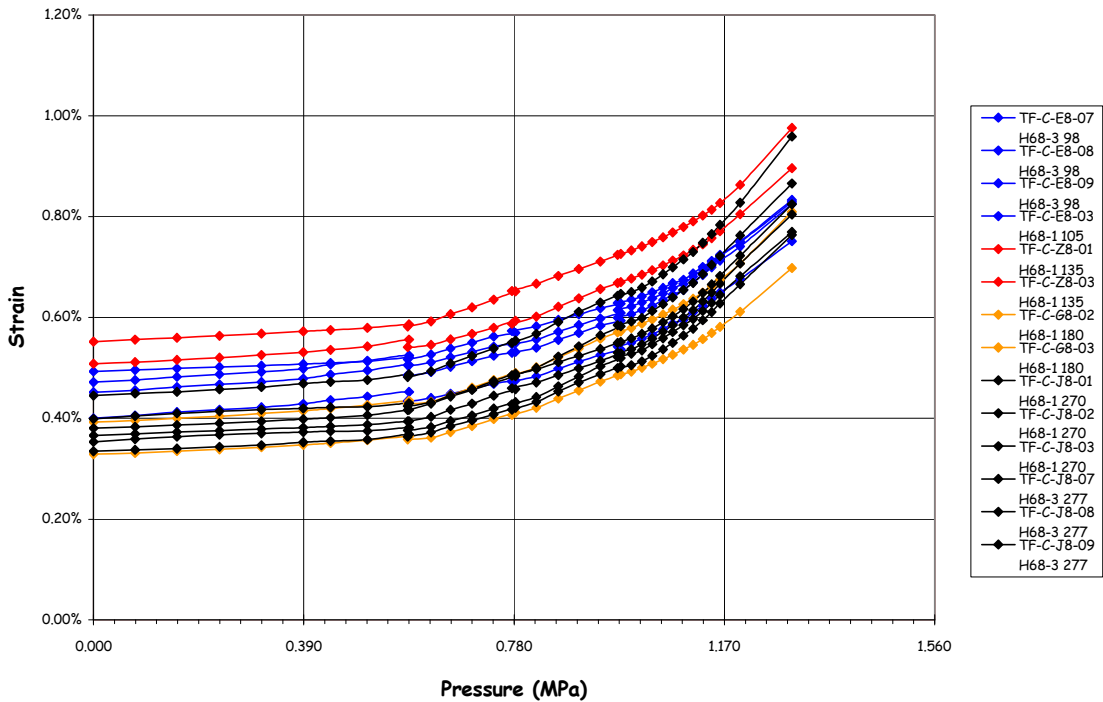


Figure 5.63 LST - H68 Tendon Strains

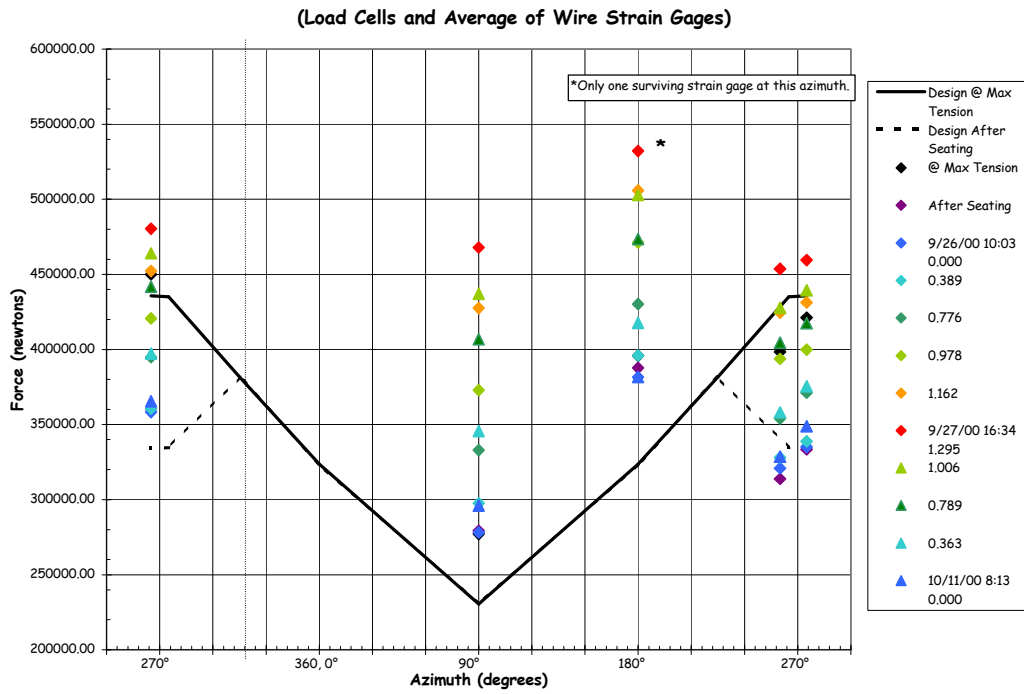


Figure 5.64 H11 Tendon Force Distribution, El. 1854

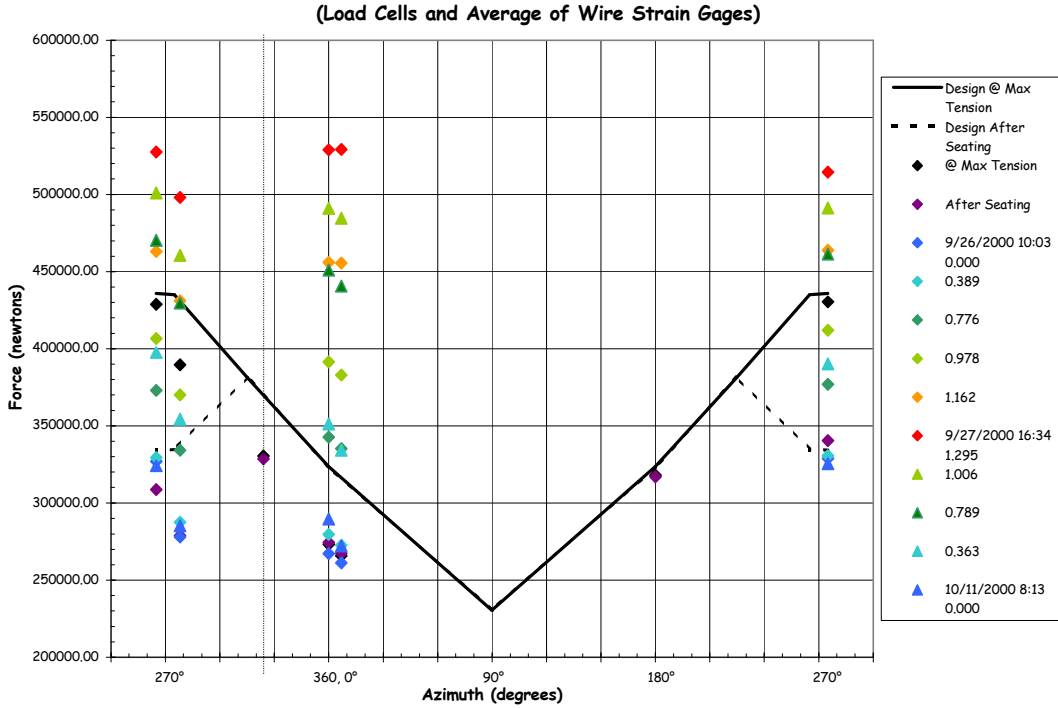


Figure 5.65 H35 Tendon Force Distribution, Elev. 4572

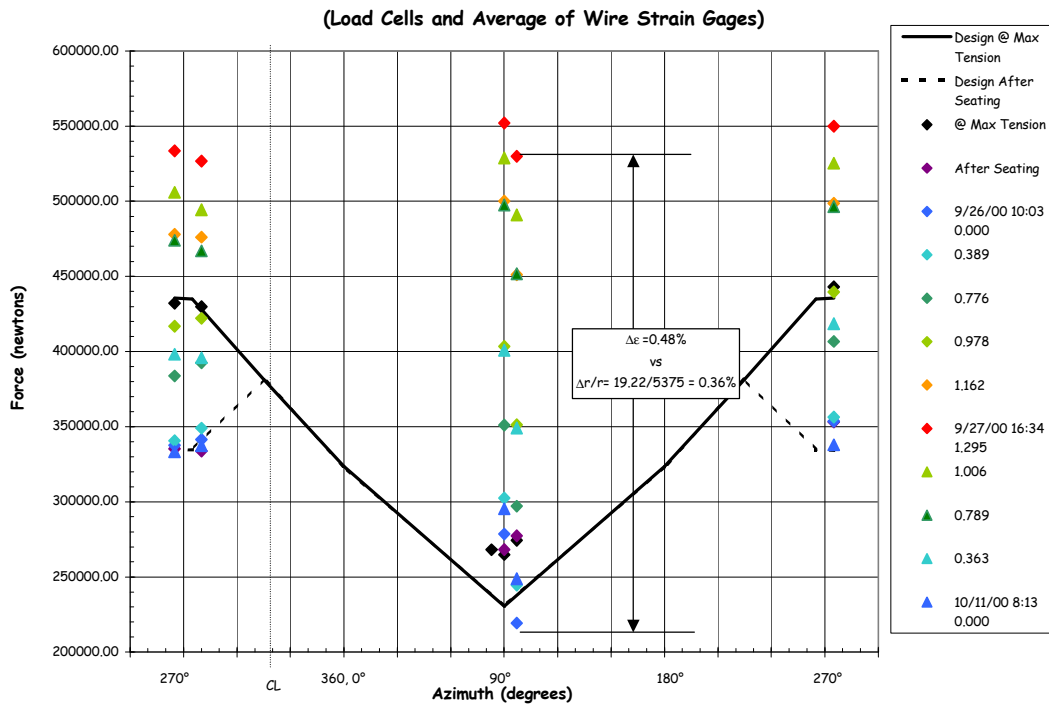


Figure 5.66 H53 Tendon Force Distribution, Elev. 6579

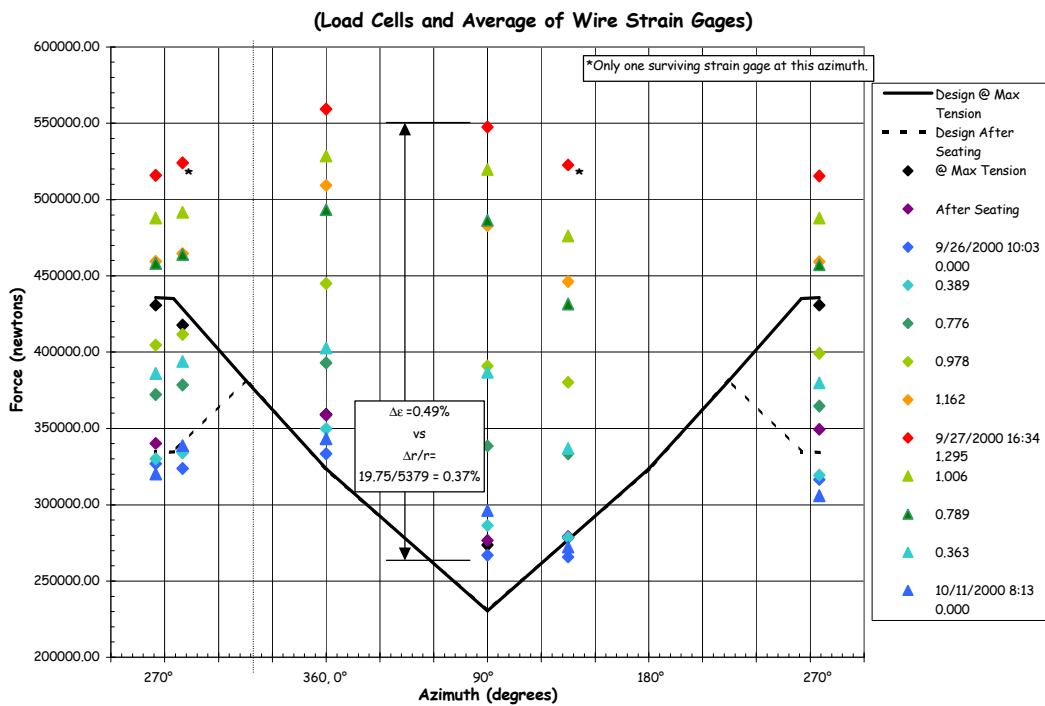


Figure 5.67 H67 Tendon Force Distribution, Elev. 8153

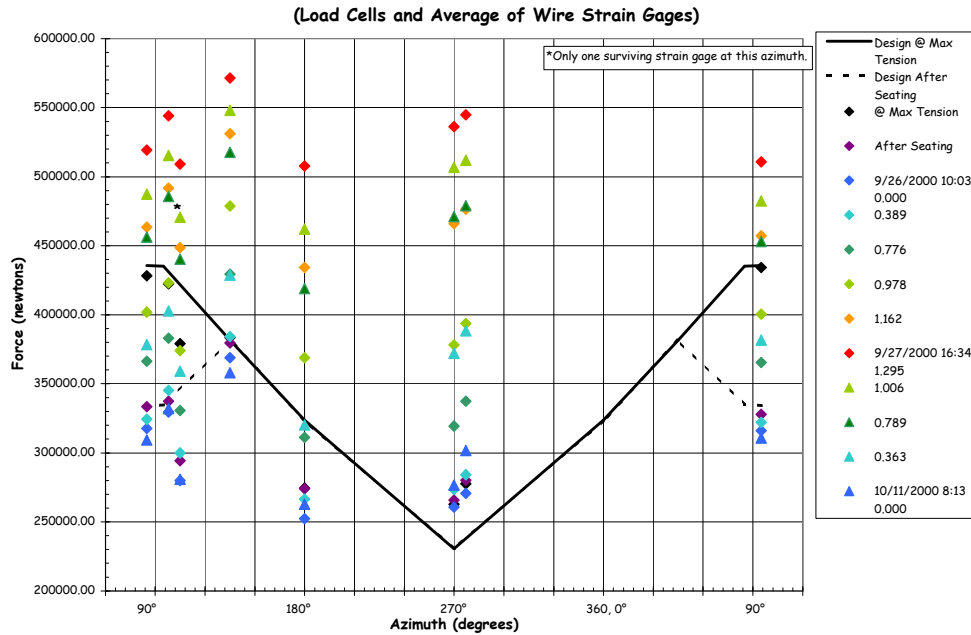


Figure 5.68 H68 Tendon Force Distribution, Elev. 8280

5.3.2.1.5 Acoustic Response

The complete reports from the Acoustic System Operator, Pure Technologies, are provided in Appendix K. As stated in Section 3.2.8, the objectives for the acoustic system were to detect tendon or rebar breaks, concrete cracking or crushing, and liner tearing/leakage. The acoustic system response data, which helped to identify when the PCCV model began leaking, was described in Section 5.2.2 (see Figure 5.17).

There were no tendon wire or rebar breaks during the LST; however, events defined as tendon ‘pings’ were reported. These tendon pings were interpreted as a readjustment or reseating of the tendon wires/strands as they were tensioned, but the magnitude of these acoustic events are much lower than those associated with a wire break. Figure 5.72 shows the location of the tendon pings are concentrated at the buttresses. Whether this is indicative of source of these events or merely reflects that any tendon events will be transmitted more rapidly along the tendon strands to the acoustic sensors on the buttresses is speculative, but reasonable. A histogram of the tendon ping events as a function of pressure is shown in Figure 5.73. The fact that the majority of tendon pings occurred around $2.0P_d$ is noteworthy, but the reason for physical significance of this is not obvious. It may be that a certain level of tension must be applied to reseal the strands, or it may simply be that this pressure was held for almost eight hours and the number of events that accumulated at this time appears to be significant.

A total of 489 cracking events were detected from March 3 to September 27, 2000. Two-hundred twenty nine of these events were recorded during the LST. These cracking events represent distinct acoustic events, as distinguished from the ubiquitous ‘crackling’ which occurred nearly continuously during the period the PCCV was monitored by the acoustic system. This crackling is believed to be the acoustic manifestation of microcracking and shearing in response to environmental and pressure loading. The acoustic events identified as cracking represent the formation or extension of discrete macrocracks in response to the applied pressure or other loads. Figure 5.74 maps the location of the cracking events during the LST, grouped by pressure bands. No obvious pattern emerges from this map except that the majority of cracks occurred in the middle section of the cylinder wall, where the strains and displacements were greatest. A histogram of the cracking events as a function of pressure, shown in Figure 5.75, however, reveals the majority of cracking events occurring in the range of 1.5 to $2.0P_d$ where the initial loss of stiffness, presumed to be due to concrete cracking, was already noted.

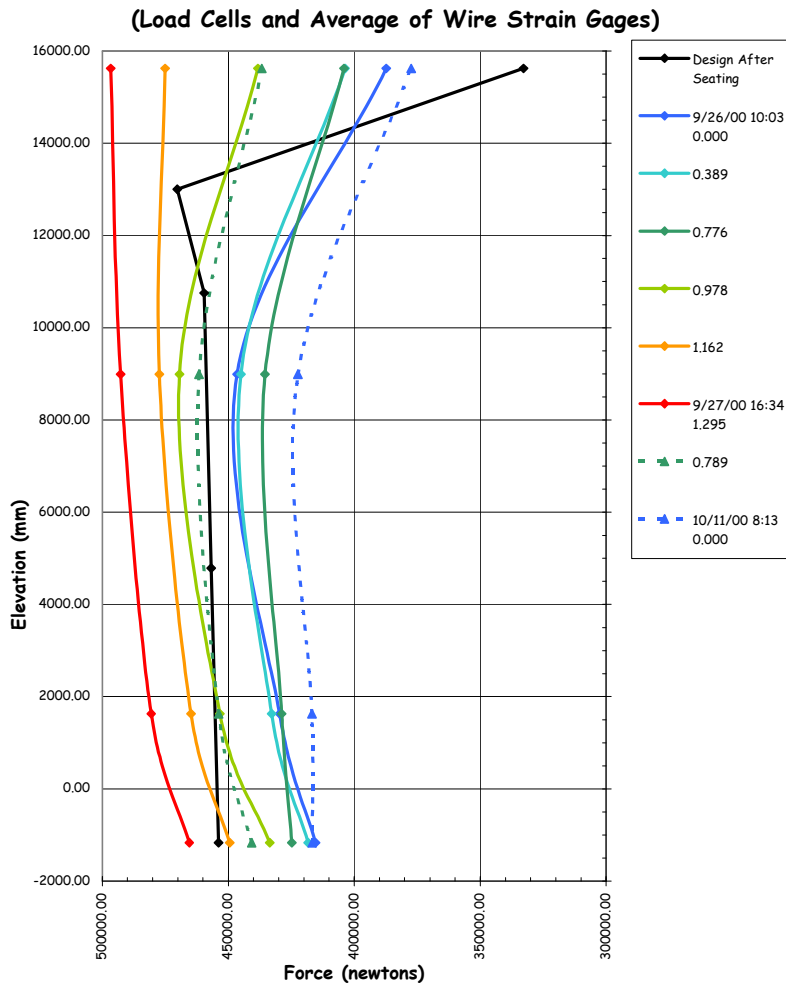


Figure 5.69 V37 Tendon Force Distribution, Azimuth 240 degrees

5.3.2.2 Posttest Inspection

Post-LST inspection of the PCCV model consisted of external crack mapping, visual inspection of the liner and metallurgical examination of the liner tears, and posttest measurements around the E/H.

5.3.2.2.1 Crack Mapping

New cracks and extensions of existing cracks within the crack mapping zones resulting from the LST (see Fig. 5.8) were traced in red and the surface was photographed to document the crack locations (e.g. Fig 5.22). The cracks were then transferred to the crack map drawing, shown in Figure 5.76, which shows all the major cracks identified after various loading stages. In general, concrete cracking was not extensive or very severe, with the exception of some areas around the E/H and some of the smaller penetrations. As noted in Chapter 3, there was no effort to measure crack widths. While it can be observed that some of the larger cracks around the E/H are near the liner tear locations, there was no further effort to correlate the crack locations with other events or data.

65-5

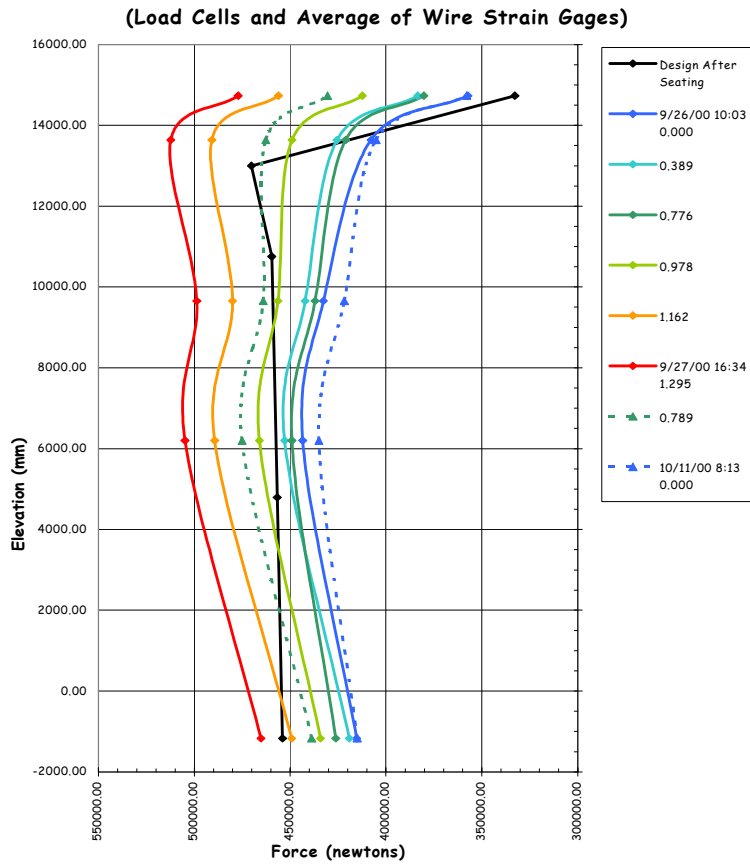


Figure 5.70 V46 Tendon Force Distribution, Azimuth 135 degrees

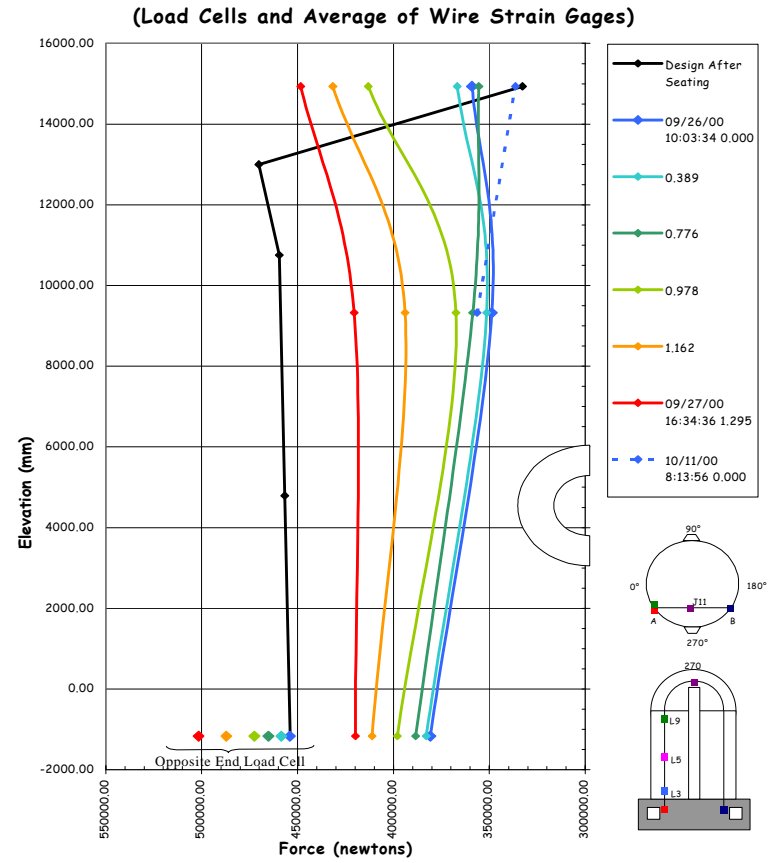


Figure 5.71 V85 Tendon Force Distribution, Azimuth 325 degrees

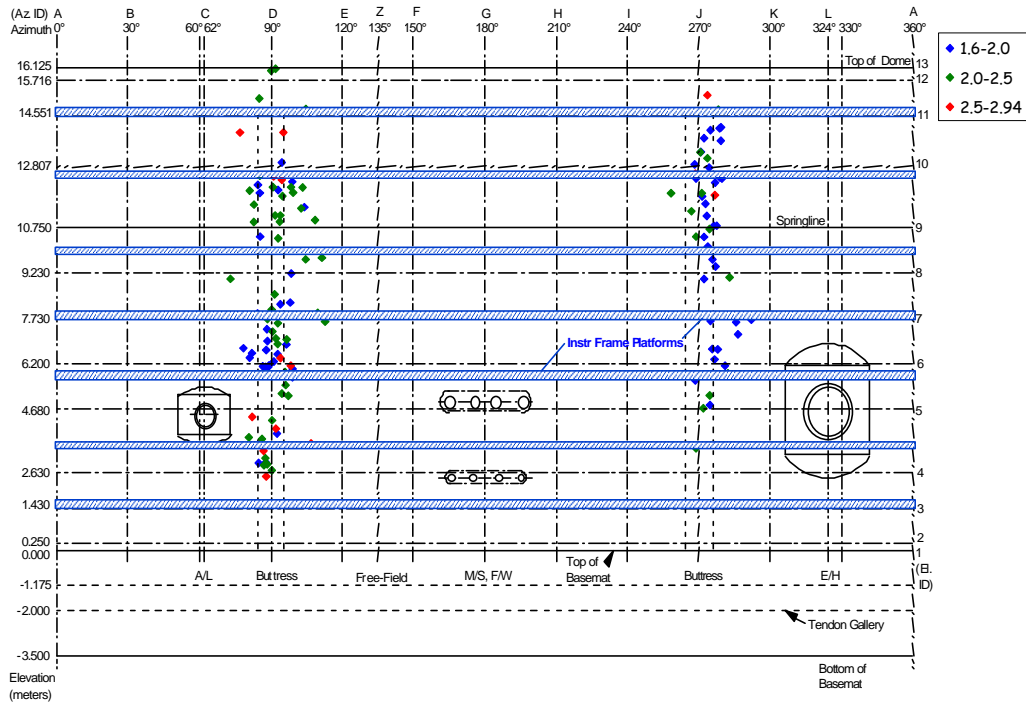


Figure 5.72 LST – Tendon Ping Acoustic Events

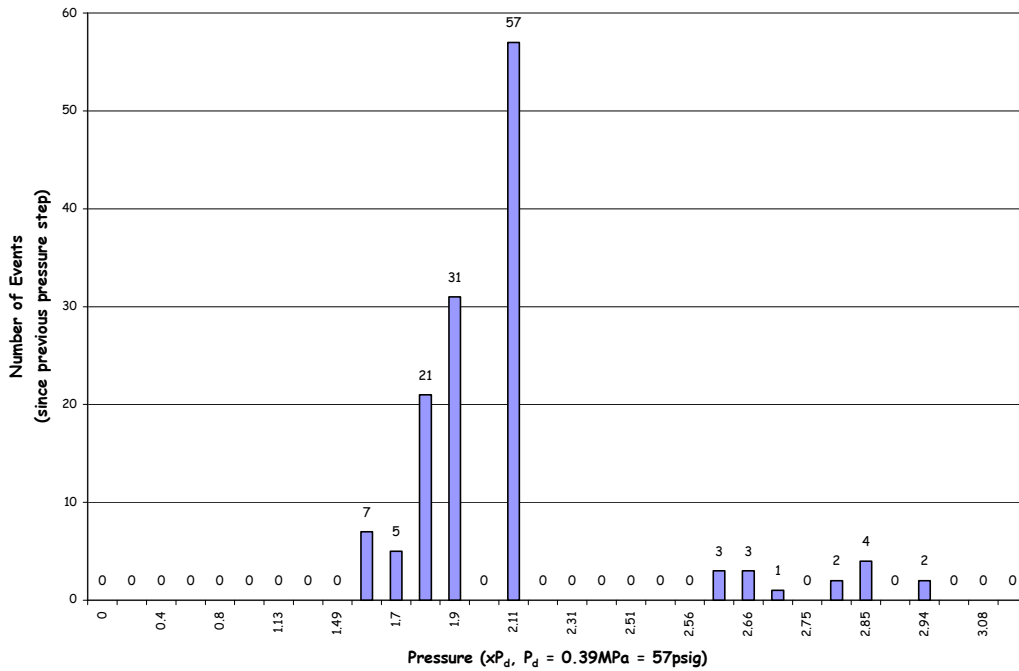


Figure 5.73 LST – Tendon Ping Event vs. Pressure Histogram

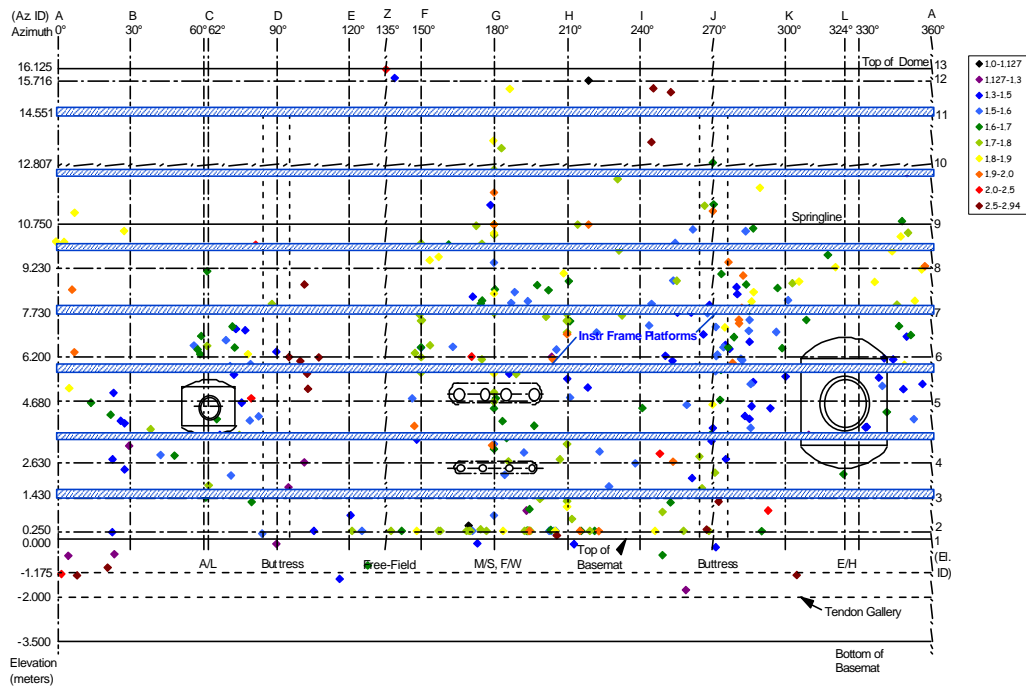


Figure 5.74 LST – Concrete Cracking Acoustic Events

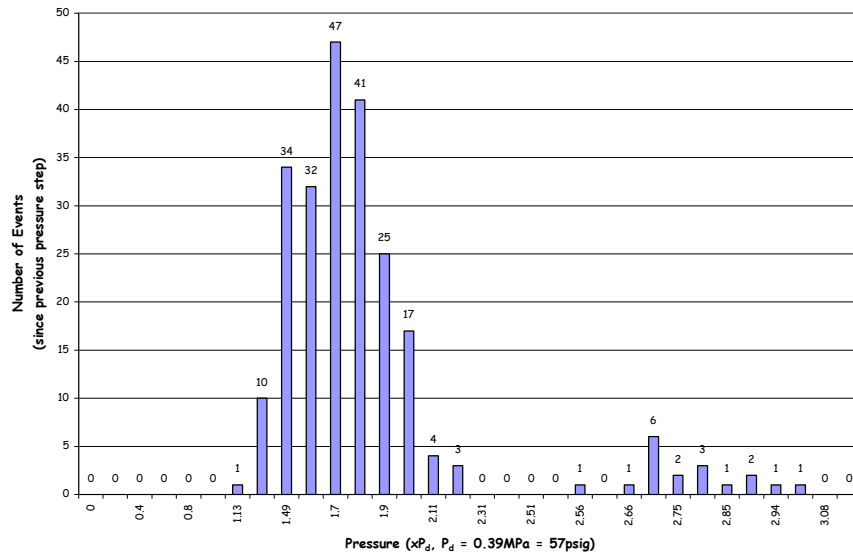


Figure 5.75 LST – Concrete Cracking Events vs. Pressure Histogram

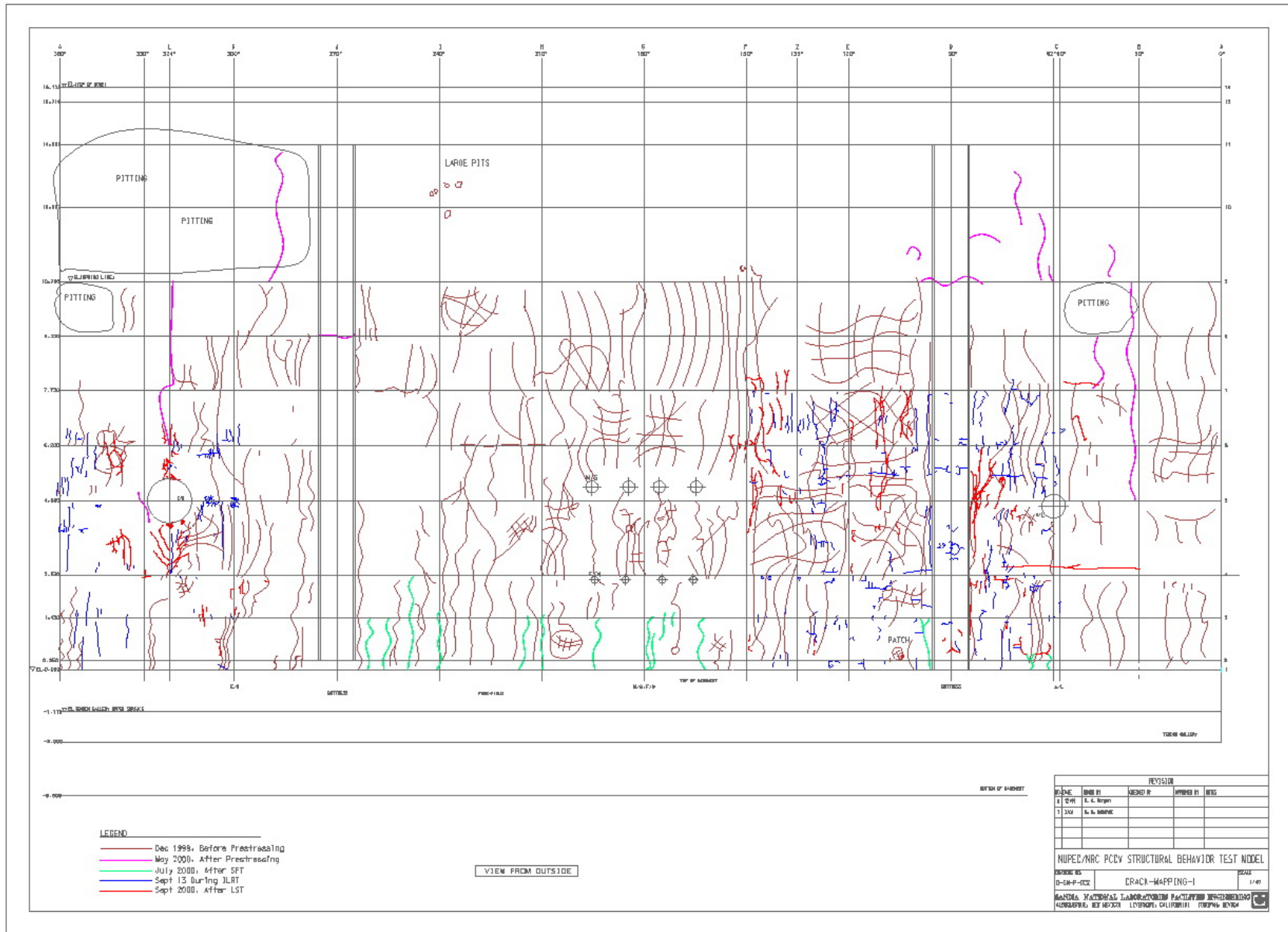


Figure 5.76 Post-LST Concrete Crack Map

5.3.2.2.2 Liner Inspection

As noted in Section 5.2.3, after entering the model following the LST, the liner surface was examined carefully and 26 discrete tears were found at 18 different locations, the grouping by location being somewhat arbitrary. The location of the tears are mapped in Figure 5.77. The location numbers are subsequently used to identify the tears.

One immediate observation was that each liner tear was at or very near a field weld seam in the liner. No tears were found in the undisturbed parent material or at a shop weld.

The acoustic events, later associated with the sound of the nitrogen gas escaping through the liner tears, are superimposed on the tear map in Figure 5.78, along with the approximate pressure levels when these events were first detected. The first tearing event appears to be clearly associated with the tears along the edge of the E/H embossment (#7, #12, #13, and #15), although it is arguable which of these occurred first. The other acoustic tearing events cannot be as clearly identified with any specific tear or tears, and, near the end of the test, it may have been difficult to distinguish the separate 'tearing' events from each other since gas continued to escape through each tear after it occurred.

A typical liner tear (#2) as it appeared during the initial inspection is shown in Figure 5.79. In addition to the liner tears, a pattern of buckling appeared throughout the middle section of the cylinder wall. The buckling pattern, also illustrated in Figure 5.79, is believed to have occurred during depressurization, when the permanently stretched liner could not accommodate the elastic recovery of the cylinder wall.

After the initial inspection of the liner, a more methodical inspection was undertaken. Each tear was photographed and matched with photographs of the 'backside' of the liner before the concrete was placed. (One early program decision was to photograph the entire length of every field weld made during the fabrication of the liner. While this was a very time-consuming and painstaking task, the benefit obtained in understanding the causes of the liner tearing was worth the effort.) A sample of the pre-LST exterior condition compared to the post-LST interior condition for Tears #7, #12, #13 and #15 at the E/H, #2 at a free-field weld seam, and #16 at a 'rathole' detail are shown in Figures 5.80 to 5.85.

The paint was then removed from each tear, allowing the liner tear to be seen without being obscured by the paint. Each tear was then photographed again for documentation. Figure 5.86 shows a close-up of Tear #13 after removing the paint. With the paint removed, it was clear that the weld was repaired or had been reworked by grinding at nearly every tear. Note the grind marks in Figure 5.86, which occurred during erection and welding of the liner. (The paint was removed by using chemical strippers; no paint was removed by mechanical methods.)

While this initial inspection was being completed, a detailed posttest liner inspection plan was being developed. After reviewing the plan with NUPEC and the NRC, the plan, consisting of the following elements, was implemented.

1. In-situ examination:
 - a. In addition to the visual/photographic records, ultrasonic thickness measurements were made at each tear location and at several baseline locations where tears did not occur.
2. Destructive examination:
 - a. Twenty-five liner specimens were removed from the model (see Figures 5.87 and 5.88).
 - b. Eighteen of the liner specimens were subjected to metallographic analysis.
 - c. Sample weld specimens were subjected to metallographic analysis.
 - d. After the liner specimens were examined by SNL, the unused portions were sent to NUPEC for further examination. The results of NUPEC's examination have been reported separately.

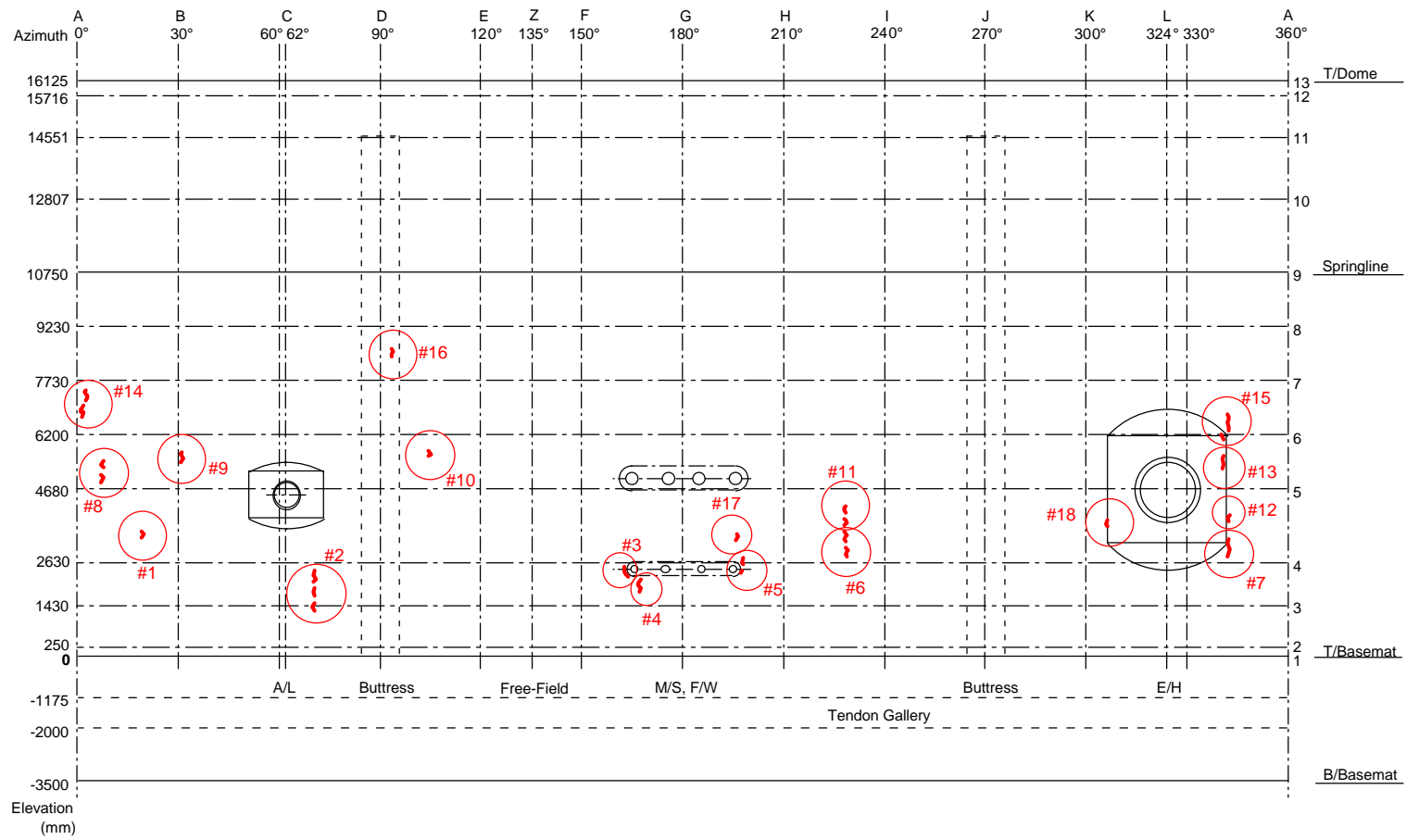


Figure 5.77 Post-LST Liner Tears

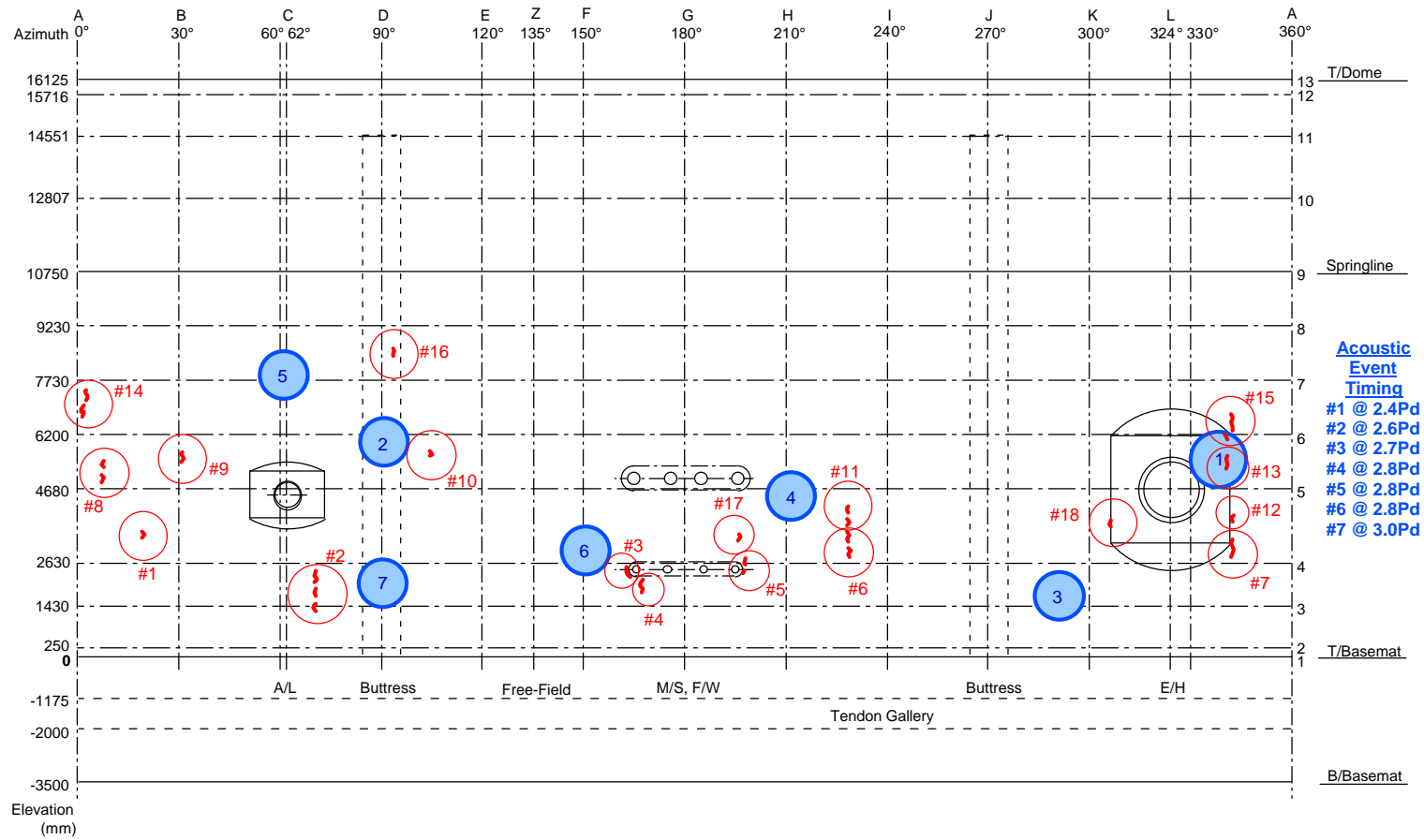


Figure 5.78 Liner Tears and Acoustic Event Locations

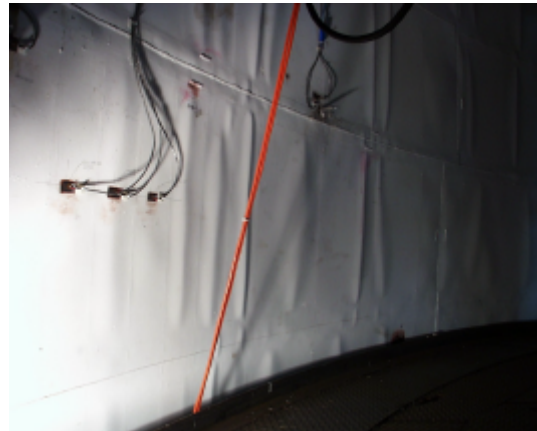
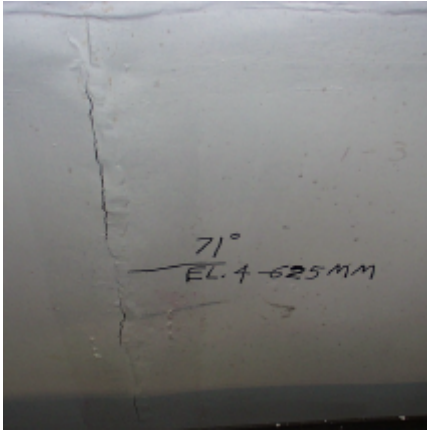


Figure 5.79 Post-LST Liner Tear (#2) and Liner Buckling

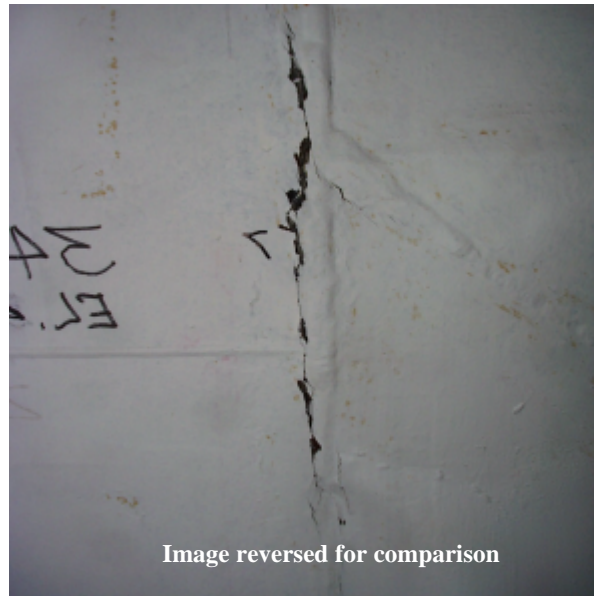


Figure 5.80 Tear #7 at E/H



Figure 5.81 Tear #12 at E/H



Figure 5.82 Tear #13 at E/H

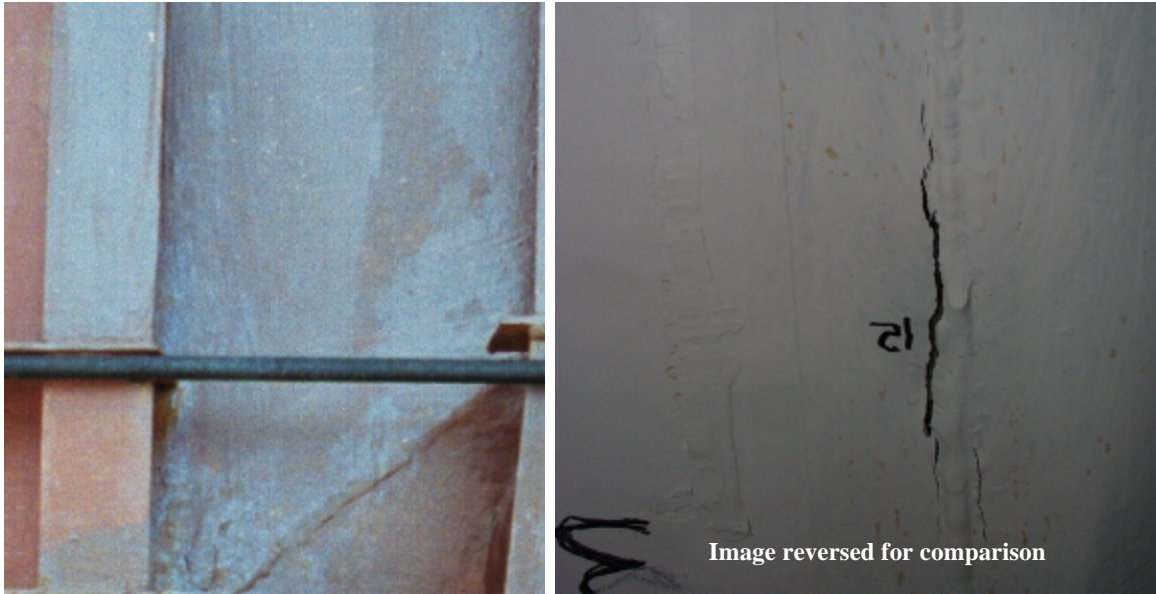


Figure 5.83 Tear #15 at E/H



Figure 5.84 Tear #2, Free-Field



Figure 5.85 Tear #16 at Rathhole Detail

The results of the liner inspection are detailed in Appendix L. The conclusions of the inspection and metallographic analysis are repeated below.

1. Nearly all of the tears occurred in areas where the liner thickness was reduced ~25% or more by grinding done in association with repair welding. Extensive localized plastic deformation culminating in ductile tearing occurred in these thinned areas as the structure was being tested. This appears to have been the most prevalent cause of liner failure.
2. In samples where quantification was possible, it appears that the reduced thickness at the point of failure was up to 50% of the local material thickness.
3. At the E/H
 - a. #15: 50%-60% reduction by grinding
 - b. #13: 25% reduction by grinding
 - c. #12: >10% reduction by grinding
 - d. #7: 25% reduction by grinding
4. @ the Free-Field
 - a. #16-1 (D7): no tear, no repair ~10% reduction in thickness (post-LST)
 - b. #16-2: tear, single weld repair, thickness reduction on both sides of weld
5. Geometric features may also have contributed to the formation of some tears. These include structural transitions, such as those at the feedwater penetration and the equipment hatch transition boundaries, discontinuities in horizontal stiffeners, and discontinuities in weld back-up bars. A missing segment in a horizontal back-up bar appears to have been primarily responsible for one tear (#16).
6. Only one tear occurred in association with a material or weld defect. A lack-of fusion weld defect was found at the initiation site of tear #1.
7. The specially produced quarter-scale liner material exhibited mechanical properties that may have made it particularly prone to plastic strain localization and tearing. While nearly conforming to the specifications for full-thickness material, the quarter-thickness plate exhibited a yield strength much higher than the specified minimum (383 MPa compared with 225 MPa) and an unusually high yield-to-ultimate-strength (YS/UTS) ratio (0.77). This high YS/UTS ratio is qualitatively consistent with extensive localized plastic strain culminating in ductile tearing in regions where more than ~25% of the liner thickness had been ground off, as was observed near most of the tears.



Figure 5.86 Close-Up of Tear #13 after Removal of Paint



Figure 5.87 Liner Specimen at Tear #2



Figure 5.88 Liner Specimen at Tear #15

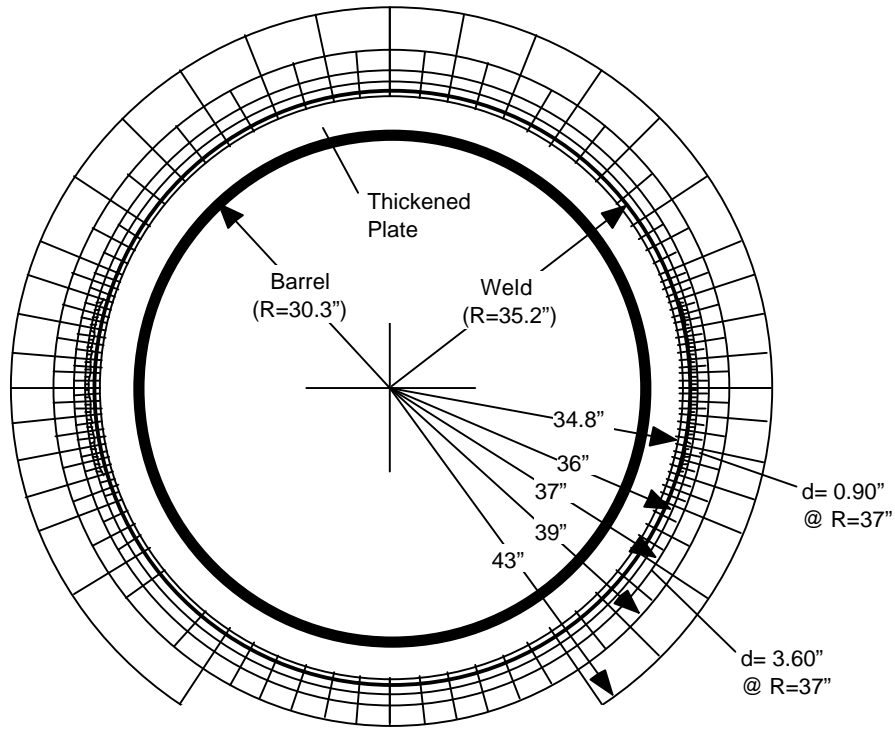
8. Tensile and hardness tests on welded test samples indicated that modest amounts of plastic strain localization should be expected in the weld-heat-affected zones, but to a much lesser extent than observed in association with the liner tears. Consistent with this, smaller (but significant) amounts of localized plastic strain were observed adjacent to some welds that had not been repaired or ground. These strains were sufficient to initiate necking in the most severely strained regions. However, with the possible exception of tear #12, there was no indication that tearing was imminent in regions other than those where repair welding and substantial grinding had been done.
9. The mechanical testing results did not suggest that deficiencies in the properties of either the base metal or weld metal, nor excessive softening in the weld-heat-affected zones, could account for the extensive localized plastic deformation culminating in tearing that appeared to occur in the liner.

In summary, it is apparent that the onset of liner tearing at $2.5P_d$ resulted, to a significant degree, from the difficulty of field welding the very thin liner. The conditions that led to the liner tearing would not be present to the same degree in the prototype, and the initiation of tearing might be delayed until a higher pressure was achieved. Nevertheless, in spite of the liner welding difficulties, it is also apparent that the near field strains in the vicinity of a liner discontinuity must be large enough to initiate a tear because all the tears were initiated at vertical weld seams within the middle portion of the cylinder wall.

5.3.2.2.3 Posttest Measurements

As described in Section 3.2.5.4, a grid was constructed around the E/H to measure the residual strain field after the test. The pretest analysis predicted large strains near the perimeter of the thickened insert plate surrounding the E/H barrel and near the anchors and stiffeners that terminated near the insert. The grid, shown in Figure 5.89, was drawn, and the position of the grid points was obtained using a 3D digital position mapping tool. After the LST, the grid points were mapped again and the pre- and posttest positions were plotted in Figure 5.90.

Unfortunately, as noted previously, the strains in this region were very small and the resulting residual displacements are barely distinguishable from the pretest positions, given the precision of the digital probe. As a result, no useful information was obtained by this effort.



E/H Inside View

Figure 5.89 E/H Displacement Grid

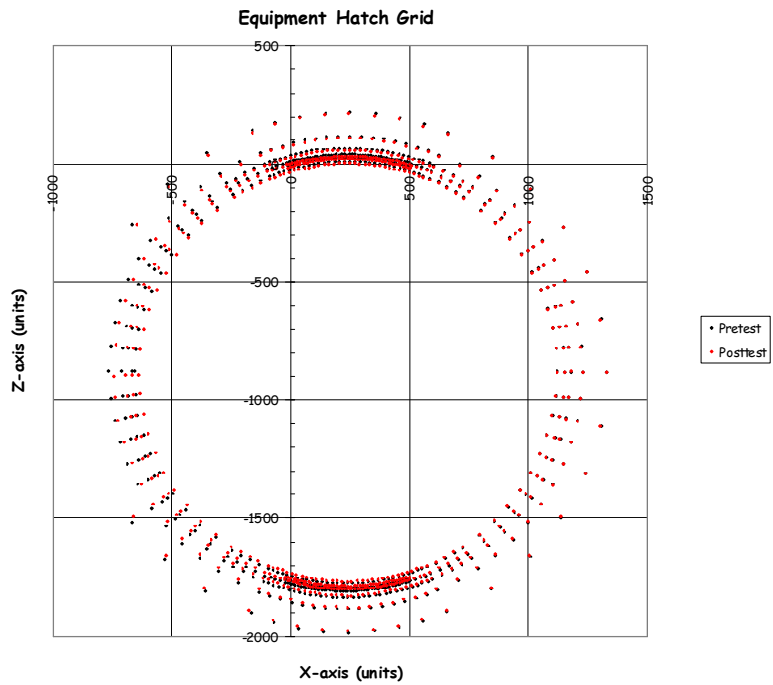


Figure 5.90 E/H Post-LST Displacement

5.3.3 Structural Failure Mode Test Results

5.3.3.1 Test Data

The Structural Failure Mode Test data (DYN only) is provided on the enclosed data CD in Excel[®] spreadsheets, as noted in Section 5.3.1. The response of every functioning transducer in the revised instrumentation suite is provided. The following sections present a synthesis of the data focusing on the critical response measurements.

5.3.3.1.1 Displacements

As for the LST, the displacement data provides the most comprehensive view of the overall or global response of the model. Since the displacement transducers had to be waterproof, a reduced suite of gages was used during the SFMT. Based on the results of the LST, two vertical arrays at Azimuth 135 degrees and 324 degrees, and one horizontal array at Elev. 4680, were employed for the SFMT, as shown in Figure 5.26. Figures 5.91 through 5.93 show the radial displacement response as a function of pressure along these cardinal lines. Since the displacement transducers had to be removed after the LST to install the elastomeric liner and new transducers were installed for the SFMT, the displacements were ‘zeroed’ prior to the start of the SFMT on November 6, before filling the vessel with water. The displacements therefore reflect only the response to pressure (including the hydrostatic pressure) and not the effects of prestressing, nor any other previous loading. Note that the pressures shown are the effective pressure, i.e. the volume weighted average pressure in the model.

During the SFMT, the displacement response of the model is essentially linear to just beyond 3.0 Pd, when global yielding begins to occur prior to rupture. The initial stiffness of the model, however, is less than the initial stiffness during the LST. Figure 5.94 compares the response at the mid-height of the cylinder (Z6) during the LST and the SFMT. (The SFMT response was offset in this figure by adding the residual displacement at the end of the LST to facilitate comparison.) This figure shows that the hoop stiffness during the SFMT is essentially identical to the post-cracking stiffness during and after the LST. It also shows that the SFMT displacement is nearly identical to the LST displacement at the maximum LST pressure, suggesting that, if the LST had continued, the response would have been virtually

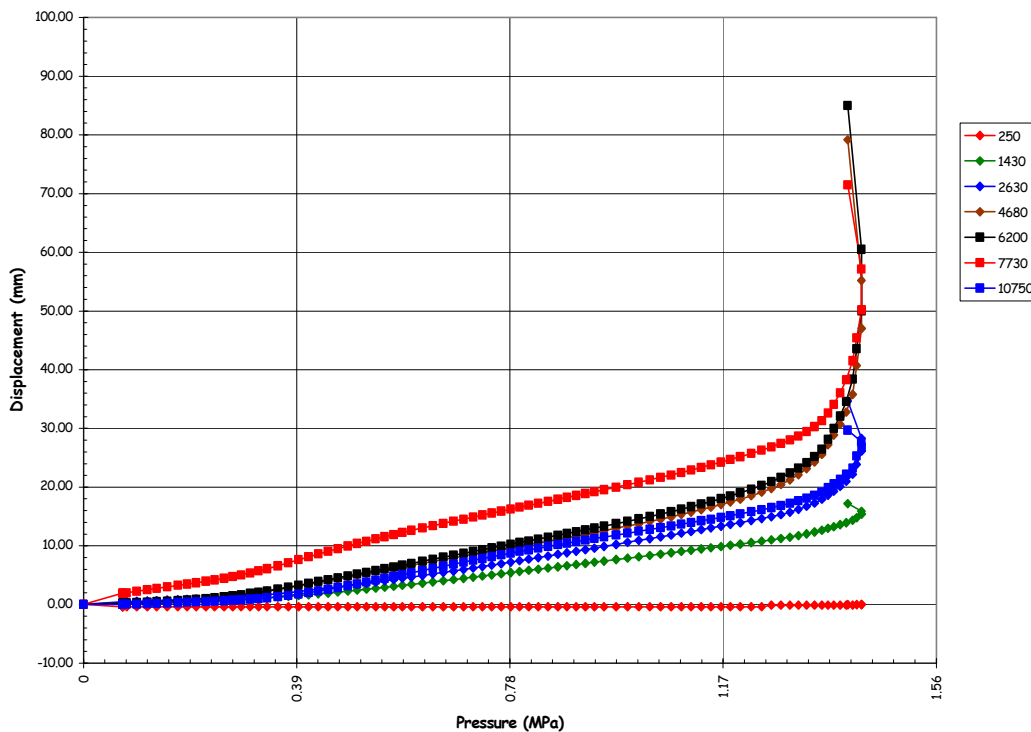


Figure 5.91 SFMT – Radial Displacement at Azimuth 135 degrees (Z)

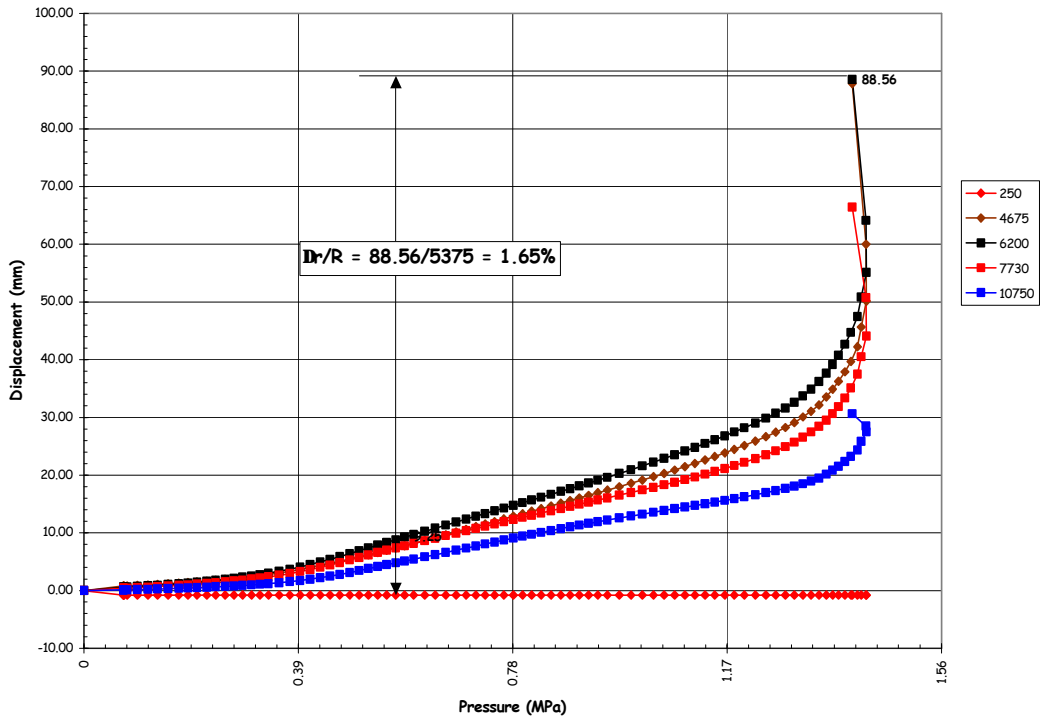


Figure 5.92 SFMT – Radial Displacement at Azimuth 324 degrees (L)

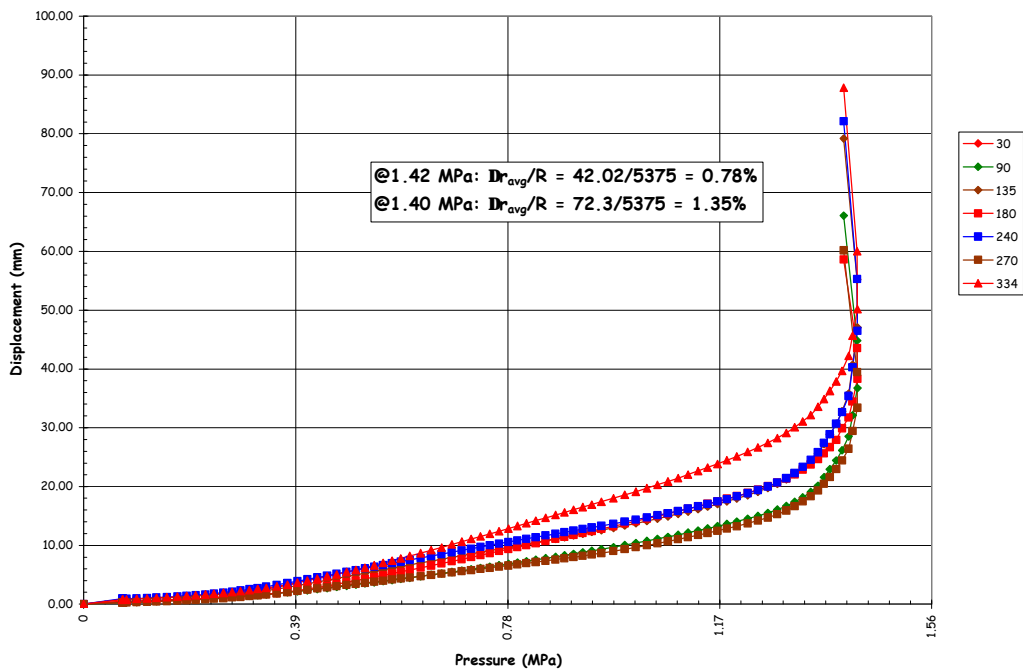


Figure 5.93 SFMT – Radial Displacement at Elev. 4680 (5)

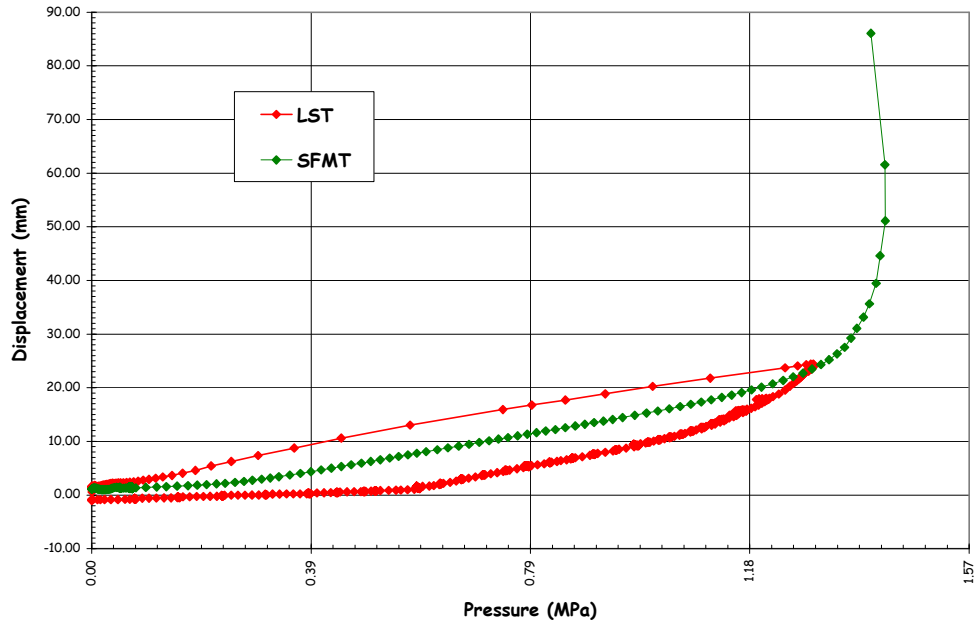


Figure 5.94 SFMT – Radial Displacement at Azimuth 135 degrees, Elev. 6200

identical to that measured during the SFMT. Similarly, the vertical displacements at the apex (offset again) are compared in Figure 5.95.

Since the SFMT was conducted as a continuous pressure test with no holds for gage stability of leak checks, there were no discontinuities in the response histories.

The peak displacements shown in the plots were the final readings obtained before the model ruptured and the gages were destroyed. The pressure values at and beyond the peak were recorded at the beginning of the data scan. Since each scan took approximately 30 seconds, the pressure may have increased (or decreased) during the scan. Note that a few data scans were completed after the peak pressure was reached. The post-peak values may indicate some ‘softening’ of the model. However, it is more likely that the plots reflect the drop in pressure due to the rapid expansion and increasing leakage just prior to rupture.

Figure 5.92 displays the displacements at Azimuth 324 degrees, which coincides with the centerline of the E/H. The largest radial displacement recorded during the SFMT, 88.56 mm, again occurred at this azimuth at elev. 6200, above the E/H. Computing the equivalent hoop strain due to pressure at this location from kinematics,

$$@P_{\text{final}} = 3.58P_d: \quad \frac{\Delta r}{R} = \frac{88.56}{5376} = 1.65\% .$$

At the peak pressure, $3.65P_d$, the displacement was 55.12 mm, yielding an equivalent hoop strain of 1.02%

Figure 5.93 compares the displacement response as a function of azimuth at elev. 4680, nominally the mid-height of the cylinder and the centerline of the E/H, A/L, and M/S penetrations. The response is not as uniform as was observed during the LST. Nonetheless, averaging the radial deformation due to pressure yields a nominal average hoop strain of 0.78% at the peak pressure $3.65P_d$. Similarly, the average hoop strain at $3.58P_d$, just prior to rupture, was 1.35%.

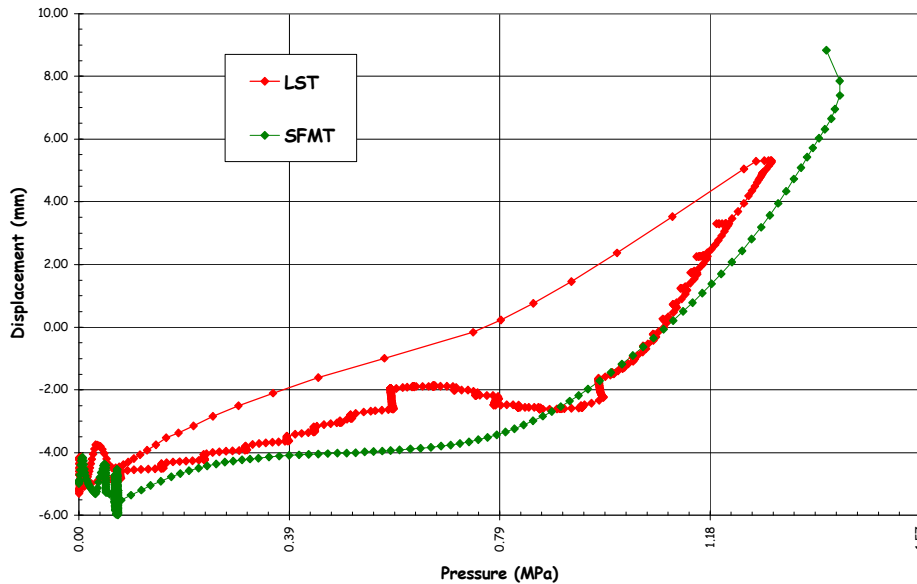


Figure 5.95 SFMT – Vertical Displacement at Apex

The vertical displacements are shown in Figure 5.96. The maximum vertical displacement at the springline was 10.84 mm at Azimuth 135 degrees, essentially the same as during the LST, and 5.94 mm at Azimuth 324 degrees, less than during the LST. The reason for the small displacement at 324 degrees is not immediately obvious; however, it might be the stiffening effect of the E/H embossment, although this was not observed during the LST. Nevertheless, it is clear that the vessel did not yield in the vertical direction and the vertical strains were still on the order of 0.1%.

Deformed profiles of the PCCV model, constructed from the displacement data in a similar manner as those constructed for the LST, are shown in Figures 5.97 through 5.100. For the SFMT, the initial position was again assumed to be defined by the as-built model survey data (Appendix C). However, since the gages were zeroed prior to the start of the SFMT, any deformations of the liner surface or the wall are not reflected in the data.

The as-built position of the PCCV model is plotted in the first portion of the figures, along with the deformed shapes due to the hydrostatic pressure (H_2O) and at approximately $1.0P_d$, $2.0P_d$, $2.5P_d$, $3.0P_d$, $3.5P_d$, and $P_{max} = 3.63P_d$. The second portion of each figure provides a more refined breakdown between $3.0P_d$ and $3.63P_d$ and the profile at $P_{final} = 3.57P_d$, immediately prior to rupture of the vessel. These figures dramatically illustrate the large deformations that occur as the vessel yields, even though the pressure is dropping. The displacement nearly doubles as the pressure drops from $3.63P_d$ to $3.57P_d$.

A most provocative observation after considering the displacement data and the global response of the model is that the relatively small pressure increase between the LST and the SFMT, from $3.3P_d$ to $3.6P_d$ (approximately 10%), made the vessel go from a relatively benign and only slightly damaged step to total collapse. It is reasonable to speculate what the response of the model might have been if the liner had not torn and leaked at $2.5P_d$, arguably prematurely, and it had been possible to pressurize it to $3.6P_d$ pneumatically.

5.3.3.1.2 Liner Strains

Since the liner was damaged during the LST and large portions were removed for metallographic analysis, the response of the liner was not a critical objective during the SFMT. Nevertheless, 18 exterior gages (the interior ones were

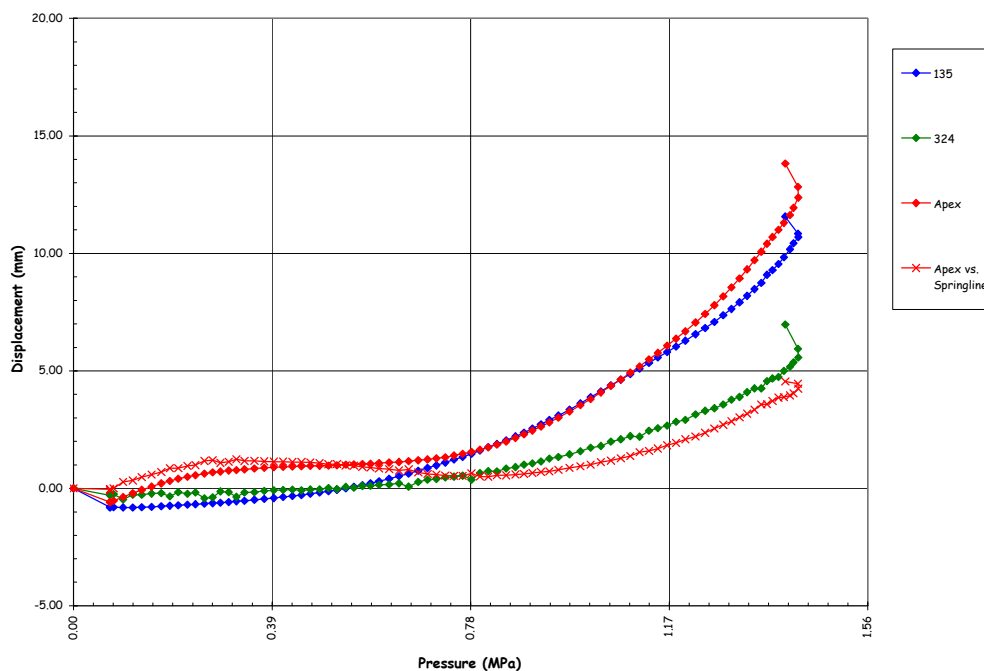


Figure 5.96 SFMT Vertical Displacements at Springline (El. 10750) and Apex

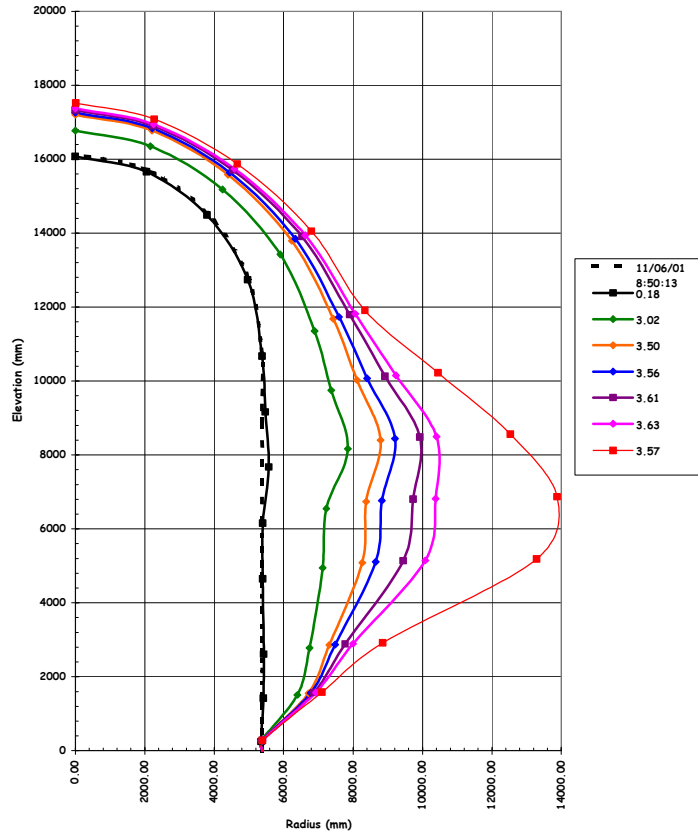
removed prior to installing the elastomeric liner) were monitored during the SFMT to provide some information on the liner response at higher pressures and for comparison with other instruments. Of the 18 strain gages selected, three failed

before filling the model with water. The remaining gages at the wall-base junction and the two external gages at D7 also appeared to have been damaged prior to the test, possibly by water leaking from the model. As a result, meaningful data was only obtained for three liner strain gages.

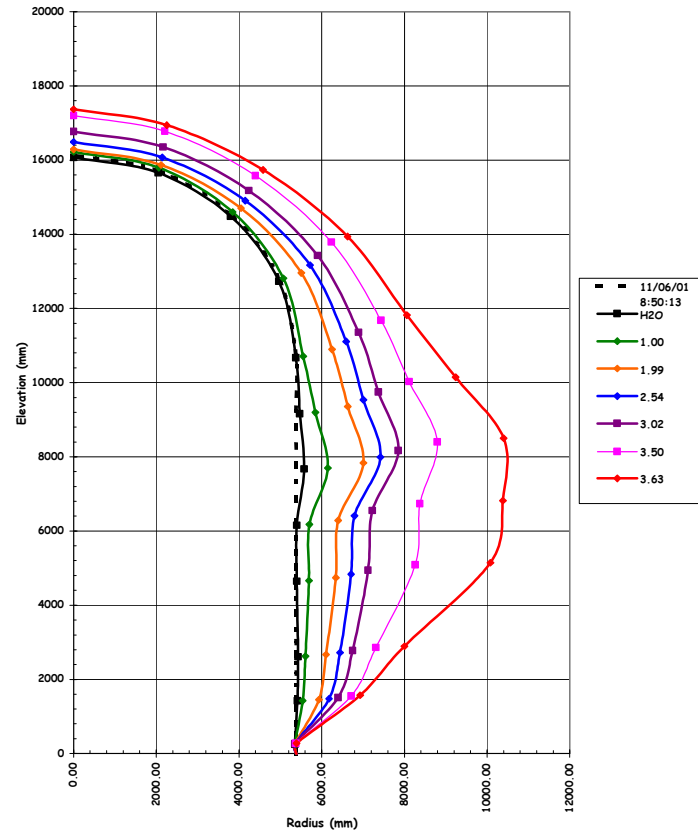
The strain histories for the surviving gages are plotted in Figure 5.101. These gages measured the hoop liner strain inside a rathole (see drawing D-SN-P-209, Appendix E) at Azimuth 0 degrees, elev. 7730 (A7) and Azimuth 135 degrees, elev. 4680 and 6200 (Z5 and Z6) at the mid-height of the cylinder. The maximum liner strains at Z5 (1.9%) and Z6 (1.5%) are consistent with the strains calculated from the displacements. At A7, nearest the location where the model ruptured, the hoop strains were consistently lower than those at Z5 and Z6, even going into compression, until the peak pressure was reached, when the strain increased rapidly to a maximum of 1.5% tension. While these were not free-field gages, they nevertheless gave some indication of the hoop strains in the liner.

5.3.3.1.3 Rebar and Concrete Strains

Eighty-two rebar and gage bar gages were selected for monitoring during the SFMT. Of these, four of the main rebar strain gages and all the gage bar strain gages appear to have failed before $0.5P_u$. The strain histories for all 31 surviving rebar gages are shown in Figures 5.102 to 5.104. The maximum free-field hoop rebar strain was 1.4% (RS-C-Z6-02). The maximum free-field meridional rebar strain was 0.3% (RS-M-D6-02). These values are consistent with the global strains based on displacement data. The rebar strains at the wall-base junction show the effect of bending but combined with the other meridional strains, confirm that the model was still essentially elastic in the vertical direction.

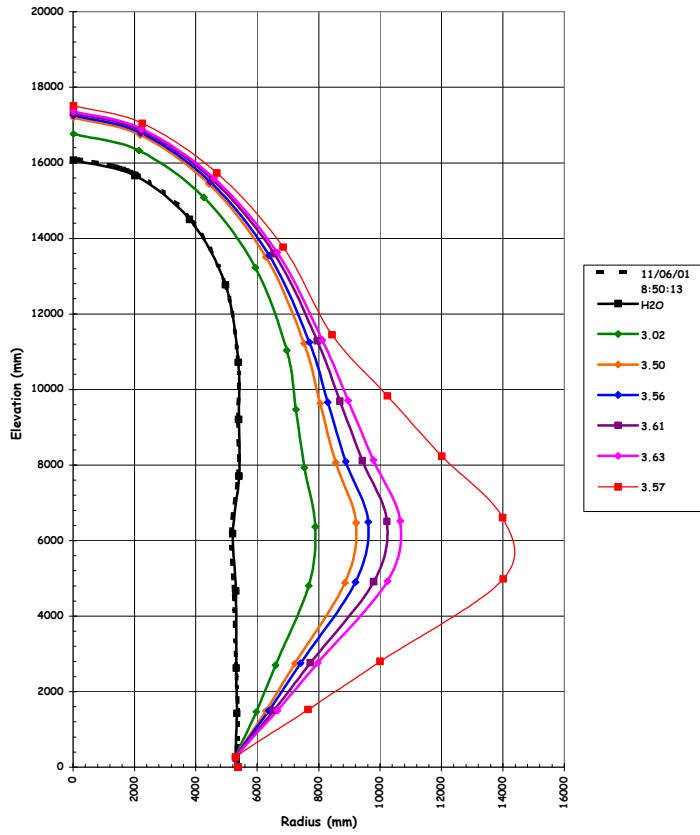


(a) $0P_d$ to $3.63P_d$

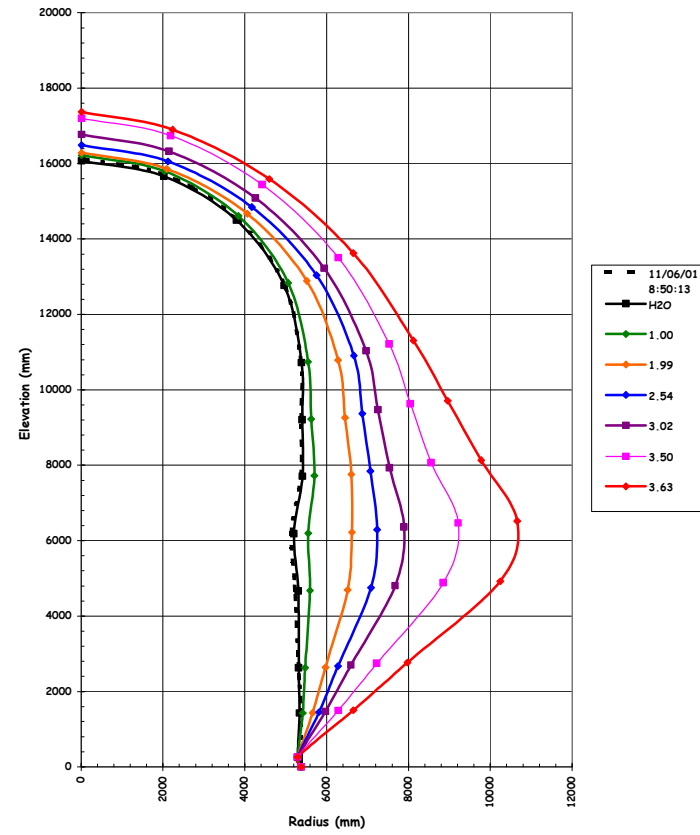


(b) $3.0P_d$ to $3.63P_d$

Figure 5.97 SFMT - Deformation at Azimuth135 Degrees (Z) \times 100



(a) 0Pd to 3.63Pd



(b) 3.0Pd to 3.63Pd

Figure 5.98 SFMT - Deformation at Azimuth 324 Degrees (L) × 100

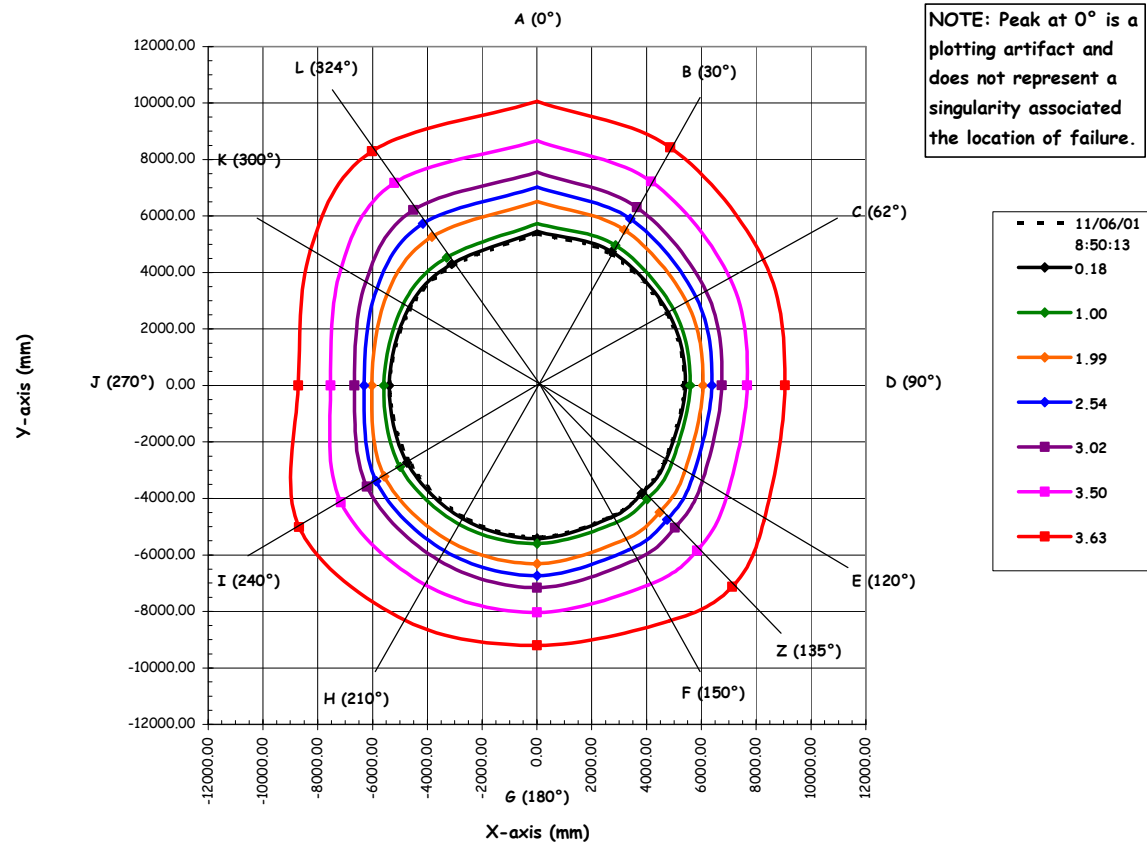


Figure 5.99 SFMT - Deformation at Elev. 4680 (5) × 100 - 0P_d to 3.63P_d

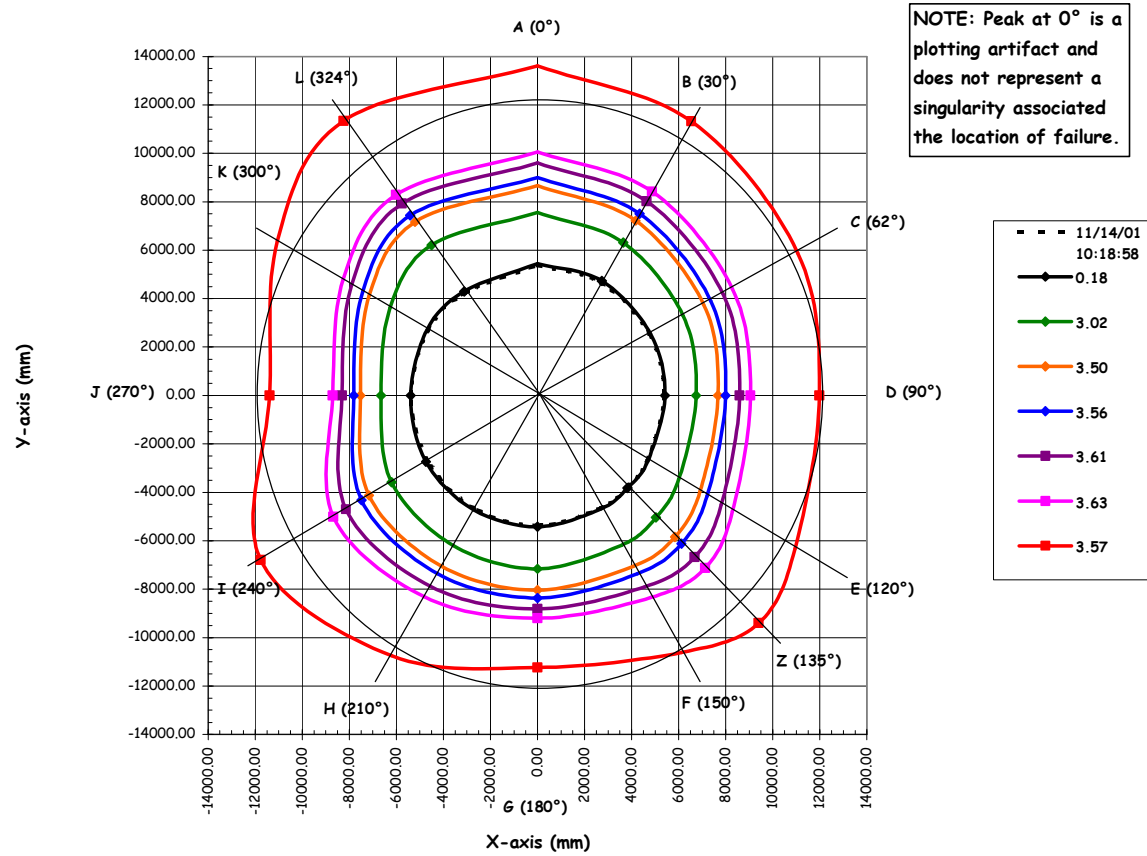


Figure 5.100 SFMT - Deformation at Elev. 4680 (5) × 100 – 3.0P_d to 3.63P_d

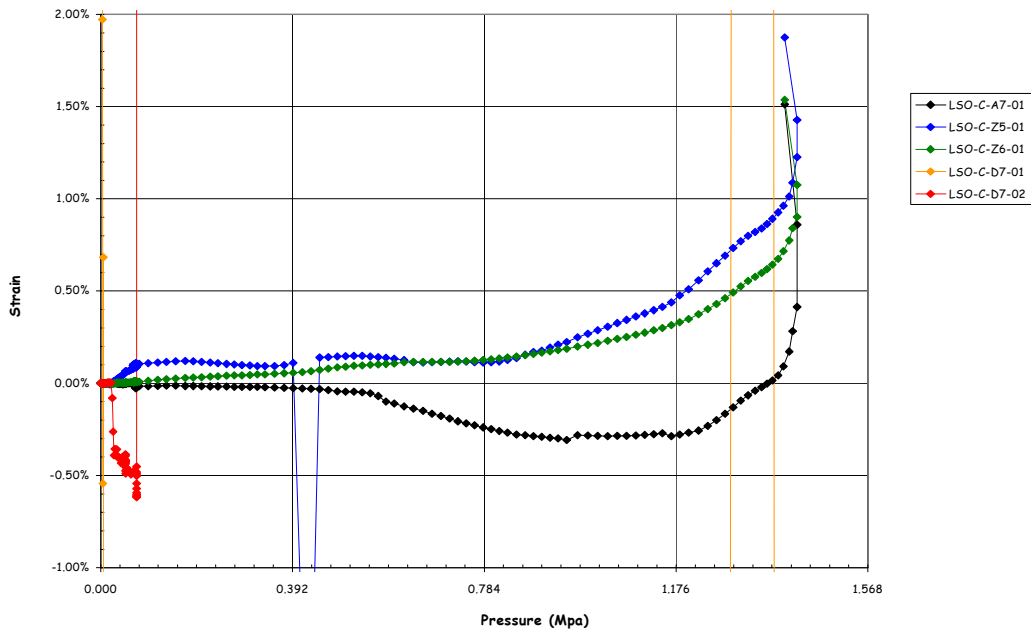


Figure 5.101 SFMT Exterior Liner Strains

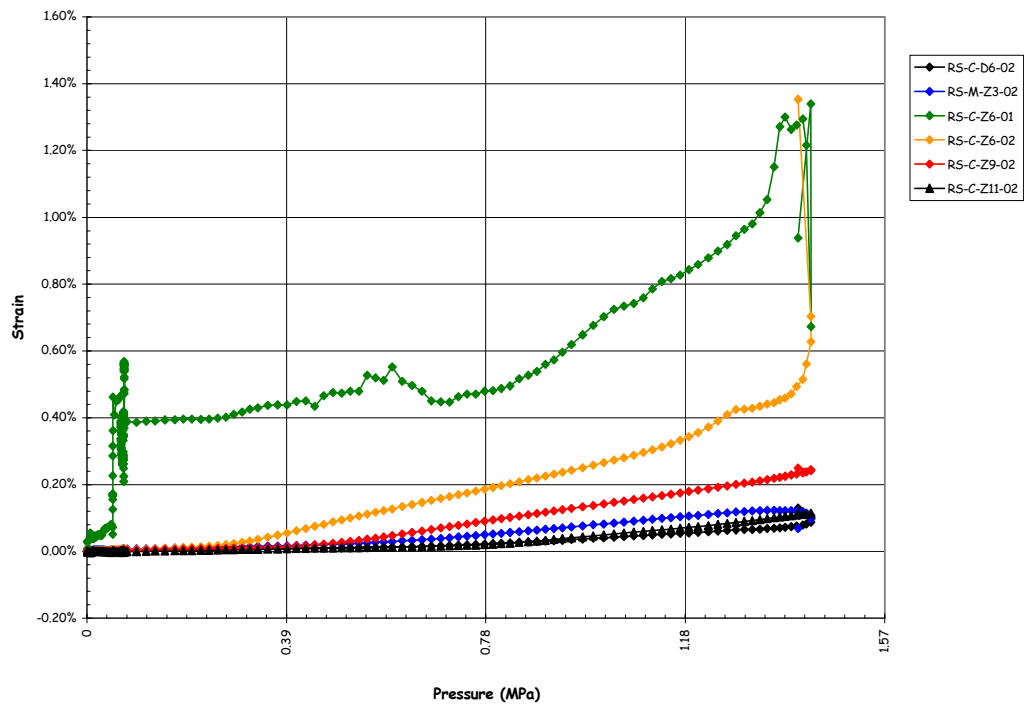


Figure 5.102 SFMT – Free-Field Hoop Rebar Strains

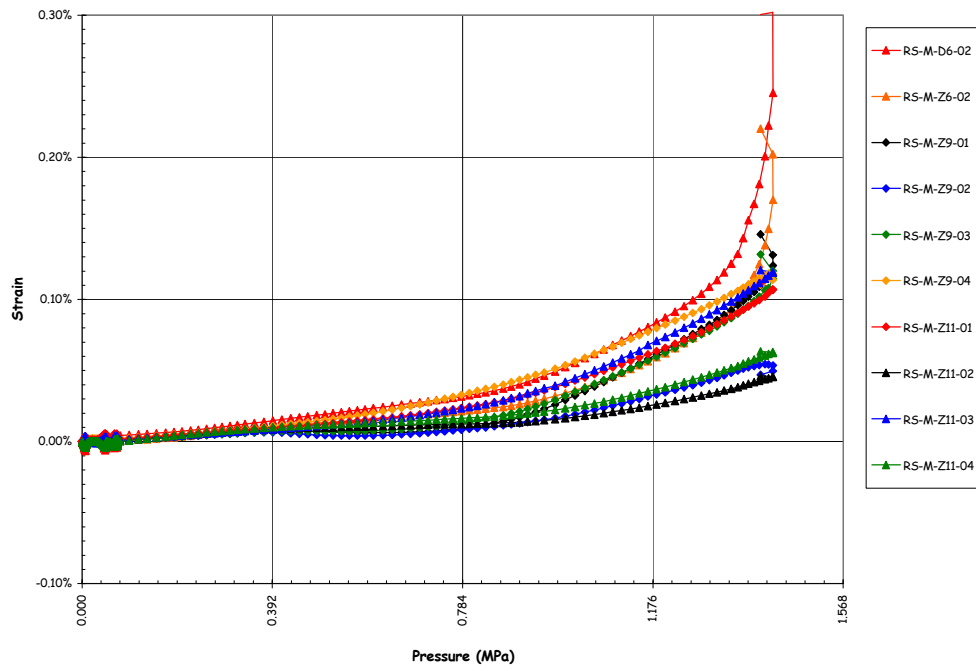


Figure 5.103 SFMT – Free-Field Meridional Rebar Strains

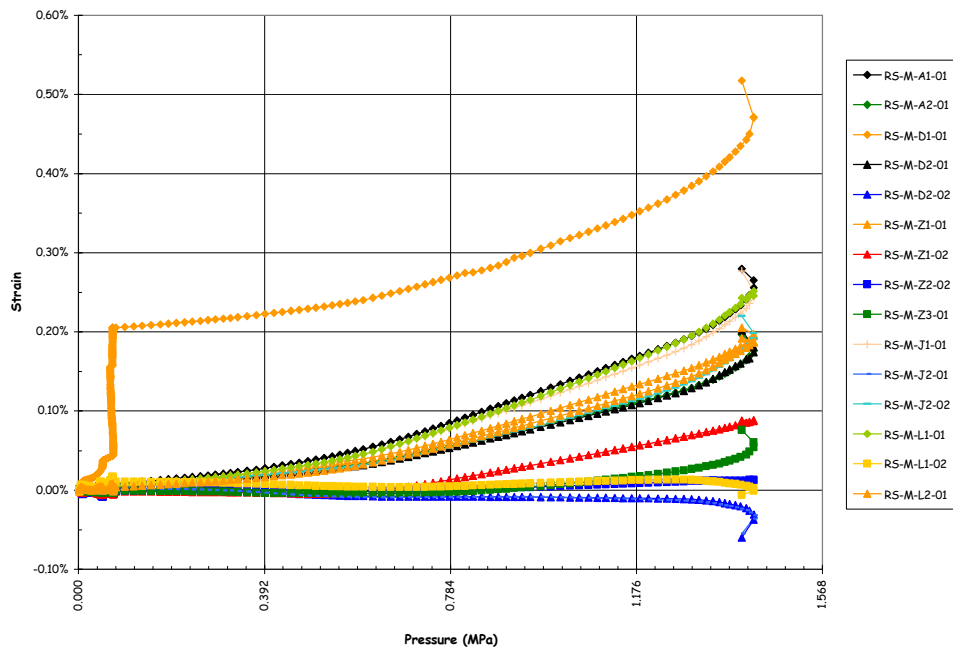


Figure 5.104 SFMT – Meridional Rebar Strains at Wall-Base Junction

Concrete strains, measured by the surviving SOFO fiber-optic gages, are plotted in Figure 5.105. The maximum hoop strain in the concrete, 1.1% (CE-C-Z6-01) at the mid-height of the cylinder, is a little lower than the displacement-based or rebar strains, but overall the concrete strains are consistent with the other measurements.

5.3.3.1.4 Tendon Forces and Strains

All the tendon load cells and strain gages that survived the LST were still functioning at the start of the SFMT and all were monitored during the test. Several load cells and tendon strain gages failed after filling the PCCV with water or early during the SFMT, presumably due to water leaks from the model damaging the gage or shorting out the wiring. The data for all the gages that were functioning at the start of the test are provided, however.

Figures 5.106 and 5.107 show the anchor forces for the instrumented tendons during the SFMT. These anchor forces are representative examples of all the tendon anchors. With the exception of one anchor on H53, the hoop tendon anchor forces increase to nearly 600 kN, which is close to the breaking strength of straight tendons in laboratory tests. It is reasonable to expect that the breaking strength of the curved tendons under field conditions would be lower than the laboratory breaking strength. Load cell TL-C-J6-01 on H53 exhibits an artificially high force near the beginning of the SFMT, most likely from moisture affecting the gage. However, the increased force due to pressure tracks very closely with the other load cells. The vertical tendon anchor forces do not show as large an increase, and the average maximum force only approaches 500 kN, well below the breaking strength. This is consistent with response during the LST and the observation that the vertical tendons did not fail prior to the rupture of the model.

Near the end of the test, sudden decreases in load were observed for several hoop tendon load cells and interpreted as individual strand wires breaking. After reaching the peak pressure, all the load cell readings dropped sharply as the tendons and the model ruptured.

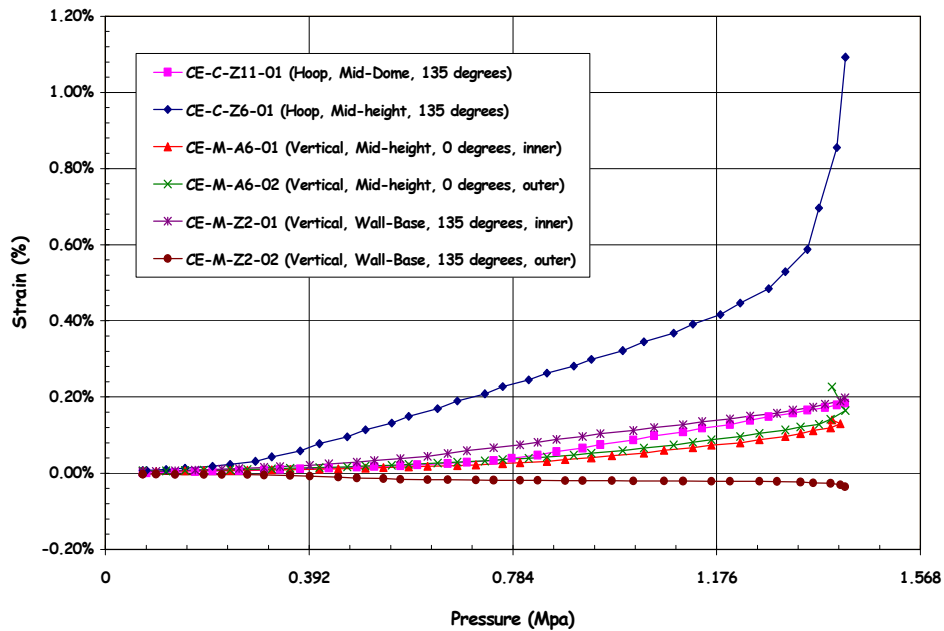


Figure 5.105 SFMT – Concrete (SOFO) Strains

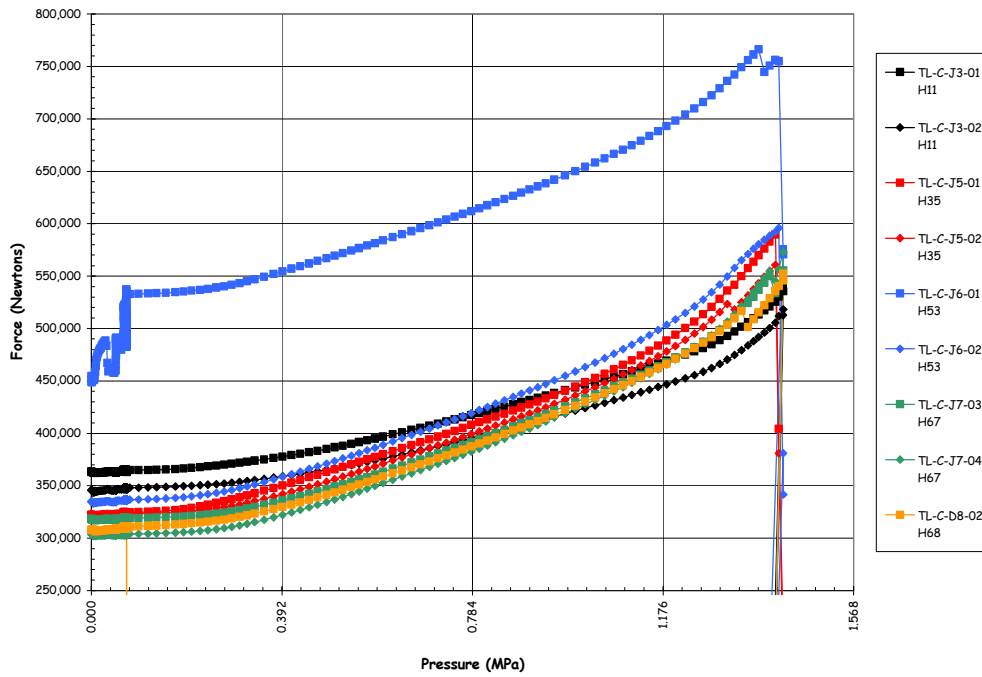


Figure 5.106 SFMT – Instrumented Hoop Tendon Anchor Forces

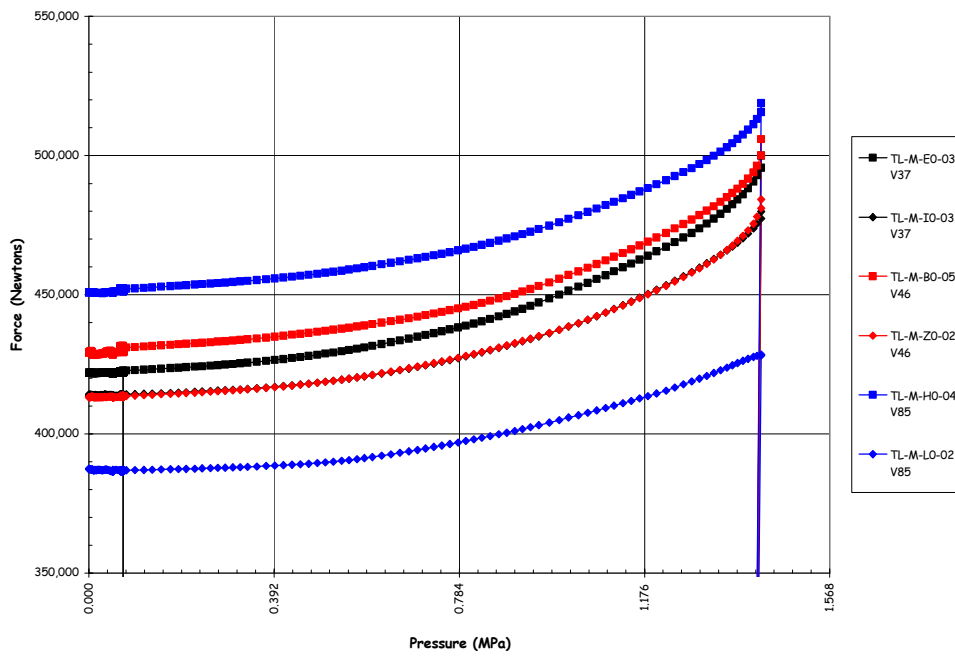


Figure 5.107 SFMT – Instrumented Vertical Tendon Anchor Forces

Tendon strains were also recorded using the surviving foil gages mounted on individual strand wires. Figures 5.108 and 5.109 show the strains for hoop tendons H53 and H68, and Figure 5.110 shows the strains for vertical tendon V46. These results are typical of the other instrumented tendons, although the magnitude of the strains vary. Since the strain gages were 're-zeroed' before the SFMT, only the strain due to pressure is plotted. The total tendon strain is the measured strain plus the residual prestressing strain, typically on the order of 0.4% for the hoop tendons and 0.6% for the vertical tendons. The hoop tendon strains at maximum pressure were therefore on the order of 1.0%, 0.4% due to prestressing plus 0.6% due to the maximum pressure of $3.65P_d$. Similarly, the maximum hoop tendon strain measure prior to rupture is on the order of 1.4% to 1.5%. There may be some local strain concentrations that were not captured by the strain gages, but this limiting tendon strain is significantly less than the ultimate strain obtained from laboratory tests of a straight tendon sample, typically on the order of 4% for the tendon and 7% for individual strands. Furthermore, none of the model tendons ruptured at the anchors where strain concentrations might be expected, but all ruptured where the deformation of the model was greatest, approximately azimuth 6 degrees.

Similarly, the strain in the vertical tendons at the maximum pressure are on the order of 0.1 to 0.2%, and the total strain is on the order of 0.7% to 0.8%. Both are well below the strain at which the hoop tendons were believed to have ruptured, reinforcing the belief that the vertical tendons did not fail prior to the rupture of the vessel.

The tendon force profiles, previously constructed for prestressing and the LST, were also constructed for the SFMT. Since the tendon strains were re-zeroed for the SFMT, it was assumed that the residual strain for each gage after the LST was the initial strain at the start of the SFMT. These residual strain values were added to the SFMT strain data and the force distribution profiles were constructed in the same manner as before. Figures 5.111 to 5.115 show the force profiles for the five instrumented hoop tendons.

One point deserves mentioning. The tendon anchor forces appear to drop off at or just beyond the peak pressure. This is an artifact of rupture occurring during a data scan. The pressure and strain values were recorded near the beginning of the scan, while the load cells were among the last instruments scanned. If rupture, which occurred in a few seconds, took place during the 30 second data scan, the DAS would associate the pressure before rupture with the load cell reading after rupture, giving the appearance that the tendon anchor forces dropped before the model ruptured.

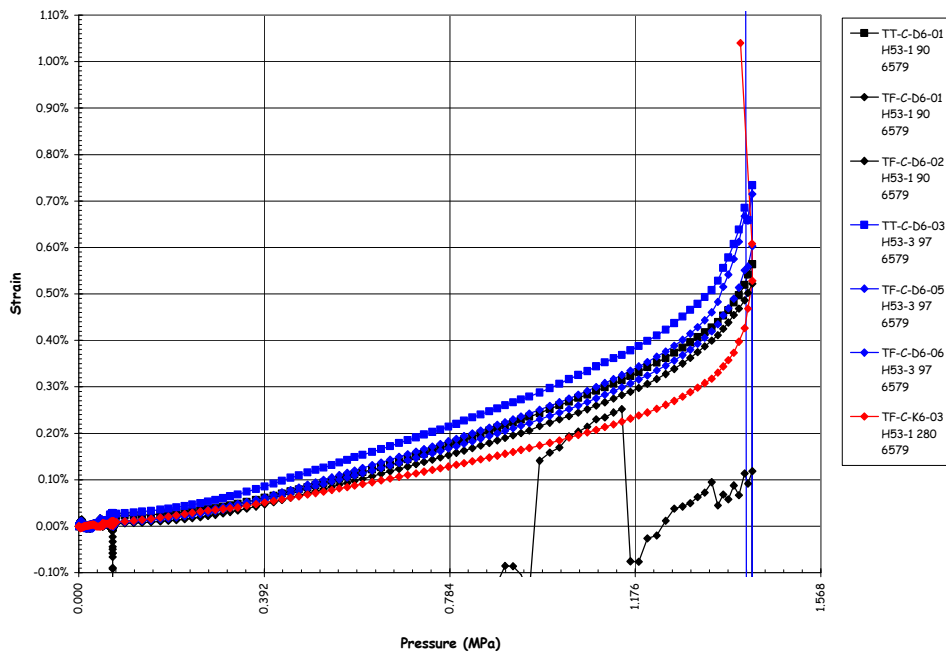


Figure 5.108 SFMT – Tendon H53 Strains

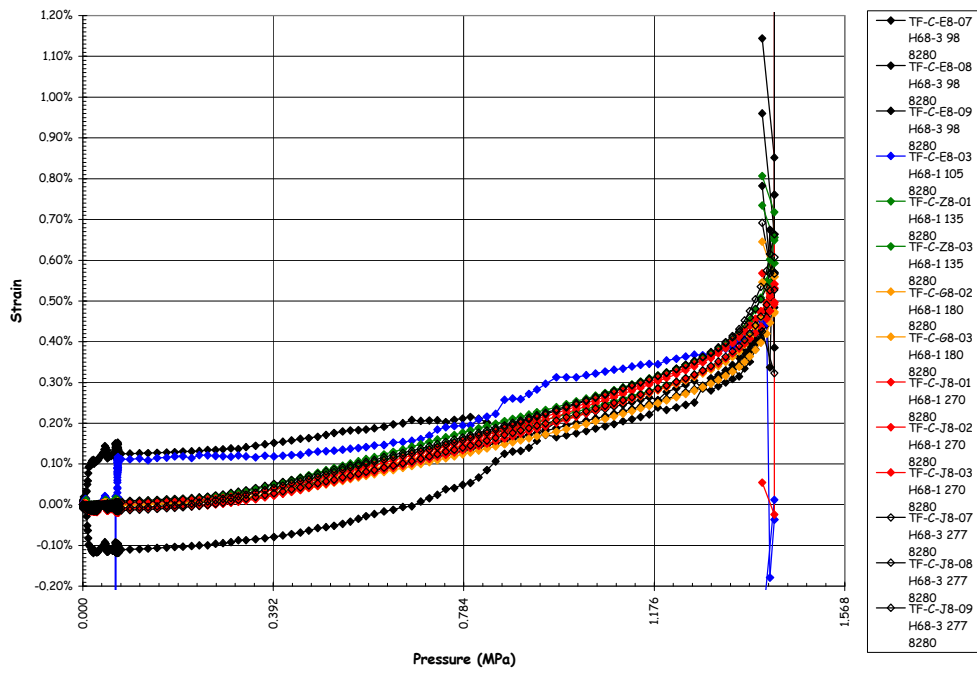


Figure 5.109 SFMT – Tendon H68 Strain

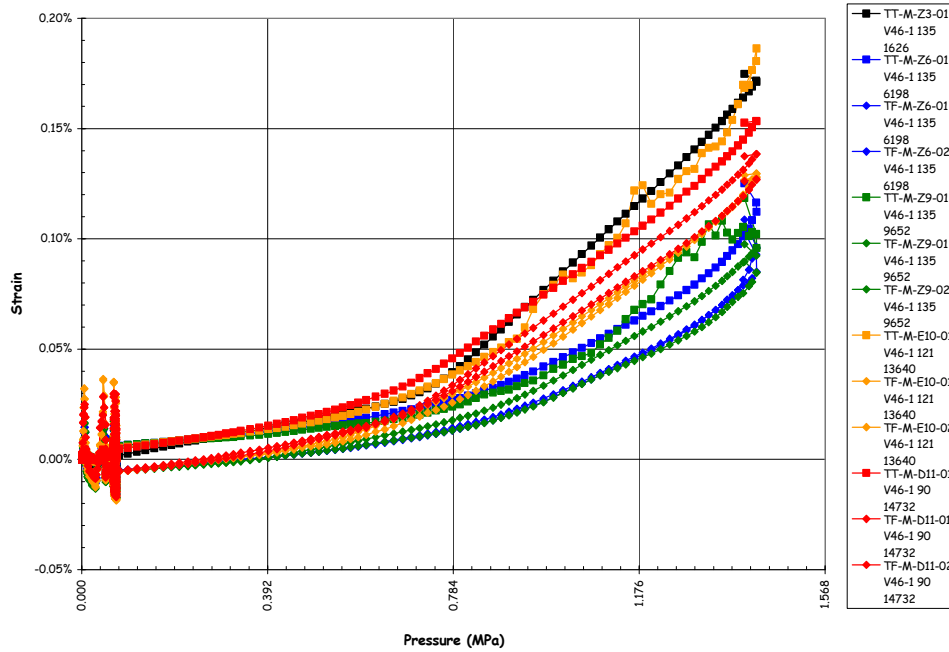


Figure 5.110 SFMT – Tendon V46 Strains

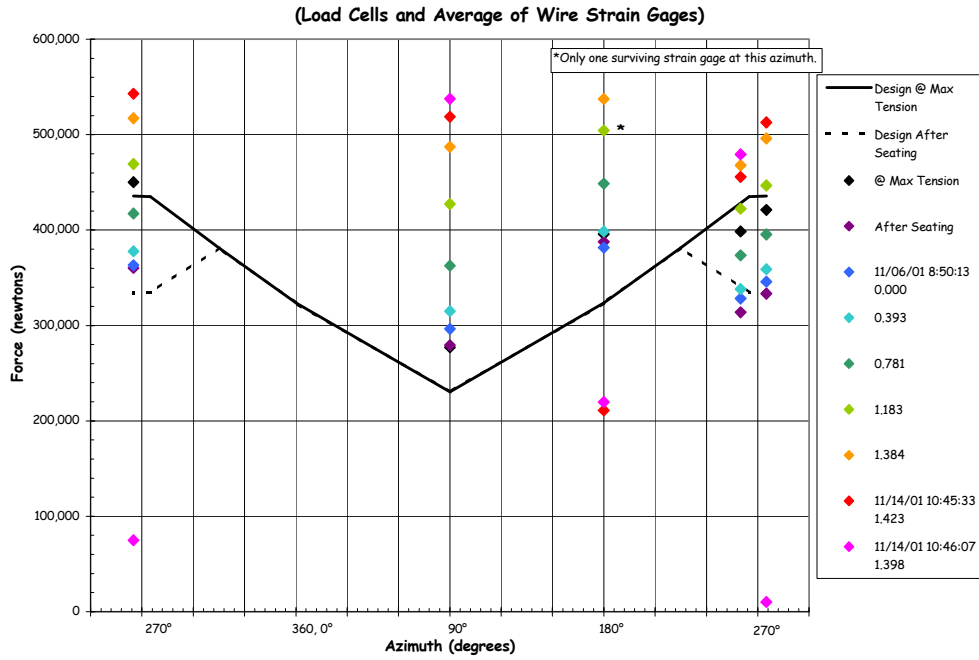


Figure 5.111 SFMT – Tendon H11 Force Distribution (Elev. 1854)

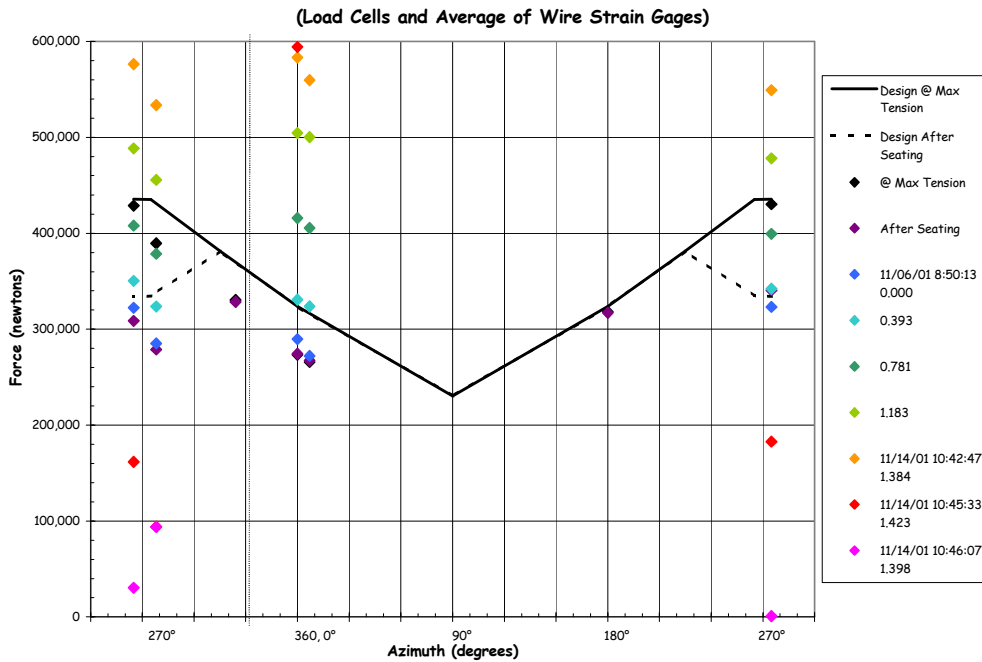


Figure 5.112 SFMT - Tendon H35 Force Distribution (Elev. 4572)

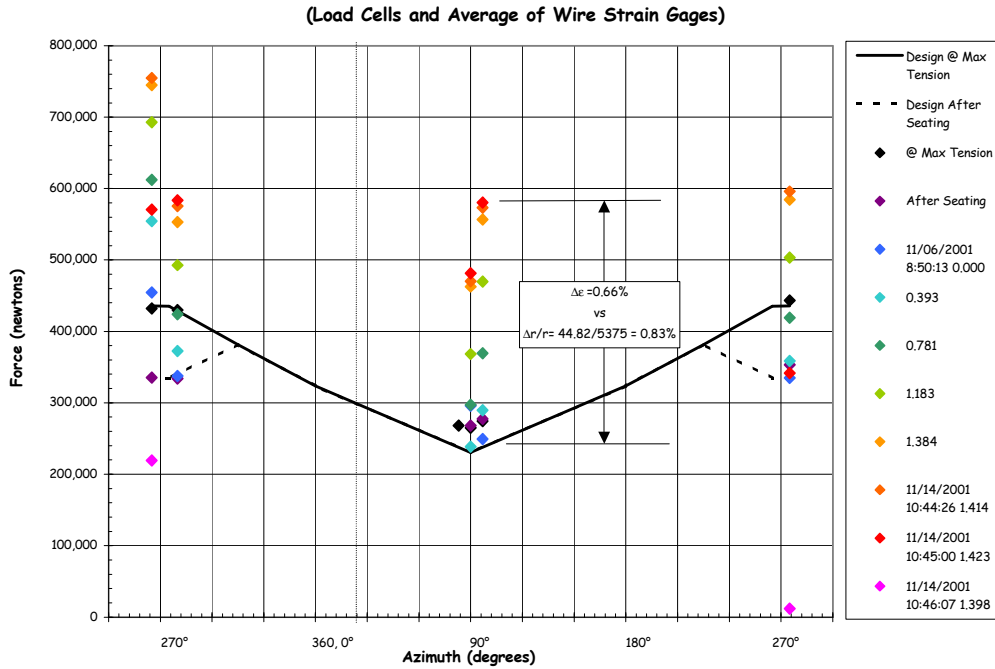


Figure 5.113 SFMT - Tendon H53 Force Distribution (Elev. 6579)

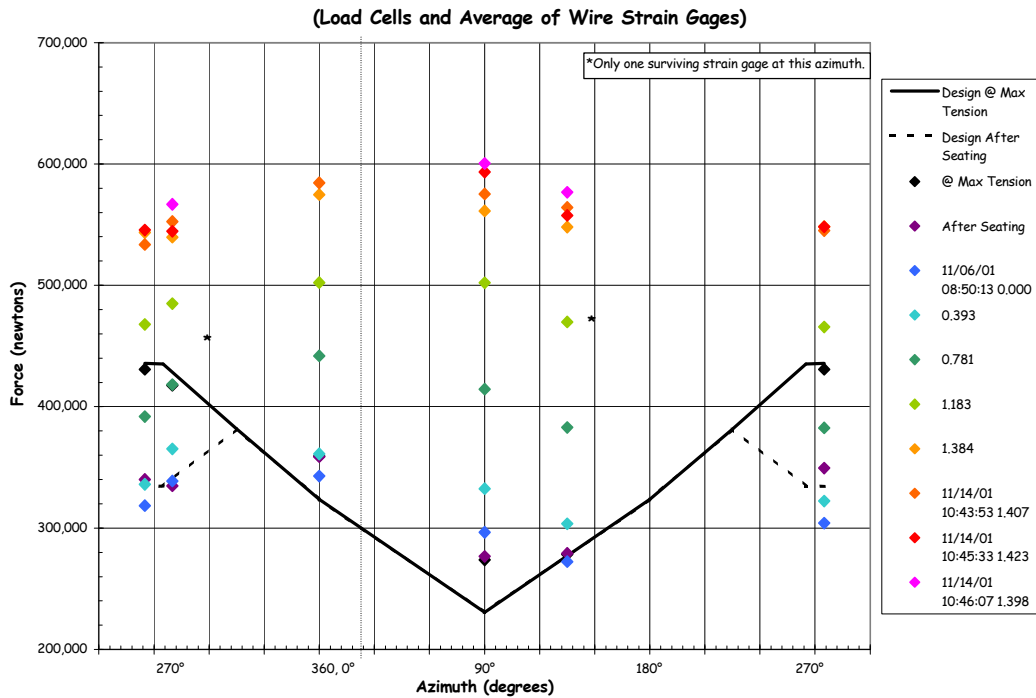


Figure 5.114 SFMT - Tendon H67 Force Distribution (Elev. 8153)

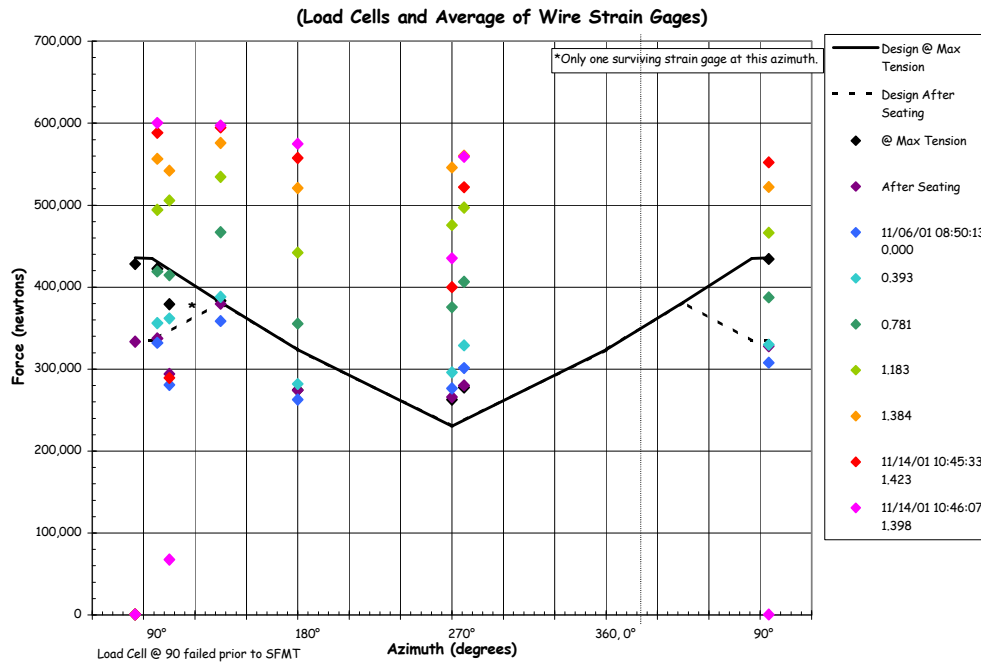


Figure 5.115 SFMT - Tendon H68 Force Distribution (Elev. 8280)

Again, the data is not adequate to assume the shape of the hoop tendon force profile between the surviving measurement positions, and only the force at the measurement locations are plotted, with no attempt to interpolate the strain between the measurement locations. As the pressure is increased, however, and generalized yielding of the model and the tendons occurs, all the plots indicate that the tendon force becomes more uniform along the length, approaching a limiting value of approximately 600 kN (135 kips). One unresolved issue is whether the tendon force equilibrates by slipping relative to the sheath or if the friction is high enough to effectively bond the tendon to the concrete.

An attempt was made to determine this by calculating the local, displacement-based strain in the wall and, assuming the tendon behaved as if bonded, adding it to the initial prestressing strains and computing the force profile from these strains. Figure 5.116 compares the force distribution obtained in this manner with the forces based on the tendon strain measurements for tendon H35 near elev. 4680 where the displacements were measured. The results compare favorably and seem to reinforce the idea that the tendons behave as if they were bonded after prestressing. While this is a compelling argument, it must also be admitted that these results are not entirely conclusive and further tests may be required to resolve this issue.

Figures 5.117 to 5.119 show the force profiles for the instrumented vertical tendons. Again, as was observed with the response during the LST, the force profile appears to become more uniform with pressure. Since the vertical tendons do not yield, tendons must slip relative to the sheath or concrete wall, even in the dome where the tendons are curved. This counters the observation made for the hoop tendons that the tendons behave as if they were bonded to the concrete. No explanation for this apparent inconsistency has been proposed, reiterating the need for further investigation of this behavior, including additional testing.

5.3.3.1.5 Acoustic Response

The acoustic monitoring system used during the LST was also employed for the SFMT, minus the interior sensors, which were removed to install elastomeric liner. Since the SFMT was not focused on detecting liner tearing/leaks, this was not a significant compromise. The focus of the acoustic system during the SFMT was to detect tendon wire breaks and any other events that might indicate structural damage. The acoustic monitoring system was put into operation at the same time the main DAS was started, prior to filling the vessel with water. (As noted in Section 5.2, it was also employed during the pneumatic leak check of the elastomeric liner.)

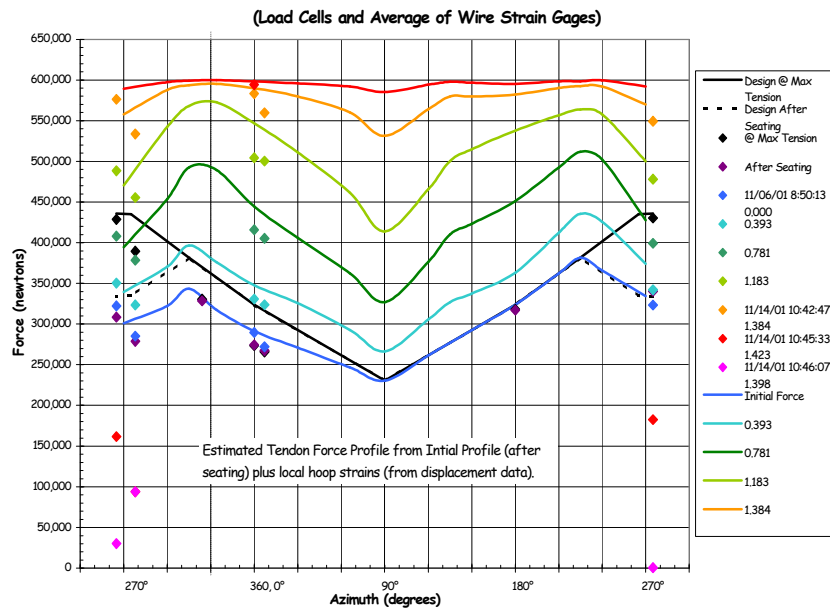


Figure 5.116 SFMT – Tendon H35 Computed and Measured Force Distribution

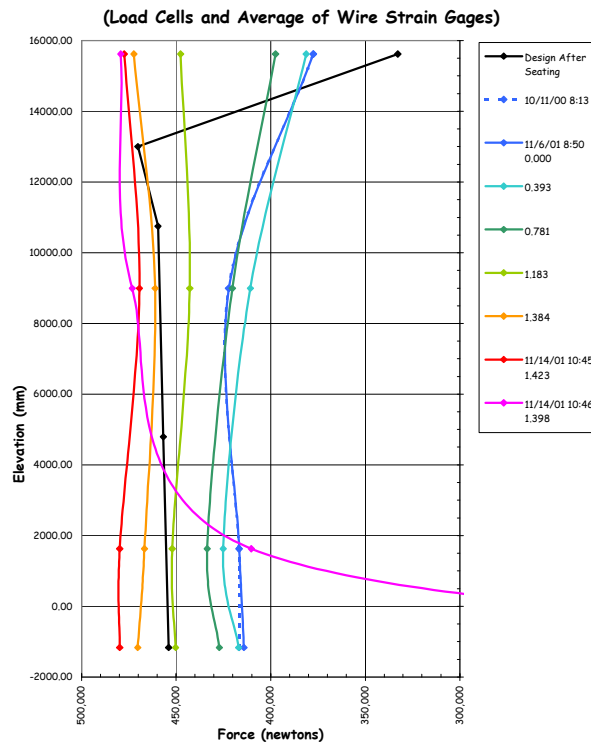


Figure 5.117 SFMT - Tendon V37 Force Distribution at Azimuth 240 Degrees

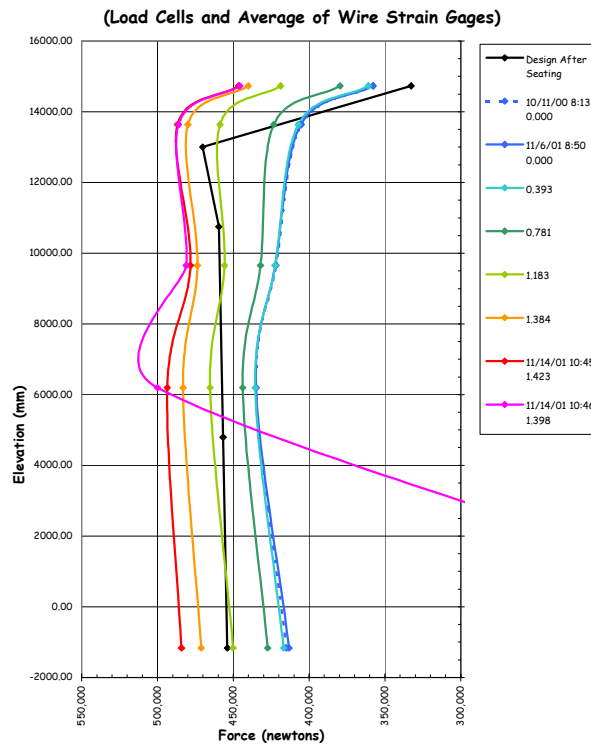


Figure 5.118 SFMT - Tendon V46 Force Distribution at Azimuth 135 Degrees

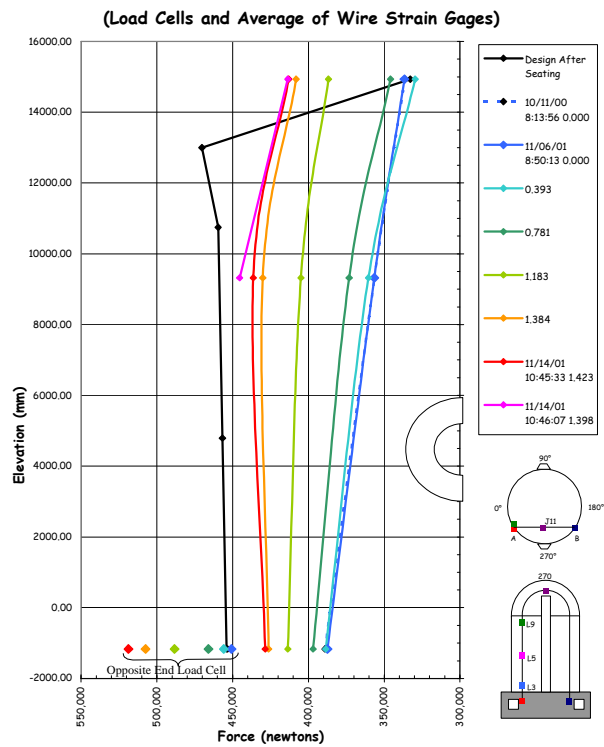


Figure 5.119 SFMT - Tendon V85 Force Distribution at Azimuth 325 Degrees

The post-SFMT reports from Pure Technologies are included in Appendix K. The acoustic event data is also included with the SFMT response data files in Appendix I (data CD). Along with a .wav file of the combined acoustic output during the final minute leading up to, and including, the rupture of the PCCV model. In addition to background noise associated with leaking, deformation, and microcracking of the model, the system identified distinct acoustic events which were categorized as concrete cracking, tendon gallery events, tendon pings, and tendon wire breaks.

Only 27 distinct concrete cracking events were recorded during the SFMT prior to rupture, continuing the trend observed during the LST, i.e., the bulk of the concrete cracking events occurred between 1.0 and 2.3P_u. The tendon pings were confined to the vertical buttresses and the tendon gallery, as during the LST, suggesting the tendons and anchors continued to readjust or reseal themselves. Since all the tendon pings occurred during the final minutes of the SFMT (10:39:30 to 10:45:26), it may also suggest some slipping at the anchors.

The tendon gallery events were all limited to the tendon gallery between 10:43:37 and 10:46:03, implying something occurred with the vertical tendons. The acoustic characteristic of these events is different from the tendon pings and suggested a different mechanism. However, no physical explanation for these events was offered or identified during posttest inspection or demolition of the model.

Fifty-seven actual or probable wire break events were identified between 10:39:47 and rupture of the model at 10:46:12. The wire-break event locations are mapped in Figure 5.120.

Other than observing the discontinuities in the tendon load cell and strain time histories that might indicate a wire break, there were no other efforts to correlate the probable wire breaks identified by the acoustic system with the other test data. While it is arguable that the probable wire break events were actual wire breaks, at least a dozen or so were confirmed by the visual records. Figure 5.121 plots the time history of all the acoustic events along with the effective pressure time history. It is readily apparent that the frequency and magnitude of the wire break events increases just prior to rupture.

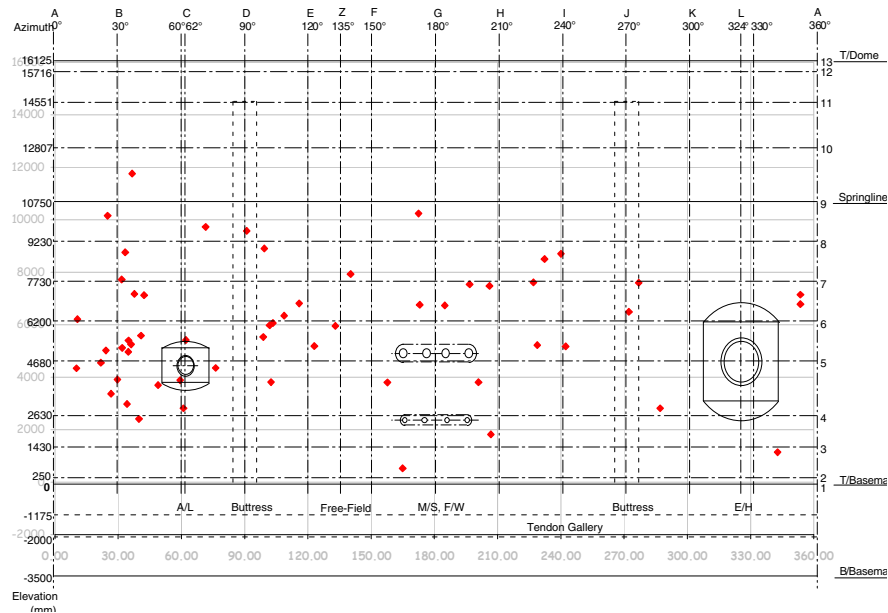


Figure 5.120 SFMT – Wire Break Map

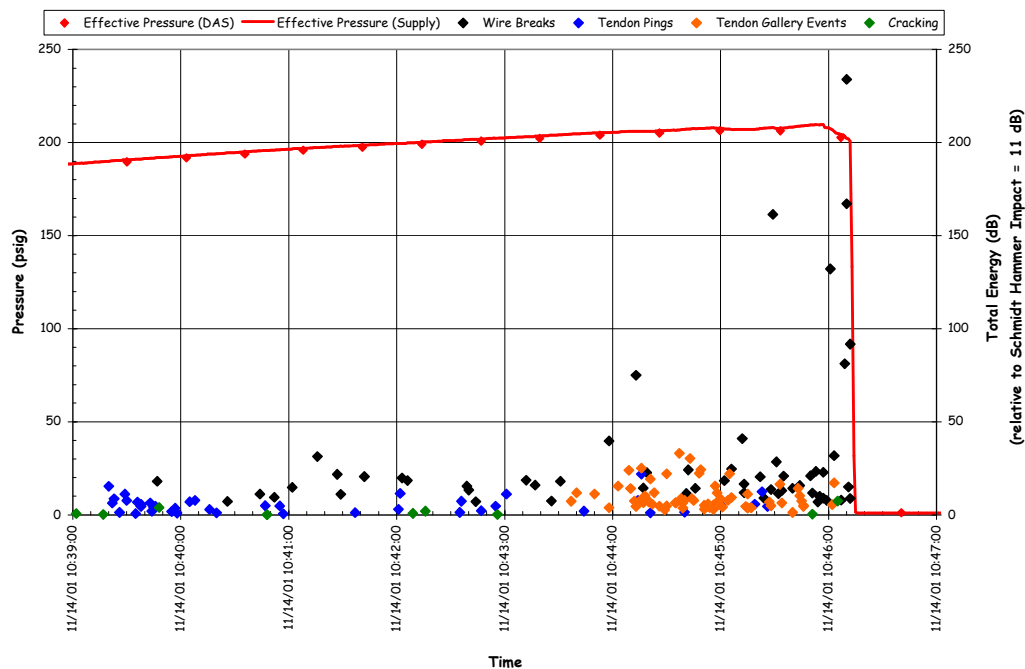


Figure 5.121 SFMT – Acoustic Event and Pressure Time History

5.3.3.1.6 Video

Due to the dynamic nature of the PCCV model rupture at the end of the SFMT, the video images were a valuable diagnostic resource for understanding the failure sequence. Four exterior digital video cameras at 0 degrees, 90 degrees, 180 degrees, and 270 degrees and two interior video cameras at the E/H and at the top of the dome monitored the model throughout the SFMT. Viewing the images in slow motion revealed that the model rupture began at the mid-height of the cylinder at approximately 6 degrees azimuth. The rupture propagated vertically in both directions until it reached a point approximately 2 m above the top of the basemat. The cylinder wall then began to open up, shearing itself from the basemat circumferentially in both directions, and meeting on the back side at 180 degrees. The vessel then ‘telescoped’ over the stem of the cylinder wall before coming to rest on the instrumentation frame.

The interior view of the E/H was distorted by the water and the resulting images were not useful. However, the camera in the dome showed the water surface dropping just prior to the rupture of the vessel, which was captured by all four external video cameras. A video file (.mpg) showing the PCCV model during the final minute of the SFMT and posttest images is included on the data CD in Appendix I. This video includes the acoustic system recording synchronized with the visual images. From close inspection of the video file, visible event times were documented in Table 5.6. The same event may have been observed at slightly different times depending on the camera viewing the event.

5.3.3.2 Posttest Inspection

Since the model was severely damaged and unstable, inspection after the SFMT was limited to an exterior survey. The exterior surface was photographed and the debris field was roughly mapped to document the model fragment locations.

The rupture lines are roughly mapped in Figure 5.122. This figure shows the approximate location of major vertical and horizontal rupture lines along with secondary tears at the E/H and adjacent to the main vertical rupture. These secondary tears are most likely associated with previous liner tears and/or cutouts.

The hoop rebar and tendons along the main rupture line were also inspected for evidence of any discontinuity or other defects that may have accounted for the location of rupture. The close-up photographs of the rebar and tendon strands in Figure 5.123 clearly show ‘necking’ of the bars and wires, indicating that they failed in a ductile manner with large local strains occurring before failure. These photographs are typical of all the tendons and bars at the rupture. The hoop

Table 5.6 SFMT Video Event Times

Time	0° Camera	90° Camera	180° Camera	270° Camera
hour:min:sec:1/30th sec (Video camera speed: 30 frames/second)				
10:45:55:28		H40 wedge ejected, strand broken		
10:45:56:01			H40 wedge ejected, strand broken(?)	
10:45:56:15		Something begins falling @ 100°, El. 5000 toward 5 o'clock		
10:45:56:26	Concrete spall above E/H			
10:45:57:00				Concrete spall (?) @ E/H
10:46:01:24		H42 wedges ejected, strand broken	H42 wedge ejected, strand broken	
10:46:03:10	Water stream starts @ 30°			
10:46:09:09		H64 strand broken/ejected		
10:46:09:12			H64 strand ejected	
10:46:11:21		Spurt of water(?) from H48 anchor		
10:46:11:26	H37 strand ejected			H37 strand ejected
10:46:12:00	Rupture initiated @ 6° (Collapse over in less than 2 seconds)			
10:46:12:01			H40 second strand ejected H37 strand ejected	Rupture
10:46:12:06			Rupture, multiple strands ejected	

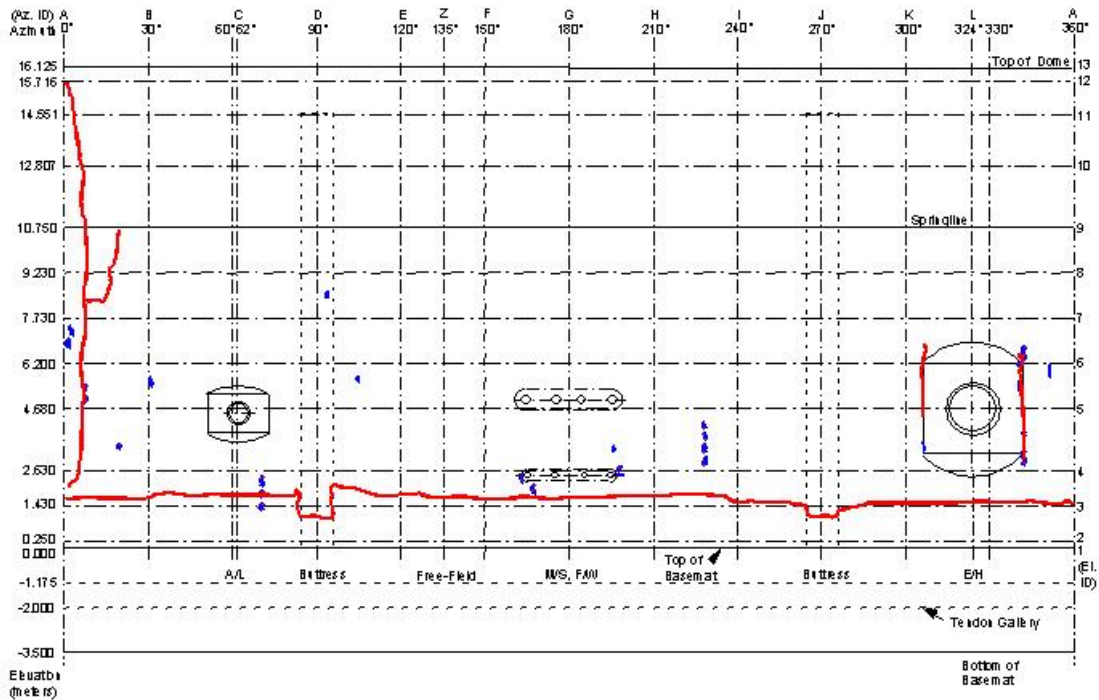


Figure 5.122 SFMT – Rupture Map

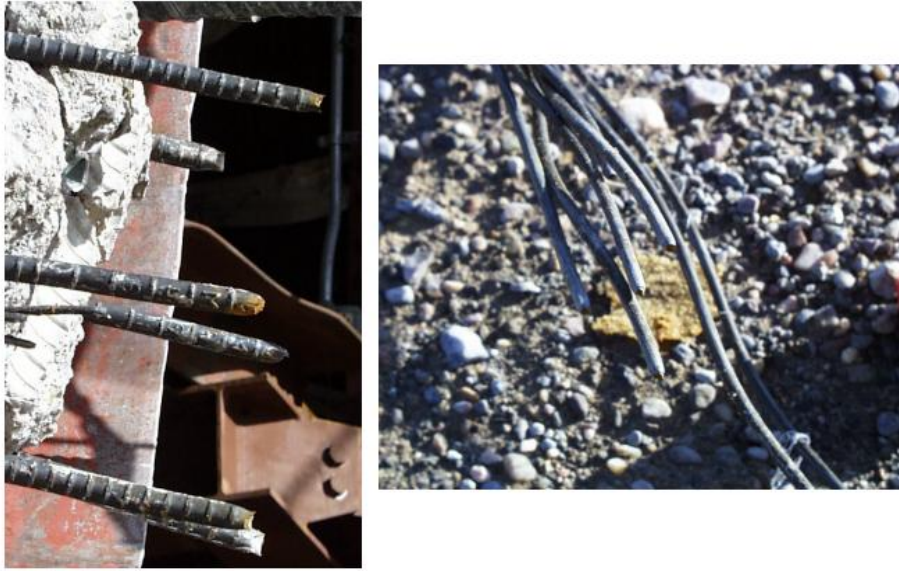


Figure 5.123 SFMT – Rebar and Tendon Strands at the Rupture Line

bars were spliced mechanically very near the rupture, but there was no evidence that any of the mechanical splices failed or that these in any way biased the location where failure began.

The position of the model after the SFMT was also noted. Figure 5.124 shows that the model displaced approximately 3" horizontally and tipped in the opposite direction of the rupture. Six tendons were completely ejected from the model and the final location of major pieces of debris were mapped on the site plan, as shown in Figure 5.125. The location of the debris was not only due to the initial rupture, but also by the flow of 350,000 gallons of water escaping from the model.

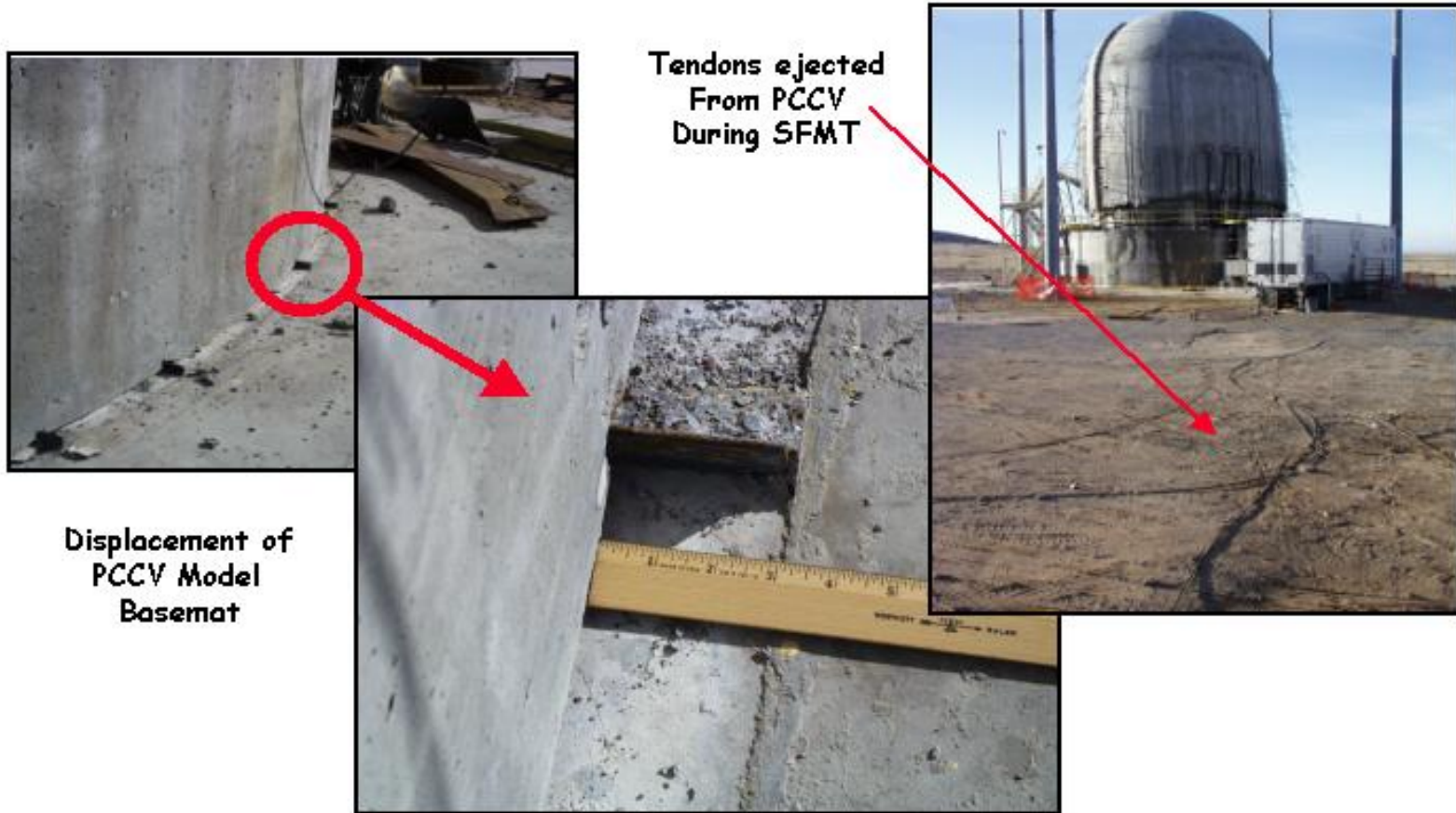
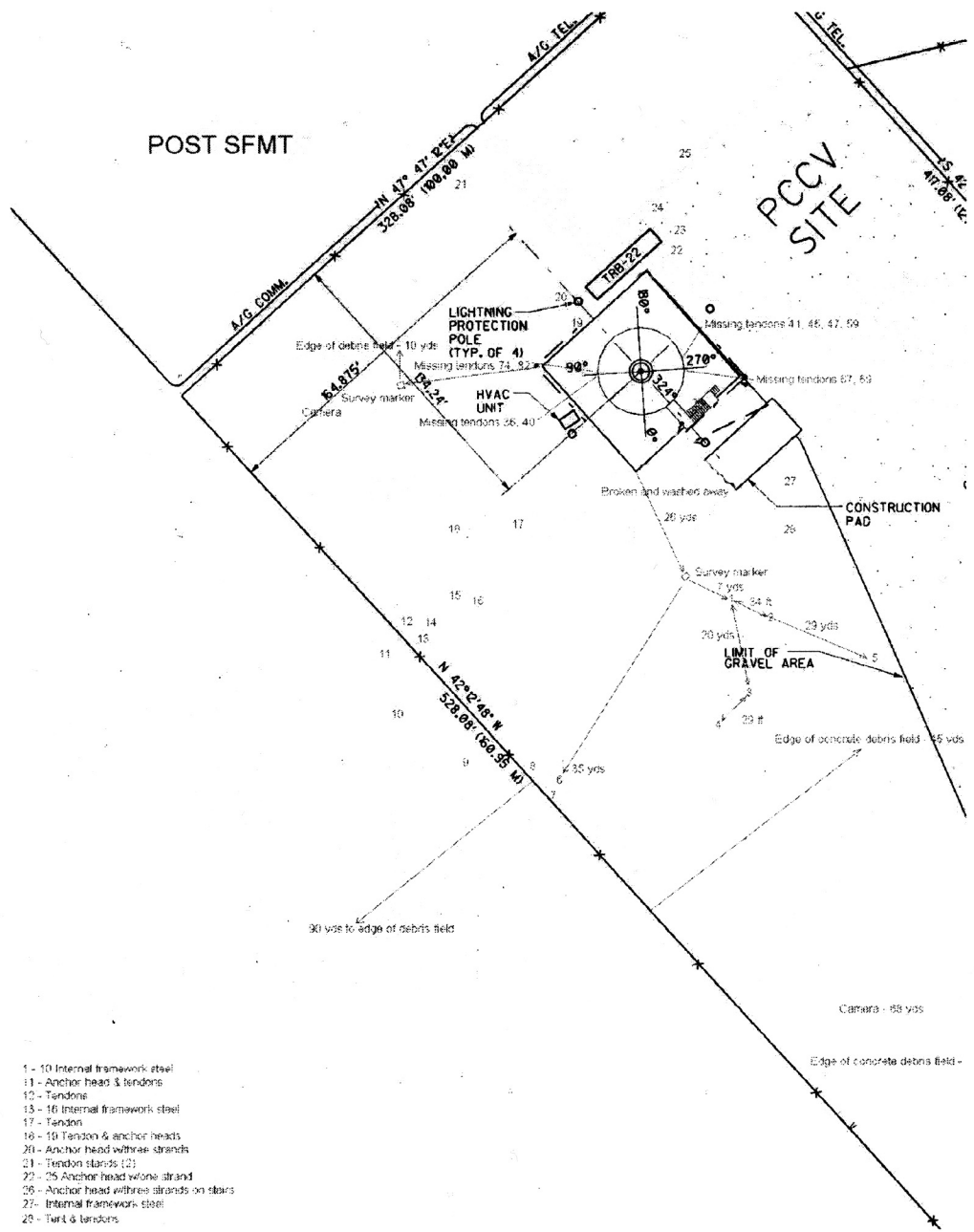


Figure 5.124 SFMT – Model Displacements



- 1 - 10 Internal framework steel
- 11 - Anchor head & tendons
- 12 - Tendone
- 13 - 16 Internal framework steel
- 17 - Tendon
- 18 - 19 Tendon & anchor heads
- 20 - Anchor head with two strands
- 21 - Tendon stands (2)
- 22 - 25 Anchor head w/one strand
- 26 - Anchor head w/three strands on stairs
- 27 - Internal framework steel
- 28 - Turn & tendons

Figure 5.125 SFMT – Debris Map

6. SUMMARY AND CONCLUSION

The overpressurization tests of the 1:4-scale PCCV model represent a significant advance in understanding the capacity of nuclear power plant containments to withstand loads associated with severe accidents. The data collected during the tests, as well as the response and failure modes exhibited, will be useful to benchmark numerical simulation methods used to predict the response of concrete containment structures. One important observation, which should not be overlooked by focusing on the technical results, is that this program not only demonstrated that international collaboration on large-scale experiments is technically and programmatically feasible, but also desirable. The experience and expertise of the Japanese and U.S. partners, along with those of the Round Robin participants and other international support, contributed to the success of the project and resulted in a much more meaningful and productive effort.

While lessons for actual plants can and should be drawn from this and previous large-scale containment model tests, such insights are beyond the scope of this report and will be addressed in a future effort. (A program has been initiated by the NRC at SNL to apply the results of the test programs to the design and operation of actual plants.) The reader is cautioned *not* to draw direct conclusions regarding the pressure capacity of actual plants from these tests or interpret these results as a demonstration of the prototype capacity. The PCCV model tests demonstrated the importance of the unique details and as-built characteristics of the model on the ultimate capacity. Any efforts to estimate the capacity of an actual containment must address the unique features of the plant under consideration.

Furthermore, no conclusions were drawn in this report regarding the analytical methods used to predict or simulate the response of the model or actual containments. These are addressed separately in the pre- and posttest analysis reports [6, 7, and 8].

The conclusions drawn from the PCCV tests in this report will be limited to a discussion of the model, instrumentation, and test design, and their adequacy in meeting the objectives of the program. Where appropriate, recommendations for further investigation are made.

6.1 Model Design

6.1.1 Scale Artifacts

The results of the test clearly demonstrate the necessity of conducting model tests at a scale large enough to:

- utilize materials that exhibit the characteristics of those in the prototype,
- represent the design details and construction methods used in the prototype, and
- avoid the presence of non-representative details and as-built conditions.

At 1:4-scale, the PCCV model achieved most of these criteria. However, even at this scale, the results of the test were subject to scale-related artifacts, most notably in the response of the liner. A variety of compromises were made in the selection of the liner material (which was similar, but not identical, to the prototype), fabrication methods, and details. The decision to scale the weld acceptance criteria (porosity, inclusion, flaw size) might have, in hindsight, contributed to possible premature liner tearing. Since it was nearly impossible to meet the weld acceptance criteria for the field welds, most were rejected and repaired, resulting in local thinning and strain localization in the vicinity of the welds. When the acceptance criteria were later relaxed, the resulting welds appeared to perform much better than those that were repaired (in that no tears were discovered at unrepaired welds). Other factors, such as using intermittent back-up bars and modified liner anchor and stiffener details, may have further contributed to the localized tearing of the liner.

This observation could lead one to conclude that the initial plan of a mixed-scale model, with a thicker liner, might have been preferable. However, that option is also fraught with difficulties. A thicker liner, which might have delayed liner tearing and leakage, could have resulted in a catastrophic failure (as witnessed during the SFMT), when it is more than likely that an actual liner would have torn before reaching the structural limit of $3.6 P_d$.

Suffice it to say that the selection of the model scale is a critical decision which should be guided by a thorough understanding of the prototype design. One must exercise care when introducing any model artifacts that could affect the results of the test.

6.1.2 Material Properties

As a corollary to the previous point, it is worth making a few observations regarding the data from tests used to define the properties of construction materials. Typically, the properties are obtained from standardized tests of small or representative samples of the construction materials. These test methods assure that the construction materials meet a minimum quality standard. Experience has shown that if these minimum standards are met, the structure will meet the design requirements. This is subtly, but significantly, different from characterizing the *in-situ* properties of a structure's constitutive elements.

Nevertheless, these standardized test results are usually all that is available, and most engineers would be happy to have actual material data rather than minimum specified properties. The difficulty arises when the properties of these sample tests are used to develop mathematical material models to predict the response of structures well beyond their design limits, especially when they include inelastic behavior and failure conditions.

The SFMT clearly demonstrated that the tendons failed shortly after the cylinder wall and measured tendon strains were approximately 1%, much less than the 4 to 7% strain obtained from laboratory tests of tendon specimens. Similarly, the measured (and calculated) liner strains at the pressure level where the liner tore were well below the ultimate strain of the liner coupons, even considering local strain concentrations.

This raises the question, then, of whether current standard material test methods are being used to perform a function for which they were not originally intended and if they are adequate for the task. If not, can alternate test methods be devised to provide a better basis for constitutive models? There have been significant advances in the computational methods used to simulate structural response, but no comparable advances in the measurement and characterization of material models on which these computational methods depend.

A second question related to the material properties is the type and amount of data considered adequate to calculate the response of actual containments. A fairly extensive suite of material tests were conducted for the PCCV model, and actual properties were used in all cases. It is not clear if this level of information would be available for all containments. If not, the quality of the capacity predictions may be reduced, with a corresponding increase in uncertainty. One way to address this question might be to use the specified properties of the PCCV model and compare the resulting capacity prediction with those based on the measured properties.

These questions pertain to the use of all structural model test data, and it is not possible to answer these questions on the basis of the PCCV test results alone. However, they are worthy of considering when the results of the PCCV model tests are utilized.

6.1.3 Prestressing System

As the critical feature of the PCCV model, the prestressing tendons deserve special attention. Again, because of the scale limitations, several compromises were made in the design of the model prestressing. Although each tendon in the prototype was represented in the model, the individual strands were larger than the prototype tendons. In addition, the tensioning and anchoring hardware could not be scaled, resulting in higher friction losses and a force profile that deviated significantly from the prototype.

It is not obvious from the test results whether the deviations from the prototype had any significant effect on the capacity of the PCCV. However, the test results, while somewhat inconclusive, did indicate that the assumptions used to predict the tendon force distribution and losses might require further investigation. This appears to be particularly true for the vertical tendons, where the losses due to wobble friction appeared to be underestimated and the losses due to angular friction appeared to be overestimated.

The test also indicated that the tendon force distribution becomes more uniform as the pressure is increased, especially beyond the elastic limits of the model. However, the mechanism by which this adjustment occurs was not clearly demonstrated. The question of whether the tendons behaved as if they were unbonded (and achieved the ‘load leveling’ by slipping relative to the concrete wall) or bonded (resulting in local yielding and increased local deformation) may be an important modeling consideration and should be investigated in more detail, especially if opportunities exist for additional large-scale testing.

It was also noted that, although the vertical tendons were initially tensioned to a higher level than the hoop tendons (nearly 25% higher after anchoring), the challenge to the vertical tendons was minor compared to the hoop tendons. (The level of the vertical prestressing is typically governed by the stress at the apex, where the effective prestressing is calculated to be significantly less than at the base.) This apparent discrepancy between the expected and observed behavior suggests that a review of the design method for the vertical tendons may be in order.

6.2 Instrumentation and Data Acquisition

In spite of a higher-than-expected gage mortality, in most cases from damage during construction, the instrumentation and data acquisition systems performed up to specifications and provided most of the data necessary to understand the response of the model and to compare with analyses. Some observations and lessons learned are warranted.

6.2.1 Displacements

The displacement data provided the most reliable source of information and insight into the model’s overall response to the pressure loads. Nevertheless, the tests demonstrated some factors that should have been considered in the design of the instrumentation and might have improved the quality of the data.

Displacement transducers are relatively inexpensive to procure and install. In hindsight, it might have been useful to install more displacement transducers, even at the cost of eliminating some other gages.

The primary difficulty in measuring displacements is finding a stable global reference point. For small structures, this may be relatively simple; but for large, exposed structures, this can be a significant challenge. In the case of the PCCV, most of the model displacements were measured relative to the stiff instrumentation frame, which was mounted on the fairly rigid basemat. This proved to be a good choice and internal measurements of the frame motion confirm that it did not move significantly as a result of basemat uplift or thermal expansion. (One minor problem discovered after prestressing was that the displacement transducers were attached to the liner, assuming it was ‘bonded’ to the concrete wall, which turned out not to be the case. This was recognized fairly quickly, but could have been avoided if the locations of the displacement measurements corresponded with liner anchor locations, or if small anchors had been attached to the liner at the displacement measurement locations before placing concrete.)

Some transducers were not or could not be mounted on the reference frame, and an incomplete understanding of the interaction between the reference and measurement locations resulted in misleading data. The most notable example of this was the measurement of uplift at the edge of the basemat. In this case, the vertical motion of the basemat’s outside bottom edge was measured relative to the top of the mudmat. This arrangement failed to recognize that the mudmat’s stiffness was insignificant compared to the basemat and that any deformation of the basemat was reflected by the mudmat. As a result, no differential displacement was measured and the initial conclusion was that no basemat uplift had occurred. While comparing this response with the analyses, which did predict some uplift would occur, the flaw in the transducers’ placement was recognized. Unfortunately, no data was obtained to confirm the analytical results. If this phenomenon had been recognized in advance, a more stable reference location could have been identified or constructed.

Other examples of such difficulty include the measurement of the radial and vertical displacement at the wall-base junction, where again some minor modifications could have eliminated all or most of the problem and ensured the desired data was obtained. The point of this discussion is not to fault the design of the instrumentation system, but to point out the importance of carefully considering the stability of the physical reference frame and interpreting the data with a thorough understanding of its practical limitations.

In designing the instrumentation for the PCCV model, efforts were made to obtain independent displacement measurements with a stable fixed reference frame. A number of optical and laser tracking systems were considered, but none of them provided a cost-effective solution with the required accuracy in harsh environmental conditions. Advances in these or other systems may, however, yield viable options for future large scale tests.

6.2.2 Liner Strains

With 559 installed on the PCCV model, the liner strain gages accounted for over one-third the total number of transducers on the model. While strain gages are relatively inexpensive to purchase, the installation, monitoring, and processing of the data represented a significant portion of the project's cost. This naturally leads to the question of whether the data obtained justified the expense.

The liner strain gages were intended to measure:

- the global or free-field hoop and meridional strains,
- the local strains near liner discontinuities, and
- the local strains in the liner anchors and stiffeners.

The free-field strain gages yielded larger maximum strains than those derived from the displacement data. For example, at the maximum LST pressure ($3.3P_d$), the liner hoop strain at Z6 was 0.90%, compared to approximately 0.5% computed from the displacement data. The difficulty of measuring global or even near-field strains from liner strain data is in the sensitivity of small gage length strain gages to local discontinuities or variations in the liner, even when these discontinuities are not readily apparent. It does not appear that these free-field liner strains reliably indicate the free-field strains in the wall. This problem might have been reduced by installing larger gage-length strain gages for the free-field measurements, thus minimizing the effect of local variations, but these are more difficult to install and even at larger gage lengths (e.g. 50 mm or 2 in) the problem is not completely eliminated.

The strain gages located near the liner discontinuities (e.g. near anchors and stiffeners, fold lines, and inserts) registered higher strains than the surrounding material and provided some valuable information for comparison with local liner analysis. Direct comparison was difficult, however, since the problem of local variations and discontinuities was exacerbated by the high local strain gradients and as-built conditions which may not be modeled. In this case, the gage length of the strain gages may have been too large to measure the peak liner strains. Individual strain gage data can be misleading, and multiple gages are required to construct a map of the strain fields in the vicinity of the discontinuity.

One other problem with local liner strain measurements is well known, but difficult to avoid. Strain gages placed near a tear typically measure smaller strains than strain gages placed in a similar location without a tear, because the tear acts as a strain relief mechanism. This phenomenon was demonstrated by the strain gages located near the E/H and M/S penetrations.

The liner anchor strain gages were generally consistent with the free-field meridional gages and the average vertical strain in the cylinder wall calculated from the displacements. In fact, the peak liner anchor strain of 0.1% is identical to the average strain derived from the displacements. This makes sense when considering that the anchors are bonded better to the concrete than the liner, suggesting that the free-field strains can be measured more accurately by mounting strain gages on the anchors and hoop stiffeners if they can be isolated from other discontinuities.

6.2.3 Rebar/Concrete Strains

The strain gages were mounted on the main reinforcing steel and on specially fabricated gage bars, expecting that these rebar strains would be an accurate measure of the local strains in the wall due to membrane and bending forces. A few fiber-optic strain gages were installed to independently measure the concrete wall strains at a few selected locations to corroborate this assumption. The test data indicates that the rebar strains are a reliable measure of the wall strains up to the onset of local yielding. At this point, the method to mount the strain gages on the rebar, which removes a small portion of the bar to provide a smooth surface on which the gage is bonded, forms a 'structural fuse.' This structural fuse

yields before the rest of the bar yields and experiences artificially higher strains, up to 0.5%, beyond yield. For the PCCV test, the post-yield behavior was of primary interest and this artifact corrupted the rebar strain data beyond roughly $1.5P_d$. Improved methods of measuring rebar strains that avoid the structural fuse problem would make rebar strain measurements more reliable indicators of the wall strain.

Overall, the displacement data provided a much more accurate and reliable measure of the local membrane wall strains than the rebar gages. The displacement data could not, however, provide any insight into the local bending strains in the wall at locations such as the wall-base junction, the springline, and the buttresses.

The fiber-optic gages yielded much better results; however, these gages are relatively expensive and experienced a fairly high mortality rate. Improvements in the installation technique and reduction in hardware costs would make these gages a much more attractive option for future tests.

Most of the gage bars were damaged during construction or after prolonged exposure to the elements. The surviving gage bars did provide some useful data and demonstrated that the concept was sound. The expense of fabrication and difficulty of installation, however, do not make this an attractive option, compared to the fiber-optic gages, for future tests.

6.2.4 Tendon Strains/Forces

The major instrumentation challenge posed to SNL for the PCCV model test was to measure the force distribution in the tendons during prestressing and pressure testing. Efforts in previous testing programs to collect force distribution data on unbonded tendons had been generally unsuccessful. A significant effort was made to investigate, develop, and demonstrate the feasibility of measuring the tendon strains within the program schedule and budget constraints. Since this was not an instrumentation development program, the effort focused on adapting or modifying 'off-the-shelf' components for this task. SNL was also limited to using transducers that would not require any modification in the basic structural components or their arrangement. (Some minor modifications, such as increasing the instrumented tendon duct diameter from 35 to 40 mm, were accepted to accommodate the instrumentation.) While the results were not completely satisfactory due to the high mortality rate (>50%) of the strain gages, a significant amount of data unique for prestressed concrete structures was collected, and the feasibility of measuring the variation in tendon strain, and indirectly force, along the length was demonstrated.

As noted above, the data obtained during the test did not conclusively provide an understanding of the tendon response mechanism beyond yield to ultimate load. Future tests, if conducted, might resolve this issue using improved tendon instrumentation. The biggest challenge for the instrumentation was surviving the harsh mechanical environment imposed on the sensors and lead wires during the prestressing operations. A number of promising non-contact sensors were investigated for the PCCV test to avoid this problem, but they were ultimately abandoned due to cost, reliability problems, or difficulty integrating them into the model. If future tests are planned, improvements in these sensors or new types of sensors might make them an attractive alternative to the methods employed in the PCCV test, and should be considered seriously. The lessons learned and the techniques developed for the PCCV test provide a solid basis for the next step in understanding unbonded tendon behavior.

6.2.5 Acoustic

The Soundprint® acoustic monitoring system provided the only quantitative monitoring of the entire model as opposed to the individual transducers that monitored discrete model elements. The acoustic monitoring system detected concrete cracking, liner tearing and leakage, and tendon wire or rebar breaks. The system successfully met all of these objectives at a relatively low cost, and almost immediately detected a liner leak at the leak rate threshold established for the test, 1% mass/day. To a lesser extent, it was also able to identify the general location of the first liner tear/leak, although detection and location of the subsequent tears/leaks was less conclusive.

Posttest analysis of the acoustic data also suggested that it might be a viable means of detecting the onset of global tensile cracking (and associated loss of stiffness). Although the acoustic capabilities to locate events were degraded during the SFMT due to the existing concrete damage and the elimination of interior sensors, the Soundprint® system was still able to detect tendon wire breaks. Because of the extensive damage caused when the model ruptured, posttest inspection was

unable to confirm the number or location of the reported wire break events. However, the wire break events that did occur were detected.

Further analysis of the extensive acoustic data obtained from prestressing through all of the pressure tests might provide further insights into the capabilities of acoustic monitoring systems to monitor containments and similar structures.

6.2.6 Video/Still Photography

Each phase of the model construction, instrumentation, and testing was photographed in detail to provide a record that could subsequently aid in the interpretation of the model response to applied loads. Thousands of still photographs and hours of video were recorded and archived for future use. In spite of this effort, there were still some features of the model or procedures that could have been documented in more detail. Nevertheless, these records, which were obtained at a relatively low cost, proved invaluable.

The best example of the records' value was in providing a partial explanation of the liner tearing mechanisms. While it was a particularly painstaking effort, the decision to photograph the exterior surface of all the liner field welds in the cylinder wall and dome before placing the rebar and concrete provided graphic evidence of the local discontinuities influence on the response and tearing of the liner. After the tears were located on the inside of the model, the photographic database provided detailed information on the condition of the backside. This information was subsequently used in the posttest examination and analysis of the liner.

In a similar, although less dramatic, manner, photographs of the transducer installations also assisted the interpretation of some test data, especially with regard to the effect of placement and mounting details. Crack mapping of the concrete wall after prestressing and pressure testing was also greatly facilitated by tracing and photographing the surface.

Since the tests were essentially static in nature (except for the SFMT), no high-speed film or video photography was used. Use of standard video cameras during the LST was limited to providing visual input of the model response for test operations. Observing a few critical locations inside the model with close-up video in an attempt to observe local damage, e.g. liner tearing, was not successful, since the locations observed did not exhibit any visible damage.

The external digital cameras used during the SFMT, however, were invaluable in capturing the sequence of rupture and damage progression of the model. Even with normal speed video, the failure of several tendons and the location where the rupture started were recorded. It is unlikely that without this visual record the sequence of the model failure would have been as clearly understood. The interior video camera that observed the water surface also gave an early indication of the model rupture, as the water surface was observed to drop rapidly just prior to rupture, although this was not immediately recognized.

6.2.7 Data Acquisition

The DAS was specifically *not* designed as a high-speed DAS, but was designed to provide accurate, real-time information on the model's response during the application of relatively slow loading over an extended period of time, to operate unattended, and to efficiently manage the large volumes of data obtained. It performed this function admirably, and the robustness of the system was demonstrated several times during power outages and other challenges such as lightning strikes. The few minor system 'failures' that occurred did not take place during critical test periods, and recovery and restart of the system was always accomplished quickly and with a minimal loss of data.

The DAS was adapted to the challenge of the rapid loading during the SFMT with only some minor difficulties noted near the end of the test, when correlation of the pressure with a specific response value introduced some error due to the relatively slow scan rate (30 sec) compared to the time over which the model rupture occurred (<1 sec). This error is insignificant as long as the time lag is recognized. However, it does point out the need to ask if rapid data acquisition capabilities are required, should future tests be conducted.

6.3 Testing

The successful completion of the tests within the programmatic constraints, i.e. cost and schedule, attest to the adequacy of the test plans and procedures. However, a few points may require further consideration and discussion.

6.3.1 Loading

The reasons for conducting static, pneumatic overpressurization tests at ambient temperature were discussed in Section 1.2.2. While the tests successfully obtained data on the response to pressurization and, secondarily, to prestressing, the application and interpretation of these results should recall that the test load does not faithfully represent the complex loading environment that will exist during a severe accident. The effects of temperature, the temporal relationship between pressure and temperature, the composition of the internal atmosphere, and the rate of loading may all affect the response and failure modes and the sequence of these events and should be considered in any evaluation of containment capacity.

Other containment model tests [45] have attempted to consider some or all of these aspects of severe accident loads. Future efforts should consider evaluating the effects of these other loads on the response of the PCCV model and possibly the prototype, and the results of these efforts may indicate a need for additional testing that includes these loads.

6.3.2 Failure Criteria

As noted in Section 1.2.3, it was not the goal of these tests to establish failure criteria, either functional or structural, for prototypical containments. Nevertheless, the test did provide some insight into issues that should be considered when establishing failure criteria for actual containments.

First, the primary functional failure criteria defined in terms of a maximum leak rate cannot be applied directly to conventional mechanistic models of containment structures that output response in terms of displacement, strain, force, stress, etc. As a result, design philosophies have focused on limiting these response variables to ensure that no leakage occurs. Further study of the relationship between leakage and structural response may provide some insights that could be applied to regulations and design requirements based on functional criteria.

Secondly, predictions of containment capacity have often been based on the structural capacity of the components used in the construction; for example, using the ultimate strength or elongation of samples of prestressing tendons, liner, rebar, etc., as the limit criteria. The PCCV model test demonstrated, as noted in the discussion on material properties, that the strain levels measured at failure can be much lower than the limiting values obtained from standard tests of sample specimens. The test results should provide some guidance on the development of appropriate failure criteria for use in future capacity calculations.

6.3.3 Leak Rate Measurements

The SIT/ILRT data, conducted in accordance with the specified procedures currently used in both Japan and the U.S., demonstrated the difficulty of accurately measuring leak rates to guarantee that they do not exceed the specified limits. Even with the relatively simple, controlled structure represented by the PCCV model and the extensive suite of instruments available during testing, it was not possible to accurately measure leak rates on the order of 0.1% mass/day. An apparent leak rate of 0.5% mass/day at $1.5P_d$ during the LST was due to thermal expansion of the model in response to ambient temperature changes and the model's direct heating. In light of these results, a review of leak rate measurement methods and the leak rate test criteria should be considered.

One area to explore might be the use of acoustic monitoring to detect, locate, and, possibly, measure leak rates. The acoustic monitoring system was able to readily detect a leak rate of 1% mass/day. Further evaluation of the data and refinement of the monitoring system might determine the feasibility of detecting even smaller leaks and possibly correlating the acoustic signal levels with leak rate.

7. REFERENCES

1. Luk, V. K., M. F. Hessheimer, G. S. Rightley, L. D. Lambert and E. W. Klamerus, *Design, Instrumentation, and Testing of a Steel Containment Vessel Model*, NUREG/CR-5679, SAND98-2701, Sandia National Laboratories, Albuquerque, NM, January 1999.
2. Porter, V. L., P. A. Carter and S. W. Key, *Pretest Analysis of the Steel Containment Vessel Model*, NUREG/CR-6516, SAND96-2877, Sandia National Laboratories, Albuquerque, NM, January, 1999.
3. Luk, V. K., and E. W. Klamerus, *Round Robin Pretest Analysis of a Steel Containment Vessel Model and Contact Structure Assembly Subject to Static Internal Pressurization*, NUREG/CR-6517, SAND96-2899, Sandia National Laboratories, Albuquerque, NM, August, 1998.
4. Ludwigsen, J. S., V. K. Luk, M. F. Hessheimer, and J. F. Costello, *Posttest Analyses of the Steel Containment Vessel Model*, NUREG/CR-6649, SAND99-2954, Sandia National Laboratories, Albuquerque, NM, February 2000.
5. Luk, V. K., and E. W. Klamerus, *Round Robin Posttest Analysis of a Steel Containment Vessel Model*, NUREG/CR-5678, SAND98-700, Sandia National Laboratories, Albuquerque, NM, January, 2000.
6. Dameron, R. A., L. Zhang, Y. R. Rashid, and M. S. Vargas, *Pretest Analysis of a 1:4-Scale Prestressed Concrete Containment Vessel Model*, NUREG/CR-6685, SAND2000-2093, ANATECH Corporation, San Diego, CA and Sandia National Laboratories, Albuquerque, NM, October, 2000.
7. Dameron, R. A., Hanson, B. E., Parker, D. R., and Rashid, Y. R. 2003. *Posttest Analysis of a 1:4 Scale Prestressed Concrete Containment Vessel Model*, NUREG/CR-6809, SAND2003-0839P, ANA-01-0330, ANATECH Corporation, San Diego, CA and Sandia National Laboratories, Albuquerque, NM, February, 2003.
8. Luk, V. K., *Pretest Round Robin Analysis of a Prestressed Concrete Containment Vessel Model*, NUREG/CR-6678, SAND00-1535, Sandia National Laboratories, Albuquerque, NM, August, 2000.
9. American Society of Mechanical Engineers, Boiler and Pressure Vessel Code, Section III, Division 2, Code for Concrete Reactor Vessels and Containments.
10. Blejwas, T. E., et. al., *Background Study and Preliminary Plans for a Program on the Safety Margins of Containments*, NUREG/CR-2549, SAND82-0324, Sandia National Laboratories, Albuquerque, NM, May 1982.
11. Parks, M. B., Horschel, D. S., and von Riesenmann, W. A., "Summary of NRC-Sponsored Research on Containment Integrity," *Proceedings of the 11th International Conference on Structural Mechanics in Reactor Technology*, August 18-23, 1991, Tokyo, Japan.
12. Parks, M.B., H.P. Walther, and L.D. Lambert. "Experiments to Determine the Leakage Behavior of Pressure-Unseating Equipment Hatches," *Proceedings of the 11th International Conference on Structural Mechanics in Reactor Technology*, Tokyo, Japan, August 1991.
13. Lambert, L.D. and M.B. Parks. *Experimental Results from Containment Piping Bellows Subjected to Severe Accident Conditions*. NUREG/CR-6154, SAND94-1711, Vol. 1. Sandia National Laboratories, Albuquerque, NM. September 1994.
14. Cherry, J. "Analysis of Containment Structures with Corrosion Damage," *Proceedings of the 24th Water Reactor Safety Information Meeting*, Vol. 1, pp. 333-352, Bethesda, Maryland, October 21-23, 1996.
15. Nakamura, S., Y. Sasaki, K. Horibe, M. Nakajima, K. Hoshino, T. Takahashi, T. Hagesawa, T. Kei, T. Meida, K. Takigushi, and H. Akiyama. "Plan of the Seismic Proving Test for Reinforced Concrete Containment Vessel: Test Plan and Test Model Design," *Proceedings of the 14th International Conference in Structural Mechanics on Reactor Technology*, Vol. 11, pp. 83-90, Lyon, France, August 17-22, 1997.
16. James, R.J., Y.R. Rashid, J. Cherry, N.C. Chokshi, S. Nakamura. "Analytical Prediction of the Seismic Response of a Prestressed Concrete Containment Vessel," *Proceedings of the 14th International Conference in Structural Mechanics in Reactor Technology*, Vol. 7, pp. 151-160, Lyon, France, August 17-22, 1997.
17. Arai, S., T. Matsumoto, M. Goto, Y. Naruse, T. Mieda, and H. Yamanaka. "Pressurization Test on the Equipment Hatch Model," *Proceedings of the 14th International Conference on Structural Mechanics in Reactor Technology*, Lyon, France, August, 1997.
18. Lobner, P., C. Donahoe, and C. Vavallin, *Overview and Comparison of U.S. Commercial Nuclear Power Plants*. NUREG/CR-5640, SAIC-89/1541. San Diego, CA: Science Application International Corporation, September 1990.
19. R. A. Dameron, R. S. Dunham, Y. R. Rashid, M. F. Sullaway, H. T. Tang, "Analytical Correlation and Post-Test Analysis of the Sandia 1:6 Scale Reinforced Concrete Containment Test," *Proceedings of the Fourth Workshop on Containment Integrity*, NUREG/CP-0095, SAND88-1836, June 1988, pp. 441-458.

20. R. A. Dameron, Y. R. Rashid, M. F. Sullaway, "Pretest Predictions of 1:10 Scale Model Test of the Sizewell-B Containment Building," *ANATECH Report to Sandia National Labs*, June 1989.
21. R. A. Dameron, R. S. Dunham, Y. R. Rashid, H. T. Tang, "Conclusions of the EPRI Concrete Containment Research Program," *Proceedings of the 3rd International Seminar on Containment of Nuclear Reactors*, August 1989, pp. 189-218.
22. Design Policy of the Test Model (Concrete Body), CTG-09-06, NUPEC, June 1993.
23. Draft Technical Code for Concrete Containment Vessels in Nuclear Power Plants, Ministry of International Trade and Industry, Agency for Natural Resources and Energy, Tokyo, Japan, 1981.
24. Reinforced Concrete Work, Japanese Architectural Standard Specification 5, Architectural Institute of Japan, Tokyo.
25. Reinforced Concrete Work at Nuclear Power Plants, Japanese Architectural Standard Specification 5N, Architectural Institute of Japan, Tokyo.
26. Miller, C. M., "Geotechnical Investigation for the Containment Technology Test Facility-West," Job No. 1-20904, Geo-Test, Inc., Albuquerque, NM, October, 1992.
27. Grush, M., Lenke, L. R. and Escobedo, T., "Strength and Creep Testing of Concrete Used in the Cylindrical Portion of the NUPEC/NRC Prestressed Concrete Containment Vessel," ATR Institute, University of New Mexico, Albuquerque, NM, January, 2000.
28. Lenke, L. R. and Gerstle, W., "Mechanical Property Evaluation of Concrete Used in the NUPEC/NRC Prestressed Concrete Containment Vessel: Prestress and Limit State Test Results," ATR Institute, University of New Mexico, Albuquerque, NM, June, 2001.
29. "PCCV Structural Behavior Test, Basic Plan of Instrumentation for the Test," Nuclear Power Engineering Center, Tokyo, Japan, March, 1992.
30. "Revised Basic Instrumentation Plan for the 1/4 PCCV Model (CTG-12-16)," Nuclear Power Engineering Corporation, Tokyo, Japan, March 16, 1994.
31. R-SN-P-001, "PCCV Instrumentation Plan," Rev. G, Sandia National Laboratories, Albuquerque, NM, February 28, 2001.
32. Dameron, R. A., Zhang, L., Rashid, Y. R., Maxwell, J. S., Vargas, M. S., "Preliminary Analytical Studies of A 1:4-Scale Model of a Prestressed Concrete Containment Vessel Model," R-SI-P-018, ANATECH Corp., San Diego, CA, November, 1997.
33. R-SI-P-002, "PCCV Instrumentation Task Plan," Rev. 2, Sandia National Laboratories, Albuquerque, NM, June, 1999.
34. JPN-12-A-1, "PCCV Structural Behavior Proving Test, Master Plan of the Project," Revision 1, Nuclear Power Engineering Corporation, Tokyo, Japan, June 22, 1994.
35. R-SN-P-007, "Prestressed Concrete Containment Vessel Model Test Plan," Revision B, Sandia National Laboratories, Albuquerque, NM, September, 2000.
36. R-SI-P-005, "ES&H Operating Procedure - Testing of the Prestressed Concrete Containment Vessel (PCCV) Model," Revision B, Sandia National Laboratories, Albuquerque, NM, October 2000.
37. R-SI-P-006, "PCCV Pressurization System Data Package," Revision B, Sandia National Laboratories, Albuquerque, NM, October 2001.
38. Japanese Standard JEAC 4203-1994.
39. MITI Code 501, Article 104.
40. 10CFR50, Appendix J "Primary Reactor Containment Leakage Testing for Water-Cooled Power Reactors."
41. American National Standards. "Leakage Rate Testing of Containment Structures for Nuclear Reactors." ANSI/ANS N45.2-1974.
42. American National Standards "Containment System Leakage Testing Requirements." ANSI/ANS N56.9-1987.
43. NUPEC Liner Examination Report (in Japanese)
44. Procedure of Equipment Hatch Cover Installation, Mitsubishi Heavy Industries, LTD, MH-K12-15, May 26, 2000.
45. Hessheimer, M. F., R. A. Dameron and W. A. von Rieseemann, "A Summary of Containment Integrity Research," Presented at the *Seminar on Containment of Nuclear Reactors* held in conjunction with the 14th International Conference on Structural Mechanics in Reactor Technology (SMiRT 14), Saclay, France, August 15-26, 1997.